A STUDY OF THE ACCRETION FLOW IN ECLIPSING POLARS

CHRISTIAN MICHAEL BRIDGE

Mullard Space Science Laboratory
Department of Space and Climate Physics
University College London

August 2004

A thesis submitted to the University of London
for the degree of Doctor of Philosophy

ProQuest LLC
789 East Eisenhower Parkway
P.O. Box 1346
Ann Arbor, MI 48106-1346

ACKNOWLEDGMENTS

There are many people who have helped and supported me while I have worked on this thesis. Specifically I wish to thank my supervisor Mark Cropper, from whom I have learnt a great deal. I consider myself fortunate to have had the opportunity to work with him.

At MSSL I would like to thank Gavin Ramsay for his help, patience, support and friendship and Mat Page for reading and commenting on this thesis. For help with the theory side of this thesis, and especially Chapter 7, I thank Kinwah Wu.

Further afield, I would like to thank Pasi Hakala, without whom I would not have had the opportunity to use the fire-fly model and the eclipse mapping model. At ESTEC, I thank Michael Perryman for allowing me access to the S-Cam 2 instrument and Jos de Bruijne and Al Reynolds for their subsequent support and help.

Finally, to all those people whom I have met, shared flats with and drank beer with, you all remain my very good friends.

ABSTRACT

This thesis is concerned with the accretion flow in the high magnetic field cataclysmic variables known as polars. I first provide a brief introduction to the subjects discussed in this thesis, followed by an introduction to the instruments used to make the observations: the optical observations were made using the S-Cam 2 superconducting tunnel junction camera and X-ray observations using *XMM-Newton.*

The chapters that follow this are concerned with two polars: HU Aqr and EP Dra. In Chapter 3, I apply an eclipse mapping technique to the optical light curves of HU Aqr to reconstruct the brightness distribution along the accretion flow. In Chapter 4 I discuss the light curves of EP Dra, a system which until now has not been well studied. The light curves of EP Dra all show variability and a unique light curve shape. Based on the observations and the eclipse mapping I make insights into the nature of the accretion flow in these two systems.

Chapter 5 presents modelling of the optical light curves of HU Aqr and EP Dra using a technique based on 'genetically modified fire-flies'. Unlike previous techniques to reconstruct the brightness distribution of the accretion flow, this places as few constraints on the location of the material as possible. This is the first time this technique has been applied to observed light curves.

In Chapter 6 I present *XMM-Newton* observations of EP Dra. I use X-ray and simultaneous optical/UV observations to provide a comparison with the observations of Chapter 4, and provide further insights into the accretion flow in this system.

Finally, I present model accretion flows irradiated by X-ray emission from the accretion shock. This allows the construction of accretion flow temperature profiles, the location of different ionized species along the flow, and the construction of theoretical Doppler maps.

Contents

List of Figures

List of Tables

Chapter 1

Introduction

This thesis is concerned with the flow of accretion material in polars, a particular type of close binary system which is a sub-group of the magnetic cataclysmic variables. I introduce this thesis with a discussion of those aspects of polars which are particularly relevant to subsequent chapters.

1.1 Cataclysmic variables

Cataclysmic variables (CVs) consist of a late main sequence secondary (valid for systems with orbital periods less than $\sim 7 - 8$ h; Smith and Dhillon, 1998) losing material from the inner Lagrangian point (L_1) to form an accretion flow. This material is accreted onto a white dwarf primary through either an accretion disc which forms at the circularisation radius (R_c), or directly along the magnetic field lines of the primary onto one or more accretion regions on the surface of the primary. CVs are ideal for the study of the accretion process for a number of reasons: their proximity to Earth (the nearest being ~ 40 pc away) means that they are bright and relatively unaffected by interstellar absorption; and the timescale of phenomena are relatively short. While the space density of CVs is uncertain, Politano (1996) predicts $\sim 2 \times 10^{-5}\,\mathrm{pc}^{-3}$, which would mean there are $\sim 10^5$ CVs in our galaxy.

As the two stellar components are in close orbit, the tidal interaction of the

primary causes the secondary to be distorted and has the effect of synchronizing the rotational period of the secondary with the binary orbital period. The time scale for the orbital and rotational periods to synchronize is short compared to the life-time of a CV (Warner, 1995), and it is therefore expected that all CVs will have synchronously rotating secondaries. Also, the orbits of the two components are circular.

CVs can be divided into two groups based on the strength of the magnetic moment of the primary, and whether this is sufficiently high as to significantly influence the material in the accretion flow. For magnetic moments of $\mu \lesssim 10^{31}\,\mathrm{G\,cm^{-3}}$ the primary is considered to be of the 'non-magnetic' type and accretion on to the primary results from the transfer of material through an accretion disk which acts as a reservoir of gas. For greater μ the disk is truncated at the inner edge by the magnetic field as material is confined to accrete quasi-radially along the magnetic field lines of the primary: these systems are called the intermediate polars (IPs). For increasing μ the formation of a disk is eventually prevented entirely, and accretion is entirely along the magnetic field lines of the primary: these are the polars, or AM Her systems.

Further discussion in this chapter is confined to those aspects of polars relevant to this thesis. A more detailed review of polars can be found in, for example, Cropper (1990) and Warner (1995). A full discussion of non-magnetic CVs and intermediate polars is referred to, for example, the reviews of Warner (1995) and Hellier (2001).

1.2 Polars

The discovery of the first polar was reported by Tapia (1977a), who observed both linear and circular polarisation of optical light in AM Her. The discovery of circular polarisation led to the conclusion that the primary must have a high magnetic field. For cyclotron emission at the fundamental frequency this leads to a field strength of $\sim$200 MG. The polarisation was later attributed to harmonics of the cyclotron

emission (Visvanathan and Wickramasinghe, 1979), which lowered the implied field strength to ~30 MG. The next polar to be discovered was AN UMa by Krzeminski and Serkowski (1977) who suggested the observed strong polarisation likened the object to AM Her. Subsequently, VV Pup (Tapia, 1977b) and EF Eri (Hearn et al., 1979) were discovered. The term 'polar' as a name for this group of objects was then coined by two Polish astronomers as a reference to the highly polarised emission (Krzeminski and Serkowski, 1977).

There are currently around 67 known polars (as of the time of writing). These span a range of orbital periods from ~78 minutes (CV Hyi; Burwitz et al., 1997) to ~480 minutes (V1309 Ori; Garnavich et al., 1994). Eleven of the known polars are eclipsing systems, that is the inclination, i, of the orbital plane to the line of sight is such that the secondary occults the accretion stream and primary. The eclipse provides an unambiguous time reference for the system which can be used to study phase-dependent phenomena, as several orbital cycles can be observed in one night. The relatively short orbital periods of polars allow the study of the short timescale phenomena which are seen in the light curves of these systems. Figure 1.1 shows the period distribution of the known polars, together with that of the eclipsing polars only. This shows that the distribution of periods for the eclipsing polars is similar to that of the polars as a group, with a peak at 100–125 minutes.

The eclipsing nature can provide constraints on a number of system parameters, including the precise inclination of the system to the line of sight, the size of the primary and the size and location of the accretion region(s). The eclipse also provides the best tool to study the accretion flow material. As the eclipse progresses and the primary star and accretion regions are eclipsed, the dominant source of the observed brightness is the accretion flow. There is a small contribution from the secondary, but this is effectively negligible compared to that of the accretion flow material at most wavelengths. Thus, the eclipse allows a diagnostic of the changing brightness along the trajectory of the accretion flow, and, if the trajectory can be constrained, information about the location of emission from the accretion flow material can be

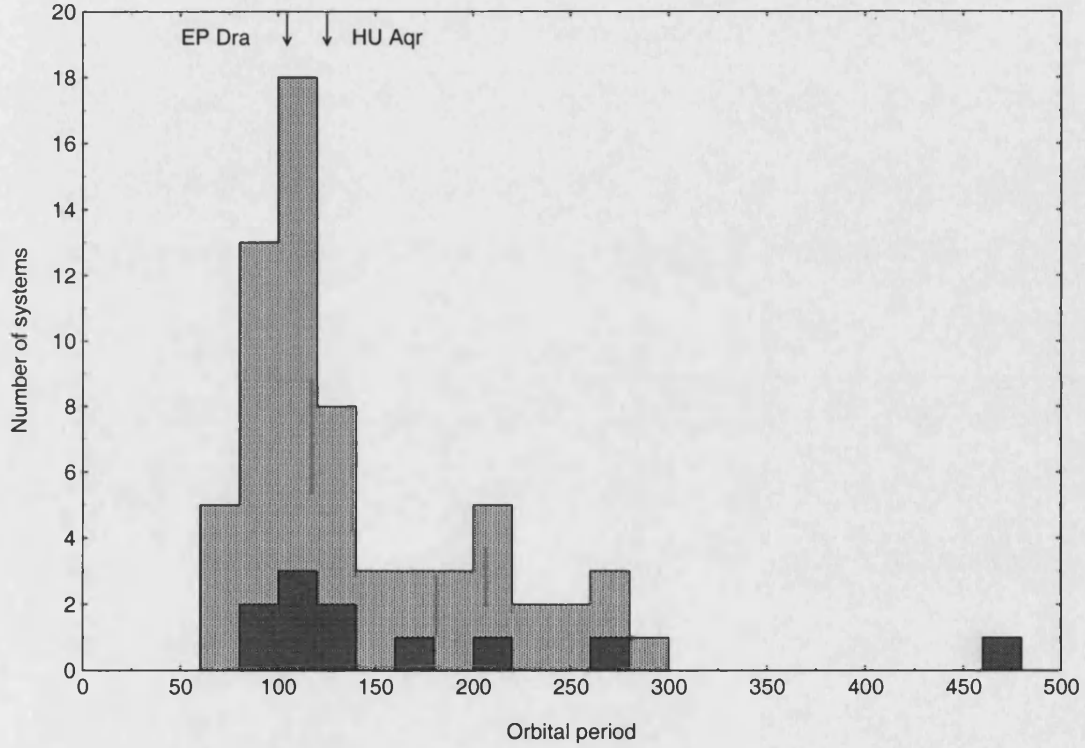

Figure 1.1: The period distribution for all polars (light shading) and for the eclipsing systems (dark shading). Periods were taken from the online catalogue CV Cat (Kube et al., 2003).

inferred.

The magnetic field strength of polars is such that, as well as preventing the formation of an accretion disc, the spin period of the primary is driven to be approximately synchronized with the binary orbital period. For most systems the difference in the periods is extremely small, and the periods can be assumed to be synchronized; however there are four systems known where the asynchronism is greater (at $\sim$1%; Ramsay et al., 2000). These are BY Cam (Silber et al., 1992), V1432 Aql (Patterson et al., 1995), V1500 Cyg (Stockman, 1988) and CD Ind (Schwope et al., 1997a; Ramsay et al., 1999). A spin period of the primary that is synchronized with the binary orbital period means that the orientation of the magnetic field of the primary with respect to the line-of-centres of the two stars is the same over relatively long timescales. This aides the study of the interaction of the material with the magnetic field, and this is seen to vary between successive orbital cycles (e.g. HU Aqr, Glenn et al., 1994).

Observations of polars show strongly variable linearly and circularly polarised emission at optical and IR wavelengths. Spectroscopically polars display high excitation UV, optical and IR spectra (Warner, 1995). A further defining feature of polars is their bright X-ray emission. This originates from the shocked accretion material as it settles on to the surface of the primary and is characterised by a hard bremsstrahlung component together with a softer blackbody component. In the case of the harder X-rays the emission arises directly from the shocked material. The soft X-rays, however originate both from near the base of the accretion column, where the material is cooler (Cropper et al., 2000) and from the reprocessing of hard X-rays intercepted by the primary (the standard model predicts approximately half the hard X-rays are intercepted; Lamb and Masters, 1979; King and Lasota, 1979).

The physics of accretion and the interaction of matter with strong magnetic fields is a complicated subject. Therefore, the reduction of the problem to the fewest number of variables is naturally desirable. In this respect, the polars present the simplest geometrical case. The systems are in circular orbits with generally

synchronous primary spin periods, hence the field geometry is preserved from cycle to cycle. There is no accretion disc, so the system is reduced to four components: primary, secondary, accretion flow and accretion regions. The accretion flow can be further simplified as the flow down the field lines is effectively one-dimensional. Although the accretion flow emits in the same wavelength region as other system components, such as the bright accretion region, by observing eclipsing systems the contribution from the accretion region and primary is obscured from view for part of the orbit.

The magnetic field in polars plays an important role in defining their properties. It is responsible for synchronizing the two stars and can be an important means of removing angular momentum from the binary system. The magnetic field also plays an important role in defining the location of accretion material and effectively defines the geometry of the accretion flow close to the primary. The polars have magnetic field strengths of $B \gtrsim 10\,\mathrm{MG}$, with the highest field system, AR UMa, having $B \sim 230\,\mathrm{MG}$ (from Zeeman-split absorption in the UV; Schmidt et al., 1996).

The precise geometric magnetic field structure of polars has not been determined conclusively. The simplest assumption would be that of a centred dipole; however AM Her (Latham et al., 1981; Wickramasinghe and Martin, 1985), MR Ser (Schwope et al., 1993a), V2301 Oph (Ferrario et al., 1995) and CD Ind (Ramsay et al., 2000), for example, have provided evidence for a non-centred dipole field distribution. Non-centred dipole fields are seen in isolated white dwarfs (Achilleos and Wickramasinghe, 1989), so it is not unreasonable to expect them in polars. Evidence for non-dipolar field structures come from Ferrario et al. (2003) who attempt to model Zeeman features in AR UMa using an offset dipolar field. While they find this to be partially successful, they do not find detailed agreement and conclude that the structure is more complicated than assumed.

1.3 The accretion flow

I have introduced the polars and I have introduced the properties of these systems in the context of CVs. I now introduce the accretion flow and the origin of the mass transfer in polars. I also discuss the role played by the magnetic field in shaping the trajectory of the accretion flow.

The accretion flow or accretion stream is that part of the system between the secondary and the primary, consisting of material lost by the secondary and accreted by the primary. The highly asymmetric optical eclipse light curve profiles in systems such as HU Aqr (Hakala et al., 1993; Schwope et al., 1993b) demonstrated that the accretion stream can contribute 50% or more of the total optical emission. The observation that the stream was so bright in polars, changed the widely accepted view that nearly all the optical emission was from the cyclotron emission regions near the magnetic poles of the primary.

1.3.1 The Roche lobe and mass transfer

The two stars in a polar system are considered to be point masses, meaning that the Roche potential can be used (Kopal, 1959). A potential Φ_R can be defined at any point in the system, and this is a function of the gravitational plus centrifugal forces. Equipotential surfaces, called Roche surfaces, are defined, the shapes of which are a function of the mass ratio q ($= M_2/M_1$; where M_2 is the mass of the secondary and M_1 the mass of the primary) and the binary separation a only. The largest closed equipotential, which is where the potential surfaces of the primary and secondary meet, defines L_1, a saddle point of Φ_R. Figure 1.2 illustrates the closed Roche equipotential for $q = 0.2$. For CVs the secondary fills its Roche lobe, while the primary lies well within it's own Roche lobe: this system is known as a semi-detached system.

Material is lost from the secondary through L_1 by either altering the size of the secondary through evolution of the star, or by shrinking the Roche lobe through

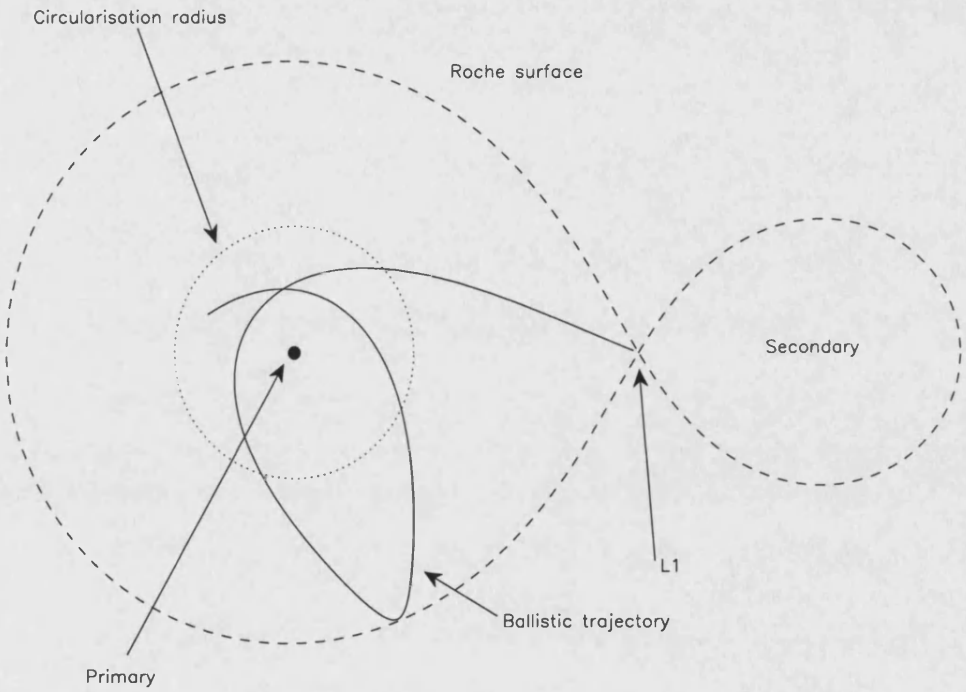

Figure 1.2: The dashed line represents the closed Roche equipotential surface for a binary system with mass ratio $q = M_2/M_1 = 0.2$. The solid line traces the trajectory of a particle released from L_1, which falls under the influence of gravitational forces alone. The particle travels around the primary (here drawn to scale) and approaches the critical Roche surface, before gravitational forces cause the particle to change direction and travel back towards the primary.

angular momentum loss from the system. The secondary may also lose material via instabilities at L_1 causing material to overflow the Roche lobe of the secondary, however this is unlikely to produce high enough mass transfer rates to be consistent with observations (Patterson, 1984). The principle method for causing mass loss is through shrinking the Roche lobe. Angular momentum can be lost from the system, through gravitational radiation (Faulkner, 1971) and also, for systems with orbital periods 3 hrs, magnetic braking (Verbunt and Zwaan, 1981), or perhaps some other unidentified mechanism.

All well studied polars show periods of low mass transfer, "low-states" (e.g. AM Her; Hessman et al., 2000). These occur at irregular intervals and can last from days to years. The variations in mass loss rate were explored by Livio and Pringle (1994) and they concluded that the most likely mechanism is star spots at L_1 which alters the density of the photosphere and is modulated by the magnetic field of the secondary. The overflow rate from the secondary into the Roche lobe of the primary may also be affected by radiation from the primary (King, 1989, 1995), resulting in an inhomogeneous accretion stream from close to L_1 (see Section 1.3.3). However, the origin of these low states is still unclear.

1.3.2 Stream trajectory and threading by the field

The trajectory of the material from L_1 can be approximately divided into two regimes: free-fall and magnetically confined. This view of the accretion stream was introduced by Liebert and Stockman (1985) who also considered a third transition region where the magnetic pressure dominates the thermal pressure of the accretion stream and the material is shattered into blobs of material prior to threading by the magnetic field lines. I consider here the two-part trajectory; the intermediate threading region is discussed in Section 1.3.3.

As the material passes from the secondary star to the Roche lobe of the primary via L_1, the trajectory is deflected by Coriolis forces and makes an angle with the

line-of-centres that is a function of q only (roughly $\sim 20°$ with respect to the line-of-centres; Lubow and Shu, 1975). As the particles fall towards the primary, their velocities increase to supersonic and the density of the stream decreases as the stream expands transversely. If the particles are assumed to leave L_1 with almost zero velocity, then the stream will be confined within the Roche lobe, with low velocities as it approaches the critical Roche surface.

In non-magnetic systems the material will approach the primary, travel past and around the back and out towards the closed Roche surface. The effect of the gravitational potential then causes the material to return back towards the primary to impact upon itself (see Figure 1.2), and through a sustained period of mass transfer, the material will form a disk at a radius R_{circ}. Alternatively, in polars, the magnetic field intercedes and accretion occurs directly along the magnetic field lines of the primary. The condition for direct accretion to occur is that the magnetic field of the primary dominates the accretion flow at a distance that is greater than the closest distance of approach of accretion material to the primary. The material is then constrained to move parallel to the magnetic field line.

The radius from the primary at which the field dominates the flow is called the Alfvén (or magnetospheric) radius R_μ. This defines the radius at which the magnetic pressure of the field ($\propto r^{-6}$ for a dipolar field) is equal to the ram pressure of the infalling material. For spherically symmetric accretion this balance of pressure can be expressed as (Davidson and Ostriker, 1973)

$$\frac{B^2(r)}{8\pi} = \rho(r) v_{in}^2(r) \tag{1.1}$$

The magnetic field strength, $B(r)$, at a distance r from the primary for a dipolar magnetic field is given by the equations $B(r) = \mu/r^3$ where $\mu = BR_1^3$ is the magnetic moment of the star for a surface field of strength B_{R_1}. Hence, R_μ for spherically symmetric infall is proportional to the density ρ and the square of the velocity v_{in} of the infalling stream material.

For steady state accretion the mass accretion rate is given by

$$\dot{M} = 4\pi\rho(r)v_{in}(r)r^2 \tag{1.2}$$

and the infall velocity is comparable to the free-fall velocity $v_{in} \approx v_{ff} = (2GM/r)^{1/2}$. R_μ is then given by

$$R_\mu \approx 2^{-2/7}\mu^{4/7}(GM)^{-1/7}\dot{M}^{-2/7} \text{ cm} \tag{1.3}$$

For non-spherical accretion, the equilibrium condition in Equation 1.1, is satisfied from continuity of mass transfer along the accretion stream, therefore $\dot{M} = \rho\pi\sigma^2 v$, where σ is the radius of the stream. Substituting appropriate values for the constants this gives (Mukai, 1988)

$$R_\mu = 6.3 \times 10^9 \mu_{33}^{4/11}\sigma_9^{4/11}M_1^{-1/11}\dot{M}_{16}^{-2/11} \text{ cm} \tag{1.4}$$

The magnetic moments of polars are $\mu \sim 10^{34}\,\mathrm{G\,cm^3}$ (Warner, 1995), hence R_μ is expect to be a few 10^{10} cm. This is comparable to the distance to L_1 and implies that the magnetic fields of the primary can readily connect with the secondaries, and material can in theory be coupled anywhere between the two binary components (e.g. Schneider and Young, 1980).

Once the material has been threaded on to the magnetic field lines, it can potentially follow the field line to one of two accretion regions where the field line intercepts the surface of the primary. The choice of which magnetic pole the material accretes at is influenced by the orientation of the system, with the condition that the material cannot pass outside the Roche lobe of the primary. However the material must have appropriate velocities to leave the orbital plane against the gravitational potential. A magnetic pole located at high-latitude (with respect to the spin axis of the primary) means the material must travel some distance in the Roche lobe of the primary before threading. This is because the magnetic fields for high-latitude magnetic poles pass outside the Roche lobe of the primary for large R_μ (Ferrario et al., 1989). For low-latitude magnetic poles, accretion can occur directly

from L_1, however only at one footpoint of the field line. The maximum distance $R_{\mu,max}$ from the primary that will lead to accretion along closed field lines can be estimated using the criterion that the field line must be entirely enclosed within the Roche lobe of the primary.

1.3.3 Inhomogeneous accretion flows

I have set out a prescription for the accretion flow in polars. This has taken the form of an initially ballistic trajectory followed by a magnetically confined trajectory channeling the material to the surface of the primary. In reality a treatment of the transition between the ballistic and the magnetic dominated region is not simple. Different parts of the accretion stream material will satisfy the equilibrium condition of Equation 1.1 at different points along the ballistic trajectory. The actual location of threading for a particular part of the accretion stream will depend upon the density of the material, and the orientation of the magnetic field lines relative to the infalling material This means that material will not necessarily all be threaded by the magnetic field at the same point.

The cross-sectional density profile of the stream can be deduced from absorption dips seen in X-ray, optical and IR light curves of high-inclination polars (Watson et al., 1989). These dips occur before the eclipse of the primary and the accretion region by the secondary, and are caused by the eclipse of the accretion region by the accretion stream (Watson et al., 1989; Watson, 1995). Inhomogeneous density profiles were developed by Stockman and Lubenow (1987) and Stockman (1988), who constructed density profile functions, such as Gaussian or exponential, for the accretion stream. Evidence for inhomogeneous accretion streams is seen in the dips in several systems, and is seen to vary from cycle to cycle, for example EF Eri (Watson et al., 1989), EK UMa (Clayton and Osborne, 1994) and UZ For (Watson, 1995).

As the magnetic pressure increases more rapidly than the accretion stream ma-

terial can adjust sub-sonically, it is shattered into 'blobs' or filaments of material (Liebert and Stockman, 1985). A highly inhomogeneous stream consisting of dense filaments or 'blobs' of material embedded in a rarefied medium was suggested by Kuijpers and Pringle (1982). Evidence for this scenario comes from the observed wavelength dependence of the dip in V1432 Aql, which is not consistent with free–free absorption in a homogeneous medium (Watson et al., 1995), but is in agreement with absorption in a stream of blobs of dense material in a less dense, optically thin medium.

The shattering of the accretion stream occurs as instabilities arise in the plasma which result in fragmentation of the accretion stream into diamagnetic blobs (that is, the material is slightly repelled by the magnetic field) and fine droplets. There are two instabilities that can operate. Firstly, Kelvin-Helmholtz instabilities which are caused by a strong shear in a fluid with a density gradient. This probably operates along the entire length of the accretion flow and results in the shredding of the accretion stream material in to droplets. The second instability is the Rayleigh-Taylor instability which occurs when a dense fluid is supported against gravity by a less-dense fluid. This occurs where the accretion stream meets the magnetic field of the primary and any lower density trapped stream material, and will result in large diamagnetic blobs of material.

Whichever method operates, the fate of the shredded and divided material depends on the relative time-scales of various physical processes as the material passes through the magnetic field. Blobs of material that have magnetic field penetration timescales greater than their dynamical timescales will plough through the field via a series of reconnections (Li, 1999), at each reconnection event the surface of the blob is eroded by Kelvin-Helmholtz processes producing successively smaller sized blobs. Figure 1.3 from Li (1999) illustrates this process and defines the width of the threading region as the distance over which the material is completely shredded. The efficiencies of the instability and the drag timescale will determine whether the blob is eroded completely by the time it reaches the surface of the primary.

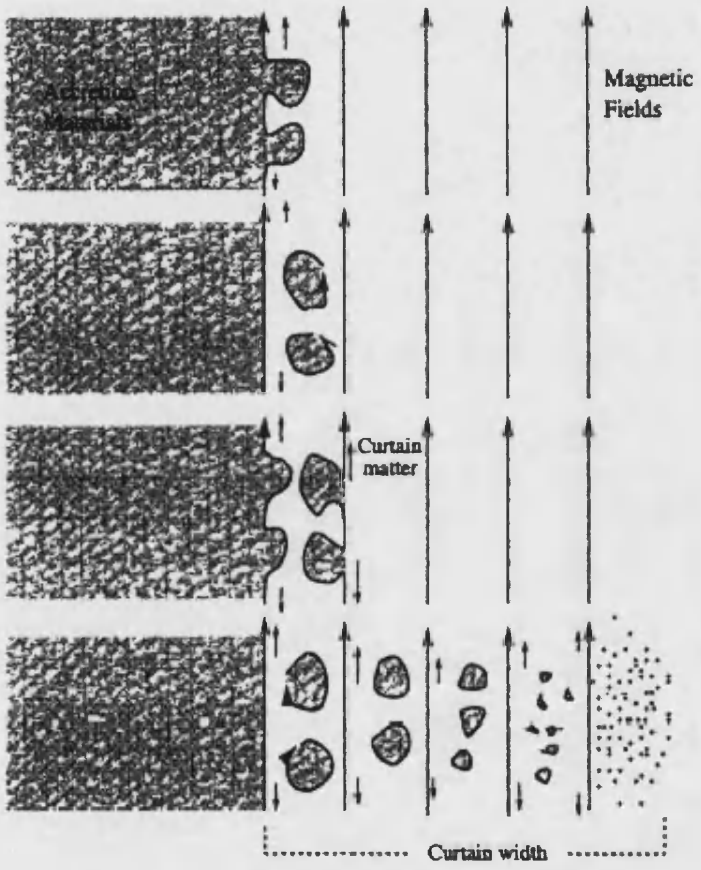

Figure 1.3: The process of accretion stream shredding at the magnetic field boundary. At each reconnection the surface layers of the blob are either magnetized or stripped to supply the accretion curtain with material. From Li (1999).

A blobby accretion flow may also be formed at L_1 from inhomogeneous mass transfer modulated by magnetic activity on the secondary around this region (Cropper and Warner, 1986). This will produce blobs of size similar to the diameter of the L_1 nozzle (Cropper and Warner, 1986). The size of blobs can be estimated from observations of flaring activity in the light curves of polars. Cropper and Warner (1986) observed strong flaring behaviour in the light curves of VV Pup. These were typically 25 s in duration, and provide an estimated blob length of $\sim 1.5 \times 10^9$ cm. Harrop-Allin (1999) concludes that the flickering observed in light curves of HU Aqr is due to the impact of these blobs of material in the accretion region. They estimate that this occurs on a time scale of ~ 30 s, and hence the length of blobs at $R_\mu = 0.2a$ is $\sim 9.3 \times 10^8$ cm. Constraints on blob sizes and numbers can also be deduced from observations of absorption dips. Watson et al. (1995) deduce a blob radius $r_b \lesssim 10^6$ cm and that there are more than $\sim$4000 in the stream at any given time.

The blobby accretion model is suggested both to explain the flaring seen in many systems, and also as a partial solution to the observed ratio of soft-to-hard X-ray flux being larger than that observed. The standard model for the one-dimensional accretion in polars, constrained by a magnetic field (Lamb and Masters, 1979; King and Lasota, 1979), predicts that the ratio should be 0.5. Observations have shown that this is not the case in many systems, particularly those observed with *ROSAT* (see Ramsay et al., 1994; Beuermann and Burwitz, 1995), which have a higher soft-to-hard ratio. The idea of an inhomogeneous accretion stream was further developed by Frank et al. (1988, 1992). Any blobs surviving from the threading region could have sufficient ram pressure to penetrate into the photosphere of the primary and create a mini-column. These blobs then thermalise in the photosphere and radiate at soft X-ray wavelengths, and may also be responsible for flaring seen in the light curves.

While Ramsay and Cropper (2004) have re-examined the *ROSAT* observations and concluded that many of the discrepancies observed in the *ROSAT* data can be

resolved with better calibration of the observations, there still remain a number of systems which show a soft X-ray excess (Ramsay and Cropper, 2004). It is suggested that this may be due to the interaction of the accretion stream with the magnetic field at the threading region.

1.3.4 Heating and cooling

Having now introduced a prescription for the location of the accretion stream material, and how this material is threaded by the magnetic field lines, I explore ways in which the stream is heated and cooled. This is important to understand in order to make progress in locating the bright emission regions and for understanding why the accretion stream contributes so much brightness to the light curves.

There are a number of mechanisms that can contribute to the heating of the accretion stream material. These include irradiation, collisional heating within the accretion stream and heating from the interaction of the accretion stream material with the magnetic field. As the accretion stream material approaches the primary, irradiative heating by X-rays from the accretion regions becomes increasingly important, particularly for the magnetically confined material which presents a large surface area to the accretion region on the primary. The accretion stream material is seen to be a good absorber of soft X-rays and EUV emission from eclipse light curves (e.g. Schwope et al., 2001; Watson et al., 1995). The ballistic stream, however, is likely to be dominated by collisional heating, and must at least be partially ionized, or else it would not interact with the magnetic field and be threaded onto the field lines.

Other possible heating mechanisms are compression of threaded material by converging field lines, and heating from hydromagnetic shocks (Liebert and Stockman, 1985; Hameury et al., 1986), magnetic reconnection or turbulence (Li, 1999), ohmic heating and collisional ionization (Ferrario and Wehrse, 1999; Harrop-Allin et al., 1999a). The secondaries can be strongly irradiated themselves (e.g. Schwope et al.,

1997b) by hard X-ray emission, which is reprocessed and emitted at softer X-ray wavelengths, resulting in heated material leaving L_1.

The majority of the emission in polars is from the post-shock flow just above the surface of the primary. Material is shocked and heated to $\sim 10^8$ K (e.g. King and Lasota, 1979), and then cools radiatively as it settles on to the surface of the primary. This cooling is both radiative, through bremsstrahlung emission at hard X-ray wavelengths and cyclotron emission in the optical and IR, and perhaps via Compton cooling for higher mass systems. The majority of the rest of the accretion stream, by contrast, emits through a combination of continuum (free–free), bound–free and line emission. The continuum emission exceeds the line emission (Liebert and Stockman, 1985; Harrop-Allin, 1999), and strong continuum emission along the entire length of the accretion stream is evident in eclipsing polars. The contribution from line-emission in the UV can be significant, and is caused by the hard X-ray emission from the post-shock material being intercepted by the accretion stream and emitted at UV wavelengths. The threading region may also be a source of cooling if gas adjusts through a series of small shocks, the accretion stream material will be cooled rapidly by continuum radiation and will be almost isothermal (Liebert and Stockman, 1985).

For a given mass transfer rate, the stronger the field, the more efficient the cyclotron cooling. This means the accretion column is slightly hotter at the shock, and also smaller in vertical extent (Wu et al., 1994) as the material cools more efficiently over a shorter distance. The balance between the cyclotron cooling and the bremsstrahlung also depends on the density of the stream material. High magnetic fields and low stream densities lead to cyclotron domination, while low magnetic fields and high stream densities lead to bremsstrahlung domination (Lamb and Masters, 1979). When bremsstrahlung is the dominant cooling mechanism the temperature of the ions and the electrons is equal ($T_i = T_e$) at each point, to a good approximation. This is known as the "single fluid" approximation. When cyclotron cooling dominates, the electrons can cool faster than they can be heated by colli-

sions with ions ($T_{cool} \ll T_{i,e}$) and the electrons and ions no longer have the same temperature. This is the "two-fluid" regime.

1.4 Techniques to study the accretion stream

There are several methods for studying the accretion flow in polars. If the polar is an eclipsing system then an eclipse mapping technique can be used. There are many variations of this technique which have been applied to both emission lines and continuum observations. Eclipse mapping techniques have been successfully employed by, for example, Hakala et al. (1993), Harrop-Allin (1999), Kube et al. (2000) and Vrielmann and Schwope (2001). These methods are discussed in later chapters.

Further to eclipse mapping methods there is Doppler tomography (see for example Schwope et al., 1999; Marsh, 2001, for overviews). Doppler tomography was first applied in the context of polars to VV Pup and the possible polar GQ Mus by Diaz and Steiner (1994a,b). This followed the extensive use of Doppler imaging in the study of non-magnetic CVs, following the work of Marsh and Horne (1988).

Doppler tomography aims to recreate the location of the emission line regions in the target system using observed emission line profiles as the projection of the velocity field along the line-of-sight. With time-resolved spectra of suitable resolution in radial velocity and binary phase, a two-dimensional map of the system can be created using observations of half a binary orbit. Further modelling is then required as a unique and straightforward conversion from Doppler space to real space is not possible because of the degeneracy of the orbital and streaming velocities in polars.

The application of Doppler tomography to polars breaks two of the implicit assumption of the technique: that the radiation is optically thin, and that it is bound to the orbital plane. The first of these is violated by the presence of optically thick radiating or absorbing surfaces, and the second by the accretion flow being confined to the magnetic field lines of the primary and lifted out of the orbital plane.

Techniques used to improve the interpretation of Doppler maps and circumvent these limitations include the decomposition of the line profiles, for example by removing narrow emission line components from the secondary, and mapping of the emission lines on to predefined surfaces, for example Roche tomography (Rutten and Dhillon, 1994).

1.5 Individual objects

I have presented those issues that are relevant to the study of the accretion flows in polars. I now briefly introduce the two eclipsing polars that I investigate in detail in this thesis: these are HU Aquarii and EP Draconis.

EP Draconis (EP Dra)

EP Dra has an orbital period of 104.6 minutes (see Figure 1.1), and was identified as the optical counterpart to a hard X-ray source in the *HEAO 1* survey by Remillard et al. (1991). The system is faint, with an average faint phase brightness of V$\simeq$18 in 1992 and 1995 and a maximum brightness of V$\simeq$17 (Schwope and Mengel, 1997). There is evidence for accretion at one region only on the surface of the primary (Remillard et al., 1991). Schlegel and Mukai (1995) observed EP Dra with the *ROSAT*-PSPC, the light curves showing both X-ray bright and faint phases, typical of a polar. They also found EP Dra to exhibit a soft blackbody component of temperature $\sim$ 15 – 19 eV. A linear ephemeris was calculated by Schwope and Mengel (1997) which corrected the previous *ROSAT*-PSPC ephemeris by a phase shift of $\sim$0.13.

HU Aquarii (HU Aqr)

HU Aqr was reported independently by Schwope et al. (1993a) and Hakala et al. (1993) as the optical counterpart of sources detected in the *ROSAT*-PSPC and -WFC. The system has an orbital period of 125.0 minutes (see Figure 1.1), and is the

brightest eclipsing polar known, with an out-of-eclipse $V = 14.6 - 15.1$ (Schwope et al., 2003). The magnetic field strength is estimated at $B \approx 34\,\mathrm{MG}$ (Schwope et al., 2003), lower than the original estimate from Schwope et al. (1993a) and of Glenn et al. (1994) of $B = 36\,\mathrm{MG}$. HU Aqr is one of the more extensively studied eclipsing polars. Optical spectroscopy is presented in Glenn et al. (1994) and cyclotron spectroscopy in Schwope et al. (2003), and the X-ray observations are discussed in detail in Schwope et al. (2001). Howell et al. (2002) present EUV and IR observations showing dips in the light curves caused by the accretion stream obscuring the accretion region. They found that the accretion region had increased in radius and temperature since previous observations, and that the IR flux was dominated by cyclotron emission from above the surface of the primary. The secondary in HU Aqr has been imaged using Roche tomography by Watson et al. (2003) which can be used to constrain system parameters such as the masses of the two component stars and the inclination. Watson et al. (2003) conclude that the accretion stream shields the secondary from the accretion region, but itself contributes to the irradiation by the secondary in HU Aqr. Continuum and line emission light curves have been used to infer the distribution of brightness along the accretion stream trajectory by Hakala (1995); Harrop-Allin (1999); Vrielmann and Schwope (2001) using eclipse mapping techniques.

1.6 Aim of this thesis

Having presented the background for the study of the accretion flow in polars, I now outline the issues that this thesis will address in the subsequent chapters.

- The actual path of the accretion stream has yet to be determined in polars, because it is difficult to isolate the emission from the accretion flow material from that of the rest of the system. The interaction of the accretion flow with the magnetic field, and the location of the threading region has generally been assumed for the purposes of constructing models of the accretion flow.

Therefore, I examine whether the trajectory of accretion material, R_μ and the threading region can be better constrained using eclipse light curves and Eclipse Mapping techniques.

- The accretion streams in polars have been observed to be particularly bright at optical wavelengths. In light of previous eclipse mapping techniques and attempts to locate the origin of the bright emission, can the previous techniques be improved to further constrain the location of the accretion flow material?

- If the location of bright emission regions along the accretion flow can be determined, is it possible to make progress in understanding why these particular regions are bright? Can this be done using models describing the heating and cooling of accretion material?

- Finally, how does this work impact upon the overall understanding of the accretion flow in polars, and how can this work be taken forward?

Chapter 2

Instrumental overview

In this chapter I briefly describe the instruments which were used for the observations described in this thesis. These are the superconducting tunnel junction (STJ) detector S-Cam 2, which was used to take the optical observations in Chapters 3, 4 and 5, and *XMM-Newton* the X-ray Multi-Mirror satellite which was used for the observations presented in Chapter 6.

2.1 The STJ instrument S-Cam 2

The CCD detector has been extensively used for astronomical observations for over two decades. While modern CCD based instruments achieve good quantum efficiencies and relatively high time resolutions, they still rely on filters to provide colour information. This degrades the efficiency of the instrument because of the restricted transmission through the filter material and the need to use a sequence of filters. The introduction of the STJ-based detector circumvents these limitations as an STJ provides *intrinsic* energy resolution. The instrument throughput is essentially close to unity, limited only by the optical materials used in its construction.

The use of STJs for astronomical optical photon counting was first proposed by Perryman et al. (1993), with the demonstration of single optical photon counting with energy resolution reported by Peacock et al. (1996). This group has developed

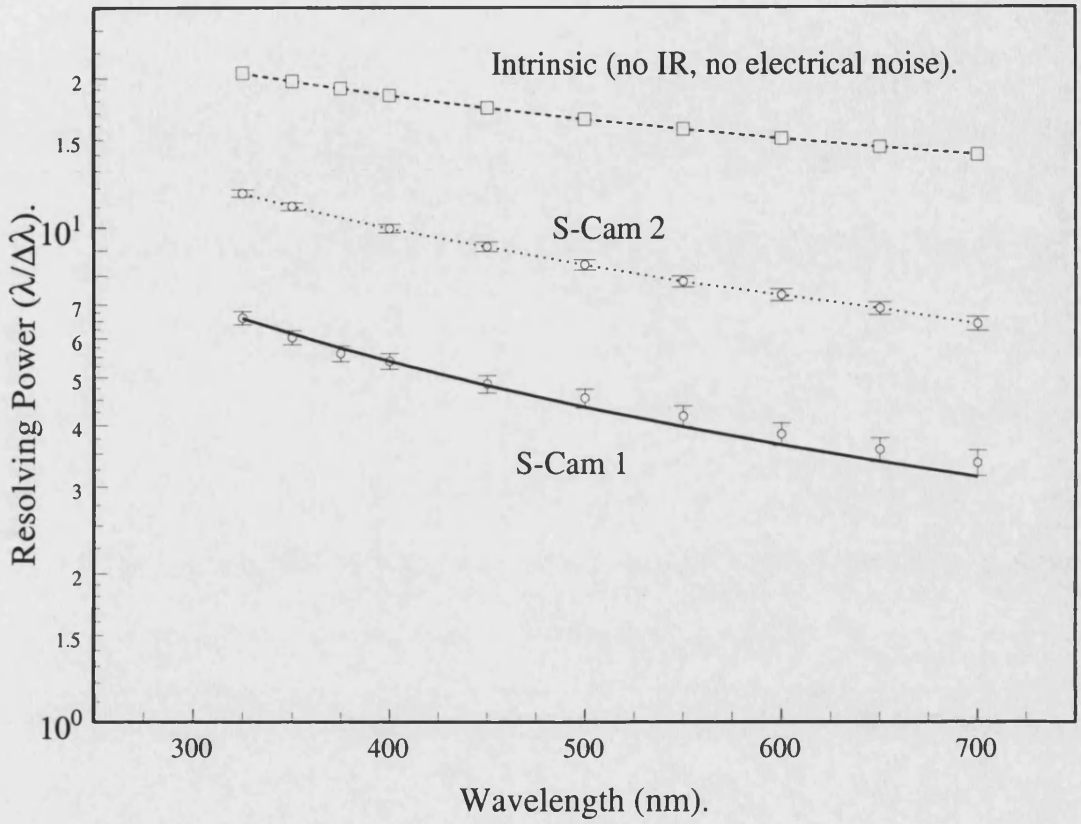

Figure 2.1: The resolving power of a typical S-Cam 1 (solid line) and S-Cam 2 (dotted line) pixel compared with the intrinsic resolving power of an STJ (upper dashed line) (from Rando et al., 2000).

an STJ-based camera, S-Cam, for use at optical wavelengths. The instrument used for these observations, S-Cam 2 is a second prototype camera with increased detector resolving power compared to that of the original S-Cam instrument (see Figure 2.1) and a factor of approximately 5 increase in the maximum count rate per pixel (see Section 2.1.3).

2.1.1 Principles of an STJ

The ability of an STJ to provide the energy of an incident photon results from the creation of free charge by the breaking of Cooper pairs (two electrons which have a net attraction at sufficiently low temperatures) in the superconductor. For a superconductor the energy gap between the ground state and the first excited state is more than 10^3 times smaller than the energy gap between the valence and conduction bands of a semiconductor (Bardeen et al., 1957). This means that a large number of free charge carriers, called quasi-particles, are created, compared to, in general, only one free electron for a semiconductor. At sufficiently low temperatures, which are about an order of magnitude lower than the superconductor's critical temperature, the number of excess charge carriers created is inversely proportional to the photon wavelength.

A signal is detected when the quasi-particles created by the incident photon tunnel across an insulating barrier under the influence of an applied d.c. potential. The barrier is required to prevent the flow of current when there are no incident photons, and hence no signal. The barrier is a thin layer (1 nm) of Aluminium Oxide sandwiched between two 100 nm thick layers of the superconducting material Tantalum. This is an individual STJ, or Josephson junction (Giaever, 1960; Josephson, 1962). A magnetic bias must be applied to the STJ to remove the effect of the Josephson current, which is the tunneling of Cooper pairs under zero voltage bias when in the superconducting state. Figure 2.2 shows a schematic diagram of an individual STJ pixel.

The tunneling of a quasi-particle across the barrier can occur several times within the typical lifetime of the particle (Gray, 1978). Each tunneling event then adds to the overall signal. This multiple tunneling enhances the responsivity of the detector, but this combined with a fluctuation in the number of quasiparticles created by the incident photon and the noise of the tunneling process from the multiple tunneling events, provides a limiting spectral resolution (Verhoeve et al., 2000).

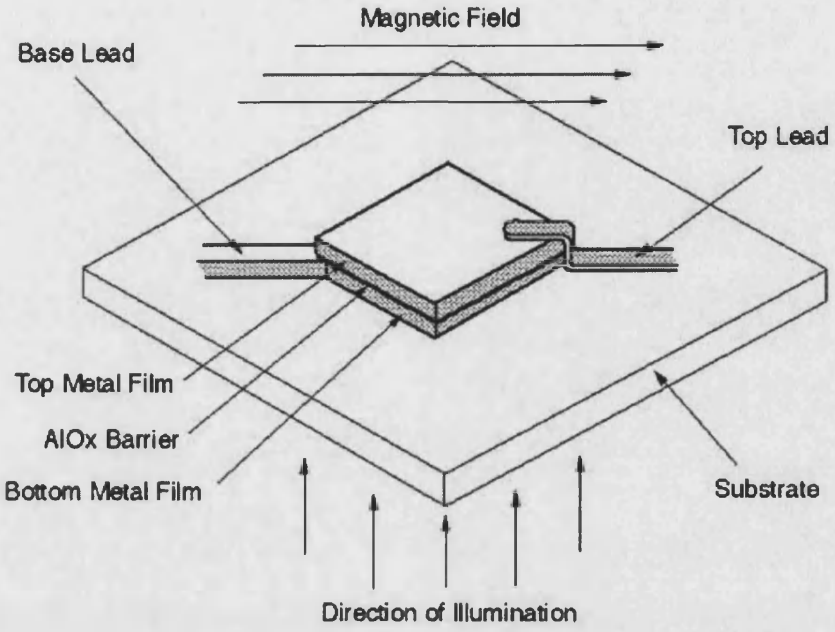

Figure 2.2: A schematic of an STJ pixel (courtesy of the ESA, RSSD web site).

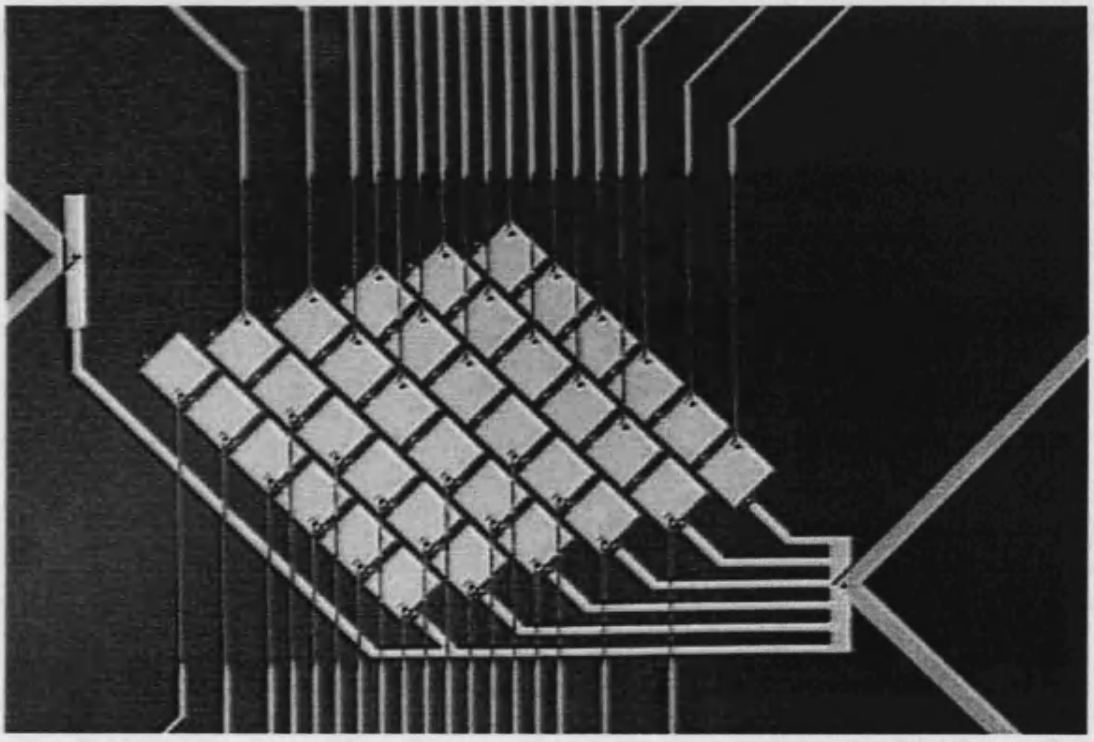

Figure 2.3: The S-Cam 2 STJ array pixel layout. Each pixel is $25 \times 25\,\mu m^2$, with gaps of $\sim 4\,\mu m$ between neighbouring pixels (courtesy of the ESA, RSSD web site).

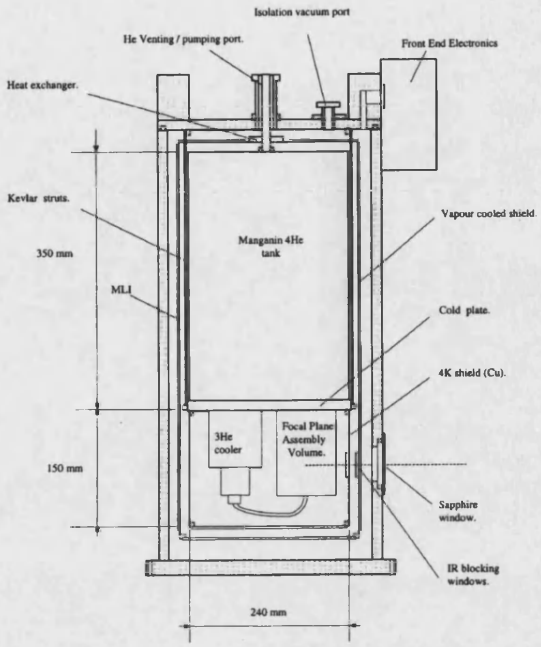

Figure 2.4: The S-Cam 2 cryostat (Verveer et al., 1999, their figure 1)

2.1.2 A Tantalum STJ array

The detector itself is an array of 36 STJ pixels deposited on a sapphire substrate. Each pixel is $25 \times 25\,\mu$m in size with a gap between the pixels of $4\,\mu$m. The pixels provide a field-of-view of $\sim 0.6 \times 0.6\,\mathrm{arcsec}^2$ per pixel, or $\sim 4 \times 4\,\mathrm{arcsec}^2$ for the whole array.

The pixels are connected together in common on the bottom surface (the base lead in contact with the substrate, see Figure 2.2), and each pixel has an individual top connection through which the STJ is readout via its own pre-amplifier and analogue electronics. The individual pixel readout is necessary to prevent a degradation in performance of the instrument, as using a multi-pixel readout technique with current technology places very stringent requirements on the manufacturing of the detector pixel array, and also reduces the maximum count rate handling capability (Verveer et al., 1999). Consequently, the shape of the array is heavily influenced

by the need to accommodate all the connections. The resulting pixel arrangement for S-Cam 2 is a 6×6 pattern, each row is offset from the next to form a diamond shape, as shown in Figure 2.3.

In order to reach the necessary operating temperature for S-Cam 2, a ^{4}He cryostat is used to enclose a ^{3}He cryosorption refrigerator (Verveer et al., 1999). The cryostat operates at 330 mK, well below the critical temperature of Tantalum (4.2 K). The design of the cryostat system aims to reduce the use of magnetic materials as much as possible, in order to maintain as uniform a magnetic bias as possible across the STJ array and avoid degradation of the detector performance. Figure 2.4 shows a diagram of the cryostat from Verveer et al. (1999).

The array is back-illuminated through the sapphire substrate. While individual STJs can be front-illuminated, when mounted in an array a dielectric coating is necessary on the front surface to insulate the electrical wiring for the individual STJ connections.

2.1.3 Performance of S-Cam 2

The intrinsic wavelength response of S-Cam 2 is very broad, from X-ray to the far IR. This range is limited in use to $\sim 340 - 700$ nm by the atmosphere at short wavelengths and optical elements to suppress IR photons at longer wavelengths.

The quantum efficiency of STJ based detectors is higher than CCD based detectors: between the U-band and R-band the quantum efficiency of pixels without optical refractive index matching coatings is greater than 70%. This drops to a few percent in the IR (Peacock et al., 1998), mainly because of reflection from the Tantalum layers. The instrumental dark current is negligible because of the low operating temperature.

The spectral resolution of an STJ array is constrained by the intrinsic properties of the material, and also by the electronics processing chain and contamination by infrared photons. The overall resolution of S-Cam 2 is $\Delta\lambda \approx 30$, 60 and 100 nm at λ

= 350, 500 and 650 nm respectively. The resolving power of an STJ constructed from Hafnium and Molybdenum is better than that of an STJ constructed from Tantalum (Verhoeve et al., 2000). However, while some junctions have been constructed using these materials, the technology has not developed far enough for the construction of arrays of STJs made from these materials.

Tantalum STJs are sensitive to infrared photons at wavelengths beyond about $2\,\mu$m (K-band). This sensitivity decreases at $5\,\mu$m and recovers at wavelengths longer than $100\,\mu$m. The suppression of infrared photons is important as they reduce the resolution of the instrument at low pulse heights and can contribute to heating of the substrate. This reduction in resolution is caused by the contribution of the small charge generated by an infrared photon during the detection of optical photons. As the individual energy of each infrared photon is small, for a given flux the photon number is high, and hence the probability of a photon arriving within the time constraints of the pulse-counting electronics is high. The addition of these small amounts of charge broadens the spectral peak. A large enough photon flux can also lead to a saturation of the device by exceeding the maximum count rate of the pulse-counting electronics.

A number of measures are taken to reduce the IR photon flux. Within the cryostat a cold copper baffle is used to reduce the field-of-view of the instrument and so limit the effects of residual IR radiation, and two filters are used to minimise the flux from the cryostat window and baffles. There are also a number of IR filters along the beam path which suppress the IR flux from the telescope. This provides an upper limit on the long wavelength range of the instrument and also has the consequent effect of reducing the optical throughput by $\sim$40%.

While the STJ is by nature a high-speed device, the actual operational speed is limited primarily by the electronics. The time resolution of S-Cam 2 is limited to $\sim 5\,\mu$s, and the arrival time of a photon is measured with respect to a GPS signal which is specified to remain within $1\,\mu$s of UTC. For S-Cam 2 there is a maximum count rate of 5 000 counts s^{-1} pixel^{-1}, with the resolution degrading slightly with

increasing count rate, mostly due to pile-up.

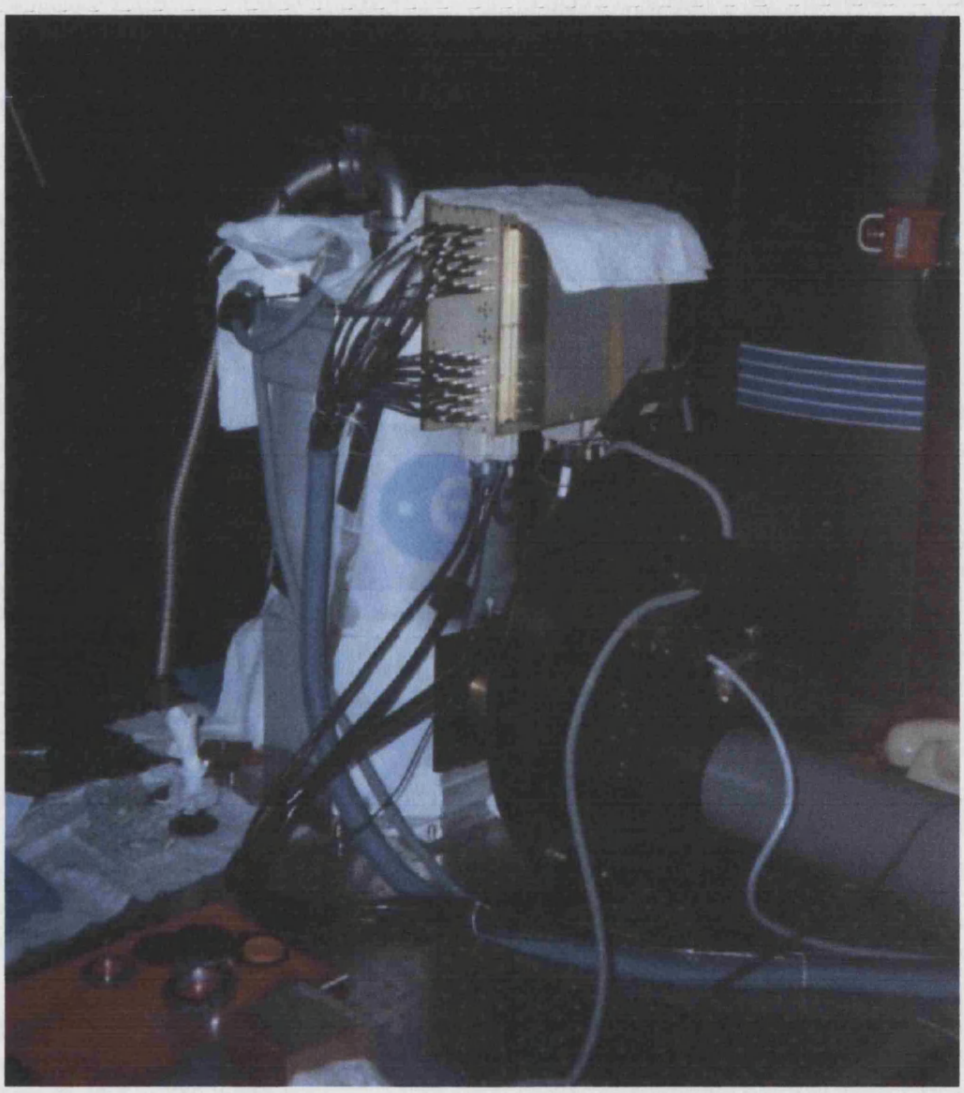

Figure 2.5: The S-Cam 2 instrument at the Nasmyth focus of the William Herschel Telescope, La Palma. The pipe in the lower right encloses the telescope light feed and leads to the instrument filter wheel. Above this are the individual pixel electronics. The cryostat is partially visible behind the filter wheel. (Photograph by the author).

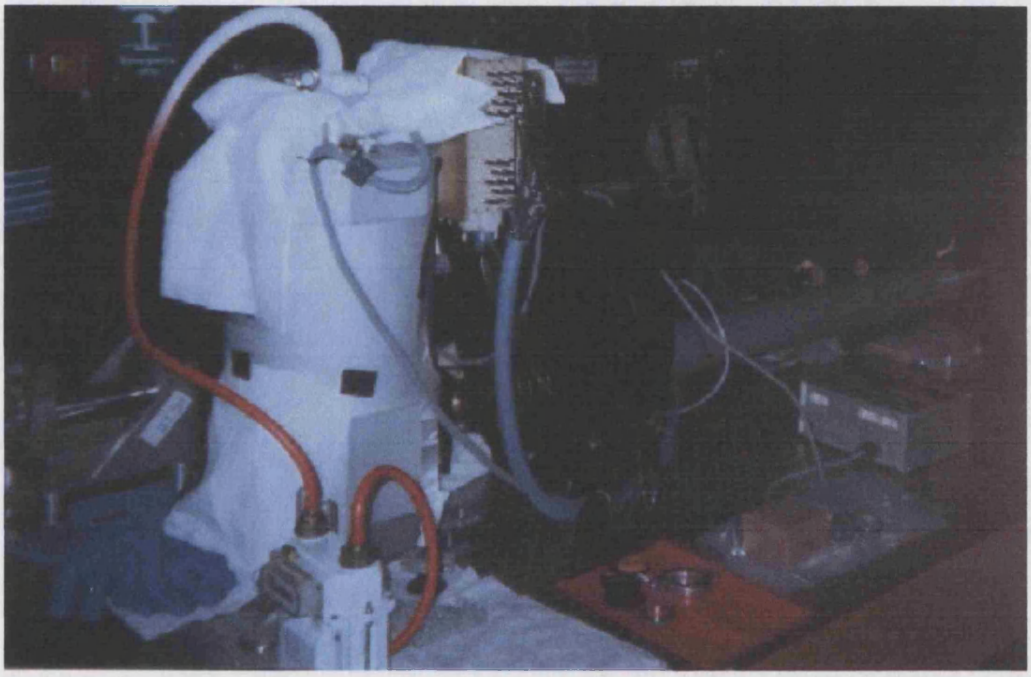

Figure 2.6: The S-Cam 2 instrument from the rear. The cryostat is visible to the left, with the filter wheel and light guide to the right. (Photograph by the author).

2.2 *XMM-Newton*

The European Space Agency's (ESA) X-ray Multi-Mirror (XMM) satellite is the second cornerstone mission of the ESA Horizon 2000 programme. *XMM-Newton* provides high-throughput X-ray spectroscopy with simultaneous optical/UV observations (Jansen et al., 2001). The observatory is 10 m long and weighs 3.9 tonnes, and at its launch it was the largest scientific satellite built in Europe. It was launched on an Ariane 5 rocket from the European Space Port at Kourou in French Guiana, in December 1999.

The orbit of *XMM-Newton* varies from 7 000 km to 114 000 km at an inclination of $\sim$–40°. The orbit is approximately 48 hours, and the satellite is in ground contact for 40 hours of each orbit. The lower orbital velocity at apogee means that most of its operations take place at high altitudes.

The satellite carries three X-ray telescopes and one optical/UV telescope for simultaneous observations at different wavelengths. The X-ray telescopes use 58 thin, gold-coated grazing-incidence mirrors, 'nested' inside one another to focus X-rays on to three detectors.

XMM-Newton has the largest effective area of any imaging X-ray satellite at 4 650 cm^2 (at 1 keV; see Figure 2.7 for a comparison with other X-ray satellites). The on-axis 1.5 keV PSF at FWHM for the EPIC cameras is 4.3 arcsec for MOS-1, 4.4 arcsec for MOS-2 and <12.5 arcsec for pn (Ehle et al., 2003).

2.2.1 *XMM* Detectors

EPIC

Two different types of detector are located at the foci of the three X-ray telescopes: two MOS (Metal Oxide Semiconductor; Turner and et al., 2001) CCD cameras, and one pn (Strüder and et al., 2001) CCD camera. These are the European Photon Imaging Cameras (EPIC), and each CCD type has different features, both in their fundamental structure and their operating characteristics.

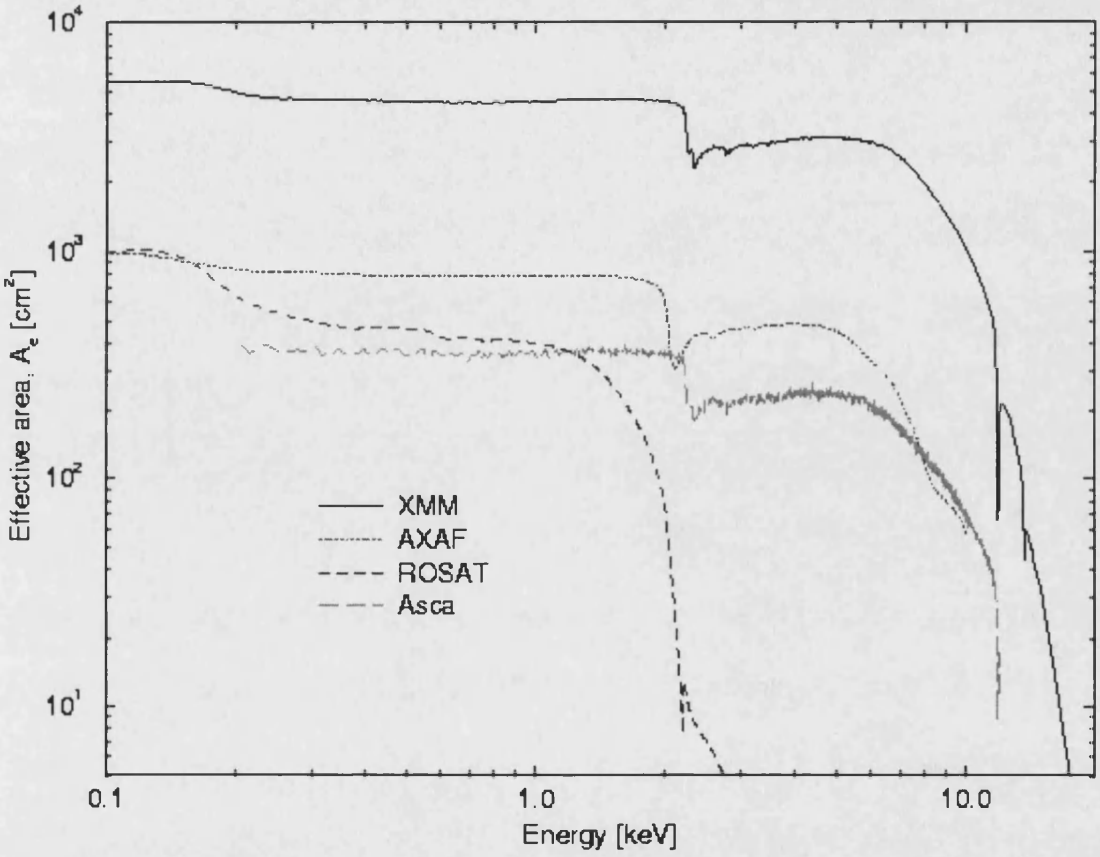

Figure 2.7: The on-axis effective area of all *XMM-Newton* mirror modules, by comparison with those of other X-ray satellites (Dahlem, 1999).

The spectral resolution of the MOS cameras is ~20−50, with a bandpass of 0.15 − 12 keV. Each camera consists of 7 front-illuminated CCDs, slightly offset from coplanar to follow the curvature of the prime focus surface, and to allow connections to the central CCD. The single pn detector has higher photon throughput and wider overall energy response, with a faster readout time than the MOS CCDs. It receives all of the incident X-ray flux from one of the X-ray telescopes. This falls onto 12 CCDs, fabricated on a single silicon wafer. The spectral resolution is again ~20−50 across a bandpass of 0.15 − 12 keV.

RGS

For two of the three telescopes (behind which the EPIC MOS cameras are located), the incident X-ray flux is split approximately in half, and each EPIC camera shares the flux with a Reflection Grating Spectrometer. The two RGS (den Herder and et al, 2001) are therefore illuminated with ~50% of the incident X-rays, which are dispersed onto a linear array of 9 CCDs. The RGS provides X-ray spectroscopy with a resolution of 0.04 and 0.025 Å (in the –1 and –2 orders respectively, at 1 keV). The energy range covers 0.33 − 2.5 keV, which is particularly rich in X-ray spectral lines.

OM

The optical monitor (OM; Mason and et al., 2001) is a coaligned 30 cm telescope. It has a wavelength range of 1700−6000 Å and is designed to provide simultaneous multi-wavelength observations of X-ray targets in four wavelength bands down to 24th magnitude.

To achieve this high sensitivity it uses micro-channel plate (MCP) intensified CCDs (MICs). There are two MCPs behind each other, which amplify the strength of the incoming signal by a factor of about 100 000 before it reaches the CCD. The PSF FWHM varies depending on the filter used, but is between 1.35 arcsec for the V-filter and 1.85 arcsec for the UVW2-filter (Ehle et al., 2003). It is also possible to obtain low resolution grism spectra, as well as high time resolution photometry.

Chapter 3

STJ Observations of the Eclipsing Polar HU Aqr

In this chapter I apply an eclipse mapping technique to observations of the eclipsing polar HU Aqr. A shortened version of this chapter has been published in *Monthly Notices of the Royal Astronomical Society* (Bridge et al., 2002).

3.1 Observations

The observations of HU Aqr presented here were taken using the S-Cam 2 (see Chapter 2) mounted at the Nasmyth focus of the William Herschel Telescope, La Palma, during 2000 October 2/3 and 3/4. Details of the observations are given in Table 3.1 where the cycle numbers are relative to the linear ephemeris of Schwope et al. (2001).

A total of five eclipses of HU Aqr were recorded. The ingress was missed for cycle 29982, and only partly recorded for 29993. The relatively high count rate of HU Aqr caused some difficulties for the data acquisition system, limiting the duration of the runs. The first three eclipses exceeded the data acquisition system limits, resulting in the loss of an absolute time reference. Eclipse 29994 is the most complete of the eclipses, but suffers from a reduced signal-to-noise ratio as it was taken with a

Table 3.1: Summary of observations of HU Aqr, where cycle number refers to the linear ephemeris of Schwope et al. (2001).

Cycle number	Date UTC	Start time UTC	Observation length (s)	Egress time BJD (TDB)	Remarks
29982	2000 Oct 2	21:11	1420		Data gap; poor seeing
29983	2000 Oct 2	23:11	1563		Poor seeing; data not used
29993	2000 Oct 3	20:13	831		Truncated ingress
29994	2000 Oct 3	22:02:42	2400	2451821.441021	ND1 filter
29995	2000 Oct 4	00:17:00	1216	2451821.527841	Truncated egress
BD+28 4211	2000 Oct 2	23:46			Standard; ND2 filter; poor seeing

neutral density filter which has a throughput reduction factor of ~10. The data gap in cycle 29982 was caused by the problems with the data acquisition system noted above. The seeing was in the range 1 to 1.5 arcsec, except at the beginning of the run for cycle 29982 and throughout cycle 29983, when it was 2 arcsec. This led to some spillage of light from the 6×6 pixel array, and I have therefore not used those data.

Observations of the spectrophotometric flux standard BD+28 4211 were taken to calibrate the data. They were made through a neutral density filter with attenuation factor ~100 and also suffered from poor seeing. This means that the absolute calibration of the data is affected, and can therefore be only approximated. Observations made on the second night (October 3/4) are further affected as no standard was observed, so the observations of the standard from the first night are used.

3.2 Data reduction

The data reduction process employs specific pipeline processing of the S-Cam 2 data (de Bruijne et al., 2002), based on the FTOOLS suite of software (Blackburn, 1995). A full description of the process is given by Perryman et al. (2001) for their observations of UZ For.

Once reduced, the data can be split *a posteriori* into different energy bands (wavelength ranges). The intrinsic STJ resolution is such that $\lambda/\Delta\lambda \sim 9$, but here I use only three bands to represent 'red', 'yellow' and 'blue' light. The energy bands are selected so that roughly equal numbers of events occur in each. The wavelength ranges for the blue, yellow and red bands here are approximately 340−470 nm, 470−550 nm and 550−680 nm respectively.

As part of the pipeline processing, the data were flat-field corrected using a single map derived from sky observations. The data were then corrected for atmospheric extinction using the standard La Palma tables of extinction values as a function of wavelength and air mass, and finally sky-background subtracted. The pipeline

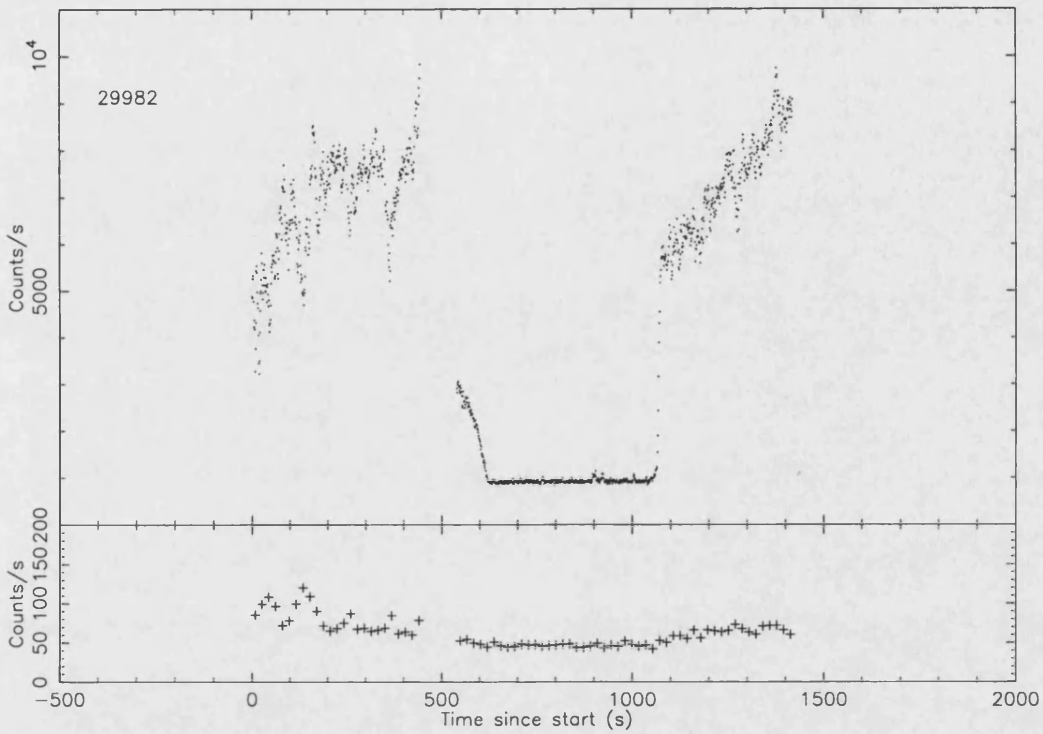

Figure 3.1: White light curve from the entire array (top panel) and sky-background pixels (1,1) and (6,6) (bottom panel) for cycle 29982. The light curves are in 1 s time bins (0.00013 phase) and the backgrounds in 18 s time bins to facilitate direct comparison. The seeing was poor for the first part of this cycle.

processing was applied to a light curve in arbitrary time bins of 1 s. The extraction of the background-subtracted light curves used the entire 6×6 array for the object and the two corner pixels (1,1) and (6,6) for the background. This reduces the chance of contamination from the object moving across the array during poorer seeing conditions. The chance of the object being detected in the corner pixels is further reduced by using the background from those phases only when the object is in eclipse. The background light level is then taken as the mean level during eclipse (to reduce the noise), and this level is subtracted from the source light curve.

Figures 3.1, 3.2, 3.3 and 3.4 show the white light curves for eclipses 29982, 29993, 29994 and 29995 before subtraction of the background, together with the backgrounds taken from the two corner pixels (1,1) and (6,6).

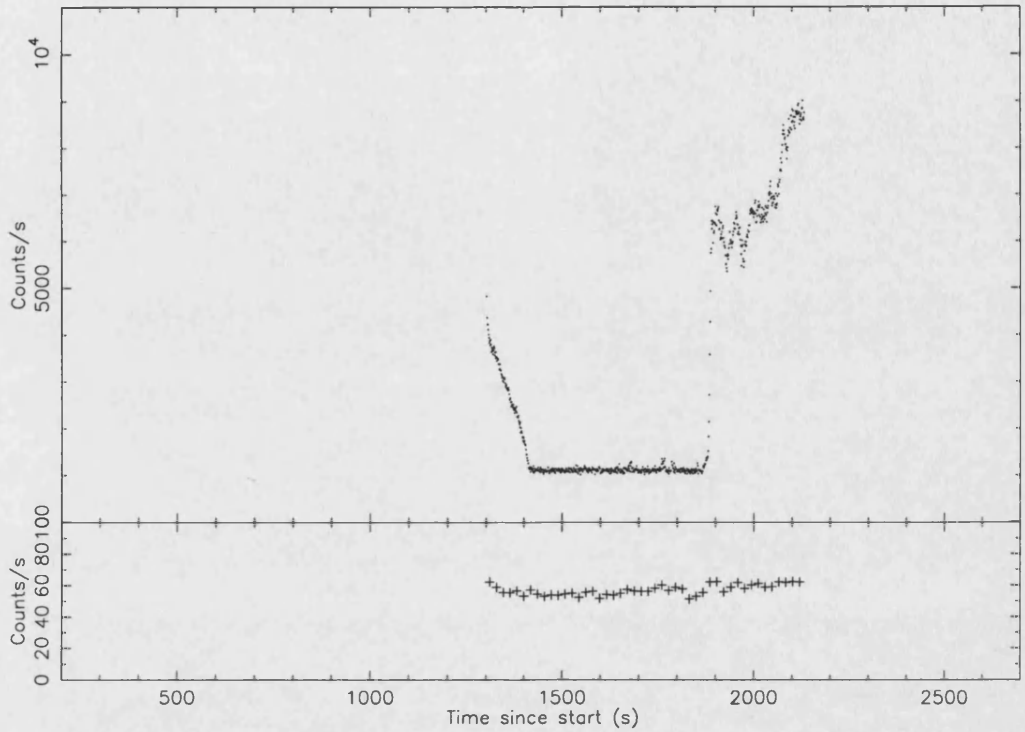

Figure 3.2: As for Figure 3.1 but for cycle 29993.

Once the data had been calibrated and reduced, they were folded on the orbital period. The linear ephemeris of Schwope et al. (2001) was used, which defines inferior conjunction of the secondary as $\phi = 1.0$. The UTC times were transformed to TDB (at the solar system barycentre, i.e. including light travel times). For cycles 29982 and 29993, where there is no absolute time reference, the egress is aligned to be at the same phase as in cycles 29994 and 29995.

Figures 3.5 and 3.6 show the white, red, yellow and blue light curves, with the colour ratios yellow/red and blue/yellow, for cycles 29993, 29994 and 29995. The secondary star has been subtracted from the colour ratios (but not the light curves) so that the change in the ratios after accretion region ingress is due wholly to the stream.

I extracted intervals of good seeing from the observation of the standard star to determine the count-rate in the yellow band, corresponding most closely to the V-band. This gave a zero point magnitude for 1 count s^{-1} in this band of 24.0,

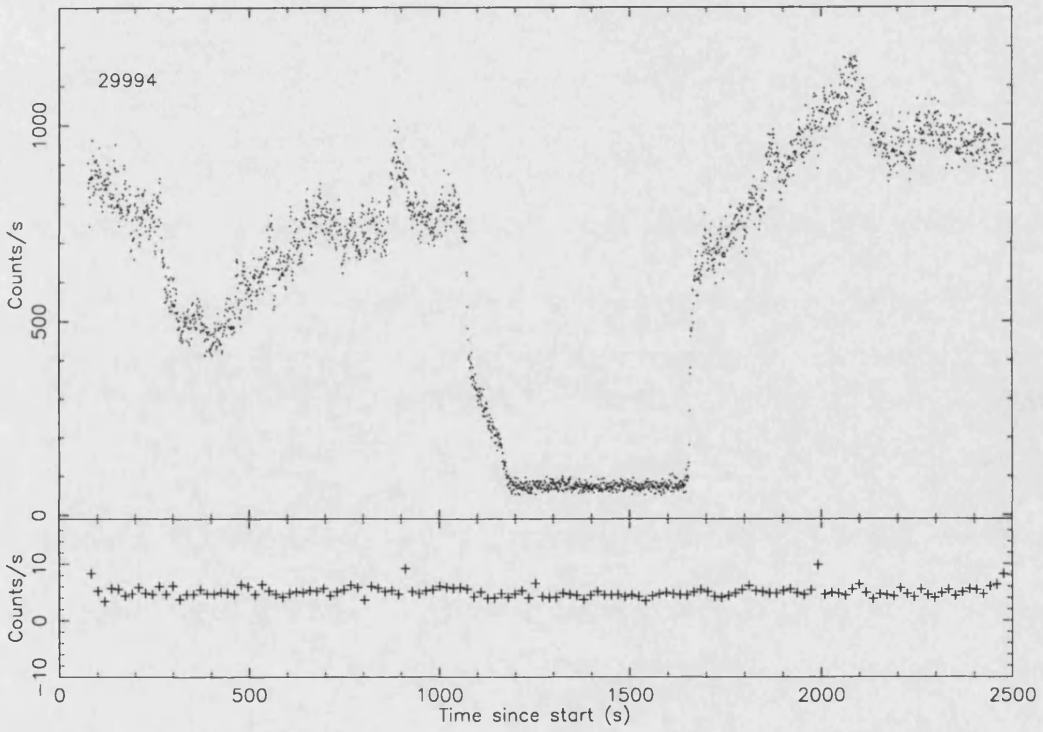

Figure 3.3: As for Figure 3.1 but for cycle 29994. A neutral density filter was used, hence the lower count rate and increased noise compared to cycles 29982 and 29995.

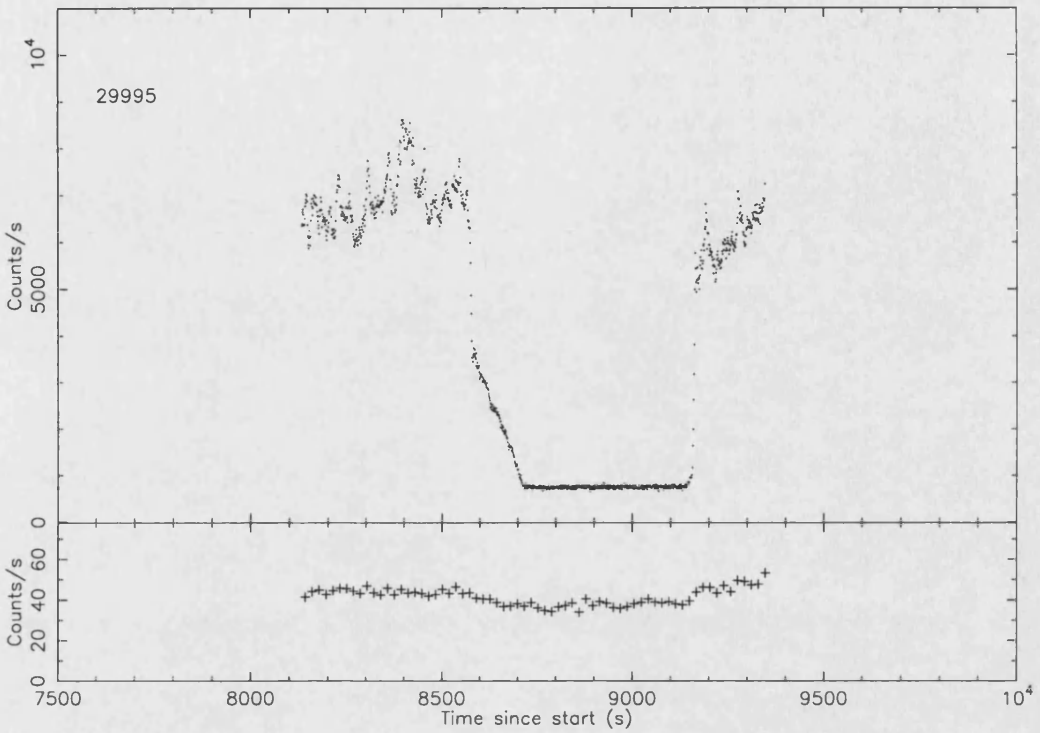

Figure 3.4: As for Figure 3.1 but for cycle 29995.

taking into account the (approximate) factor of 100 from the neutral density filter. The corresponding maximum brightness at $\phi = 1.1$ in Figure 3.6 is $V = 14.7$. This indicates that HU Aqr was in a high accretion state at the time of these observations (cf Schwope et al., 2001).

3.3 The Light Curves

The light curves in Figures 3.5 and 3.6 show a number of features that are characteristic of an eclipsing polar system. The most prominent feature is the eclipse itself, which starts with the limb of the secondary star eclipsing the accretion stream. At about $\phi = 0.964$ the bright accretion region on the white dwarf is eclipsed in a few seconds (the white dwarf is also eclipsed around these phases, but is much fainter), and this is followed by the eclipse of the remaining accretion stream. After this only the secondary star is visible, and the sequence is then approximately reversed on

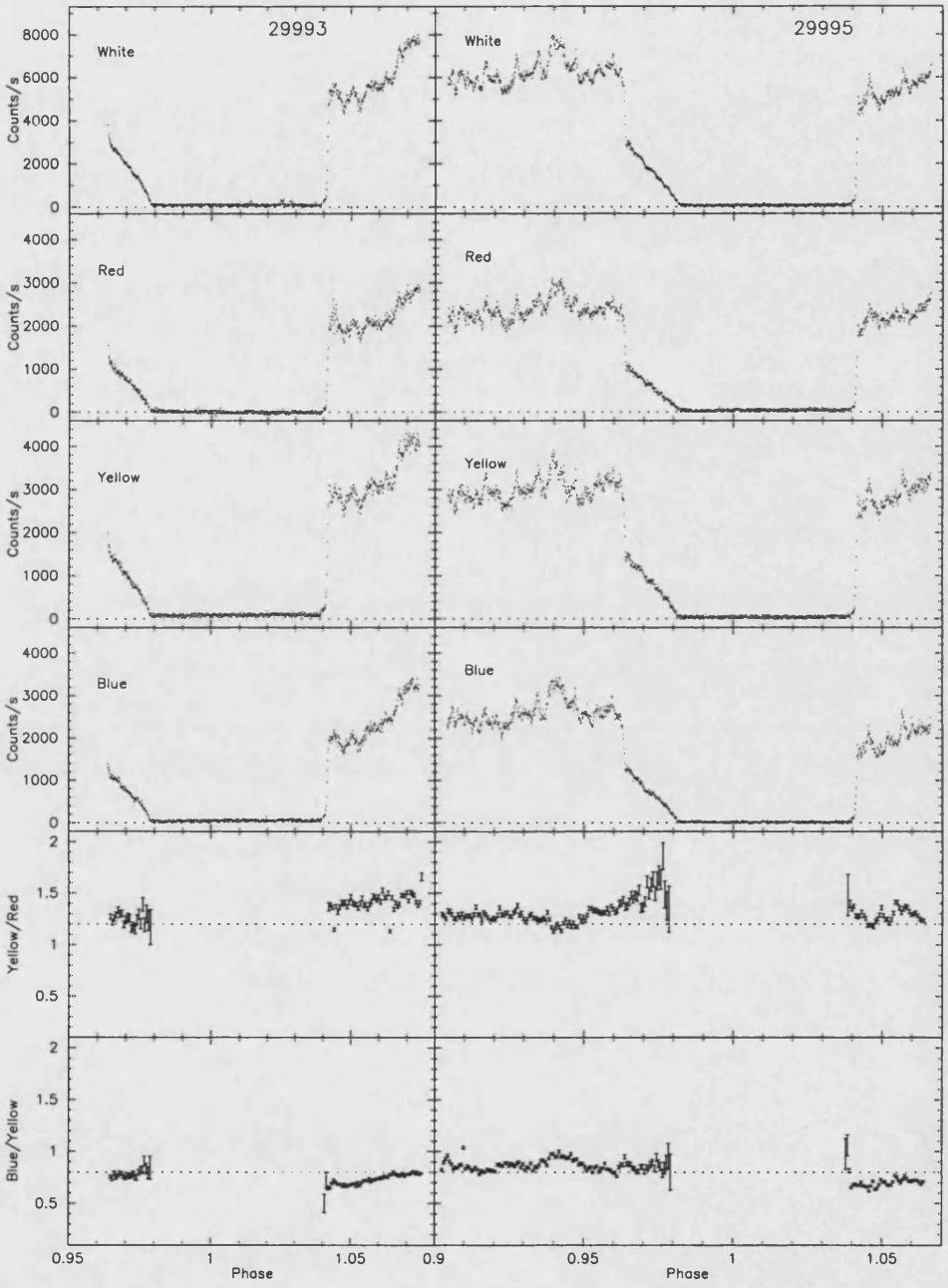

Figure 3.5: The sky-subtracted phase folded light curves for eclipses 29993 (left) and 29995 (right), representing from the top white, red, yellow and blue light, with a resolution of 1 s (0.00013 phase). The colour ratios are binned in 5 s bins and the contribution from the secondary during total eclipse has been removed. Points with errors over 0.5 in the colour ratio plots have been omitted for clarity – these occur during complete eclipse when there is effectively zero count rate after subtraction of the secondary contribution. To facilitate comparison, dotted lines have been placed at the arbitrary levels of 0.8 and 1.2 in the blue/yellow and yellow/red ratios respectively.

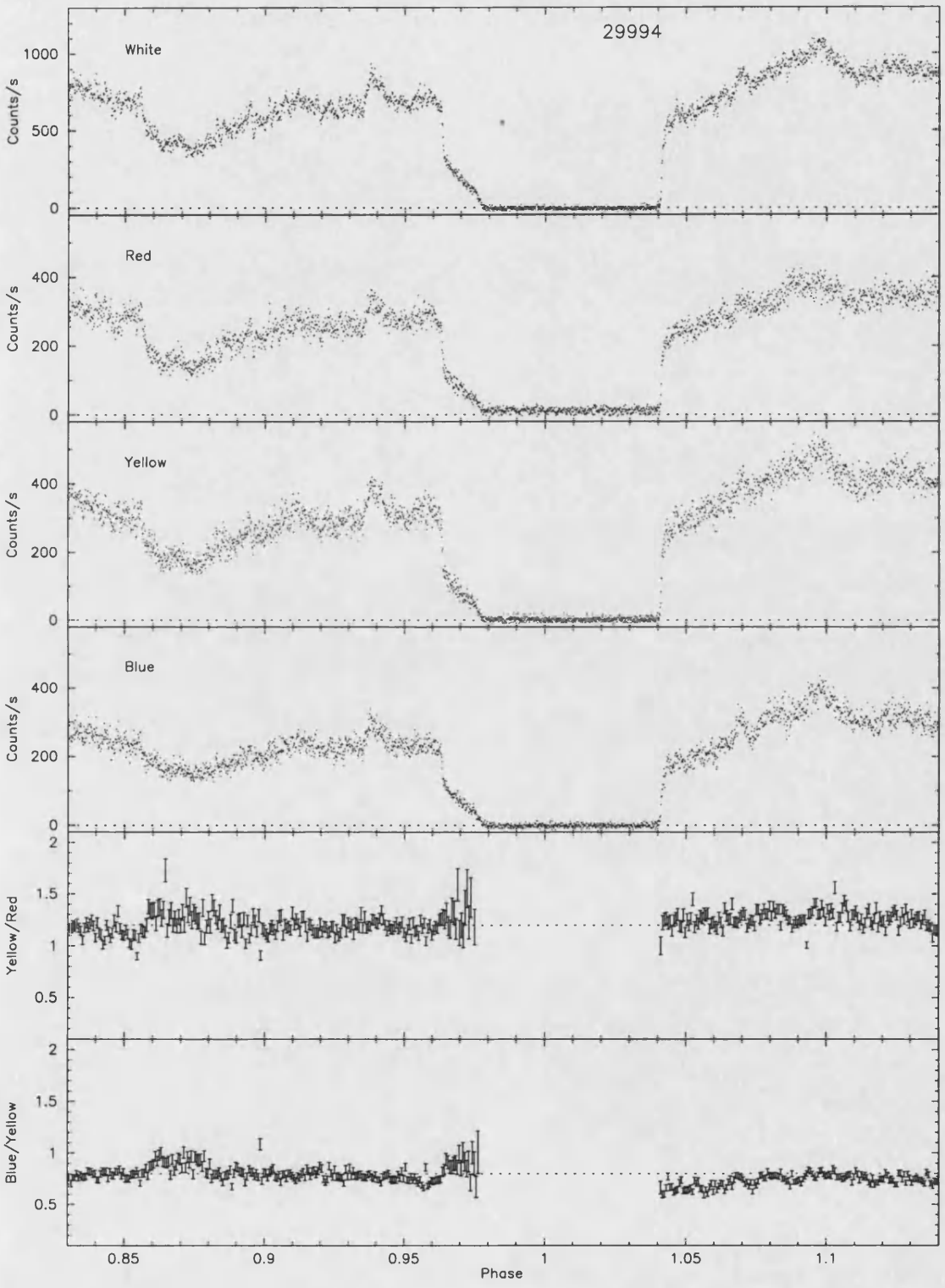

Figure 3.6: As for Figure 3.5 but for eclipse 29994. The count-rate is lower than cycles 29993 and 29995 by a factor of 10 because of the neutral density filter.

egress.

3.3.1 Pre-eclipse dip

Prior to the eclipse of the white dwarf a pre-eclipse dip is evident in Figure 3.6, which shows this dip centred at $\phi \approx 0.872$. The dip is caused by the obscuration of the accretion region on the white dwarf by the magnetically confined section of the accretion stream. Consequently the phase of the centre of the dip is directly related to the azimuth of the coupling region, where the stream is threaded onto the field lines of the white dwarf. The centre of the dip in eclipse 29994 corresponds to an azimuthal angle of 46° which is within the range of values found by Harrop-Allin et al. (1999a) of 42° to 48° for their light curves.

Schwope et al. (2001) investigated the correlation between the phase of the dip and the soft X-ray luminosity, and concluded that the dip ingress occurs earlier in phase when the system is brighter. The ingress of the dip at $\phi \approx 0.856$ indicates that the soft X-ray luminosity is at the higher end of the range, as expected for the bright state of the system.

The dip is visible only in cycle 29994, the other observations being too short to cover the relevant phases. I cannot therefore relate its movement between successive eclipses to the change in stream eclipse profile as discussed in Section 3.3.3.

3.3.2 Accretion region eclipse

The soft X-ray data in Schwope et al. (2001) suggest that there is only one accreting pole. It is possible that there is a second accreting pole, as discussed in Harrop-Allin et al. (1999a). However, there is no evidence for such a pole in our eclipse profiles, so for the purpose of the modelling I assume accretion onto one pole.

Around $\phi \approx 0.964$ the accretion region has been completely eclipsed and the accretion stream is thereafter the dominant source of the observed brightness, with a small contribution in the red band from the secondary. The accretion spot profile on

ingress and egress is shown in Figure 3.7. The profile is constructed by subtracting successive intensities over 1 s time intervals (0.00013 phase) and hence shows the rate of change of intensity of the light curves. The profile on egress is the mean of cycles 29982, 29993 and 29995 and is therefore more reliable than the ingress profile, which uses only cycle 29995. The profile may be asymmetrical, with the leading edge (corresponding to later phases) of the cyclotron emitting region being brighter than the trailing edge. The accretion spot ingresses last for $\sim$7 s and the egresses are $\sim$8 s. This is unchanged from the durations measured by Case (1996) in the data used by Harrop-Allin et al. (1999a) and should be compared to the duration of 1.3 s for the soft X-ray eclipses of Schwope et al. (2001). These times imply that the extent of the cyclotron emitting region is $\sim$15° in the optical compared to $\sim$3° in soft X-rays. From soft X-ray absorption modelling, Schwope et al. (2001) suggest that the threading region is extended in azimuth, but the soft X-ray emission originates over only a small range of azimuths: the larger region seen in the optical is therefore likely to be the result of this extension in azimuthal threading. The suggested reason for such compact X-ray emission is insufficient material in the accretion stream to power bright X-ray emission at the foot points of the magnetic field lines (Schwope et al., 2001), and instead most emission is from neighbouring spectral regimes (such as the optical as seen here). The cyclotron emitting region is significantly more extended than those in UZ For, where Perryman et al. (2001) found both regions extended over $3° \pm 1°$.

In the cycles where there is absolute time information (29994 and 29995) the egress takes place at $\phi = 1.0413$ in both cycles, 10 s later than predicted by the linear ephemeris. This indicates that the observed-minus-calculated (O−C) residuals in Schwope et al. (2001) figure 4 are continuing to increase. In case there are systematic differences between the optical and soft X-ray egress times, the Harrop-Allin (1999) data in their figure 1 was rephased on the new ephemeris, including the UTC-TDB time correction of 59 s appropriate to the Schwope et al. (1997b) ephemeris epoch. The data were taken on cycles $\sim$1322 in figure 4 of Schwope et al. (2001), and the

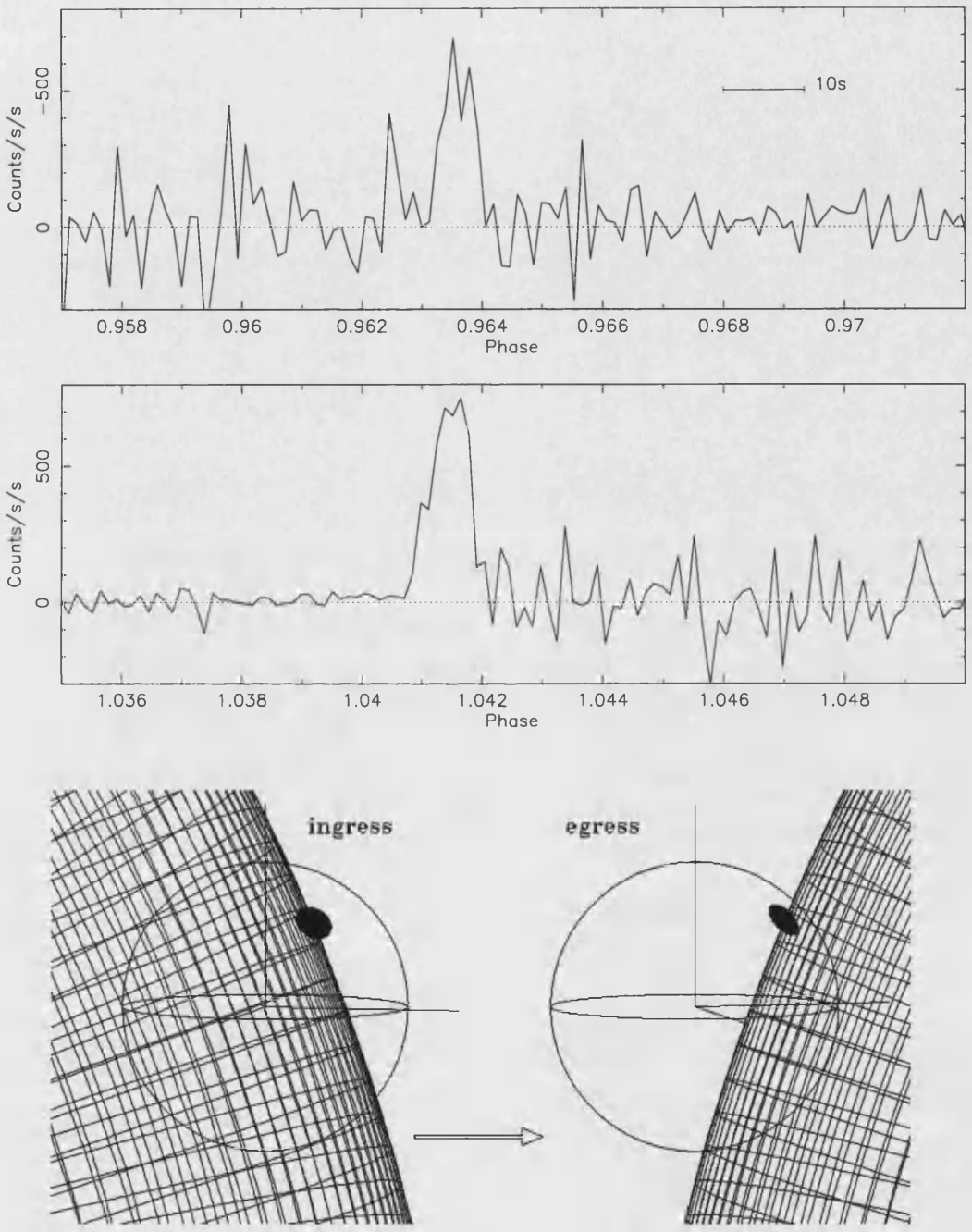

Figure 3.7: Top, the accretion spot profile on ingress (from cycle 29995) and egress (the average of cycles 29982, 29993 and 29995). The profiles are constructed by subtracting successive intensities over 1 s time intervals. The ordinate of the upper plot is inverted to facilitate comparison. Bottom, the view of the eclipsing limb at accretion region mid-ingress and mid-egress. The accretion region subtending 15° is drawn to scale. The radius of the white dwarf is assumed to be $0.017a$, where a is the binary separation.

O−C of -1.6 s is in agreement to within ∼1 s with those determined from the soft X-ray data. The continuing increase in O−C residuals is an indication that the period in the linear ephemeris of Schwope et al. (2001) is slightly too short, and is in the opposite sense to that expected from their quadratic ephemeris which predicts a decrease in the O−C residuals. A period of 0.086 820 4212 d would eliminate the observed 10 s residuals.

The duration of the eclipse from the centre of the accretion region ingress to the centre of its egress is $\Delta\phi = 0.0778 \pm 0.0002$ in cycles 29993, 29994 and 29995. This is the same as that found by Harrop-Allin et al. (1999a) ($\Delta\phi = 0.0779 \pm 0.0002$) and Schwope et al. (1997b) ($\Delta\phi = 0.0779$). The lack of variation in the duration of the eclipse is remarkable and implies that the accretion spot is at a constant latitude for these observations. On the other hand, this is shorter by 6 s than the $\Delta\phi = 0.0782 - 0.0792$ found by Schwope et al. (2001) from the soft X-ray eclipses, but there the ingress was uncertain due to the low count-rate and absorption.

For a particular mass ratio q, the width of the eclipse determines the inclination of the system. Using $q = 0.25$ (Schwope et al., 2001), the inclination is 85.0° (assuming $M_1 = 0.9M_\odot$ and $\beta = 40°$, $\zeta = 50°$, where M_1 is the mass of the white dwarf and β, ζ are the magnetic colatitude and longitude of the accretion region respectively. β, ζ define the location of the accretion spot on the surface of the primary; see below).

3.3.3 Stream eclipse variations

Complete ingress of the stream occurs at $\phi = 0.982, 0.979, 0.977$ and 0.982 for eclipses 29982, 29993, 29994 and 29995 respectively. During the period of complete eclipse the secondary is the only contributor to the light curve and provides a constant contribution that is greatest in the red band, as expected, with no contribution in the blue band.

Figure 3.8 shows more clearly that the observations reach total stream eclipse

at different phases even though the spot ingresses/egresses both occur at the same time. This rapid change in the accretion flow–magnetic field interaction between successive eclipses was first observed by Glenn et al. (1994) who found a difference in the time it took for the stream to be completely eclipsed of more than a minute between their two successive eclipses.

The shape of the accretion stream eclipse profile in the observed light curves gives a qualitative prediction of where brightness enhancements can be expected in the accretion stream. When the stream is brighter at later phases in the stream eclipse, as in cycles 29982 and 29995 (Figure 3.8), there must be more emission in the threading region, as this is the only part of the stream still visible. For the same reason, if the final stage of the stream eclipse takes place at later phases, the threading region must have moved: thus in cycles 29982 and 29995, either the accretion stream is brought further out from the line of centres during the ballistic part of the trajectory, or the magnetically channeled stream rises further out of the orbital plane (I address this in Section 3.4 below). This could be caused either by a small change in the location of the accretion spot on the surface of the primary, moving the accretion spot further from the line of centres, or perhaps a change in the density of the stream material along the accretion stream. Likewise, if the accretion stream is fainter near the white dwarf, the system brightness will be fainter immediately after accretion region ingress. This may be the case for cycle 29995 (Figure 3.8).

3.3.4 Colour variations

For cycle 29995 there is a rise in the yellow/red ratio during the stream ingress (Figure 3.5), so that successively more red light is blocked from the stream as the eclipse progresses. This implies that the last part of the stream to be eclipsed, near the threading region, emits relatively less at longer wavelengths than the rest of the stream. This rise is not evident in cycle 29993, but may be present at a reduced

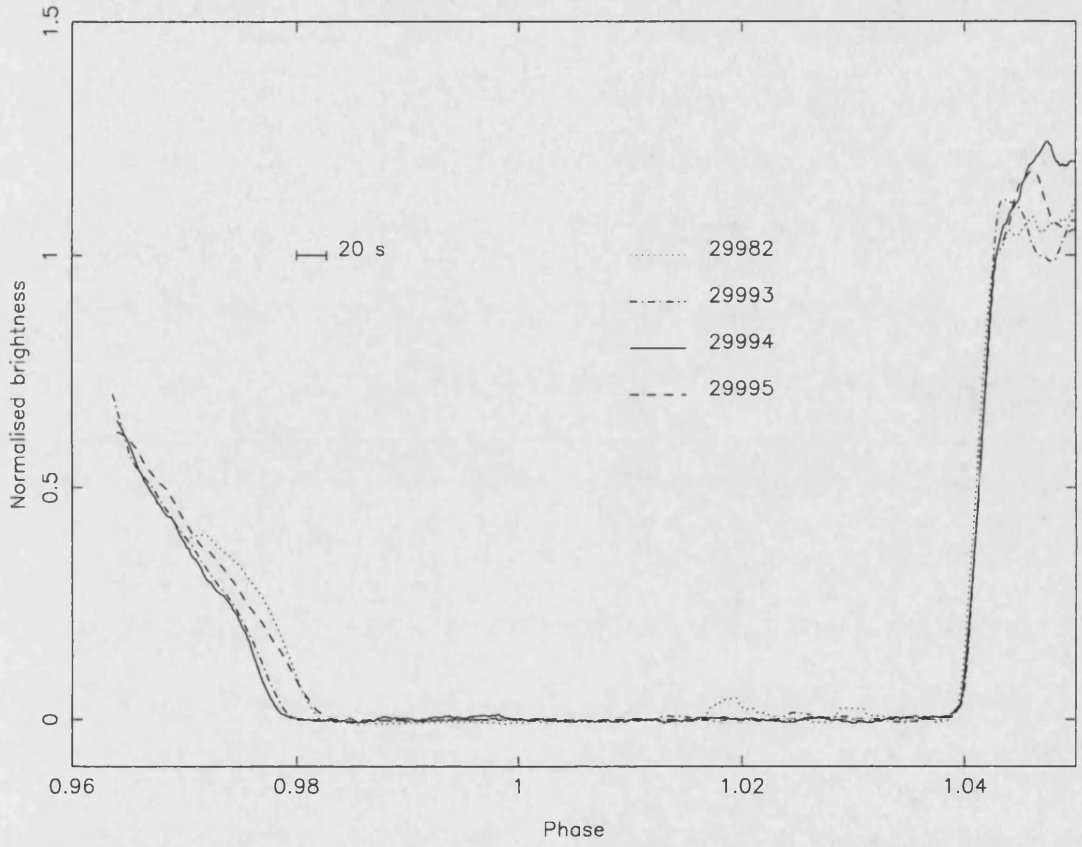

Figure 3.8: The ingress and egress of eclipses 29982 (dotted), 29993 (dash-dot), 29994 (solid) and 29995 (dashed) smoothed over a running average of 20 s. The ordinates are normalised to 1 at the end of spot egress, and to 0 at total eclipse.

level in cycle 29994 (Figure 3.6). This trend is consistent with a threading region which is increasingly hotter in the three successive eclipses. At the same time as the large yellow/red ratio change in cycle 29995 there is no change in the blue/yellow ratio.

After eclipse, when the stream close to the primary is uncovered first, the different yellow/red ratios in cycles 29993 and 29995 are consistent with a hotter stream near the white dwarf in eclipse 29993 than in 29995. An increase in the blue/yellow ratio after eclipse is seen in all three cycles (29993, 29994 and 29995) and also implies that the magnetically confined stream material is becoming hotter towards the threading region.

The pre-eclipse dip around $\phi \approx 0.87$ in cycle 29994 (Figure 3.6) is also slightly bluer than at earlier or later phases. This was also the case in the light curves of Harrop-Allin et al. (1999a). This implies that the absorption is likely to be free-free absorption which has a greater effect with increasing wavelengths (Watson et al., 1995), and is the expected absorption mechanism for material in the accretion stream (King and Williams, 1985).

3.4 Indirect imaging

I have inferred from a qualitative analysis of the light curves that the trajectory and/or intensity of the stream varies over successive orbital periods, and brightness enhancements can be identified along the stream length. However, it is more difficult to infer the location of the brightness enhancements without a model for the stream trajectory. In particular, at stream ingress there is no information on which parts of the stream are eclipsed at which phases. Using an eclipse mapping method, a model accretion stream can be created by placing model stream points along a predetermined trajectory. This trajectory consists of a ballistic section from L_1, coupling to a magnetically confined section which follows the dipole field line, and originates where the material is threaded in the orbital plane by the field lines of

the white dwarf.

The use of eclipse mapping originates from the early 1980s when Horne (1983) developed the technique to reconstruct the surface brightness distribution of accretion discs. The method was extended to accretion streams by Hakala (1995) and applied to the eclipse light curves of HU Aqr. The Hakala (1995) technique used an arc connecting L_1 to the white dwarf. This technique was developed and improved by Harrop-Allin et al. (1999b) with the extension to a two part trajectory, and was applied to observations of HU Aqr in both a high and low accretion state (high and low mass transfer; Harrop-Allin et al., 1999a, 2001).

The eclipse mapping of accretion streams has also been applied to emission-line observations (Sohl and Wynn, 1999; Vrielmann and Schwope, 2001; Kube et al., 2000). Kube et al. (2000) used HST Faint Object Spectrograph spectra of the eclipsing polar UZ For to map the accretion stream line emission at C IV λ1550, and Vrielmann and Schwope (2001) used the emission line light curves of Hβ, Hγ and He II λ4686 of HU Aqr. These line-emission methods both use a three-dimensional stream so the model can reproduce the out-of-eclipse features, such as the pre-eclipse dips (Watson, 1995), and data from the entire orbit of the system is fitted. They can also reproduce the effect of differing brightness distributions between the irradiated and un-irradiated faces of the stream, an effect which is not reproduced in the model of Harrop-Allin et al. (1999b). On the other hand, the Harrop-Allin et al. technique has the benefit of being sensitive to the total emission from the stream (not just the line emission), and also has the advantage of access to high signal-to-noise ratio data, which is crucial for producing robust fits.

3.4.1 Methodology

The model accretion stream is constructed using a ballistic trajectory, as described by Lubow and Shu (1975). This trajectory is defined by the 'free-fall' motion from L_1 in the gravitational potential due to the primary and secondary. At some threading

radius R_μ the trajectory instantaneously assumes the path of the dipole field line of the primary. The model system is rotated, causing the Roche lobe filling secondary to eclipse the accretion stream and white dwarf. The brightness of the visible model stream points is then summed at each phase to form a model light curve. This is performed a number of times for a number of identical stream trajectories, but with initially different random brightness distributions. The best fit model light curve is then optimized with the genetic algorithm (GA), which evolves the best fit light curve with a technique analogous to that of biological evolution.

The GA proceeds by ranking the individual model light curves according to their 'goodness-of-fit', which is measured with a 'fitness function' (see Harrop-Allin et al., 1999b). This function is a combination of a χ^2-term and a maximum entropy regularisation term:

$$F = \sum_{i=1}^{N} \left(\frac{\text{model}_i - \text{data}_i}{\sigma_i} \right)^2 - \lambda \sum_{j=1}^{M} S_j \qquad (3.1)$$

The left hand term is the χ^2 and the right is the regularisation. $\lambda > 0$ is a Lagrangian multiplier and the entropy $S_j = p_j - m_j - p_j \ln(p_j/m_j)$. N is the number of data points in the original light curve, M is the number of data points in the model accretion stream, model_i is the brightness of the ith point in the model light curve and data_i is the brightness of the ith point in the original light curve with σ_i its uncertainty. p_j is the normalised brightness of model stream points j and m_j is the local geometric mean of the brightness of the emission points neighbouring point j on the model stream. m_j is defined as $\sqrt{p_{j-1}p_{j+1}}$ and for the first and last points as $\sqrt{p_j p_{j+1}}$ and $\sqrt{p_j p_{j-1}}$ respectively for point j.

The GA preferentially selects those model light curves that have better fitness functions to 'breed' the next generation of accretion stream brightness distributions. These 'child' solutions are then used to produce the next generation of model light curves, and the process is repeated until the stopping criterion is reached. The cross breeding of two parent solutions is performed by selecting at random for each child

stream point the brightness of the corresponding stream point from either parent. There is a given probability (which is small) that a particular brightness point is mutated. This is done in order to introduce genetic variations and hence explore the whole parameter space, and provides the GA with the ability to climb out of local minima. The mutation takes one of three possible forms: the stream point can be reassigned a brightness from a uniform distribution, be replaced by a random brightness from a Gaussian distribution centred on the old value and with unit variance, or replaced with the mean brightness of the two neighbouring brightness points. After the final stages of the GA, a more conventional line-minimisation routine (Powell's method, e.g. Press et al., 1992) is used to reach the final minimum of the solution. This approach is used for reasons of efficiency. Genetic algorithms are efficient at searching multi-dimensional space, but prohibitively intensive computationally at identifying a precise global optimum. Therefore, the GA is used to place the solution in the neighborhood of the optimum and Powell's method is used to converge to the exact minimum.

Within the fitness function, the value of λ is important and effects the resultant brightness distribution. Choosing an appropriate value is a trade-off between minimising the χ^2 and maximising the entropy. With a large value of λ the model attempts to reduce the entropy at the expense of the χ^2 and the features of the light curve are not reproduced. However, too small a value of λ causes the model to fit noise features and artifacts within the light curve. A suitable value of λ was found by trial and error, and this value was fixed for the model fitting. A value of λ that evolves over the course of the GA was tried by Harrop-Allin et al. (1999b), but was found to produce no noticeable difference to that of a model using a fixed λ. I therefore use a value of $\lambda = 5 \times 10^4$ for all the model fits presented here, and the same value of λ is used for Powell's method.

The accretion stream itself is taken to be physically thin in that it does not eclipse the primary, and so features such as the pre-eclipse dip (e.g. Watson, 1995) are not reproduced by the model. However, the brightness contribution of each

stream point is taken as the sine of the angle between the line-of-sight and the tangent to the stream at that point. This is essentially a projection effect, thus mimicking an optically thick stream. The white dwarf is excluded from the model, despite the egress of the white dwarf being visible in the light curves immediately before the egress of the accretion region.

3.4.2 Stream map artifacts

For the interpretation of the model fits to the eclipse profiles, there is a need to establish how dependable the results from the fitting process are. This is particularly important when, as here, the observations do not cover the entire duration of the stream eclipse. There is also the more general question as to the sensitivity of the fits to the system parameters, and to the weights assigned to the different parts of the light curve. The use of different weights on different parts of the light curves causes the model to place more emphasis on the fitting of these areas.

If two or more stream regions are eclipsed or revealed at the same time, then there will be an ambiguity as to which model point their brightness should be assigned. This can produce artifacts in the form of enhanced or reduced brightness regions in the stream. This effect is particularly important in the cycle 29993 and 29995 observations because the ingress and/or egress of the stream is truncated, so certain regions of the stream are observed only once. Measurements during both ingress and egress break this ambiguity, as different pairs of stream points are covered or revealed at the same time. For observations where the egress is truncated (cycle 29995), the model has difficulty breaking the ambiguity which exists when assigning brightness to points either in the magnetically confined region or the ballistic stream. For observations where the pre-eclipse light curve is missing, there is a lack of information on the accretion region, and parts of the stream towards the secondary (cycle 29993). Figure 3.9 illustrates those parts of the system visible during the phase range of cycle 29995. The dark shading indicates parts that are never visible, medium shaded

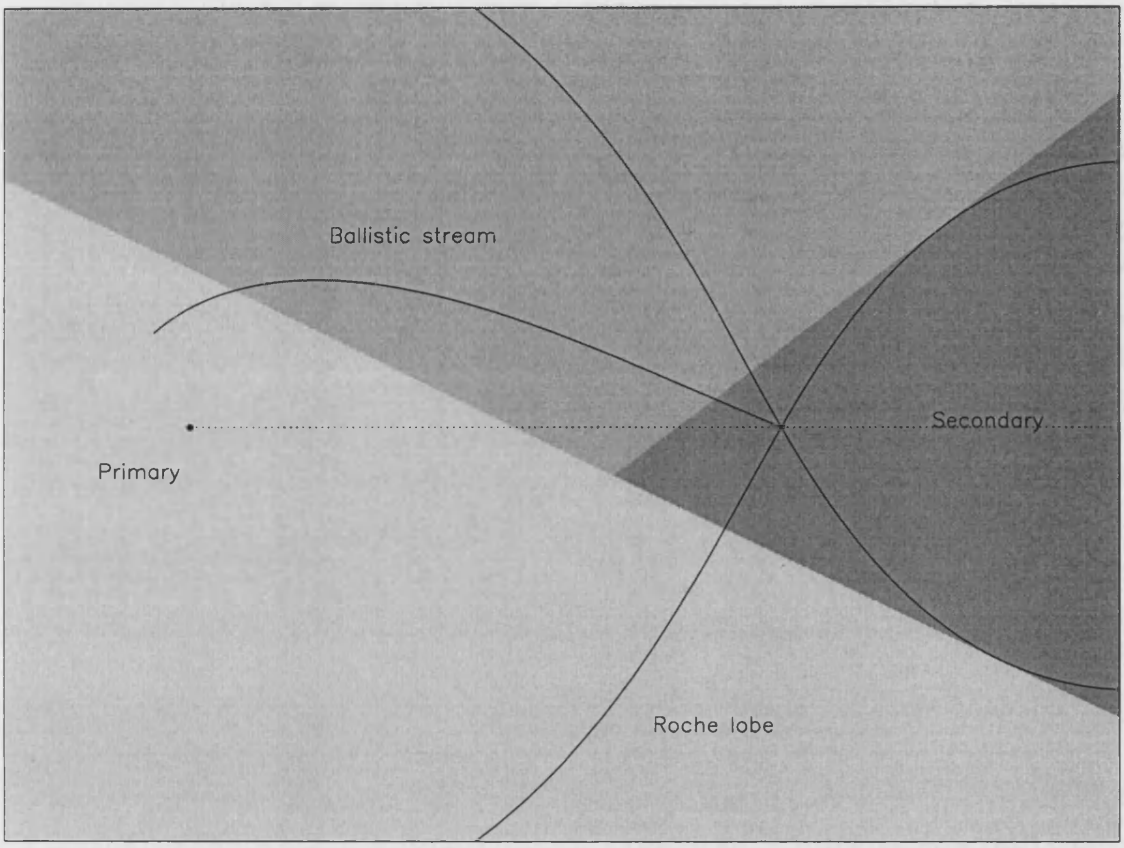

Figure 3.9: Diagram illustrating those parts of HU Aqr observed in the phase range of cycle 29995. The dark shading indicates those parts that are never observed, medium shading those that are observed only at ingress, and light shading those observed at both ingress and egress. Also indicated are the primary, secondary, Roche lobe and a ballistic accretion stream.

regions are visible once at ingress and light shaded regions are visible twice, at ingress and egress.

In order to identify the effect of using incomplete eclipses, I have carried out simulations on synthetic streams to identify the location and amplitude of the artifacts which may be introduced. The synthetic streams used to create the model light curves are shown in the right hand panel of Figure 3.10 as solid lines. The generated model light curves are shown in the left hand panels covering the phase ranges appropriate to cycles 29994, 29995 and 29993. The model fit light curves are

shown as dotted lines in the left hand panels and the resulting stream brightness distributions are shown as crosses in the right hand panels. The input synthetic streams have a bright region near the white dwarf, one in the threading region, and an underlying constant component. Weights are assigned to different sections of the light curve to influence the relative contribution of the different parts of the light curve to the fitness function. This means that we can place more importance on fitting features in the stream than to fitting pre-eclipse features, which the model is not intended to include. They are as follows: the weights after accretion spot ingress until end of stream ingress are a factor of 100 greater than those within the dotted vertical lines, which in turn are a factor 100 greater than those outside the dotted vertical lines. This is in line with those for the fits to real data (see later) and ensures that even in the longest eclipse, cycle 29994, the effect of the changing accretion region brightness with phase, or that of absorption in the pre-eclipse light curve, is minimised. The consequence, however, is that very little information is available on that part of the ballistic stream close to the secondary. Hence, these parts of the derived model accretion stream (crosses in Figure 3.10) are not shown in the fits in the right panel. In cycles 29993 and 29995 the region over which information on the ballistic stream is available is reduced even more.

The cycle 29994 stream fits are reconstructed with excellent fidelity. There is some enhancement at a distance of $\sim 0.35a$ (where a is the binary separation) from the primary, which occurs as a result of the bright region near the primary being eclipsed at the same time as this region. (If equal weights are assigned to the entire synthetic light curve this enhancement is removed.) Flux in this enhancement should be reallocated to the region close to the white dwarf. The enhancement is increasingly worse for cycles 29995 and 29993, but this aside, the stream is reproduced sufficiently well for brightness structure in the threading region or close to the white dwarf to be deduced with some degree of confidence, so that the behaviour in the magnetically confined part of the stream is well-constrained.

The results of the model fits show that the reconstructed stream brightness

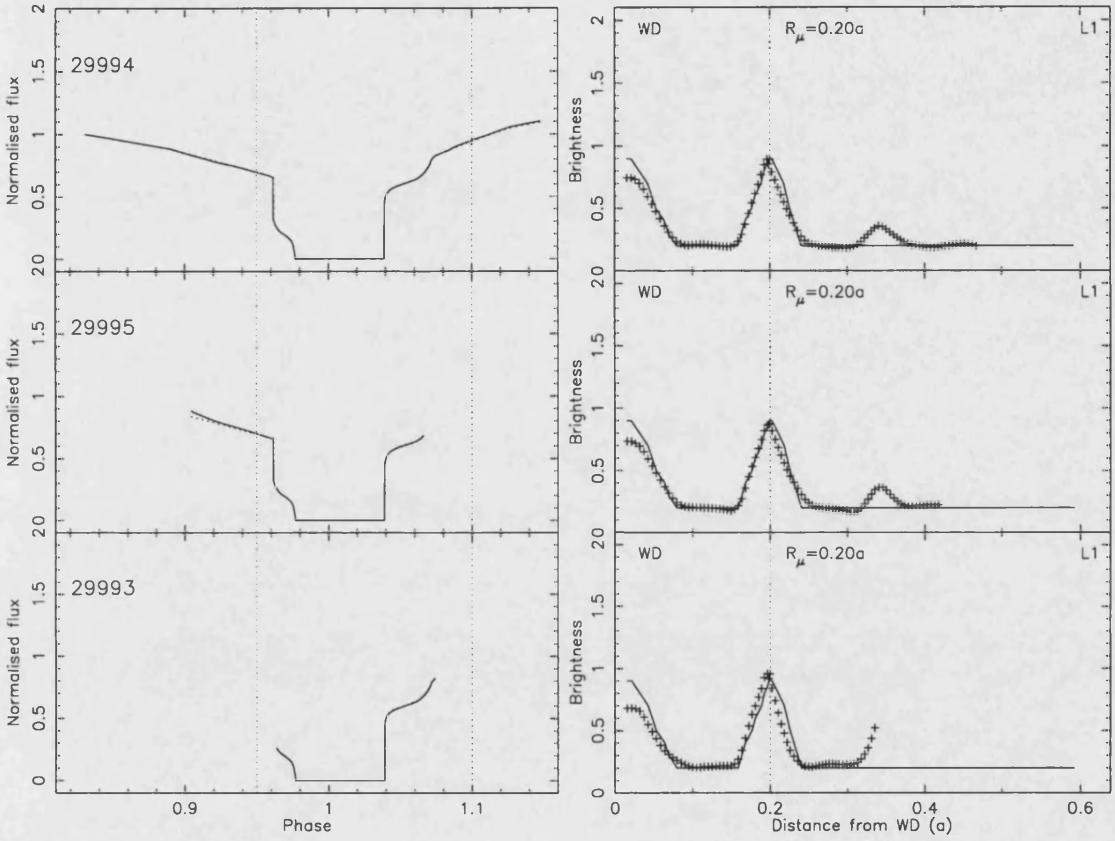

Figure 3.10: The left hand panels show fits to synthetic light curves generated using the synthetic streams (solid line) in the right hand panel, over phase ranges equivalent to those in cycles 29993, 29994 and 29995. The dotted vertical lines mark the range over which the fitting is applied. The right hand panels show the resulting stream brightness distributions as a function of distance from the white dwarf in units of the binary separation. The solid lines denote the synthetic stream, and the crosses the derived stream. The vertical dotted line indicates the threading region and marks the division between the ballistic section of the stream (to the right) and the magnetically confined section (to the left). Only those parts of the derived stream which are constrained by the fits are shown.

distribution close to the white dwarf depends to some extent on the brightness defined for the accretion spot, which is a user-input quantity fixed for the duration of the model. If this value is too low, the model over-compensates in this region by assigning more brightness to points close to the white dwarf. In the synthetic data fits, this accretion spot brightness is known, but in fits to real data, a judgment has to be made as to the best value to use. Further, with real data, the effects of the flickering accretion spot on egress reduces the confidence with which the stream profile can be reproduced on the egress pass. This is minimised by our weighting scheme, but may cause an increased enhancement at $\sim 0.35a$ in the fit.

Having investigated the effects of modelling truncated light curves and the dependence upon the accretion region brightness, I have changed the manner in which the technique is applied compared to Harrop-Allin et al. (1999b). I have chosen to use a restricted modelling technique, which relies on the ingress of the accretion stream alone. The light curves have been further truncated to remove all phases up to and including the ingress of the accretion region, and those phases after $\phi = 1.0$ (i.e. during total eclipse). This removes the uncertainty associated with the brightness of the accretion region on egress, which affects the brightness distribution towards the white dwarf. It also removes the reliance upon the egress of the stream, the emission from which is combined with the variable emission from the accretion region. However, the modelling is subject to the ambiguity of the brightness of multiple stream points eclipsed in the same phase interval: therefore the interpretation of the model results must be carried out with care, but some progress can be made by referring back to the light curves and the colour ratios.

3.4.3 Fixed parameters and R_μ

A number of parameters is required to produce a model light curve and reproduce the stream brightness distribution. These fall into two types: physical parameters such as the masses of the two component stars which will define the Roche lobe and

hence the secondary, and geometric parameters such as the location of the accretion region on the white dwarf which defines the magnetic field geometry and hence path of the magnetically confined material (see Harrop-Allin et al., 1999b, for details). In particular the model is sensitive to the exact value chosen for the parameter R_μ, but the value can be constrained using the model stream geometry. If R_μ is too large then the model needs to assign a large amount of brightness to a few points in the threading region. Conversely if R_μ is too small then no emission is assigned by the model to these points. From brightness maps for a range of values of R_μ, the end point of the ballistic trajectory, at the threading region, can be determined and so provide a constraint on the value of R_μ. The model fits of the light curves used here show that the technique depends heavily on the data being of a sufficiently high signal-to-noise ratio, which is important because of this sensitivity to the value of R_μ. Therefore, in order to determine the most appropriate value of R_μ to use I further restrict the application of our model technique to cycles 29993 and 29995 (Figure 3.5).

Figure 3.11 shows model fits to the 'blue' light curve of cycle 29995 for different values of R_μ. The stream maps highlight the dependence of the fits on a correct value for R_μ. For a value of $R_\mu = 0.18a$ the brightness of the threading region is low. This lack of emission, or 'hole', is caused by R_μ being too small – the data are incompatible with emission at the end part of the resulting long ballistic stream. On the other hand, if R_μ is too large, so that the model ballistic stream is shorter than it is in reality, a pile up of excess brightness at the threading region is seen, as in the stream map for $R_\mu = 0.26a$. The inappropriateness of the latter can be deduced from the poor fit to the region at $\phi = 0.98$ (corresponding to the threading region) for values of R_μ which are too large (insets to Figure 3.11).

For all of the modelling I used fixed values of $M_1 = 0.9M_\odot$, $q = 0.25$ and $i = 85.0°$ (Harrop-Allin et al., 1999a; Schwope et al., 2001). Table 3.2 gives the values of R_μ and the field orientation parameters for each cycle. I estimate the range on the values of β and ζ as $\pm 10°(1\sigma)$.

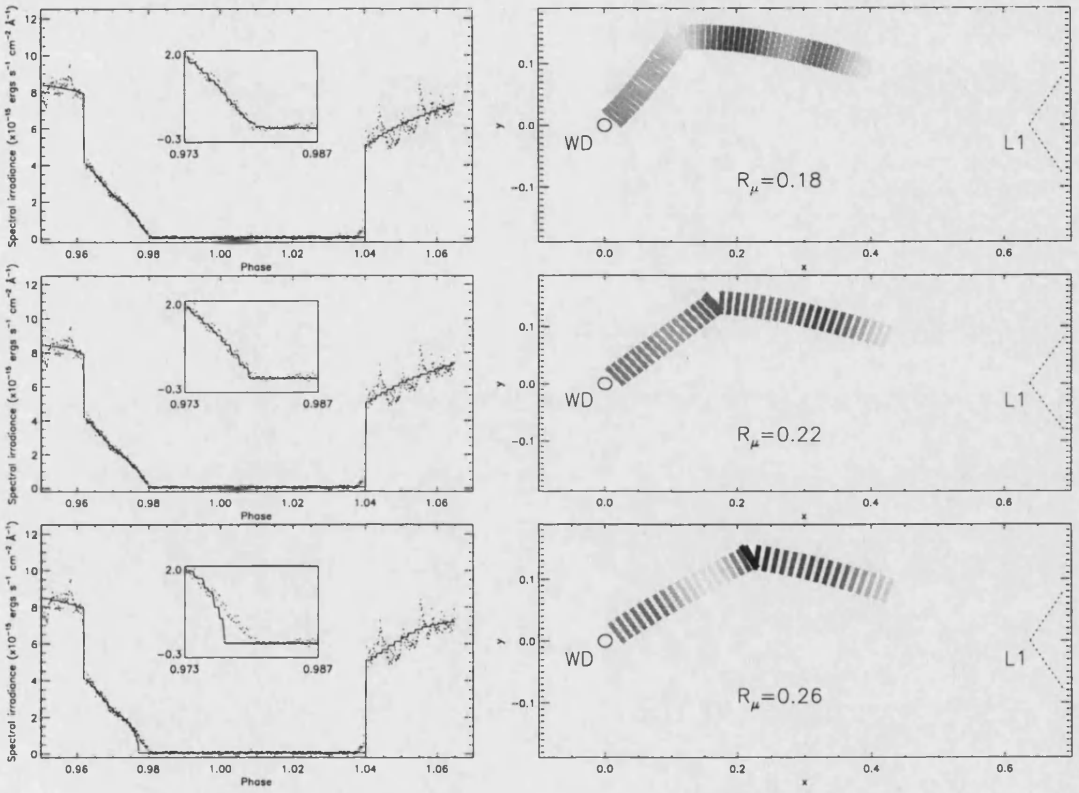

Figure 3.11: Fits to the 'blue' light curve of cycle 29995 with different values for the threading radius R_μ ($0.18a$, $0.22a$ and $0.26a$). The stream brightness maps on the right are grey scale plots with brighter stream emission being represented as darker. The gradual closing of a 'hole' at R_μ illustrates the sensitivity of the model to its location. The insets in the left hand panels show a close-up view of the fit at the threading region. For this cycle the value of $R_\mu = 0.22a$ represents the best stream trajectory.

Table 3.2: The values of the coupling radius (R_μ) and location of the accretion spot (β and ζ, magnetic colatitude and longitude respectively) for cycles 29993 and 29995. Values of β and ζ have an estimated range of $\pm 10°(1\sigma)$.

Cycle number	R_μ	β	ζ
29993	$0.26a$	55°	30°
29995	$0.22a$	60°	40°

The values of the three parameters in Table 3.2 are different from those found by Harrop-Allin et al. (1999a). I find $R_\mu = 0.22a - 0.26a$ (1.3×10^{10} cm to 1.6×10^{10} cm), whereas Harrop-Allin et al. (1999a) found $R_\mu = 0.17a - 0.20a$ (1.0×10^{10} cm to 1.2×10^{10} cm). This difference can be attributed to an improved stream trajectory compared to that of Harrop-Allin et al. (1999b). This arises from an incomplete treatment of the appropriate forces in the frame of reference chosen by Harrop-Allin et al. (1999b), where the method fails to take complete account of the rotation of the binary system about the centre of mass. The component of the force missed from the calculation of the ballistic stream therefore leads to an incorrect propagation of the velocity of the stream points. The difference is small, but because of the grazing angles, the resulting R_μ is significantly different, with the Harrop-Allin et al. trajectory underestimating the values for R_μ (Figure 3.12).

The decrease in the value of R_μ from cycle 29993 to 29995 implies that the stream penetrates further into the magnetosphere before threading onto the magnetic field lines (Figure 3.13). The effect of the change in the threading radius can be seen in Figure 3.8. The values of $\beta \sim 60°$, $\zeta \sim 40°$ found here are also larger than those used by Harrop-Allin et al. (1999a), but consistent within the uncertainties. Any change in these parameters would imply that the location of the accretion spot has moved further from the line of centres and the altered geometry of the magnetic field carries the accretion stream further round the white dwarf from the line of centres (see Section 5). The values are in agreement with those found by Schwope et al.

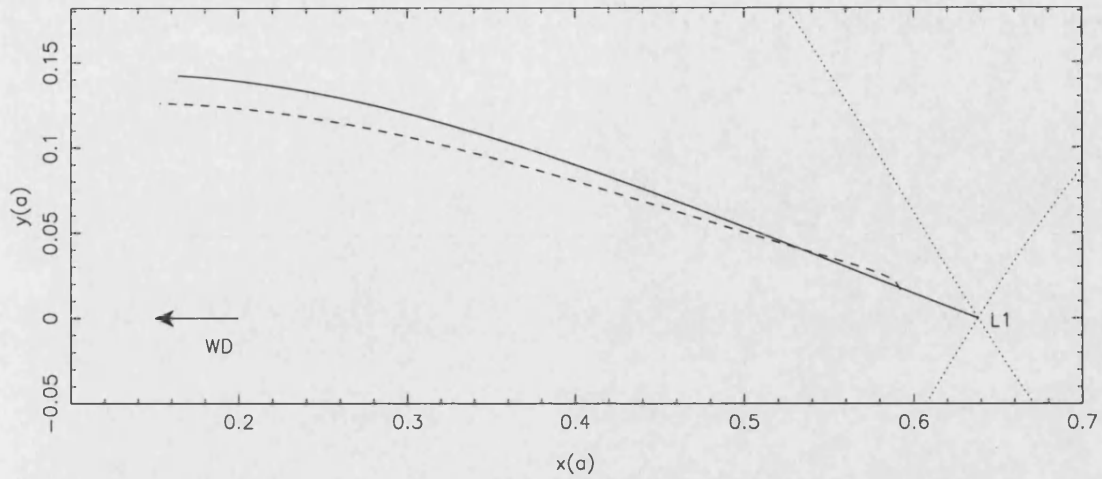

Figure 3.12: The two different stream trajectories obtained using the method of Harrop-Allin et al. (1999b) indicated by the dashed line, and that used here is indicated by the solid line. The dotted line indicates the Roche lobe of HU Aqr.

(2001, their figure 6).

3.4.4 Model results

With the values of R_μ determined above, the model can be used to find the best fit brightness map, from which the brightness per unit stream length along the stream trajectory can be determined. This is independent of the actual length of the stream eclipsed in any particular phase interval, and is important as there are different lengths of ballistic and magnetically confined stream eclipsed in a given phase interval.

The eclipse of the accretion stream is divided into three sections, as illustrated by the shaded regions in Figure 3.13 and labeled 1, 2 and 3. These enclose a section of the ballistic accretion stream plus the section of magnetically confined stream that is nearest the white dwarf (interval 1), the section nearest the threading region (interval 3) and the stream between the two (interval 2). The results are represented in Figure 3.14 as a brightness per unit stream length in these eclipse phase intervals. Figure 3.14 presents the results of the modelling in two columns representing the

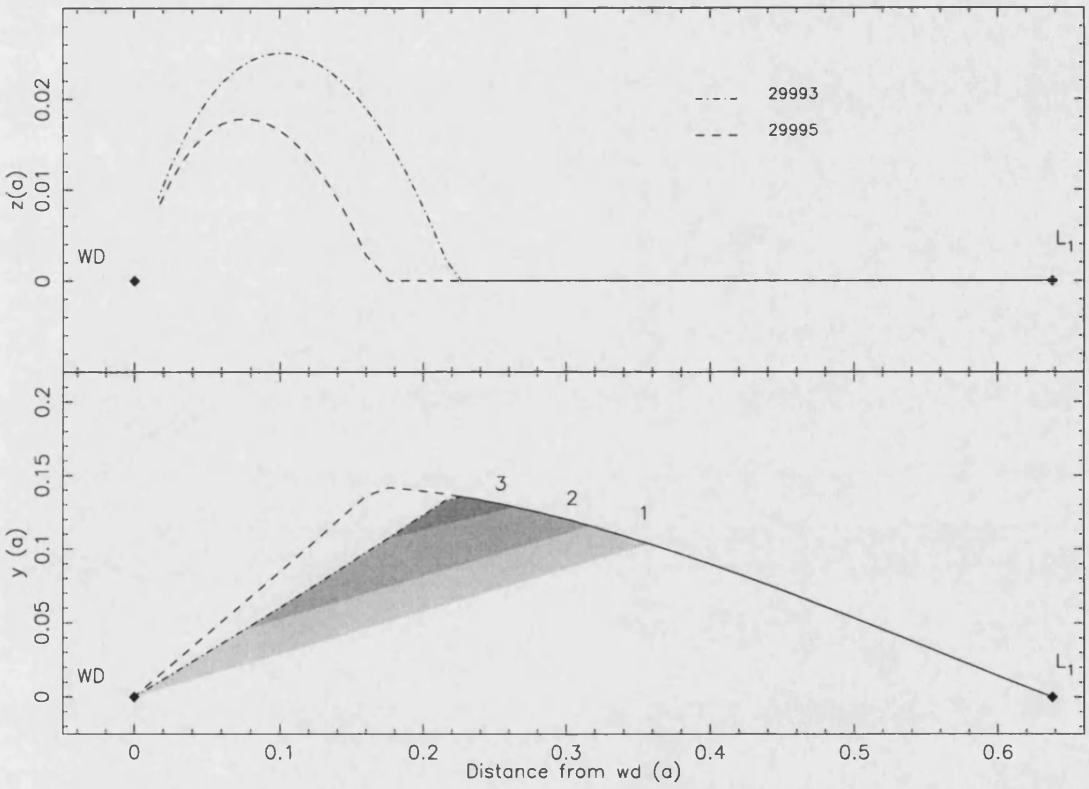

Figure 3.13: The upper plot shows the model stream points for cycles 29993 and 29995 looking parallel to the orbital plane, while the lower plot shows them looking down onto the orbital plane. The difference in the stream trajectories is evident. The shaded regions are three equal phase intervals encompassed by the ingress of the white dwarf and the final ingress of the threading region for cycle 29993. These correspond to those parts of the stream used to form sections 1, 2 and 3 in Figure 3.14. (For cycle 29995 the definitions are equivalent.)

two cycles presented here and the three rows the three energy bands: red, yellow and blue. The ordinate of Figure 3.14 then represents the total brightness of points eclipsed in these intervals per unit stream length, i.e. points in the ballistic and magnetically confined sections of the stream eclipsed in that phase range. The results have been calibrated into energy units using the standard star observation in order to facilitate comparison between the different bands (however, this calibration is only approximate as noted earlier).

Figure 3.14 shows that there is enhanced brightness in the section containing the threading region in all bands in cycle 29993, but only in the yellow and blue in cycle 29995. The section containing those parts of the stream nearest the white dwarf are also bright in cycle 29993. However, in cycle 29995 this is only seen in the blue. The brightness of the different sections is consistent with the colour ratios from Section 3.3.4. In Figure 3.14 the threading region in cycle 29995 is hotter than that in cycle 29993 as the ratio of the yellow to red is greater for cycle 29995. This is again consistent with the colour ratios (Section 3.3.4). However, the blue to yellow ratio is similar in the two eclipse ingresses, suggesting that the increase has occurred in both blue and yellow bands.

3.5 Discussion

3.5.1 Comparison with earlier results

The model fits of Harrop-Allin et al. (1999a) and Harrop-Allin (1999) for one pole accretion, show a general enhancement in the threading region and towards the white dwarf. Some eclipses (for example cycle 3723 and 3724 in Harrop-Allin, 1999) show significantly greater brightness in the threading region of the white dwarf than others (such as the immediately preceding cycle 3722).

Enhanced brightness regions are also found by Vrielmann and Schwope (2001) and Kube et al. (2000) who apply similar modelling techniques. Vrielmann and

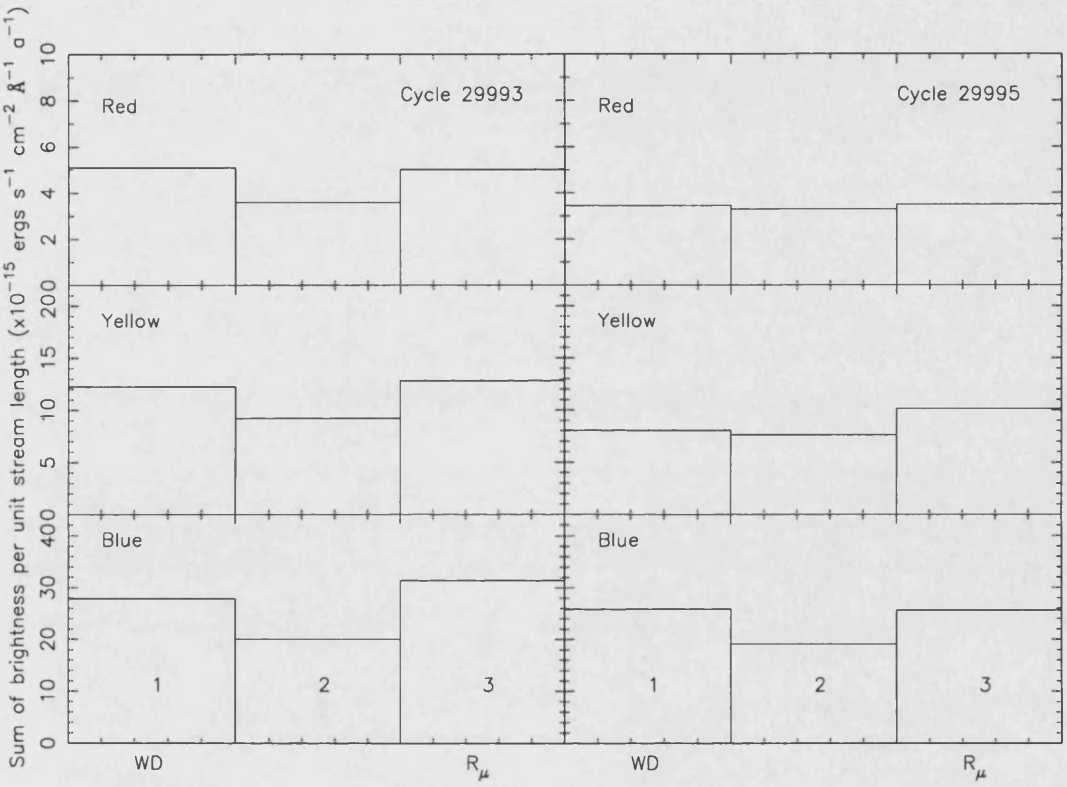

Figure 3.14: The above plot shows for cycles 29993 and 29995, in each band, the total brightness per unit stream length in three sections of the stream. These intervals include a section of the ballistic trajectory plus those parts of the stream nearest the white dwarf (section 1), the threading region (section 3) and the magnetically confined stream between the two (section 2), cf. Figure 3.13. A brightness enhancement at the threading region is evident in both cycles, but an enhancement towards the white dwarf is not seen in the red and yellow bands of cycle 29995.

Schwope (2001) apply their Accretion Stream Mapping technique to Hβ, Hγ and He II λ4686 observations of HU Aqr. They find a brightness enhancement at the threading region, but not towards the white dwarf, similar to cycle 29995. Kube et al. (2000) used the CIV λ1550 line emission from UZ For (with a three-dimensional stream model). They found three regions of enhanced brightness: one on the ballistic accretion flow, and two on the magnetically confined section. They suggest that the enhancements on the magnetically confined section are caused by irradiation of denser sections of the stream with a large area near the accretion region, and a smaller region near to the threading region. This may be the case in cycle 29993, where I find a bright stream near the white dwarf, and again near the threading region. Although Kube et al. (2000) find no enhancement actually at the threading region, this may be a result of an increase in the density of the stream as it approaches this point, resulting in an increase in the continuum optical depth, and hence a decrease of the CIV λ1550 equivalent width, and so is not necessarily indicative of a faint stream in this region.

3.5.2 Heating in the magnetically confined stream

Heating of the magnetic section of the stream has been studied by Ferrario and Wehrse (1999) for a stream which is assumed to thread onto the field lines at a coupling radius r_c (our R_μ) from the white dwarf, over a radial distance Δr_c in the orbital plane. This provides an opportunity for a comparison between our observationally derived results, and the main points of their theoretical model results.

Ferrario and Wehrse (1999) consider two heating mechanisms: irradiation by the X-ray component from the accretion shock (the soft X-rays being up to $\approx$ 4000 times more efficient at heating the stream than the hard X-rays) and the effects of magnetic reconnection in the stream-field interaction across the threading region Δr_c. The comparison I make with these theoretical models is qualitative, as the geometrical structure of the magnetically confined accretion flow in Ferrario & Wehrse is funnel-

shaped, compared to our linear trajectory. However, our results showing brightness enhancements towards the threading region are consistent with their models which incorporated magnetic heating in the threading region. This implies that some magnetic heating mechanism is needed in this region.

3.5.3 Temporal variations in the stream profile

I conclude, based on the colour ratios, that the threading region was brighter and hotter in cycle 29995 than in cycle 29994 (Section 3.3.4). There are therefore significant changes in the threading region on the timescale of the orbital period (125 mins).

Although detailed fits to only two cycles are presented here, it can be seen that there is a difference in the brightness in different colour bands between the two eclipses (Figure 3.14). This confirms the variability seen in the colour ratios and in the stream eclipse profiles of the light curves in the different colour bands (Figure 3.5, 3.6). The large brightness enhancement near the white dwarf in cycle 29993 could be irradiated material which cools over the timescale of the next orbital period, leaving a fainter region as seen in cycle 29995 where the observed enhancement is less pronounced. However, without the detailed modelling of the intermediate cycle, which has been excluded for reasons discussed previously, I cannot be certain and it will require more high signal-to-noise ratio observations of consecutive eclipses to investigate whether this in fact occurs. What is clear from the model results, and indeed directly from the raw light curves and colours, is that the emission from the whole stream is highly dynamic and unstable.

Dramatic changes in the stream eclipse profiles were also observed in the low state (Harrop-Allin et al., 2001; Glenn et al., 1994). These cycle-to-cycle changes in stream brightness and trajectory require a revision of how the stream is viewed, and of the manner in which the magnetic heating takes place in the threading region. Future treatments may need to consider large scale magnetic instabilities, and quasi-cyclic behavior.

3.5.4 Mass transfer rate

The mass transfer rate can be estimated from the values of R_μ in Table 3.2 using Equation 1.4. This equation does not take into account the secondary magnetic field and assumes a centred, dipolar magnetic field for the white dwarf without any distortion of the field by the stream. The derived mass accretion rates will therefore be very approximate. The radius of the stream can be estimated from the pre-eclipse absorption dip (e.g. Watson et al., 1995). If it is assumed that the material at R_μ is causing the absorption, σ is given by

$$\sigma \approx \frac{\pi R_\mu \Delta\phi}{\sin i} \tag{3.2}$$

because the inclination is high.

The width of the pre-eclipse dip from Figure 3.6 is $\Delta\phi = 0.055$, which gives values of $\sigma_9 = 2.3 - 2.7$ for $R_\mu = 0.22a - 0.26a$, and these values are comparable to the value of $\sigma_9 = 3$ used by Harrop-Allin et al. (1999a). Using $B = 37$ MG (Glenn et al., 1994) and $R_9 = 0.622$ (using the formulation given in Warner, 1995), we obtain values of $\dot{M} = 2.0 - 1.1 \times 10^{16}$ g s^{-1} ($3.1 - 1.8 \times 10^{-10}$ M$_\odot$ yr^{-1}) for $R_\mu = 0.22a - 0.26a$.

This $\dot{M}$ is within the range of values found by Schwope et al. (2001) of $\dot{M} = 0.378$- $- 4.41 \times 10^{16}$ g s^{-1} ($0.6 - 7 \times 10^{-10}$ M$_\odot$ yr^{-1}) from the X-ray spectral flux, and $\dot{M} = 1.83 \times 10^{16}$ g s^{-1} (2.9×10^{-10} M$_\odot$ yr^{-1}) calculated by Heerlein et al. (1999) from their accretion model. It is however lower than the values quoted by Harrop-Allin et al. (1999a), where they find $\dot{M} = 8 - 76 \times 10^{16}$ g s^{-1} ($12.7 - 121 \times 10^{-10}$ M$_\odot$ yr^{-1}). However, their values of R_μ are probably under-estimated for the reasons discussed in Section 3.4.3, thus implying their values of $\dot{M}$ are over-estimated.

3.6 Summary and conclusions

I have carried out high signal-to-noise ratio observations of HU Aqr using S-Cam 2 on the WHT on two nights. The system was in a high accretion state, and from the single sharp change in the eclipse profile and archive soft X-ray light curves in this state, I infer that matter was accreting at only one pole on the white dwarf. At the onset of the eclipse, the accretion stream is the source of more than half of the optical emission from the system. The system brightness was similar from orbit to orbit, and the eclipse duration remained constant, but the shape of the accretion stream eclipse changed significantly, ending at $\phi = 0.979$, 0.977 and 0.982.

I find eclipse durations which are unchanged from past optical studies (Harrop-Allin et al., 1999a; Schwope et al., 1997b), but shorter than those deduced in the soft X-rays by Schwope et al. (2001). However, the location of the accretion region is similar to that found by Schwope et al. (2001), so that there is no evidence that the optical emission is from higher latitudes on the white dwarf than the soft X-rays. This indicates that the duration of the soft X-ray eclipses may be affected by absorption, as they suggested.

The duration of the egress of the accretion region in the optical is 8 s, compared to 1.3 s in soft X-rays (Schwope et al., 2001). This indicates clearly that the region emitting cyclotron radiation subtends an angle that is greater by a factor of $\sim$5 by comparison with the soft X-ray emitting region, which Schwope et al. (2001) calculated as subtending an angle of 3° from the centre of the white dwarf.

I have found significant changes in the colour of the accretion stream from one eclipse to the next. This indicates that the threading region is hottest in the last of the eclipses by comparison with the previous two (see Section 3.3.4). I have modelled the stream using the technique of Hakala (1995) and Harrop-Allin et al. (1999b). This finds that most of the emission originates from two places: close to the white dwarf and in the threading region. By comparison with the models of Ferrario and Wehrse (1999) this indicates that magnetic reconnection is required in the threading

region. The modelling clearly identifies an increase in brightness in the threading region for both cycles and an enhancement towards the white dwarf for cycle 29993. This work shows that the use of the highest signal-to-noise ratio data is necessary.

From the change in brightness of the heated regions in the model streams, and the varying stream eclipse profiles, I suggest that the magnetic heating in the threading region may be unstable. The implications of the highly variable stream trajectory and brightness profile should be recognised in future investigations of the stream properties. A systematic study of series of consecutive eclipses is required to investigate the characteristics of the magnetic heating and stream instabilities.

Chapter 4

Variability in the Accretion Stream in the Eclipsing Polar EP Dra

In this chapter I present observations of EP Dra, proposing a combination of cyclotron beaming and absorption in the accretion flow to explain the observed eclipse light curve variations between consecutive cycles. I have not applied the model technique used in Chapter 3 for reasons discussed there, but provide a discussion of the system from an analysis of the light curves.

A shortened version of this chapter has been published in *Monthly Notices of the Royal Astronomical Society* (Bridge et al., 2003).

4.1 Observations and reductions

The observations of EP Dra were made at the William Herschel Telescope, La Palma, on the nights of 2000 October 2/3 and 2000 October 3/4. The S-Cam 2 instrument was located at the Nasmyth focus and a total of six eclipses of EP Dra were obtained. Table 4.1 gives the cycle number (relative to the ephemeris of Schwope and Mengel (1997)), date, start time and length for each observation, as well as the time of

Table 4.1: Summary of observations of EP Dra for the nights of 2000 October 2/3 and 2000 October 3/4. Cycle numbers are with respect to the ephemeris of Schwope and Mengel (1997).

Cycle number (56900+)	Date	Start time (TDB) (2450000.0+)	Observation length (s)	Time of mid-eclipse (TDB) (2450000.0+)	Time of mid-ingress (TDB) (2450000.0+)	Time of mid-egress (TDB) (2450000.0+)
62	2000 Oct 2	1820.36254	1496	1820.37575	1820.37382	1820.37850
63	2000 Oct 2	1820.44230	1800	1820.44840	1820.44649	1820.45128
64	2000 Oct 3	1820.50681	2523	1820.52106	1820.51913	1820.52387
76	2000 Oct 3	1821.38171	2400	1821.39294	1821.39097	1821.39572
77	2000 Oct 3	1821.45653	2111	1821.46559	1821.46368	1821.46835
78	2000 Oct 4	1821.53007	1393	1821.53825	1821.53631	1821.54112

mid-eclipse (defined as orbital phase $\phi = 0.0$), mid-ingress and mid-egress of the steep components of the eclipse (all times are in TDB - barycentric dynamical time - which includes light travel time correction to the solar system barycentre). Two of the observations (cycles 62 and 64) have data gaps caused by the instrument exceeding the data acquisition limits.

The useful observational wavelength range of S-Cam 2 is approximately 340--680 nm (Perryman et al., 2001). This time I have split the wavelength range into four bands, which are labeled here as U (340–400 nm), B (390–490 nm), V (500--600 nm) and R_c (590–680 nm) and which correspond very broadly to those of the Johnson-Cousins $UBVR_c$ system (Bessell 1990, and references therein). The light curves were background subtracted using a mean value from off-source pixels taken from the mid-eclipse phases. See Chapter 3 and also Perryman et al. (2001) for a detailed discussion of the data reduction process.

The 'white' light curves are shown in Figure 4.1, and Figure 4.2 shows the white light eclipse of the white dwarf, accretion region and accretion stream on an expanded scale, making clear the rapid changes at ingress and egress. The $UBVR_c$-bands are shown in Figures 4.3, 4.4, 4.5 and 4.6, where each figure shows the three consecutive eclipses for each of the two nights of the observations. The U-band and R_c-band light curves are binned in 4 s intervals and the B-band and V-band in 1 s. The light curves have been calibrated in energy units using observations of the standard star BD+28 4211, which were taken on the first night. A standard star was not observed on the second night so cycles 76 to 78 are only approximately calibrated. The maximum brightness is $V \approx 17$ at $\phi = 1.2$, consistent with that measured by Schwope and Mengel (1997).

The seeing for the first night was ~1.5 arcsec, and for the second night ~1 arcsec. Some of the variability in the eclipses of the first night may in part be due to the occasionally poorer seeing, causing the point spread function to spill over the edges of the 6×6 array. A number of sharp dip features (e.g. at $\phi \sim 0.96$ in cycle 62) can be attributed to this.

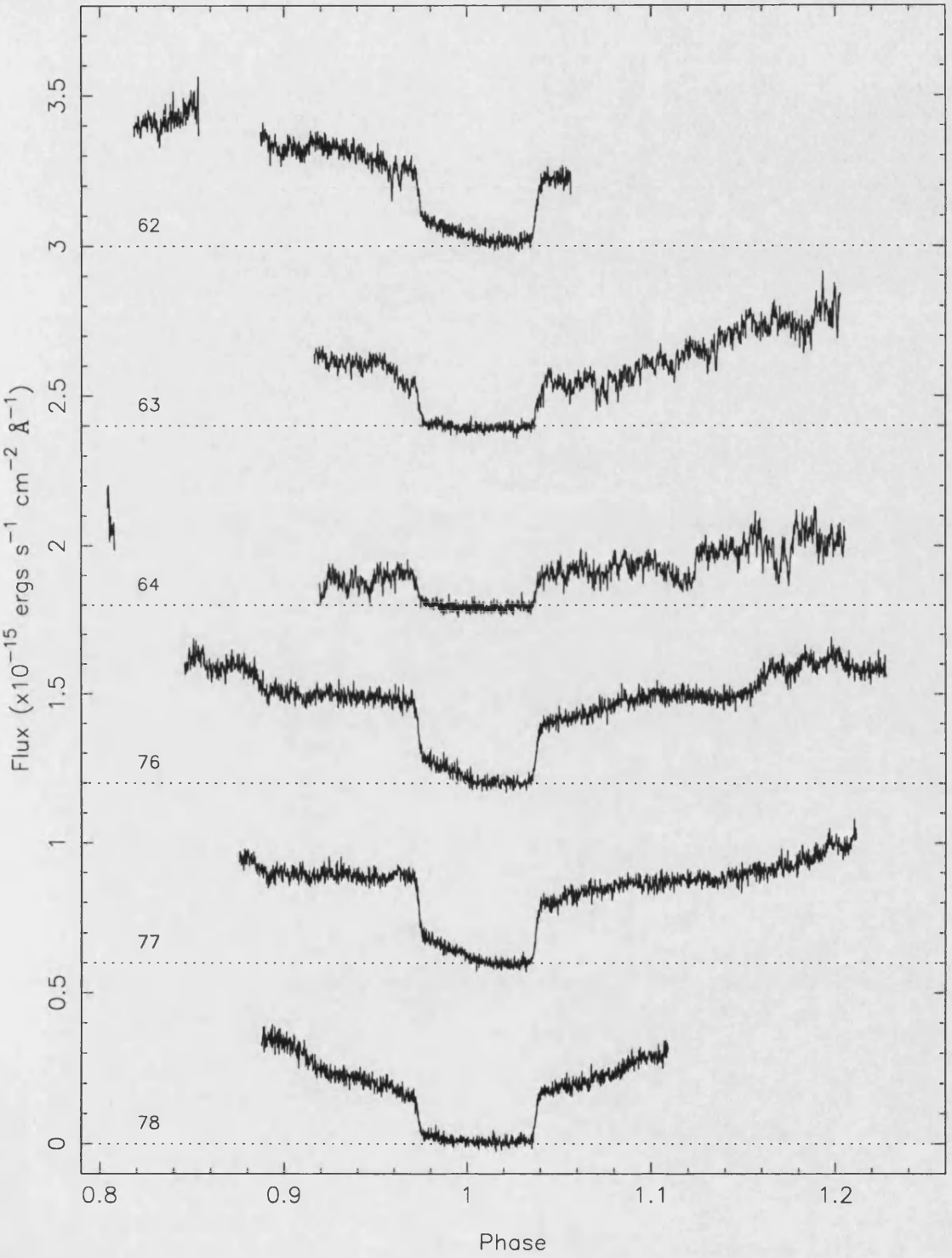

Figure 4.1: White light curves for EP Dra in 1 s time bins. Each cycle is offset vertically by 0.6×10^{-15} ergs s^{-1} cm^{-2} Å^{-1}, and phased according to the ephemeris of Schwope and Mengel (1997).

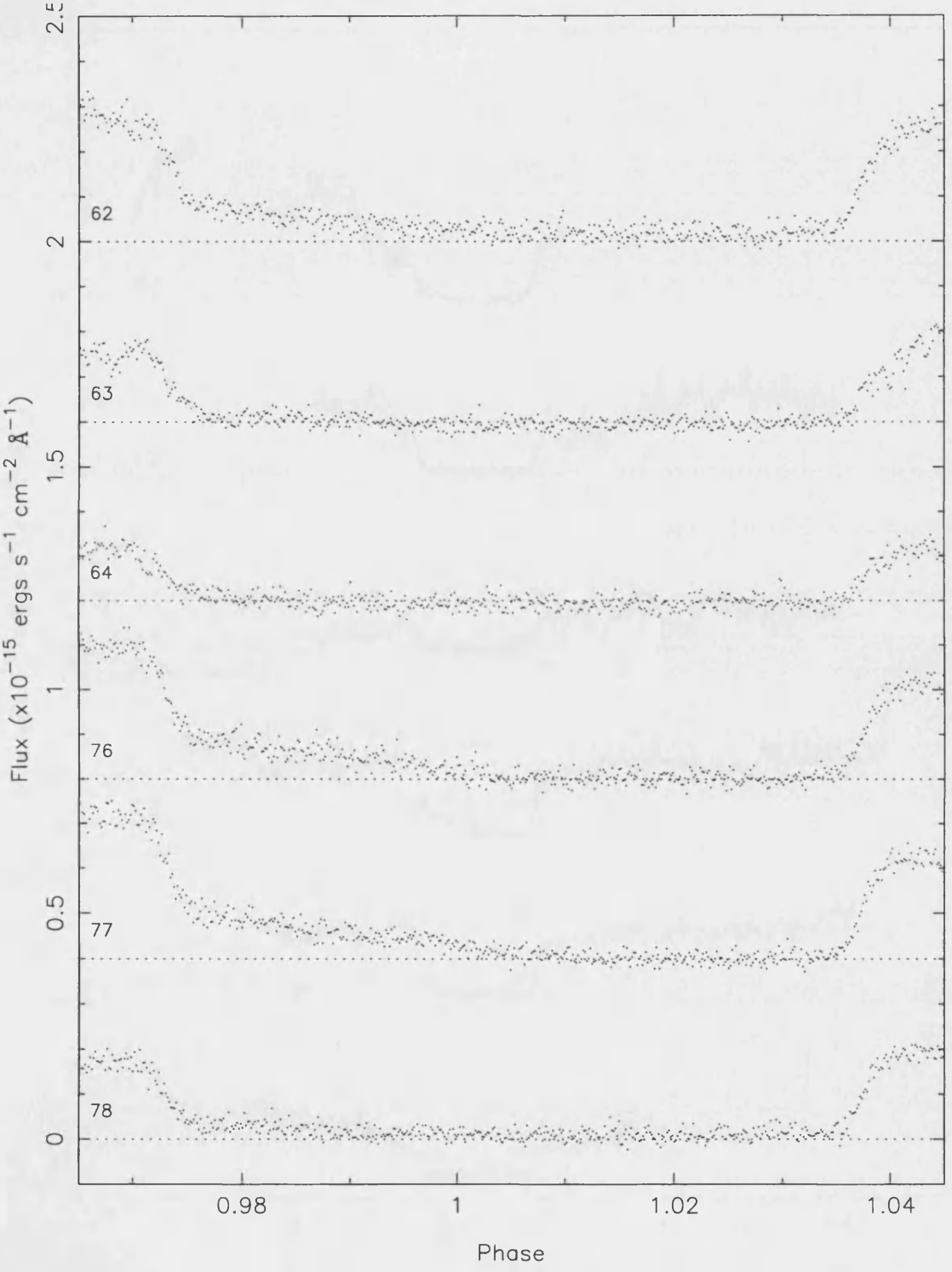

Figure 4.2: The 1 s time binned white light eclipse, showing the accretion region and stream ingress in more detail, highlighting the variability between consecutive eclipses. Each cycle is offset vertically by 0.4×10^{-15} ergs s^{-1} cm^{-2} Å^{-1}, and phased according to the ephemeris of Schwope and Mengel (1997).

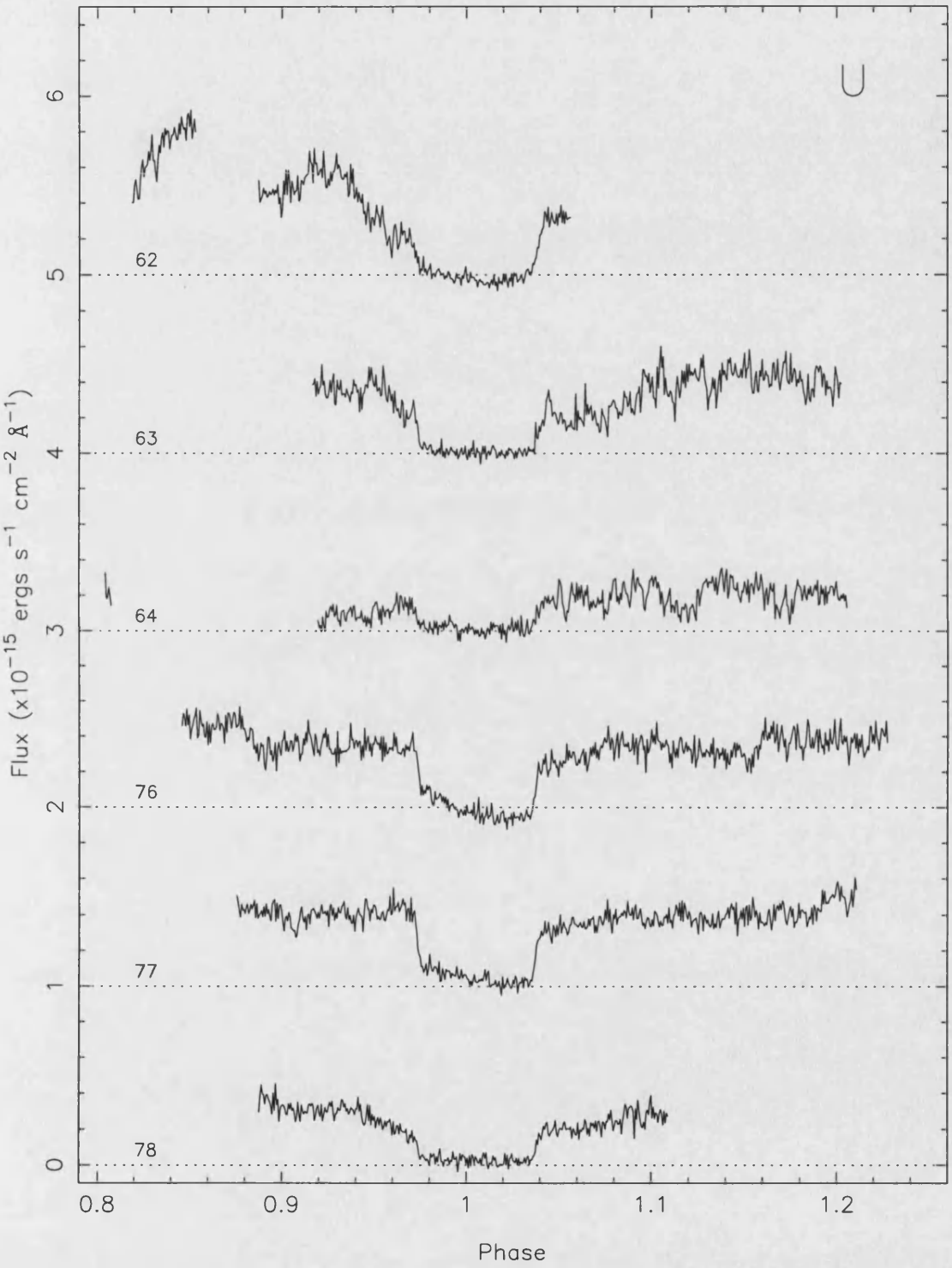

Figure 4.3: U-band light curve for all six cycles binned into 4 s time intervals and phased with respect to the ephemeris of Schwope and Mengel (1997).

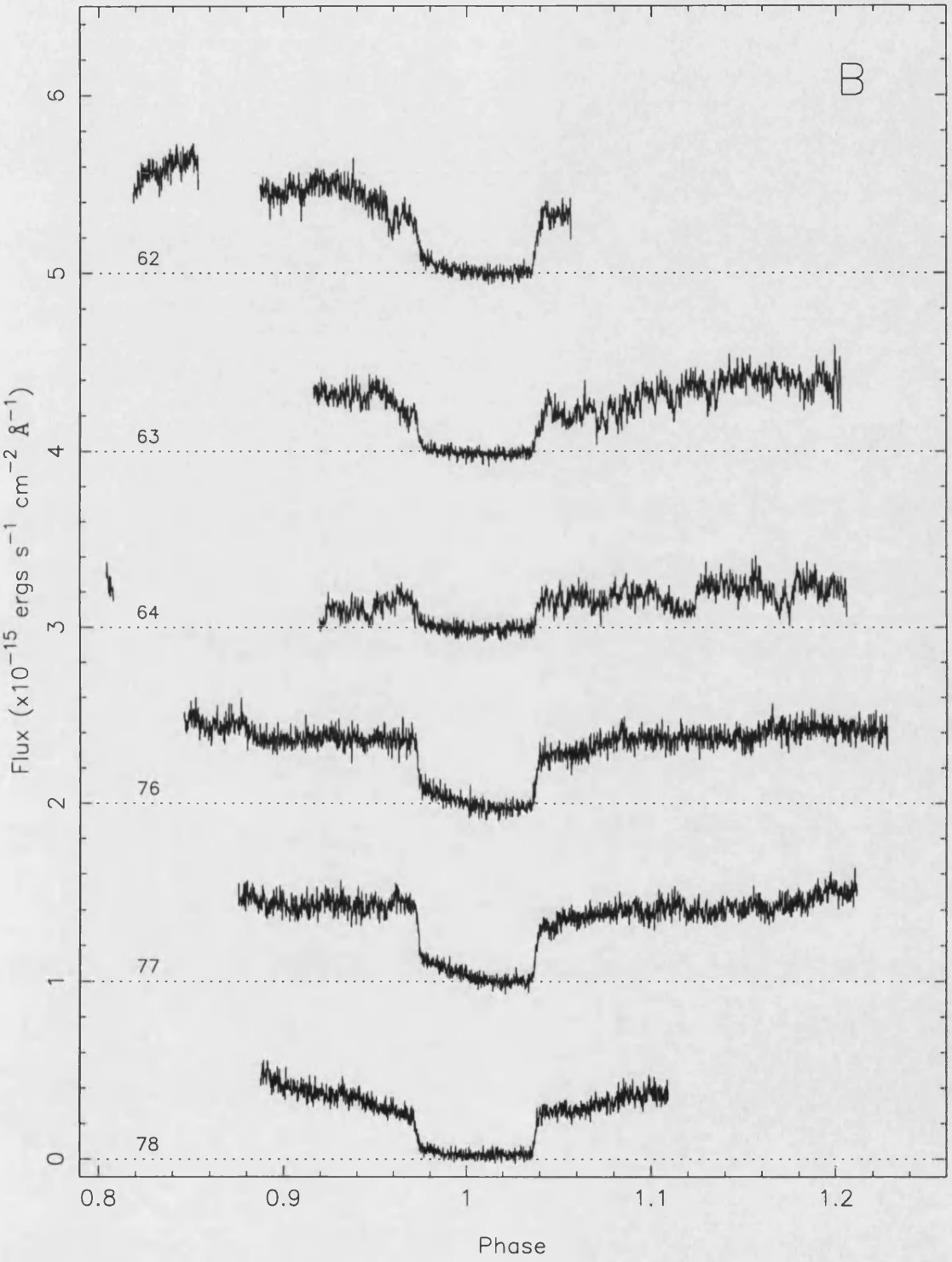

Figure 4.4: *B*-band light curve for all six cycles binned into 1 s time intervals and phased with respect to the ephemeris of Schwope and Mengel (1997).

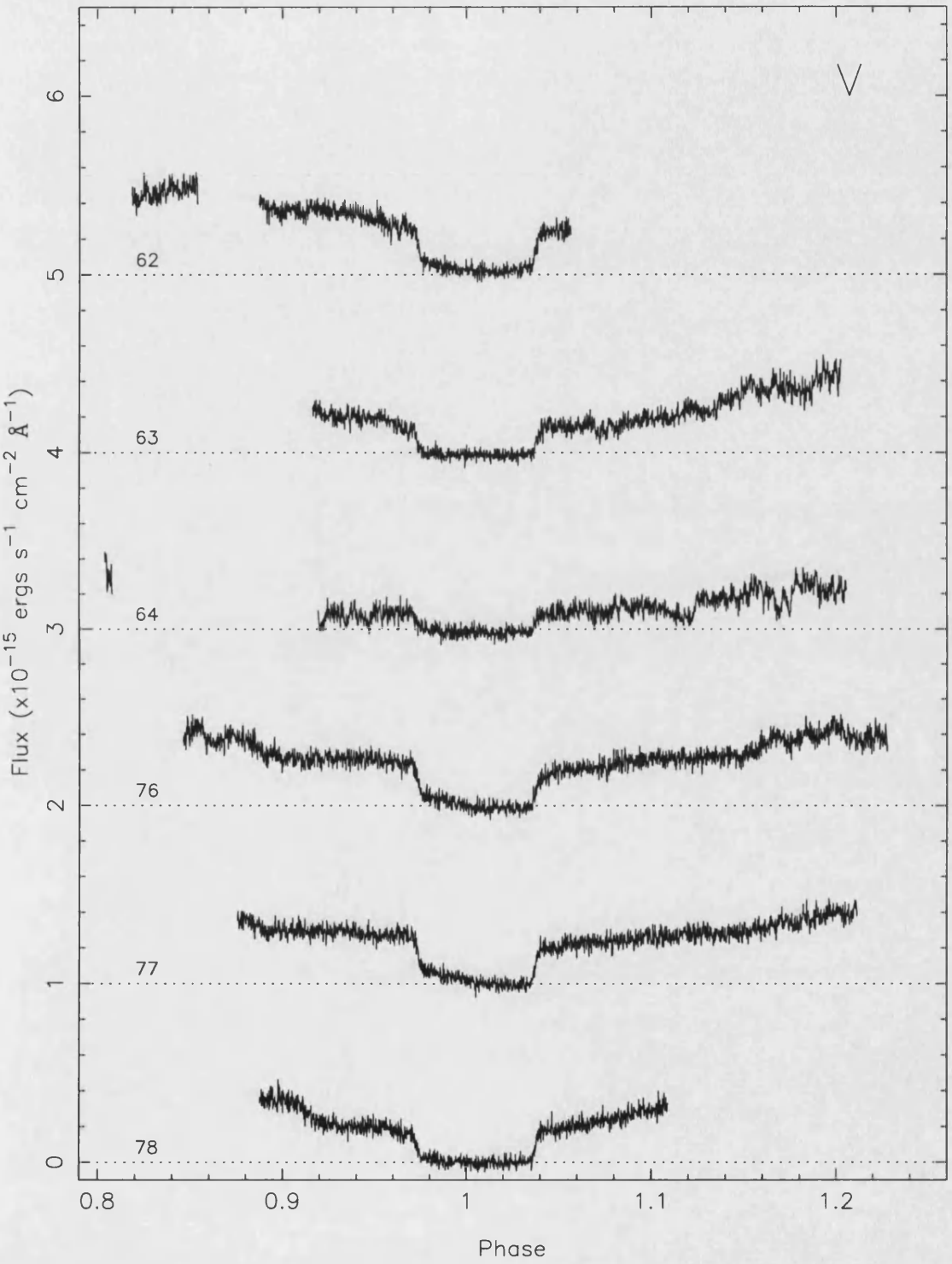

Figure 4.5: V-band light curve for all six cycles binned into 1 s time intervals and phased with respect to the ephemeris of Schwope and Mengel (1997).

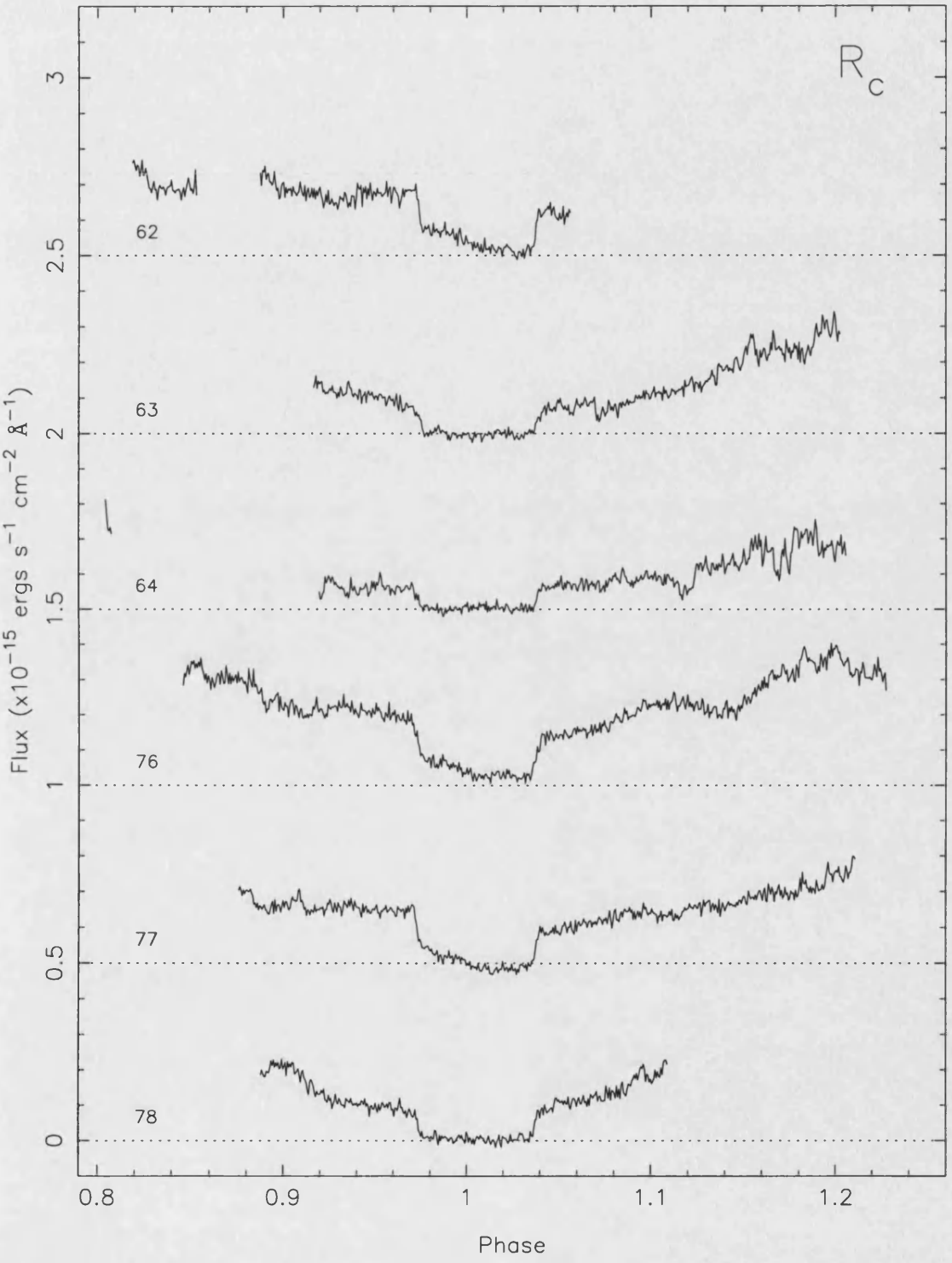

Figure 4.6: R_c-band light curve for all six cycles binned into 4 s time intervals and phased with respect to the ephemeris of Schwope and Mengel (1997).

4.2 Light-curve features

4.2.1 White dwarf and accretion region eclipse

The most prominent feature of the light curves is the eclipse of the white dwarf and accretion stream by the secondary between $\phi = 0.972$ and $\phi = 1.04$. The duration of the eclipse (measured between the mid-point of the steep eclipse components) is the same for all cycles, 6.8 minutes, equivalent to $\Delta\phi = 0.0646$.

The eclipse of the white dwarf photosphere and the accretion region is rapid compared to the eclipse duration. To characterise the rapid eclipse the six white light curves are binned into 3 s time bins, then for each time bin the brightness of the previous time bin is subtracted. Figure 4.7 shows the mean of these six differential light curves. The width of the complete ingress and egress of the white dwarf and accretion region is 36 s which is comparable to the expected ingress duration for the white dwarf of 37 s (assuming a mass for the white dwarf of $M_1 = 0.43\,M_\odot$ and mass ratio $q = 0.31$; Schwope and Mengel (1997)). The amplitude of the brightness change at ingress is greatest at bluer wavelengths, which is as expected for a hot accretion region and white dwarf.

HU Aqr (Chapter 3) and UZ For (Perryman et al., 2001) show a rapid drop in flux at eclipse ingress lasting a few seconds, which is taken as evidence of a bright, compact accretion region. In contrast, there is no evidence for such a rapid drop in EP Dra. However, there is some asymmetry in Figure 4.7 which implies the presence of an accretion region in some form. The presence of an accretion region is also evident from the observation that the amplitude of the rapid ingress varies with the brightness of the accretion stream, and this is illustrated in Figure 4.8. Were there no contribution from an accretion region, no correlation would be expected. Therefore, the rapid decline in flux must include the eclipse of an accretion region with the eclipse of the white dwarf, despite a compact accretion region not being directly evident in the eclipse. By comparison with HU Aqr and UZ For, the absence of a compact accretion region is surprising.

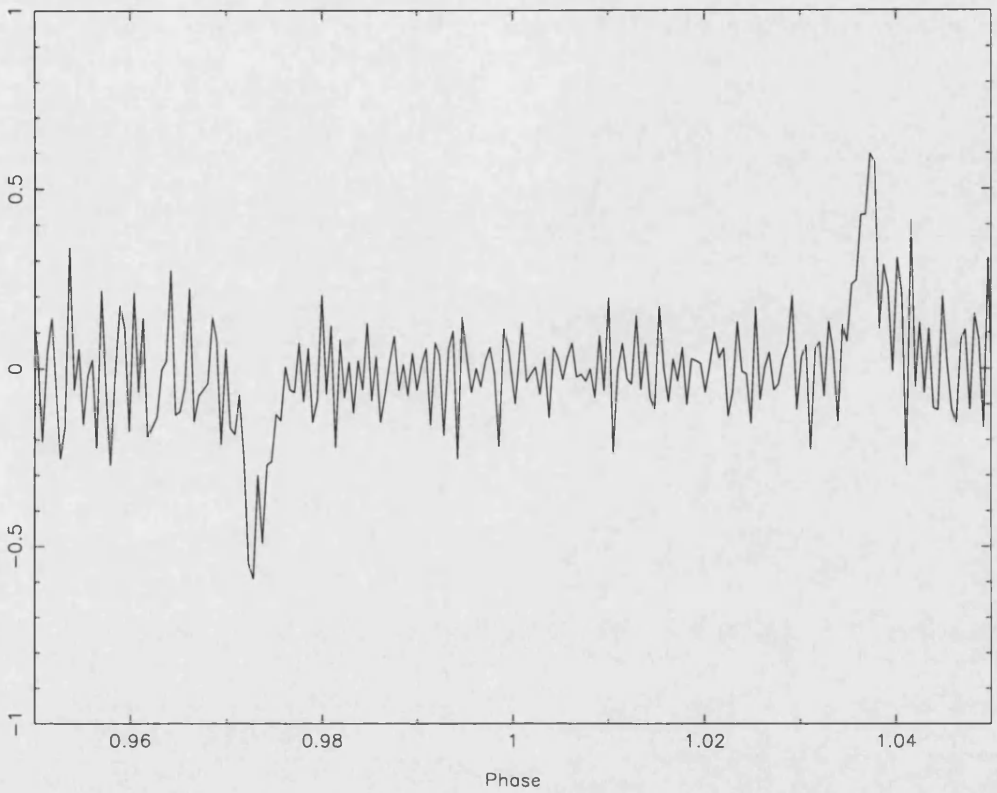

Figure 4.7: The mean of the six 3 s differential white light curves.

Following the rapid 36 s decline in brightness seen at ingress, the stream is the major contributor to the observed brightness. The secondary is expected to contribute a small amount of emission in the R_c-band, however we do not see evidence for this during eclipse, probably because of the signal-to-noise ratio of the light curves.

4.2.2 Stream eclipse

In our light curves the stream eclipse ingress, from $\phi \simeq 0.975$ onwards, takes two forms: a long ingress from a relatively bright stream (cycles 62, 76 and 77) and a short ingress from a faint stream (cycles 63, 64 and 78). Figure 4.9 shows the eclipse profile of all six cycles, and the two forms of stream eclipse are clear. There is also a decline in flux preceding the ingress of the white dwarf and accretion region in cycles 63 and 78 where the stream is relatively faint.

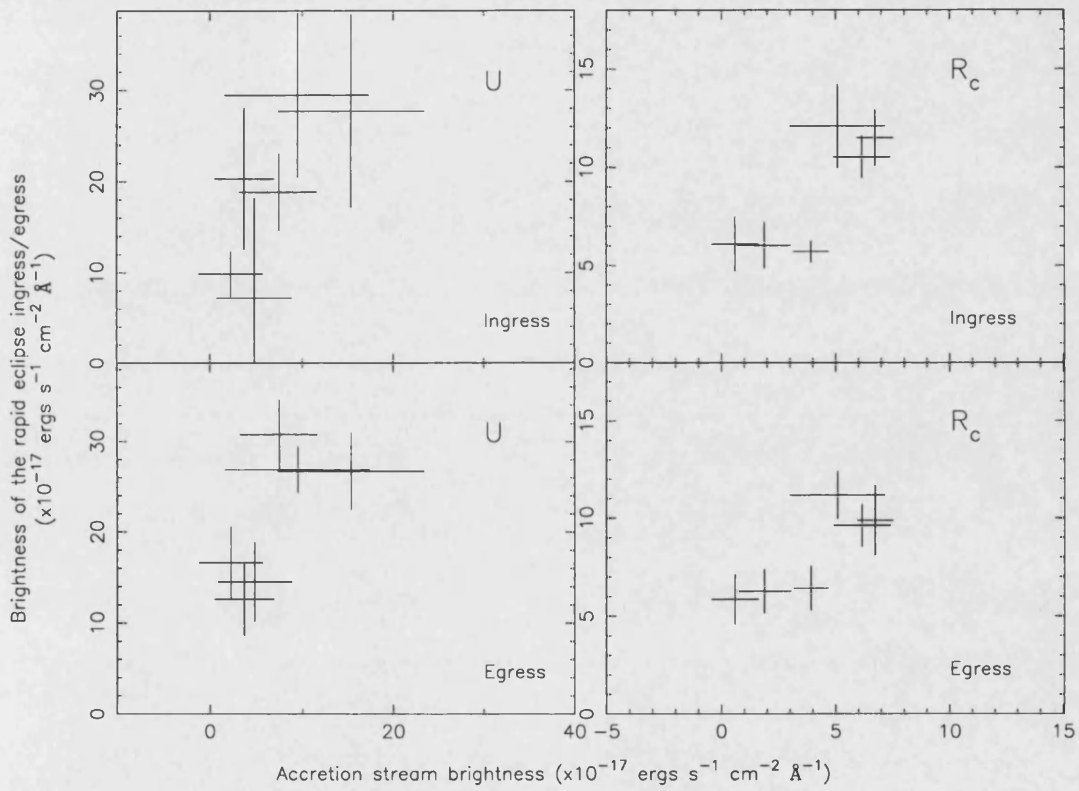

Figure 4.8: White dwarf and accretion region brightness against stream brightness on ingress and egress for the U-band and R_c-band light curves. The stream brightness is measured immediately after the steep eclipse ingress at $\phi = 0.975$.

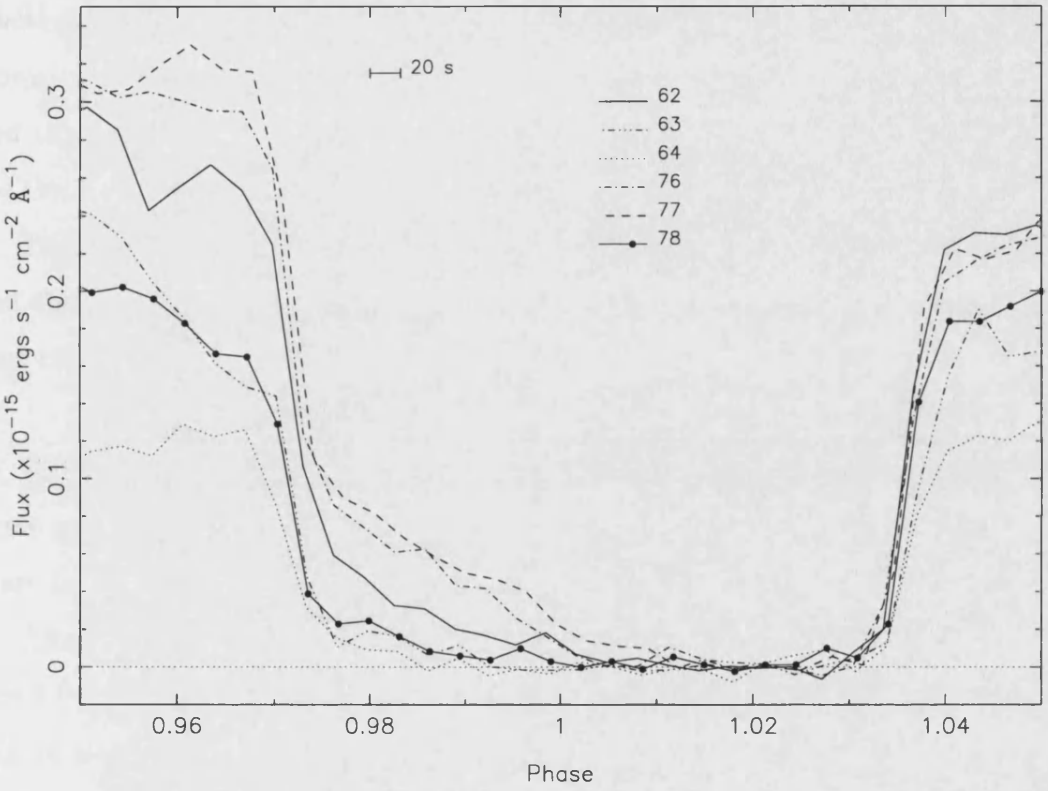

Figure 4.9: The six white light curves centred on the eclipse by the secondary. They have been binned into 20 s time bins, which removes any features related to the eclipse of the white dwarf and the accretion region. The contribution from the secondary has been subtracted.

4.2.3 Out of eclipse

The prominent feature before and after the eclipse is the decline in brightness at phase $\phi = 0.874$ in cycle 76 and subsequent rise at $\phi = 1.16$. This is seen in all bands in Figures 4.3, 4.4, 4.5 and 4.6. The duration of the decline is $\sim$100 s, ending at $\phi = 0.89$. The reduced phase coverage in cycle 77 means that it is not certain whether the feature at ϕ=0.88 is the same feature as that in the preceding cycle. However, the similarity in the shape of the light curve compared to that of cycle 76 and the location of the feature suggests proceeding with the assumption that they are the same. I refer to this pre-eclipse decline and post-eclipse rise as the 'trough'.

There is a bright stream in cycle 76; however, in cycle 78 the stream is fainter and the trough is identified as starting at the later phase of $\phi = 0.90$. I also infer that the rise at $\phi = 1.08$ in cycle 78 is the counterpart of that at $\phi = 1.16$ in cycle 76.

Following the start of the trough, cycles 76 and 77 show a relatively flat light curve prior to the eclipse of the white dwarf. In cycles 62, 63 and 78, after ϕ=0.95, there is a decline in flux prior to the eclipse ingress.

After the rapid egress of the white dwarf photosphere and accretion region at $\phi = 1.04$, there is no obvious stream egress in cycles 63 and 64, corresponding to a lack of a stream brightness at ingress. In cycles 76, 77 and 78 the accretion stream egress is seen as a gradual increase in flux, followed by a relatively flat light curve in cycles 76 and 77.

4.3 Discussion

4.3.1 Accretion region location

In determining the location of material confined to magnetic field lines, the values chosen for R_μ, and the colatitude and longitude of the accretion region are important. Different estimates for the location of the accretion region are proposed by Remillard

et al. (1991) and Schwope and Mengel (1997). Based primarily on their circular polarimetry data, Remillard et al. (1991) concluded that there was only one accretion region, at a colatitude of $\sim 18°$ and longitude $\sim -17°$. On the other hand, Schwope and Mengel (1997), modelling the bright cyclotron peaks in optical observations, found a colatitude of $\sim 60°-70°$.

As I am unable to say with certainty what the true location of the accretion region is, both possibilities of high and low latitude accretion are considered in the following discussion. To proceed, the mass ratio ($q = 0.31$; Schwope and Mengel (1997)) is used to create a model Roche lobe and white dwarf with a magnetic pole at a given colatitude β, and longitude ζ. Dipole field lines are then constructed passing through a given R_μ. By varying R_μ for a given magnetic pole location, field lines can be created that eclipse a given part of the polar system at a phase given by features observed in the light curves. Although Remillard et al. (1991) and Schwope and Mengel (1997) quote the location of the accretion region, I use these values for the location of the magnetic pole, noting that this will cause accretion at a region offset from these values for a given R_μ.

4.3.2 Stream variations

The observed stream variations (Figures 4.1 and 4.9) are essentially caused by a change in the visibility of material confined to the magnetic field lines of the white dwarf. This could be caused by an asynchronism in the white dwarf spin and orbital periods, causing a changing magnetic field to be presented to the incoming accretion stream. However, this is considered unlikely due to a lack of a change in the relative position of the bright phase and eclipse between the observations of Remillard et al. (1991) and Schwope and Mengel (1997).

Alternatively, there is either a change in the amount of bright material on visible field lines or material is located on different field lines. These can be caused by a change in R_μ, from a variation in the mass transfer rate and an inhomogeneity in the

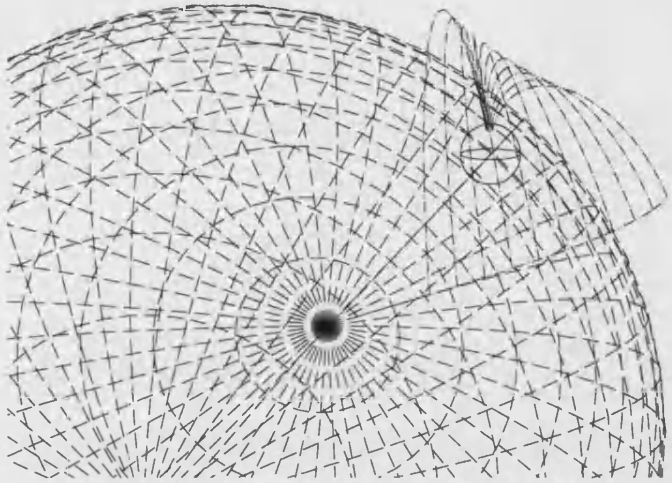

Figure 4.10: Plot of the geometry of EP Dra consistent with a variable brightness stream for $\phi = 0.98$. The magnetic field lines are still visible, causing a long stream ingress in the light curves for bright stream material confined to these field lines. The magnetic pole is located at $\beta = 18°$ and $\zeta = -17.0°$ (assuming the values for the accretion region in Remillard et al. (1991) are the same as the magnetic pole).

flow. It is not possible from our data to isolate either possibility as the cause, and it is probable that both contribute to the observed stream variability. Variations in the accretion stream eclipse profile have been observed in many eclipsing polars, for example in HU Aqr (Glenn et al., 1994; Harrop-Allin, 1999; Bridge et al., 2002) and V895 Cen (Salvi et al., 2002).

An estimate of R_μ can be made from the phase at which visible magnetic field lines are completely eclipsed in our geometric model. Figure 4.10 shows an example for accretion at low colatitude where magnetic field lines are visible far out of the orbital plane. I find that a longer stream ingress requires a smaller R_μ for a high colatitude accretion region (Schwope and Mengel, 1997), compared with that from a low colatitude (Remillard et al., 1991).

4.3.3 Trough feature

I consider the two mechanisms that could explain the trough: absorption and emission. Absorption would occur from material lost by the secondary, with the initial drop in the light curves resulting from the onset of the absorption. Alternatively, the feature could be caused by the changing cyclotron emission with phase.

Emission

Schwope and Mengel (1997) observed a sharp rise to and decline from the bright phase (which is indicative of the cyclotron beaming effect) in their V-band light curves of EP Dra. The phase range of our light curves is much less than that of Schwope and Mengel (1997) so the same behaviour is not observed either side of the eclipse; however, the trend of our light curves is consistent with such a rise to and fall from maximum. Figure 4.11 shows our V-band light curves with the Schwope and Mengel (1997) figure 1 V-band data from 1995. The Schwope and Mengel (1997) data has been scaled vertically to show the coincidence of the features.

The wavelength at which the cyclotron emission peaks is dependent upon the magnetic field strength of the white dwarf, with increasing field strength shifting the peak to shorter wavelengths. For EP Dra, the field is $\sim$16 MG (Schwope and Mengel, 1997) so the orbital variability is expected to be greatest towards redder wavelengths. This would cause a significant change in the shape of the light curves in the different colour bands, and hence a prominent feature in the colour ratios, see Figure 4.12. As a signature of the cyclotron emission, a sharp peak is expected in the R_c-band followed by a gradual decline, and conversely in the U-band a more gradual rise in flux to a maximum at $\phi \approx 0.97$, at which point the accretion region is eclipsed, as for example in WW Hor (Bailey et al., 1988, their figure 1).

Thus while there is evidently some cyclotron beaming, the absence of any significant features in the light curves or consistent variations in the colour ratios implies that cyclotron beaming is only partially responsible for the observed light curve

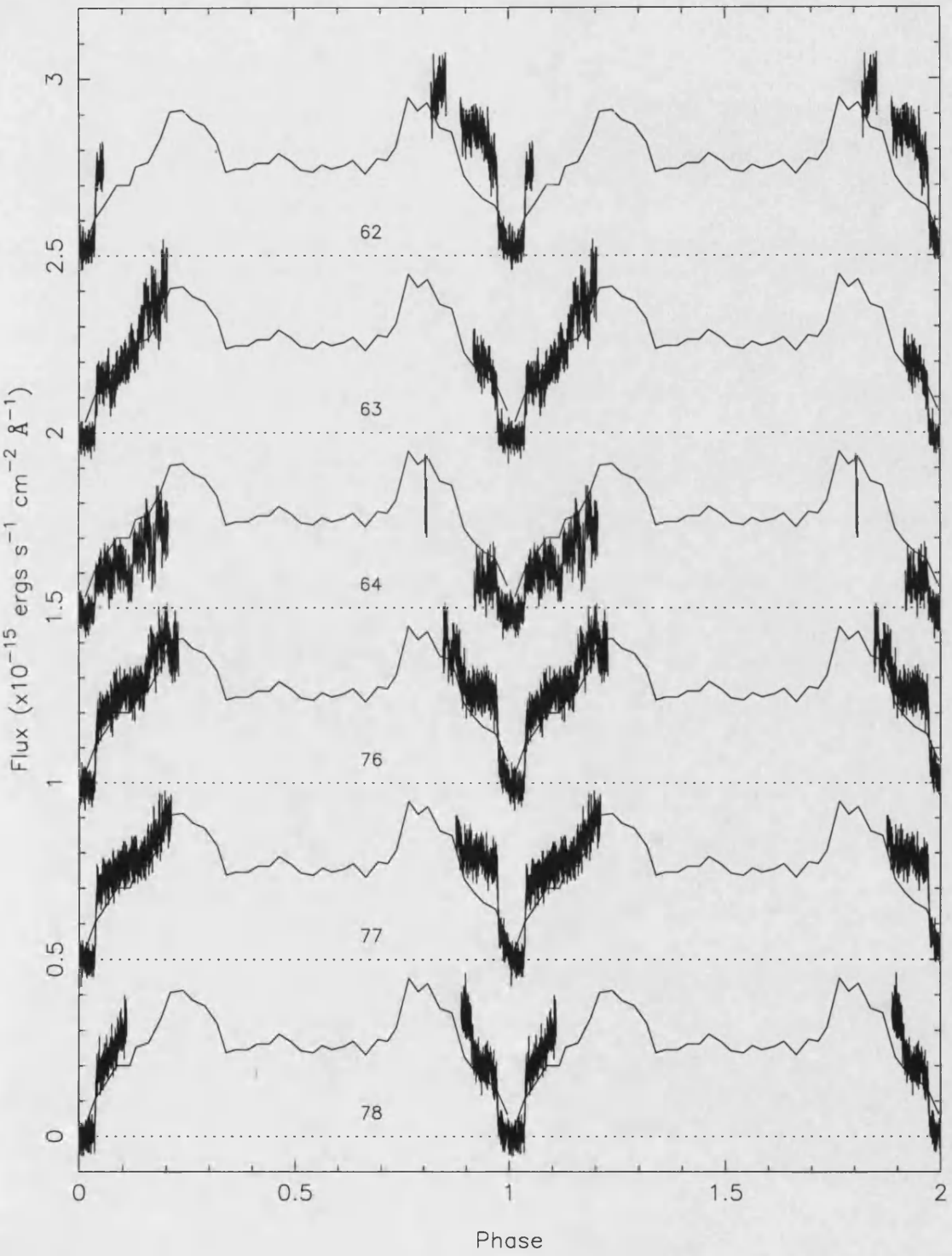

Figure 4.11: The V-band light curves of EP Dra plotted on the same phase range as those of Schwope and Mengel (1997, their figure 1). Over plotted as a solid line is their 1995 V-band observation for comparison.

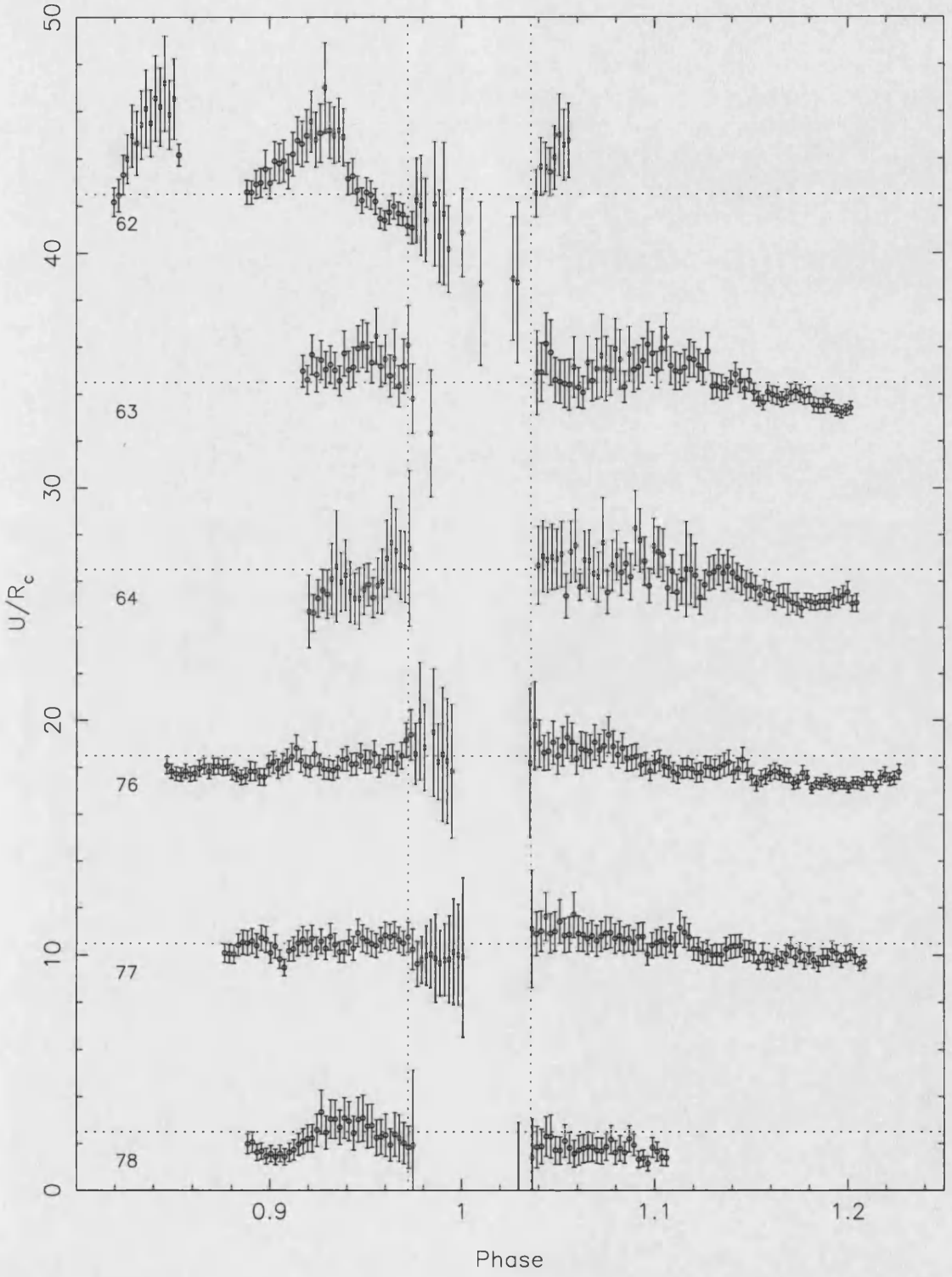

Figure 4.12: U/R_c colour ratios for all six eclipses binned in 15 s intervals. Those points with errors greater than ±5.0 have been omitted and each ratio has been offset by 8 for clarity. The horizontal dotted line is offset by 2.5 in each cycle for comparison, and the vertical lines denote the start of the rapid ingress and egress seen in the light curves.

shape, and cannot explain the flat light curve observed pre-eclipse and post-eclipse.

Absorption

A second possible cause of the trough is absorption by obscuring material lost from the secondary in an accretion flow. This would be supported by the correlation between the presence of this feature and the brightness of the stream (Section 4.2.3), and also changes in R_μ caused by differing amounts of material in the stream (Section 4.3.2).

The U/R_c colour ratios become redder during the decline in flux in cycle 76 between $\phi \approx 0.88$ and 0.89. This effect is more pronounced in cycle 78 where there is a significant dip towards the red and rise to the blue again during the extended decline between $\phi \approx 0.89$ and 0.925. In the U-band and B-band of cycle 62 there is a rise in flux and a corresponding decrease in the R_c-band at phases corresponding to the end of the extended decline in cycle 76. The most likely cause is the onset of absorption by material in the accretion stream. The increased absorption at shorter wavelengths is contrary to the expected free-free absorption in the accretion stream (King and Williams, 1985) seen in Chapter 3, which predicts increasing absorption at longer wavelengths (Watson et al., 1995). The observed variation of the light curves with the colour ratios suggests that the absorption process is likely to be bound-free absorption of the Balmer continuum. This is predominantly in the U-band, and the variations in the colour ratios and light curves are explained by variations in the amount and density of material confined by the magnetic field lines of the white dwarf.

4.3.4 The accretion flow

The phase of the onset of the trough is later than that of the pre-eclipse dip seen in the light curves of HU Aqr (Harrop-Allin et al., 1999a, ; Chapter 3), which was identified as the eclipse of the accretion region by the strongly collimated accretion

stream. This phase is determined by the geometry of the field lines carrying the accreting material, so a difference between systems is not unexpected. While the onset of the trough feature is consistent with an eclipse caused by the accretion stream, the lack of a subsequent rise in the light curves indicates that it cannot be due to a well collimated stream. Instead the extended phase range of the trough is more consistent with an accretion stream forming a curtain of material at it threads on to different magnetic field lines at different points along the trajectory. This accretion curtain could then cause absorption over the phase range of the trough as observed in the light curves (Figures 4.1, 4.3, 4.4, 4.5 and 4.6). The extent of an accretion curtain can be estimated using the eclipse light curve features and the geometric model introduced earlier.

A value of R_μ can be estimated by varying the parameter until the field lines begin to pass in front of the accretion region at the phase set by the start of the trough in the light curve. For those cycles with brighter streams and accretion regions, where the onset of the trough is earlier, I find values of $R_\mu \sim 0.14a$ (for $\beta = 65°$) and $0.19a$ (for $\beta = 18°$). For those cycles where the onset of the trough is later at $\phi = 0.90$, I find $R_\mu \sim 0.16a$ (for $\beta = 65°$) and $0.22a$ (for $\beta = 18°$). The outer edge of the curtain, where material threads closest to the secondary, can be estimated from the end of the egress of bright stream material around $\phi = 1.1$, and is independent of β. This assumes there is no significant continuum emission from the ballistic section of the accretion stream, where material is expected to be faint and cooling as it falls. For those cycles where the bright stream egress is clearly seen, we find a value of $R_\mu \sim 0.42a$. For those cycles with fainter streams the egress of the stream is not seen. The inference is therefore that brighter streams result in a wider accretion curtain, with more material in the accretion stream penetrating further into the magnetosphere.

For faint stream cycles a decline in flux is seen immediately before the eclipse of the accretion region (see Section 4.2.2). This could be due to the eclipse of stream material which is threading early in the trajectory, and which should emit

through magnetic heating. Alternatively the decline could be caused by absorption by material along the line of sight to the white dwarf and accretion region (see Section 4.3.3).

The trough is absent in the observations of Remillard et al. (1991) and Schwope and Mengel (1997). The stream also appears to be fainter in both previous observations, although this may be due to the poorer sampling. The lack of a bright stream may be the cause of this absence of a trough in their light curves, if the two are linked as suggested here.

An extended accretion curtain with material being threaded at different R_μ would allow material to accrete over an extended region on the white dwarf. The foot points of the field lines would form an arc shape on the white dwarf surface. There is evidence in the light curves presented here for such an extended accretion region (Section 4.2.1), and this would be consistent also with the optical cyclotron models of Schwope and Mengel (1997) which show evidence for an accretion arc or ribbon.

An extended accretion region which has material in the accretion flow immediately above the surface of the white dwarf may produce absorption close to the white dwarf. For a compact accretion region at low colatitude the angle between the line-of-sight and the field lines is large, towards the perpendicular. However, for a large extended accretion region at high colatitude, the angle is smaller and the region is hence optically thick over a larger phase range. Therefore, there may well be absorption in the curtain far from the white dwarf pre-eclipse, but post-eclipse the absorbing medium close to the white dwarf may well be more important.

4.4 Conclusions

I have analysed the first high signal-to-noise ratio and high-time resolution data of EP Dra taken on two consecutive nights at the WHT using S-Cam 2. The eclipse light curves show variability in the accretion stream and accretion region over the timescale of the orbital period. There is no direct evidence in the light curves for

the expected rapid eclipse of a small accretion region on the white dwarf. The rapid eclipse seen in the light curves is a combination of emission from the white dwarf photosphere and the accretion region. There is evidence for the variability of the accretion region from the variation in brightness of the rapid eclipse ingress with the varying accretion stream brightness.

Variability seen in the light curves on a longer timescale is influenced to some extent by cyclotron beaming. However, from the colour dependence, there is probably also a contribution from absorption, and this is seen as a trough in the light curves of the second night. I attribute the absorption to bound-free absorption by material in an extended accretion curtain obscuring the accretion region and white dwarf. There may also be significant absorption by material located close to the white dwarf above the accretion region.

Accreting material is threaded onto many field lines along the accretion stream trajectory, and the location in phase of the onset of the trough or absorption dip provides an estimate of the location of the edge of the accretion curtain. Variations in the brightness of the accretion stream seen after the ingress of the white dwarf and the accretion region are caused by a change in the location of bright stream material in the accretion curtain and/or a change in the extent of the curtain. From the extent of the accretion curtain, the presence of an extended accretion arc is inferred at the foot points of the accreting field lines, however this region is still small compared with the size of the white dwarf, so the absence of a direct signature for it in the light curves remains unexplained.

Chapter 5

Accretion stream mapping with genetically modified 'fire-flies'

In this chapter I apply a new eclipse mapping technique to the light curves of HU Aqr and EP Dra (see Chapters 3 and 4). A shortened version of this chapter has been published in *Monthly Notices of the Royal Astronomical Society* (Bridge et al., 2004).

5.1 Motivation

Attempts to determine the brightness distribution of the accretion stream material has evolved in complexity from initially one-dimensional streams confined to the orbital plane (Hakala, 1995), to three dimensional tubes carrying material far out of the orbital plane (Kube et al., 2000; Vrielmann and Schwope, 2001). These methods have been applied to both emission line (Kube et al., 2000; Vrielmann and Schwope, 2001) and continuum observations (Hakala, 1995; Harrop-Allin, 1999, Chapter 3). The assumption common to all previous model techniques is that of a stream trajectory determined prior to the modelling process, and fixed for the duration of the model. In an attempt to remove as many of the assumptions about the stream location as possible, a technique has been developed by Hakala et al. (2002), which makes fewer assumptions about the location of bright stream material.

In principle, stream material can be located anywhere within the Roche lobe of the primary.

The application of the technique to synthetic data sets was demonstrated in Hakala et al. (2002), and here, for the first time, the method is applied to the optical light curves of two eclipsing polars EP Dra and HU Aqr. The two systems show variations in the brightness and trajectory of the accretion stream over the timescale of the orbital period (Chapter 3 and 4), with EP Dra also showing a variation in brightness over a longer phase range. This variation appears to be related to the brightness of the accretion stream, and is attributed to a combination of cyclotron beaming and absorption in an extended accretion curtain (Chapter 4).

The eclipse mapping technique based on the model of Harrop-Allin (1999) was found in Chapter 3 to be particularly sensitive to the input parameters and the signal-to-noise ratio of the data used, when applied to the selected light curves of HU Aqr, and hence restricted the interpretation of the results. This new model technique is applied to the EP Dra and HU Aqr light curves in an attempt to circumvent these limitations.

5.2 Data sets

Light curves of EP Dra and HU Aqr were obtained on the nights of 2000 October 2/3 and 2000 October 3/4. The observations were taken using the superconducting tunnel junction instrument S-Cam 2 (see Chapter 2). S-Cam 2 provides simultaneous spectral information through the ability to record the energy of each incident photon, as well as the time of arrival and position on the detector array. The HU Aqr light curves presented in Chapter 3 have therefore now been split into energy ranges that more closely resemble those of the Johnson-Cousins $UBVR_c$-bands (Bessell, 1990, and references therein), as for EP Dra and detailed in Chapter 4. Table 5.1 gives the cycle number, start time (TDB) and total observation length for those light curves used in the modelling presented here. The observations of EP Dra are too faint to

Table 5.1: Summary of the observations of EP Dra and HU Aqr. Cycle numbers are with respect to the ephemeris of Schwope & Mengel (1997) for EP Dra and Schwope et al. (2001) for HU Aqr.

	Cycle number	Eclipse centre (TDB) (2450000.0+)	Observation length (s)
EP Dra	56962	1820.37575	1496
	56976	1821.39294	2400
	56977	1821.46559	2111
	56978	1821.53825	1393
HU Aqr	29994	1821.43744	2400
	29995	1821.52426	1216

provide high enough signal-to-noise ratio light curves when divided into $UBVR_c$-band energy ranges (V$\approx$17 for EP Dra compared to V$\approx$15 for HU Aqr). Therefore I use the 'white'-light curves.

The effect of low signal-to-noise ratio data on the fits is that the fire-fly swarm is broadened. In light of these considerations, I have chosen cycles 29994 and 29995 of HU Aqr as having the best signal-to-noise ratio and sufficient phase range, and cycles 56962, 56976, 56977 and 56878 from EP Dra. The choice of consecutive orbits of light curves means that the changing brightness and eclipse profile of the accretion stream can be compared for consecutive eclipses. The observed light curves were binned into 4 s time bins. This is to reduce the computational time required for the model. The EP Dra light curves have been truncated compared to those presented in Chapter 4, to cover the eclipse phases only, and hence the 'trough' feature identified in the longer phase coverage light curves is not evident.

5.3 The Model

5.3.1 Overview

The model is described in detail in Hakala et al. (2002), so I provide only a brief description here. The model uses a number of bright emission points, dubbed 'fire-flies', that are free to move within the Roche lobe of the primary. Each fire-fly has an angle-dependent emission, given by

$$F_{fly} = F_0 + A\cos(\alpha) \tag{5.1}$$

where F_0 is the minimum brightness of a fire-fly, A is the amplitude of angular dependence and α is the angle between the primary, the fire-fly and the observer. This angular dependence was included for two reasons: firstly to account for the effect of the X-ray heating of the side of the accretion stream facing the primary, and secondly to mimic the effect of the optical thickness of the stream near the eclipse phases. The model evolves a best fit light curve and hence fire-fly distribution, by summing the brightness of the fire-flies visible at each phase of the light curve.

The model creates a number of initially random fire-fly 'swarms', and each of these swarms is used to create a model light curve. The swarms are then evolved towards a final solution using a genetic algorithm (GA; see Charbonneau, 1995, for a review) which evaluates the goodness of fit of each model light curve to create the next generation of fire-fly swarms. The generation of the 'child' swarms proceeds in a slightly different manner from that used in Chapter 3. The model selects two parent swarms, with each parent being chosen as the best-fit swarm from five randomly selected swarms. Two child swarms are then created by selecting fire-flies at random from the parents. There is a small probability that each selected fire-fly will be mutated, either being replaced by a new random fire-fly, or being moved in position. If the resulting child swarms are evaluated to be better fits than their parents they will replace them in the model. This process is repeated until the

model converges, or a pre-set number of generations has passed.

The location of the fire-flies defines an emission volume, and so the precise location of an individual fire-fly within that volume is not necessarily important or unique. The bright sections of stream are seen as a larger number of fire-flies concentrated in a smaller volume.

5.3.2 Evaluation of the fit

The goodness-of-fit (F) of a particular model light curve is a combination of the χ^2-fit of the fire-fly generated model light curve to the observed light curve, plus an optional regularisation term derived from a self-organising map (SOM; Kohonen, 1990). F is expressed as

$$F = \sum_{i=1}^{n} \left(\frac{D_i - M_i}{\sigma_i} \right)^2 + \lambda S_{\rm reg} \tag{5.2}$$

where the left-hand term is the χ^2-fit of the data points (D_i) with errors σ_i to the model points (M_i). The right-hand term is the SOM regularisation ($S_{\rm reg}$) with the Lagrangian multiplier λ (cf Equation 3.1 in Chapter 3).

The SOM places a curve through a given swarm, with ends located near the primary and L_1. The fire-flies are constrained to prefer to lie at minimal distance from this curve, and hence those swarms that follow the shape of the curve more closely have correspondingly better fitness functions. The details of the application of a SOM to the fire-fly model are given in Hakala et al. (2002). They did not specifically explore the effects of two important parameters in the regularisation, that of the neighbourhood kernel width and the number of nodes (or sections) in the curve. As this technique is applied here to real data for the first time, the effects of varying these two parameters are briefly explored.

For a test dataset, I have chosen the 'white'-light curve of HU Aqr cycle 29995 (Chapter 3), and apply the same input parameters to the model, varying either the kernel width or the number of nodes. Figure 5.1 shows the resulting regularisation

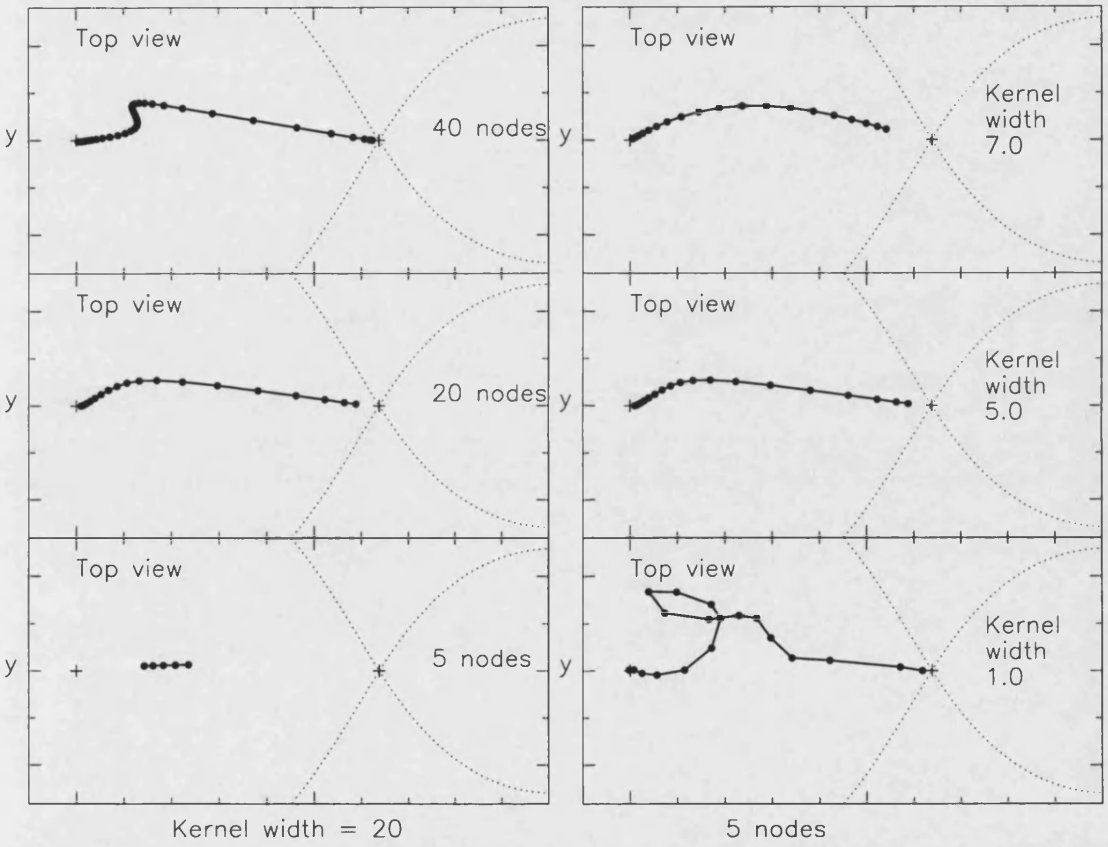

Figure 5.1: The left hand column shows regularisation curves for different numbers of nodes and the right hand column different neighbourhood kernel widths. The middle two curves represent the values used for the modelling presented here.

curves. To create a best-fit curve through a particular fire-fly swarm, the model selects a random fire-fly ($\mathbf{P}$) and finds the nearest node ($\mathbf{N}_w$). This node is then moved towards the fire-fly. Formally this is done using the following

$$\mathbf{N}_i(t+1) = \mathbf{N}_i(t) + h(i,w)(\mathbf{P} - \mathbf{N}_i(t)), \forall i \tag{5.3}$$

where $\mathbf{N}_i(t+1)$ is the new node position, $h(i,w)$ is the neighbourhood kernel which depends on the distance of node $\mathbf{N}_i$ from $\mathbf{N}_w$. The effect of $h(i,w)$ is such that as well as moving $\mathbf{N}_w$, each adjacent node in the curve is also moved; however the amplitude of the movement is reduced for each subsequent node. The amount by which the movement is reduced is set by the kernel width $\sigma(t)$.

$$h(i,w) = \alpha(t) \exp \frac{-\|r_i - r_w\|^2}{2\sigma(t)^2}, \forall i \tag{5.4}$$

$\alpha(t)$ is a time-dependent learning rate and $-\|r_i - r_w\|^2$ is the squared distance between $\mathbf{N}_w$ and $\mathbf{N}_i$.

For each swarm this process of moving the nodes is repeated for around 10--20 times the number of fire-flies in the swarm. The use of a large kernel width will propagate larger amplitude movements further along the curve, leading to a smoother, or 'stiffer', curve. The number of nodes has a similar effect: a large number of nodes leads to localised turns in the curve as the amplitude of the node movement decreases in a relatively short distance along the stream. In general, the ratio of the number of nodes to the kernel width affects the strength of the regularisation by altering the stiffness of the regularisation curve.

The regularisation curve is a constraint on the fire-fly distribution, and the form of the curve is important as it can impose preconceived ideas of a stream trajectory on to the fire-fly swarms. The choice of the most appropriate values for the kernel width and the number of nodes is set by the need to allow the model to create a stream that is sufficiently stiff as to reproduce a 'physically realistic' accretion stream, but not too stiff as to place too much constraint over the evolution of the fire-

fly distributions. The effects of the regularisation can be significant in shaping the fire-fly swarm, as can be seen from Figure 5.1. This will influence the model results and their interpretation. However, we can make progress towards an optimal means of regularisation by excluding the more extreme regularisation parameters, such as that found for small kernel widths or large numbers of nodes. With this in mind, we have chosen to use 20 for the number of nodes and 5.0 for the neighbourhood kernel width, as in the middle plots of Figure 5.1. These are the same as those used by Hakala et al. (2002) for their fits to synthetic data. When interpreting the results, the choice of kernel width and node number, and the possible influence on the interpretation of the resulting fire-fly distributions, must be borne in mind.

5.3.3 Fixed parameters

The fixed parameters include those describing the binary system, such as the mass ratio and inclination of the system to the line of sight, and parameters such as the number of swarms, number of fire-flies per swarm and the brightness dependence of the fire-flies. The number of fire-flies and swarms chosen must reflect the need to introduce enough diversity into the population to explore the whole parameter space and reach a unique solution, while the number of iterations must be sufficient to reach convergence. In practice, the number of iterations is also constrained by the computational time required for a model fit.

Several of the parameters can potentially be determined using the model fitting itself. The inclination i and the brightness dependence of the fire-flies, which affects F_{fly}, can be varied to determine the best value from the fitness function. This was demonstrated in Hakala et al. (2002) for synthetic data sets, and here I apply it to observed light curves (see Section 5.4.1). The brightness dependence is varied through the user input value of the emissivity ratio $\varepsilon = 1/(F_0 - A)$ (see Section 5.3.1). This defines the brightness of the directly opposing faces of the fire-fly – i.e. the brightness of the fire-fly in the direction facing the primary, compared to that facing

directly away from the primary. A third parameter is used to mimic the effects of the accretion region on the primary: the value for the brightness of the accretion region is fixed at the ingress, and then, using a 'pole trend' parameter, the angular dependence of the emission from this region is accounted for by increasing this value linearly with phase to match the egress brightness. In those observations covering a small phase range this was found to have little effect, as the model effectively uses fire-flies to compensate for an inappropriate brightness at the accretion region. However it is important for HU Aqr cycle 29994 which has a longer egress phase range (see Section 5.4.2). The pole trend cannot, of course, account for flaring seen in the longer egress light curves.

5.4 Results

5.4.1 Constraining system parameters

The value of the binary inclination can be constrained using the fire-fly model. Figure 5.2 shows the fitness function for a range of values of i for EP Dra cycle 56976 and the V-band of HU Aqr cycle 29995. Figure 5.2 indicates a value of $i = 79 - 80°$ for EP Dra and we use $i = 79.5°$ for subsequent modelling. This value is in good agreement with the value of $i = 80°$ derived by Remillard et al. (1991) from their observed eclipse duration. For HU Aqr we used a value of $i = 85°$ which is in good agreement with the value from Schwope et al. (2001) of 85.6°.

Constraints can be placed on the values of ε, and I find that ε is constrained to be within approximately ± 0.1 of the optimal value. The value of ε is also linked to the value of the pole trend. A decrease in the value of ε means that the fire-flies are brighter on the side facing the primary, seen after eclipse on accretion stream egress. This is also when the model is providing the most contribution to the cyclotron emission through the pole trend parameter. The phase dependence of the emission from the fire-flies therefore implies that this parameter ε will most

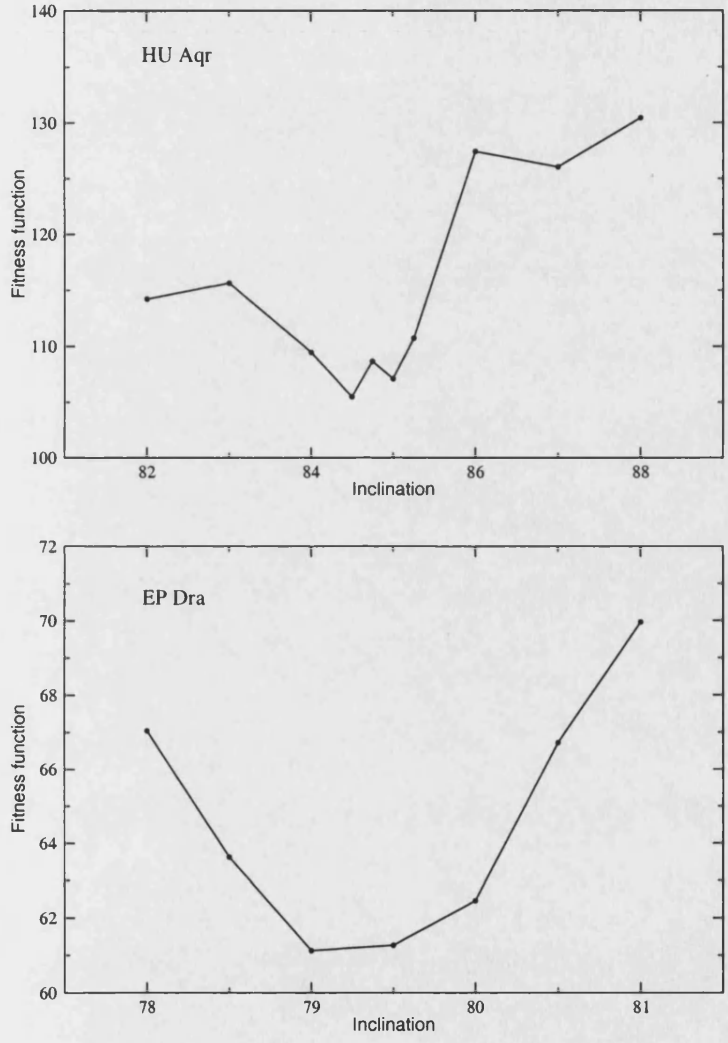

Figure 5.2: The upper plot shows the fitness function for a range of values of inclination for the V-band of cycle 29995 of HU Aqr, and the bottom plot that for cycle 56976 of EP Dra.

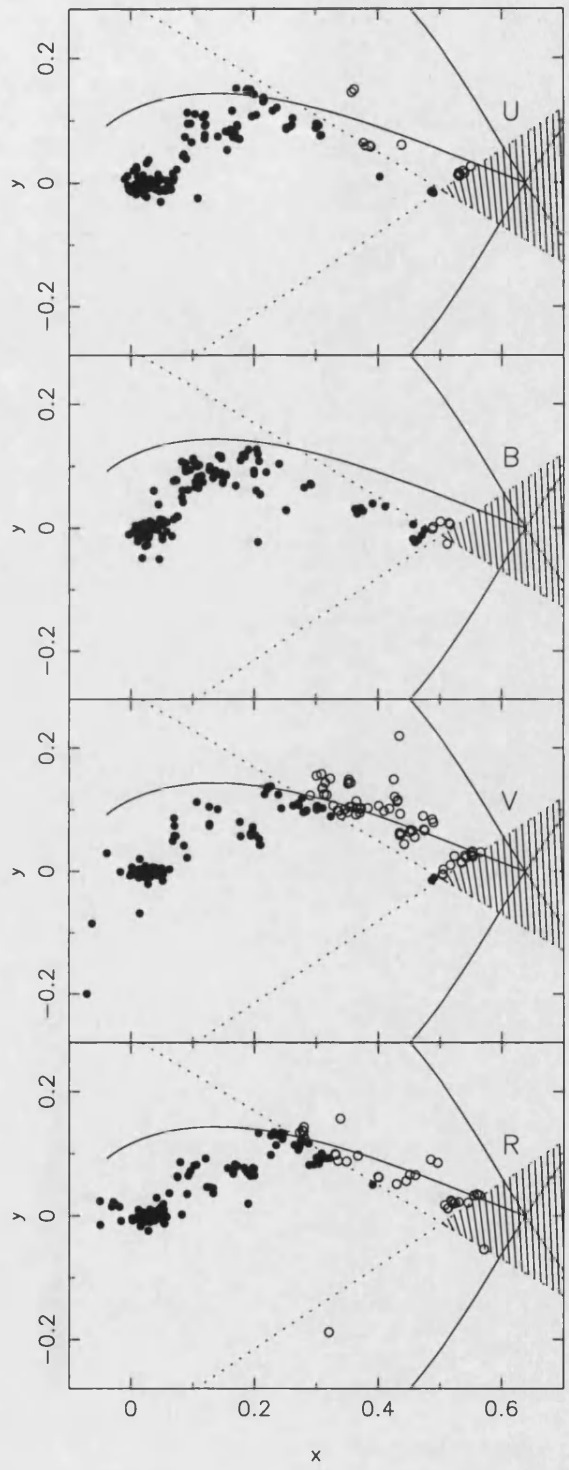

Figure 5.3: The fire-fly distributions for the model fits to the light curves of HU Aqr for cycle 29994, looking down onto the orbital plane. The Roche lobe and a ballistic accretion stream are represented with solid lines, and the two dotted lines indicate those parts of the system observed in the phase range of the light curves.

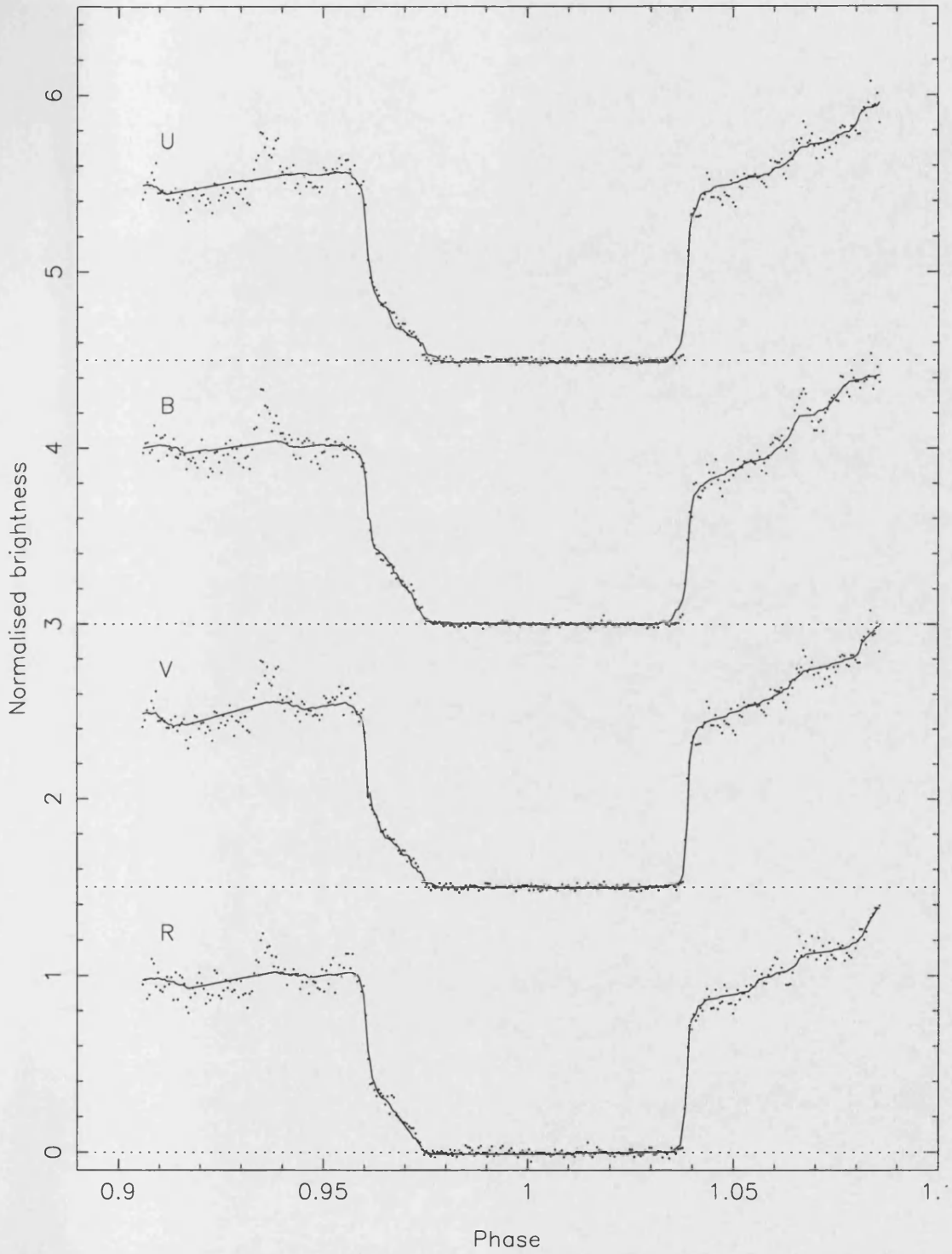

Figure 5.4: The model fits (solid line) to the observed $UBVR_c$-band light curves (dots) of HU Aqr. Each light curve and fit is offset vertically by 1.5 for clarity.

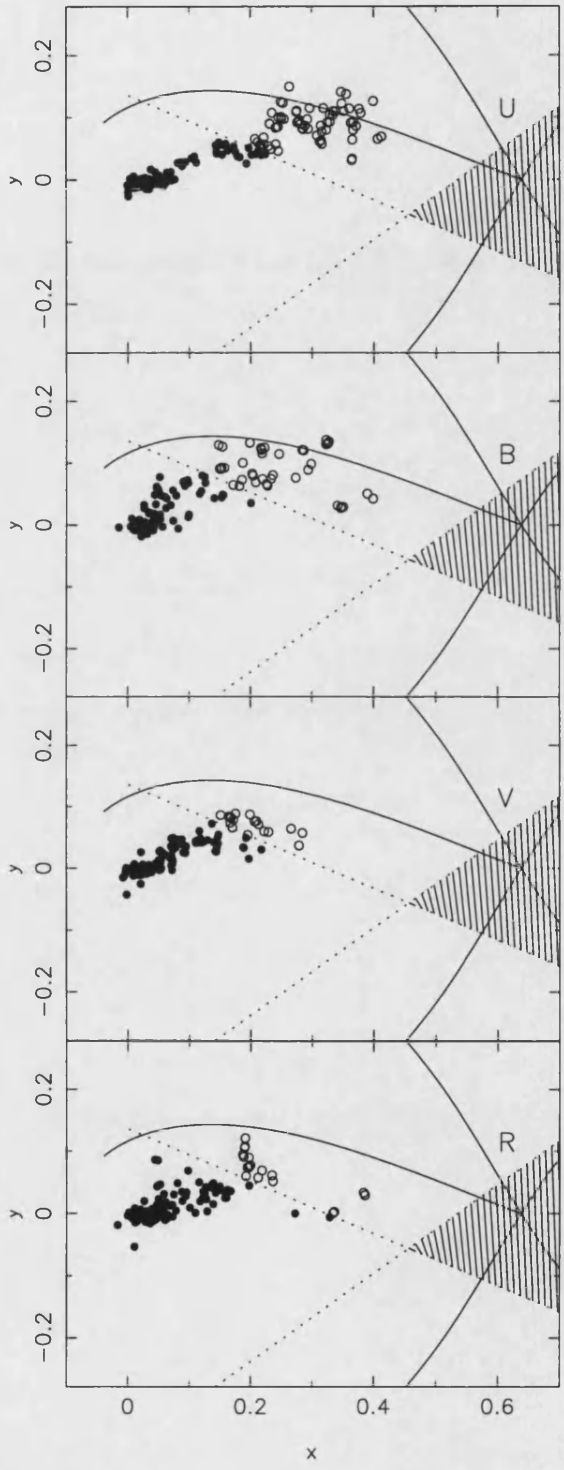

Figure 5.5: As for Figure 5.3, but for HU Aqr cycle 29995.

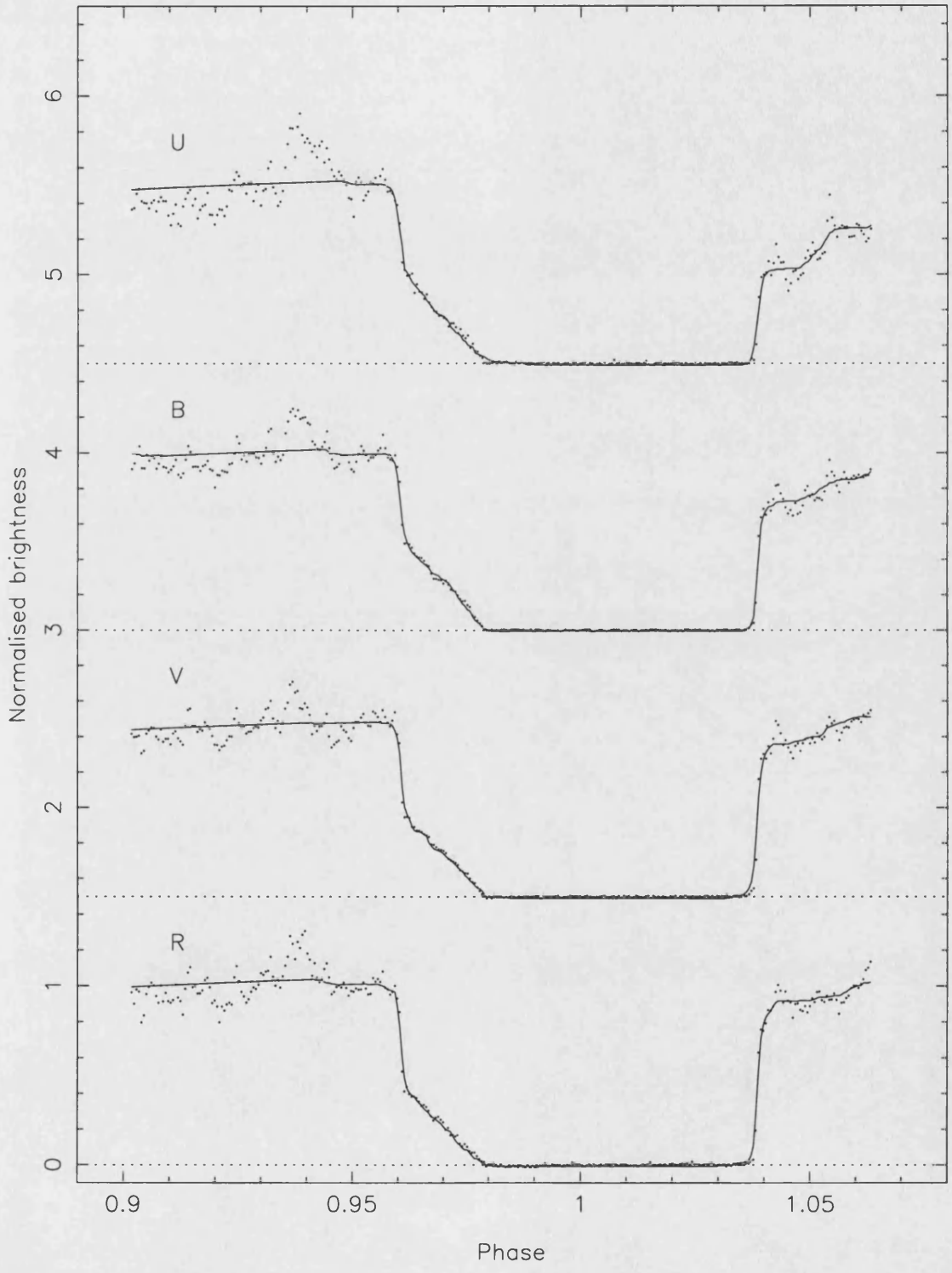

Figure 5.6: As for Figure 5.4, but for HU Aqr cycle 29995.

likely play a more important role in long phase-range light curves, as suggested by Hakala et al. (2002).

5.4.2 HU Aqr

The results of the fire-fly modelling of HU Aqr are shown in Figures 5.3 and 5.4 for cycle 29994 and in Figures 5.5 and 5.6 for cycle 29995. Figures 5.3 and 5.5 show the distribution of fire-flies, and Figures 5.4 and 5.6 the corresponding model fits to the observed light curves. The dotted straight lines in Figures 5.3 and 5.5 define the regions of the system seen from the first to last phases in the light curves. The shaded area is therefore never seen, and thus any fire-flies in this region make no contribution to the model fits and are excluded from the plot. Those fire-flies that are seen on both ingress and egress are shown as filled circles, while those seen either on ingress or egress alone are represented as hollow circles. The high value of $i = 85.0°$ means that the fit is constrained mainly in the orbital (x-y) plane and less so in the x-z plane. A plot of the x-z plane fire-fly distribution is not included for this reason.

The phase range of the observed light curve for cycle 29994 of HU Aqr is longer on egress than that for HU Aqr cycle 29995, which means that the pole trend is more important for this cycle. However, the B-band fit of cycle 29995 does require a higher value of the pole trend than the UVR-band fits. The shorter egress in cycle 29995 means that changing the value of ε has no effect, and the same value of $\varepsilon = 0.2$ is therefore used for all four bands. (This means that the fire-flies are 5 times brighter facing the primary, than when facing away.) For cycle 29994 the value is different in the different bands because of the greater influence of the cyclotron emission on the model fits after the egress of the accretion region. The values for the $UBVR$-bands were 0.25, 0.2, 0.3 and 0.2 respectively.

In Figure 5.3 there is a concentration of fire-flies close to the primary, and there are also many fire-flies defining the trajectory of material from L_1 to the primary.

However, most of the fire-flies are located to be in the region where we expect the material to be following the magnetic field lines of the primary. The increased number of fire-flies along the indicated ballistic trajectory in the V-band and R-band compared to the U-band and the B-band appears to be a result of the increase in the model light curve around $\phi \approx 0.937$, which coincides with the large increase in the observed light curve centred on $\phi \approx 0.935$. Fig 5.5 indicates that for HU Aqr cycle 29995, most of the emission comes from the region close to the primary and nearly all the fire-flies are located where we expect the material to be threaded onto the magnetic field lines of the primary.

The differences between the bands for HU Aqr cycle 29994 are noticeable in the ballistic stream. There are more fire-flies closer to L_1 in the V-band and R-band, and more in the region where we expect material to be coupled to the magnetic field lines in the U-band and B-band. There is little emission from a ballistic trajectory in all the bands of cycle 29995, and there are few V-band and R-band fire-flies close to the calculated ballistic trajectory in cycle 29995. Instead the fire-flies located in the region where we expect material to be coupled to the magnetic field lines, and in the case of the V-band and R-band, the fire-flies are even closer to the primary and would be expected to have been lifted further out of the orbital plane along the magnetic field lines.

A lack of material near the indicated ballistic trajectory in cycle 29995 is either because there is a lack of material actually located in this region, or that it is significantly fainter compared to the material located near the primary. In this case the model will preferentially place the fire-flies in the brighter region. The difference in the brightness between the cycle 29995 and cycle 29994 accretions streams is emphasized in Figure 3.8, where the cycle 29995 eclipse light curve is brighter for longer, indicating a brighter magnetically confined section of the accretion stream. The fact that a constant ε is used for the different bands means also, that any small variations in the cyclotron emission will be compensated for by the model using fire-flies at the primary to mimic the smaller variations.

Model fits to synthetic data created from a given fire-fly distribution have been shown in Hakala et al. (2002) to reproduce the original breadth of the accretion material well for high signal-to-noise ratio data. We therefore expect the broad accretion stream indicated in the fire-fly distributions to reflect the true location of stream material. That this broad width of material is located where we expect it to be confined to the magnetic field lines implies that the material is threaded on to many different field lines originating from the calculated ballistic trajectory (indicated by a solid line in the figures).

5.4.3 EP Dra

The fire-fly distribution and model fits for EP Dra are shown in Figures 5.7 and 5.8 respectively. Four eclipses are shown, one from the first night and three consecutive eclipses from the second night. The fire-fly distributions in Figure 5.7 show emission located close to a calculated ballistic trajectory in cycles 56962 and 56976, with the consequence that there is a larger relative decrease in the light curve prior to the accretion region and primary ingress than cycles 56976 and 56977. This is seen in the fire-fly distributions as a larger number of fire-flies located close to the calculated ballistic trajectory. In cycle 56978 the rapid decrease in flux prior to the rapid eclipse of the accretion region and primary indicates that material is located towards the ends of the trajectory, i.e. close to the primary and L_1. As the data and model reach total eclipse earlier in phase compared to the preceding two cycles, there is evidently no material located far from the line-of-centres towards the calculated ballistic trajectory, and the model places the fire-flies along the line joining L_1 to the primary. There is the possibility that this material is coupled directly on to the magnetic field lines at L_1, this would however cause a fire-fly distribution like that in Figure 5.7.

The fire-fly distribution in cycle 56978 is expected to be very different from that of the preceding two cycles as the light curves are very different. The fire-flies

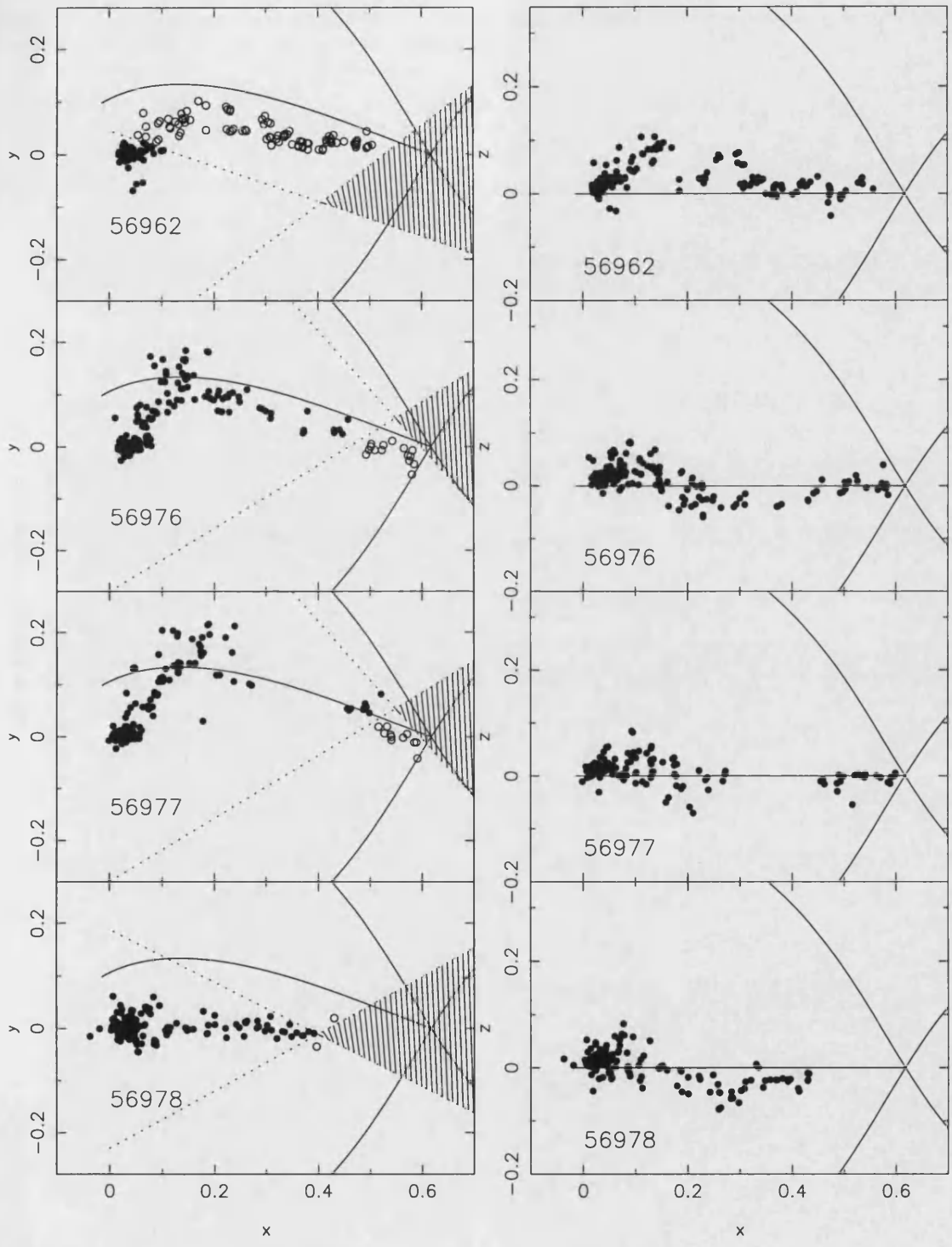

Figure 5.7: The fire-fly distributions for the model fits to the 'white'-light curves of EP Dra. The left column shows the view looking down onto the orbital plane, and the right column the view parallel to the orbital plane. The Roche lobe and a ballistic accretion stream are represented with solid lines, and the left column includes two dotted lines to indicate those parts of the system observed in the phase range of the light curves.

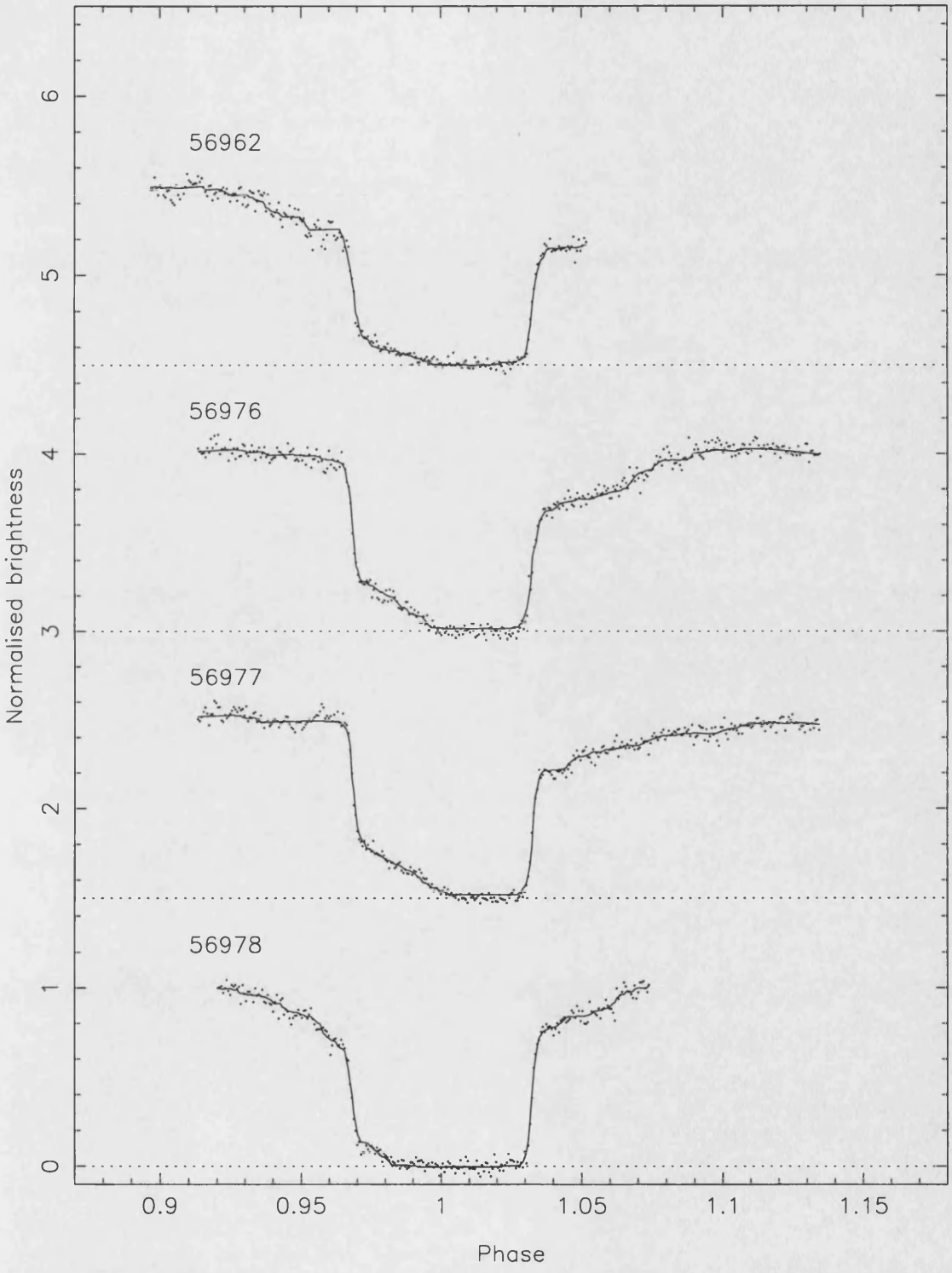

Figure 5.8: The model fits (solid line) to the observed $UBVR_c$-band light curves (dots) of EP Dra. Each light curve and fit is offset vertically by 1.5 for clarity.

indicate that the brightest region is close to the primary, with material along the line-of-centres. This is seen in the light curves as a gradual decrease in emission prior to the eclipse of the accretion region, and a relatively faint stream after this eclipse, when compared to the previous cycles. The increased brightness near the primary in this cycle may also be compensation for a larger brightness between the ingress and egress levels of the light curve, due to a change in the cyclotron emission.

The distribution of fire-flies for cycles 56976 and 56977 show that there is material located in a relatively large region towards the end of the calculated ballistic accretion stream. This region is located closer to the primary than that in the HU Aqr fire-flies, which is indicative either of a weaker magnetic field or a higher mass transfer rate. A weaker magnetic field explanation is consistent with the derived field strengths for HU Aqr of $B = 37$ MG (Glenn et al., 1994) and EP Dra of $B \approx 16$ MG (Schwope and Mengel, 1997).

The distribution of fire-flies in the z-direction is better constrained for EP Dra than HU Aqr, because of the lower inclination of $i = 79.5°$. Figure 5.8 includes plots of the fire-flies in the x-z plane.

5.5 Discussion

The results show that the previously assumed two part ballistic plus magnetic trajectory is a good approximation to the flows delineated by the fire-fly distributions.

5.5.1 Changing stream brightness

Together, the three EP Dra eclipses from the second night (56976, 56977 and 56978) show a change in the location of bright material, which is related to a change in brightness in the observed light curve, and thus a change in the brightness of the accretion stream material. This change is not *a priori* necessarily directly indicative of a change in the temperature of this material as the brightness of stream material is dependent upon both the density and temperature structure of the stream. However,

as the density is relevant for an optically thin stream, and the presence of absorption dips (Chapters 3 and 4) implies that the stream is optically thick, so the increased brightness is mainly indicative of increased temperature.

The change in brightness of the ballistic section of the accretion stream between cycle 56976 and 56977 can be explained if material is stripped from the ballistic stream in many places along the ballistic trajectory. This material is channeled onto the magnetic field lines of the primary, resulting in a decrease in the amount of material in, and hence brightness of, the ballistic stream. We do not necessarily see this material defined by the fire-flies because it is fainter than the region where most of the material is coupled to the magnetic field lines. As this coupled material reaches the primary there is an increase in the emission from this region of the system, as in cycle 56978. Alternatively, the change in brightness may be caused by a change in the rate of loss of material from the secondary resulting in a change in the amount of material along the ballistic section of the stream. The time-scale for material to travel from L_1 to the primary is $\approx$1000 seconds. Therefore, large changes in the amount of material along the accretion stream are possible between consecutive cycles.

5.5.2 Stream heating

The distribution of fire-flies in the different bands for HU Aqr is indicative of stream heating processes in both a coupling region and near the white dwarf. This was found in Chapter 3 for HU Aqr, and is predicted by the theoretical models of Ferrario and Wehrse (1999). The location of the bluer fire-flies further from the primary in the U-band of cycle 29995 could be indicative of irradiated stream material. The accretion stream will be strongly irradiated by X-ray emission as it reaches the threading region and rises from the orbital plane along the magnetic field lines. These U-band fire-flies are located further from the primary by the model, to indicate where the observed emission is brightest. Alternatively, the bright U-band emission may

indicate that the material is heated by processes in the magnetic coupling region.

5.5.3 Comparison with previous results

The HU Aqr fire-fly distributions are consistent with the location of the bright regions in the modelling of Chapter 3 and Harrop-Allin (1999), which show variations in the brightness of the threading region and regions near the primary. The one-pole accretion models of Harrop-Allin (1999) show that the magnetically confined regions of the accretion stream are the brightest, with the U-band and B-band emission being greatest towards the threading region. In particular their brightness distribution resembles the fire-fly distributions of cycle 29994, as there is still some emission from the ballistic section of their model accretion stream.

The threading region has been observed to move significantly between cycles (Glenn et al., 1994, , Chapter 3). The fire-flies will not necessarily show a movement in the location of the threading region, unless it is significantly larger than the width of the fire-fly swarm. This is demonstrated in Figure 5.9, which shows the U-band fire-flies from HU Aqr cycles 29994 and 29995. In Chapter 3 a change in the threading radius was found between the two cycles modelled in that chapter. However the HU Aqr cycle 29994 modelled here was not included and in fact represents the intermediate cycle (see Section 5.2). Figure 3.8 shows the superimposed eclipse profiles of the HU Aqr cycles observed on the same nights. The figure indicates that the two cycles 29994 and 29995 have different eclipse profiles and hence different threading radii.

Bridge et al. (2003) suggested the presence of an extended curtain of material as being the cause of absorption over an extended phase range, and being at least partially responsible for the trough feature seen in the light curves of EP Dra. The fire-fly distribution in Figure 5.7 supports the idea that accretion material is threaded by many field lines. Schwope and Mengel (1997) suggested the presence of an accretion curtain, and their evidence for an extended accretion arc on the surface

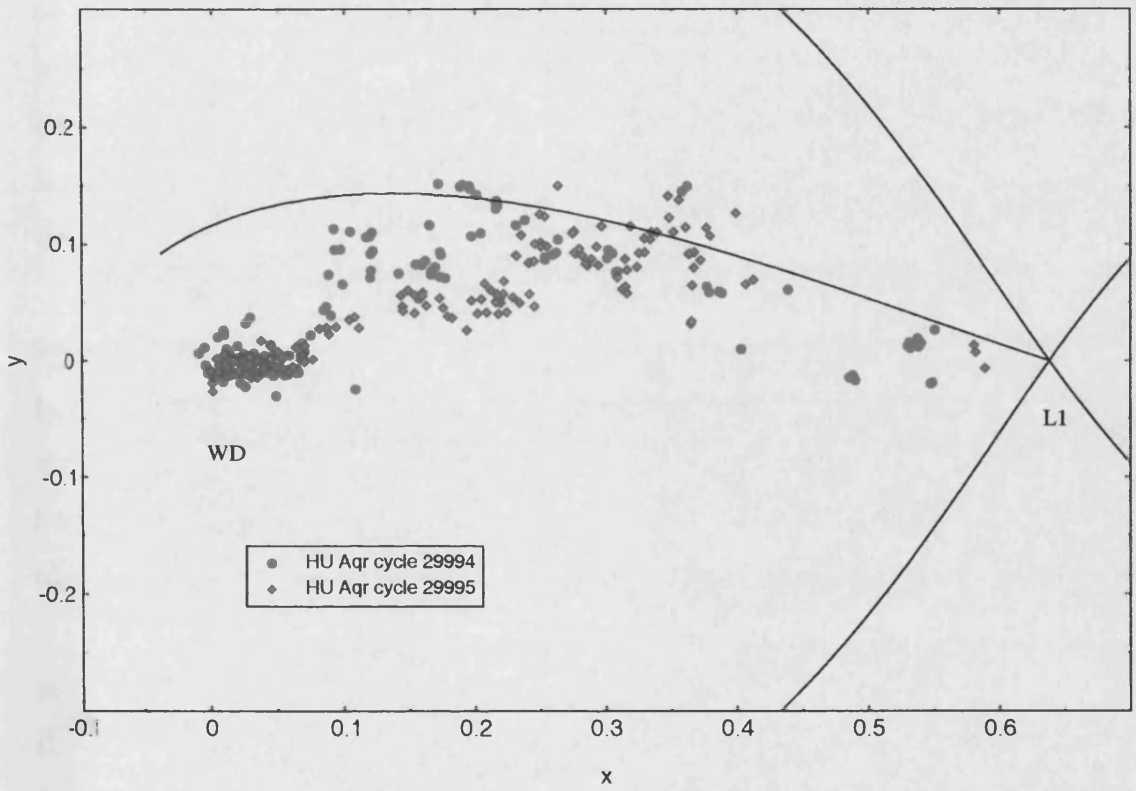

Figure 5.9: The U-band fire-flies from HU Aqr cycle 29994 (*red*) and 29995 (*blue*) overlaid on the same figure. The Roche lobe and a calculated ballistic accretion stream are shown.

of the white dwarf further supports the idea that material is threaded onto many field lines (see Chapter 4).

5.6 Conclusions

We have applied the technique of eclipse mapping using genetically modified fire-flies to the eclipse lights curves of EP Dra and HU Aqr. The modelling shows that the technique is applicable to relatively good signal-to-noise ratio light curves of adequate phase range. These distributions of fire-flies show that the previously assumed ballistic free-fall plus magnetically confined streams are a good approximation for the accretion streams in polars.

We applied the model to $UBVR_c$-band light curves of HU Aqr cycles 29994 and 29995, and 'white'-light curves of EP Dra cycle 56962, 56976, 56977 and 56978. We have demonstrated that the technique will distinguish regions of brightness in the different colour bands. This may indicate different temperatures or densities, and hence heating and/or cooling processes in the accretion stream or the location of photoionised material.

The fire-flies distributions in both HU Aqr and EP Dra show the accretion stream to be brighest near to the primary. A possible threading region is present at which the fire-fly distributions appear to deviate from a calculated purely ballistic trajectory, and this region is seen to be broad, implying accretion along many field lines.

Differences in the location and concentration of fire-flies between the three cycles, 56976, 56977 and 56978, of EP Dra indicate a changing brightness distribution between the cycles. This could be the result of a change in the temperature of the accretion stream material, or a change in the amount of material stripped from the ballistic trajectory and coupled to the magnetic field lines of the primary.

Chapter 6

X-ray and UV observations of EP Dra

The optical observations of EP Dra are discussed in Chapter 4 (Bridge et al., 2003) and I have modelled the brightness distribution and shape of the accretion flow in EP Dra in Chapter 5. In this chapter I present X-ray and simultaneous optical/UV observations of EP Dra made with *XMM-Newton*. These observations are, to date, the highest quality X-ray and the first UV observations of EP Dra.

6.1 Observations

EP Dra was observed with *XMM-Newton* on 2002 October 18, approximately two years after the optical observations in Chapter 4. A summary of the observations is given in Table 6.1. The EPIC-MOS start time is earlier than that of the EPIC-pn, and the observation is slightly longer in duration. There were four simultaneous OM observations in three filter bands: the V-band, UVW1 (2400−3400 Å) and UVW2 (1800−2400 Å). The RGS data are of low signal-to-noise, and are therefore excluded from further discussion. The source counts were extracted from an aperture of 29″ for the EPIC-pn and 44″ for the EPIC-MOS, centred on the source, and the backgrounds were extracted from annuli around the source aperture of radii 98″ for

Table 6.1: *XMM-Newton* observation summary for EP Dra from 2002 October 18.

Instrument	Mode	Filter	Duration
EPIC MOS 1	Partial window	Thin	18005 s
EPIC MOS 2	Partial window	Thin	18022 s
EPIC PN	Large window	Thin	17670 s
OM	Image	V	4399 s
OM	Image	UVW1	4400 s
OM	Image	UVW2	4399 s
OM	Image	UVW2	1800 s

EPIC-pn and 147″ for EPIC-MOS. The data were processed using the *XMM-Newton* Science Analysis Software version 5.4.

This chapter focuses on the light curves and their implications for the understanding of the accretion stream. I use the X-ray spectra of EP Dra as a tool to investigate the processes of absorption and emission in the accretion stream. A full discussion of the spectra and their implications in the wider context of X-ray emission from polars is given in Ramsay and Cropper (2004); however they do not actually show the spectra so these are presented in Section 6.3. As the EPIC-MOS spectra are of lower signal-to-noise, I use the EPIC-pn spectra only.

6.2 Light curves

The EP Dra light curves cover nearly three complete cycles of EP Dra (orbital period 104.6 minutes). Figure 6.1 shows the time series for EPIC-pn and combined EPIC-MOS(1+2) light curves, together with the OM observations. Figure 6.2 shows the phase folded and combined EPIC light curves with the OM observations.

The light curves are phased on the ephemeris of Schwope and Mengel (1997), based on $\phi = 0$ as the centre of optical eclipse. The X-ray light curves are offset in

eclipse by $\Delta\phi = 0.00686$, equivalent to 43 s. The origin of the timing offset has not been resolved satisfactorily, with independent analysis of the light curves providing the same results. The ephemeris of Schwope and Mengel (1997) is used to phase the optical light curves in Chapter 4 and these are aligned as expected with $\phi = 0.0$ corresponding to the centre of eclipse. It is possible that the source of this timing discrepancy may be a change in the physical conditions within the EP Dra system, and the phasings are indeed correct, however the offset of the UV light curves in the same manner indicates that this is extremely unlikely.[1]

In order to proceed I have adjusted the light curves to align the UVW1-band steep eclipse components about $\phi = 0$, consistent with the ephemeris of Schwope and Mengel (1997) and the optical eclipse light curves of Chapter 4. This same correction is then applied to the X-ray light curves. In the following discussion the phases stated must therefore be regarded as being subject to uncertainties caused by the phase discrepancy.

6.2.1 X-ray

I have split the phase folded light curves into soft-band and hard-band which correspond to the energy ranges $0.15 - 0.5\,\mathrm{keV}$ and $0.5 - 10\,\mathrm{keV}$ respectively. This effectively separates the softer blackbody emission from the harder bremsstrahlung emission typically seen in these systems (Warner, 1995).

EP Dra shows a distinct bright phase of higher count rate lasting $\Delta\phi \approx 0.64$ in

[1] Since the original analysis of this data the timing issues surrounding EP Dra have been resolved by Ramsay et al. (2004). The original XMM-Newton X-ray and S-Cam 2 optical observations are phased correctly; however the period in the ephemeris of Schwope and Mengel (1997) is found to be slightly incorrect. The OM observations of EP Dra are phased incorrectly due to a bug in the SAS OM fast chain analysis software. The coincident alignment of the OM and S-Cam 2 observation is purely by chance. Figure 4 of Ramsay et al. (2004) presents the data on an updated ephemeris, and using OM observations with the correct times. The egress phase is offset in the X-ray and optical light curves because of the difference in the exact location of the different emission regions on the surface of the primary.

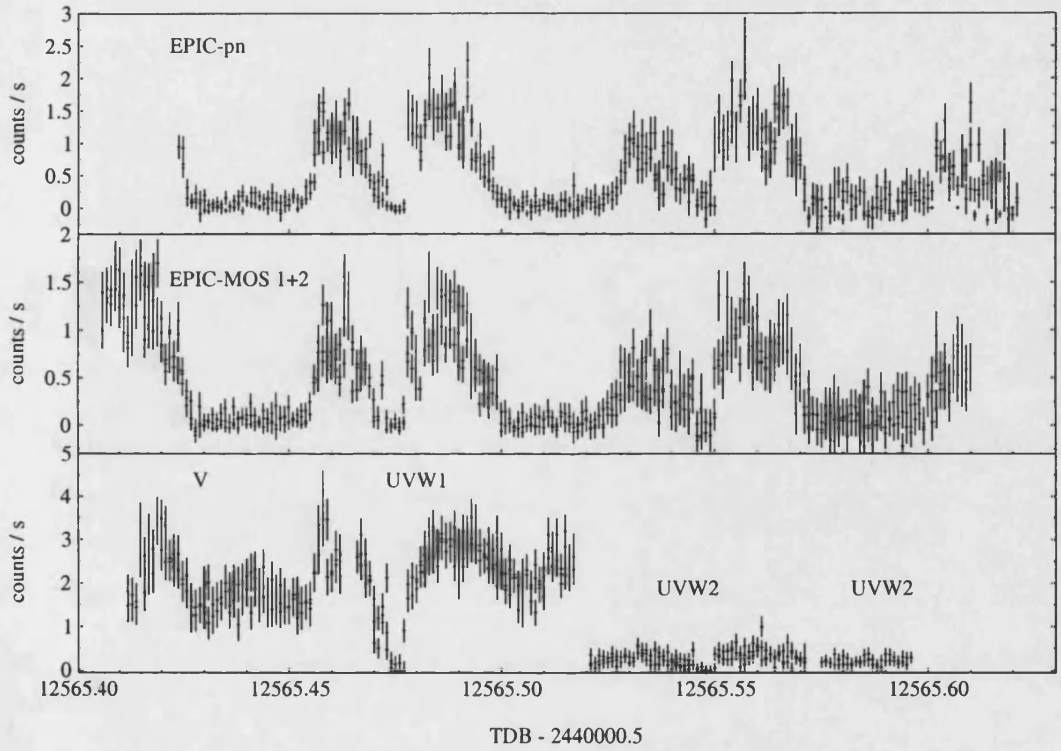

Figure 6.1: The EPIC-pn, combined EPIC-MOS(1+2) and OM light curves for EP Dra. The X-ray light curves are in 30 s time bins, in the energy range 0.15- – 10 keV. The V-band and UVW1 light curves are in 30 s time bins and the UVW2 light curves are in 40 s time bins.

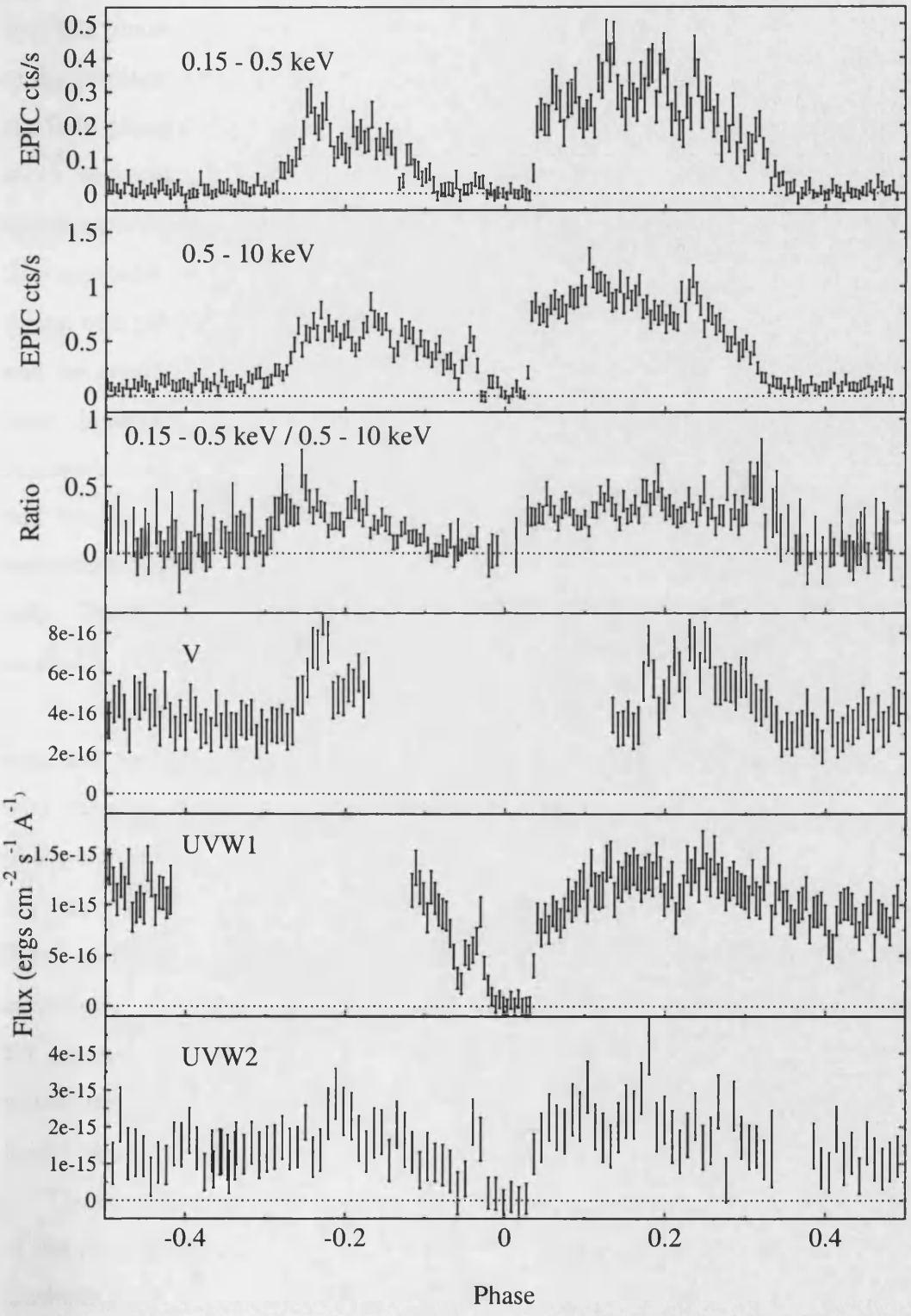

Figure 6.2: The phase folded and combined EPIC and OM light curves. The EPIC light curves are in 30 s time bins, as is the UVW1 light curve. The V-band light curve is in 40 s time bins, and the UVW2 light curve is in 60 s. The horizontal dotted lines indicate zero counts.

the soft-band and $\Delta\phi \approx 0.63$ in the hard-band. The longer bright phase compared to the faint phase indicates that the accretion region is located in the upper hemisphere of the primary, or if located in the lower hemisphere it is spatially extended. During the faint phase (corresponding to those phases where the accretion region and post-shock accretion flow are on the far side of the primary), there are very low, yet significant count rates (soft: $0.014 \pm 0.003\,\mathrm{counts\,s^{-1}}$; hard: $0.06 \pm 0.01\,\mathrm{counts\,s^{-1}}$). The approximate centre of the bright phase is marked by the eclipse of the accretion region and primary by the secondary star. The rapid eclipse ingress of the primary and the accretion region is not seen in the soft-band and only partially in the hard-band, however, the egress is clearly seen in both bands. The eclipse reaches the minimum counts at eclipse centre. For the soft-band this is $0.001 \pm 0.004\,\mathrm{counts\,s^{-1}}$ and for the hard-band it is $0.03 \pm 0.03\,\mathrm{counts\,s^{-1}}$. This implies that there is no significant X-ray emission from the rear face of the secondary or from an extended halo. The X-ray eclipse duration is $\Delta\phi \approx 0.065$, which is approximately the same as that in the optical (Chapter 4).

The shape of the rise to and fall from the bright phase in the soft-band is as expected for an optically thick emission region; that is the observed flux varies with viewing angle. The sharper rise in the hard-band starts slightly earlier in phase compared to the soft-band rise, indicating that the hard X-ray emitting region appears over the limb of the primary before the soft X-ray emitting region. The hard X-ray emission is expected from the top of the accretion shock, where the material is hottest, and the softer emission from the base of the shock and the surface of the primary where the hard X-rays are reprocessed. Therefore, the slope of the rise in the hard-band indicates that the accretion shock must have a significant vertical height above the surface of the primary, or alternatively it is extended in longitude.

The hardness ratio softens as the soft X-ray emitting region is seen over the limb of the primary, before a soft X-ray dip at $\phi \approx -0.2$. This is followed by a gradual hardening towards the eclipse centre, indicating a decrease in the soft X-rays. The soft-band reaches minimum counts at $\phi \approx -0.086$, lasting until a brief rise at $\phi \approx$-

-0.028. However, there is no significant soft-band emission until after eclipse egress. The hard-band exhibits a gradual decline to a minimum at $\phi \approx -0.054$, before a brief rise and the subsequent eclipse by the secondary of the accretion region and primary at $\phi \approx -0.029$. There is also a dip at $\phi \approx -0.13$ seen in both soft and hard-bands, which almost reaches zero counts in the soft-band.

After the steep eclipse egress at $\phi \approx 0.035$ the hardness ratio is roughly constant as the soft and hard X-ray emitting regions are both visible. There is a dip and sharp rise around $\phi \sim 0.22$ in both the soft and hard bands, possibly caused by an accretion event on the primary. This is followed by the gradual decline from the bright phase to the faint phase. The end of the bright phase occurs slightly earlier for the hard-band compared to the soft-band, and this is also seen in the hardness ratio, which softens around $\phi \approx 0.33$, consistent with the hard X-ray emitting region being eclipsed first by the limb of the primary. This discriminates between the height and longitude degeneracy mentioned earlier, and indicates that the hard X-ray emitting region leads the soft X-ray emitting region in phase.

6.2.2 UV and optical

The V-band observation does not cover the eclipse by the secondary, but the eclipse is seen in the UVW1 and UVW2 observations. A variation in the flux of the UVW1 light curve with phase implies that the there is a viewing angle-dependent contribution to this flux. The V-band shows a strong rise in brightness at $\phi \approx -0.26$, which is later than the start of the soft-band and hard-band rise and is most likely caused by cyclotron emission from the post-shock stream material (cf Schwope and Mengel, 1997). As the cyclotron is expected from the top of the accretion shock, this implies that the emission region is extended in longitude rather than vertical height above the surface (see previous section 6.2.1). The decrease in brightness post-eclipse is more gradual, starting earlier than the soft and hard X-rays. The approximate location of the V-band and UVW1 rise and fall implies a location for

the emission region coincident with that of the X-rays.

Following the initial rise in the V-band there is a drop in brightness at $\phi \approx -0.23$. The soft-band shows a similar feature, but not the hard-band. The UVW2-band has a local minimum in counts at $\phi \approx -0.055$, which is coincident with the location of the X-ray hard-band pre-eclipse dip, and the clear pre-eclipse dip in the UVW1-band. The UVW1-band dip reaches a minimum at $\phi = -0.056$, slightly later than the hard-band pre-eclipse dip, and shows a more structured eclipse profile than the hard-band. The UVW2 light curve shows a decline which appears to be coincident with the soft X-ray decline in the pre-eclipse bright phase. After the eclipse there is a dip in the UVW1 light curve at $\phi \approx 0.12$, also seen in the soft-band, but not the hard-band (in fact there is a slight increase in the hard-band emission).

The brightest V-band magnitude is 16.6, at $\phi = -0.22$. This is comparable with that of $V \approx 17$ of Schwope and Mengel (1997) and the S-Cam 2 observations of Chapter 4, and indicates that EP Dra was in a similar accretion state. The UVW1-band reached a magnitude of 16.0 at $\phi = 0.25$, and the UVW2-band an apparent magnitude of 16.4 at $\phi = 0.18$. The fluxes for the OM UV observations are derived from OM observations of isolated white dwarfs. These give maximum fluxes for UVW1 $\sim 1.4 \times 10^{-15}\,\mathrm{ergs\,cm^{-2}\,s^{-1}\,\AA^{-1}}$, for UVW2 $\sim 3.5 \times 10^{-15}\,\mathrm{ergs\,cm^{-2}\,s^{-1}\,\AA^{-1}}$ and for the V-band observations $\sim 8.7 \times 10^{-16}\,\mathrm{ergs\,cm^{-2}\,s^{-1}\,\AA^{-1}}$.

6.3 Spectra

I extracted spectra from the pre-eclipse and post-eclipse bright phases combining single and double events (as for the light curves). The spectrum was fitted using the XSPEC (Arnaud, 1996) spectral analysis package and the epn_lw20_sdY9_thin.rsp response matrix.

The post-eclipse spectrum is extracted from $\phi \sim 0.06 - 0.3$. The spectrum is shown in Figure 6.3 with the model fit and the residuals (data less model). The spectrum is fitted with a blackbody and single temperature bremsstrahlung, both of

which are typically seen in polars (Warner, 1995); together with a neutral absorber. The bremsstrahlung temperature is fixed at 30 keV as it is not well constrained by the data, while the blackbody has a best fit of 30 ± 1 eV with absorption of 8×10^{15} cm^2. The spectrum shows an Fe Kα emission line, which is fit with a Gaussian at 6.7 keV, and is again typical of polars. The best fit gives a $\chi^2_\nu = 1.25$ (148 degrees of freedom). The spectrum of EP Dra from *ROSAT*-PSPC observations was fitted by Schlegel and Mukai (1995). They too used a fixed temperature bremsstrahlung of 30 keV, finding that the component was necessary but the fit to the data was independent of the exact value of the temperature used. Their estimate for a blackbody temperature was $\sim$15 eV with an upper limit of $\sim$70 eV, which is consistent with the value given here.

Also shown for comparison in Figure 6.4 is the pre-eclipse bright phase spectrum with the post-eclipse bright phase model (from Figure 6.3) overlaid for comparison. The spectrum and the ratio shows that the softer part of the spectrum is affected considerably by absorption compared to the post-eclipse spectrum. There is no satisfactory fit using the same model as for the post-eclipse spectrum, and Figure 6.5 shows the best-fit using the post-eclipse model with $\chi^2_\nu = 2.2$ (69 degrees of freedom). This indicates that at first glance the absorption mechanisms are more complicated than assumed.

The bolometric unabsorbed fluxes from Ramsay and Cropper (2004) for the soft and hard-components are $f_{\rm soft} = 7.13 \times 10^{-12}$ ergs cm^{-2} s^{-1} and $f_{\rm hard} = 1.30 \times 10^{-11}$ ergs cm^{-2} s^{-1} respectively. The luminosities can be estimated by assuming the hard X-rays are emitting isotropically and the soft X-rays are from a slab on the surface of the primary (see e.g. Ramsay and Cropper, 2002). For a distance of 300 pc, as estimated as a lower limit by Remillard et al. (1991), this gives luminosities of $L_{\rm soft} = 1.92 \times 10^{31}\,{\rm sec}(\theta)$ ergs s^{-1} and $L_{\rm hard} = 1.4 \times 10^{32}$ ergs s^{-1}, where sec(θ) accounts for the observed viewing angle to the soft X-ray emitting slab. The uncertainties in the luminosities will be dominated by the uncertainties in the distance, and hence are not quoted. These flux values are typical of those observed for polars

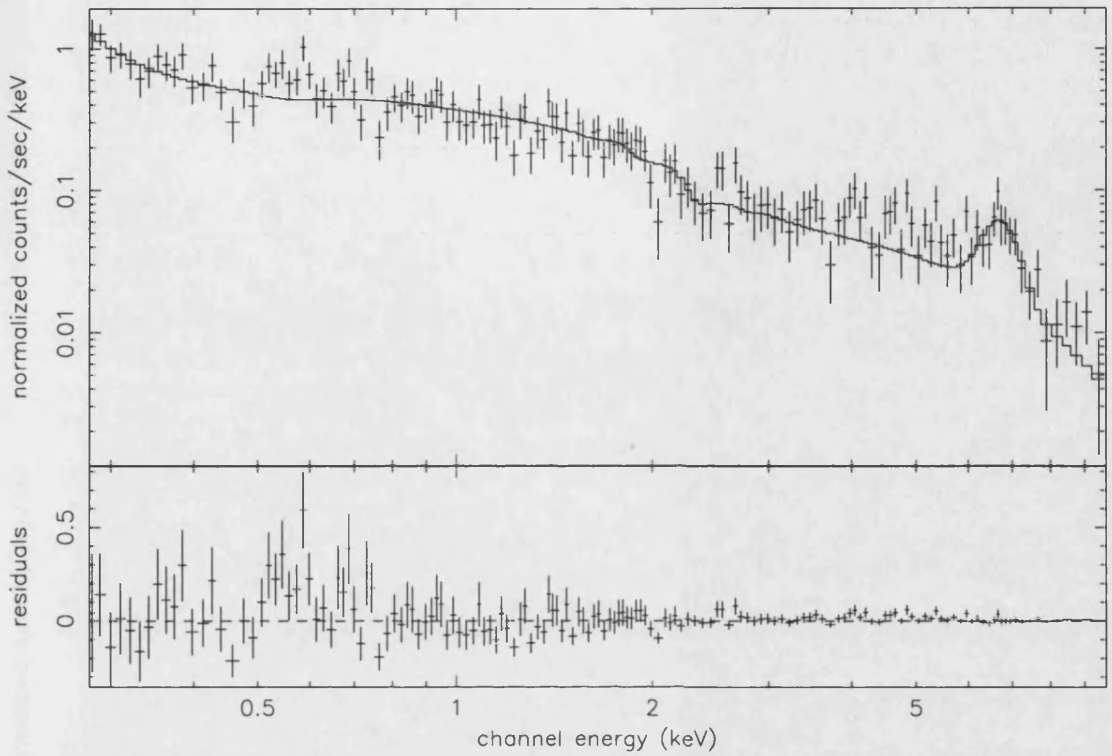

Figure 6.3: The post-eclipse bright phase spectrum with best-fit model and residuals.

(see for example Ramsay and Cropper, 2004).

6.4 Absorption in the accretion stream

The accretion stream in polars will obscure the emission region on the surface of the primary when the magnetically confined stream material is between the line-of-sight of the observer to the emission region on the primary. Watson et al. (1989) showed that pre-eclipse dips observed in the IR, optical and X-ray light curves of EF Eri were caused by the accretion stream. A pre-eclipse dip is observed in the optical light curve of HU Aqr cycle 29994 at $\phi \approx 0.872$ in Chapter 3, and is seen also in HU Aqr in the optical light curves of Harrop-Allin et al. (1999a) and the soft X-ray light curves in Schwope et al. (2001). In HU Aqr the dip illustrates that the stream is relatively well collimated and most of the accretion stream material is threaded on to the magnetic field lines over a relatively short distance along the

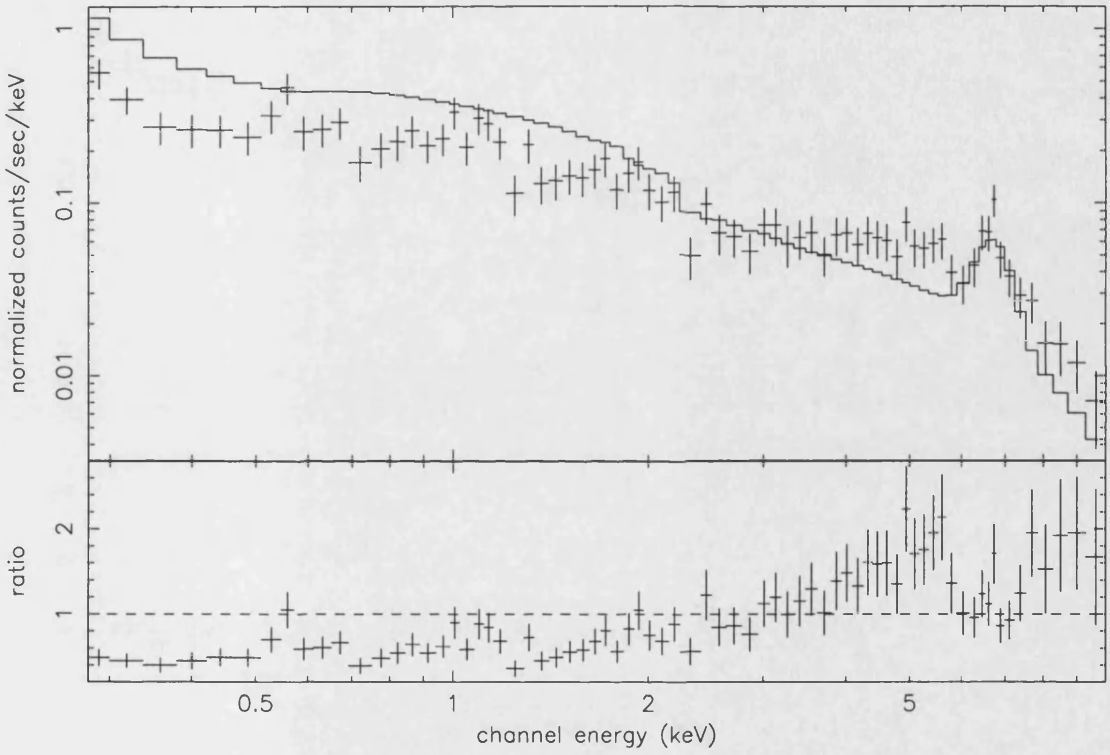

Figure 6.4: The pre-eclipse bright phase spectrum with the post-eclipse model overlaid (see Figure 6.3).

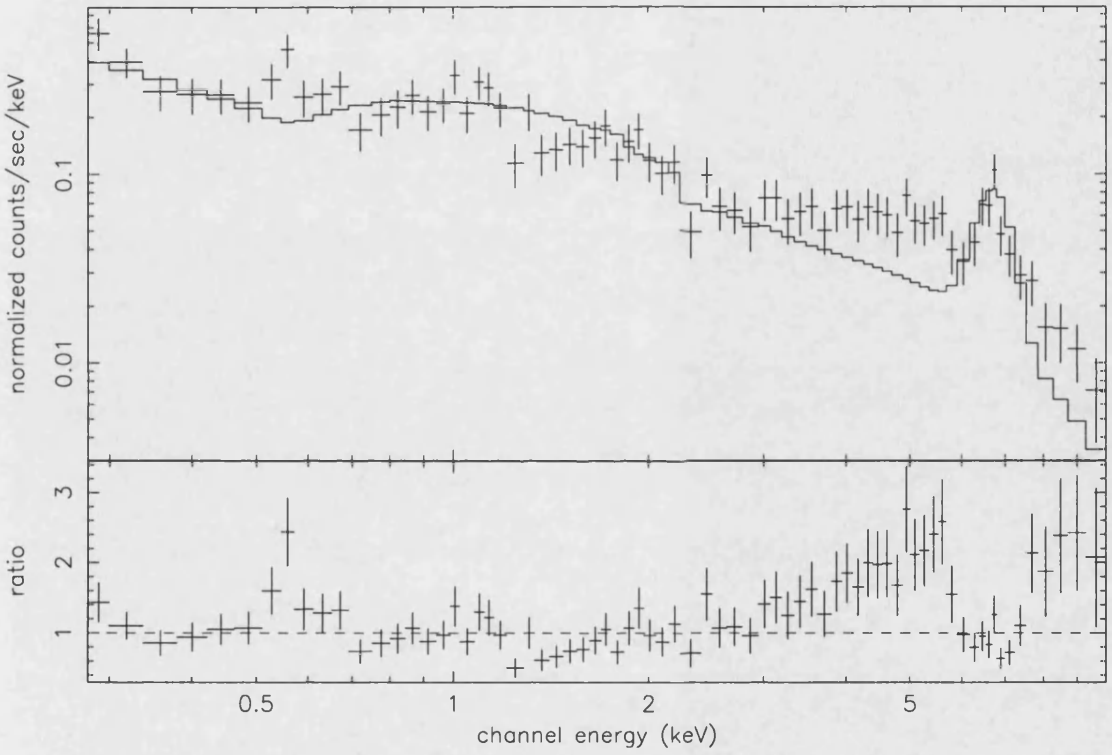

Figure 6.5: The pre-eclipse bright phase spectrum, where the post-eclipse model has been fitted (cf Figure 6.3 and 6.4).

ballistic trajectory. In contrast to the clear dip seen in HU Aqr, the optical light curves of EP Dra in Chapter 4 do not show a pre-eclipse dip, but I concluded there that the 'trough' feature evident in all bands of EP Dra is caused, at least partially, by absorption in a curtain of accretion material.

The light curves of Figure 6.2 show a number of dips, and the UVW1-band in particular has a clear dip at $\phi \approx -0.056$ identified as the pre-eclipse dip. The amount of absorption in the accretion stream needed to account for these dips can be estimated from the absorbing column of neutral hydrogen (n_H) necessary to reduce the post-eclipse spectrum brightness level to the pre-eclipse brightness level. Having established the best-fit model spectrum in Section 6.3, the value of n_H is increased until the soft-band count rate of the model is equal to that of the observed light curves. The values of n_H required are shown in Figure 6.6 as a function of azimuthal angle from the line of centres, the increasing absorption with decreasing angle is evident. The use of neutral absorption is not completely physically correct as shown by the pre-eclipse spectral fits (Figures 6.3 and 6.4).

A similar method can be used to estimate the absorption in the UV-bands. This is done using the interstellar reddening of Seaton's law (Seaton, 1979), and is implemented within XSPEC by the UVRED model component. Note that the use of UVRED assumes dust reddening in the UV, and provides a lower limit on the absorption as the accretion streams in polars do not contain dust. This additional component is necessary as the neutral absorber model component (WABS within XSPEC) does not extend to UV energies. By adjusting the E_{B-V} parameter, the flux of the model can be adjusted to match the decrease in flux seen in the light curves. This leads to a value for the neutral absorption column density from the relationship given by Bohlin et al. (1978) as

$$n_H = E_{B-V} \times 4.8 \times 10^{21} \,\mathrm{atoms\,cm^{-2}\,mag^{-1}} \tag{6.1}$$

For the UVW1 light curve, the absorption in the pre-eclipse dip is measured from the ingress brightness level to the bottom of the pre-eclipse dip, giving a reduction

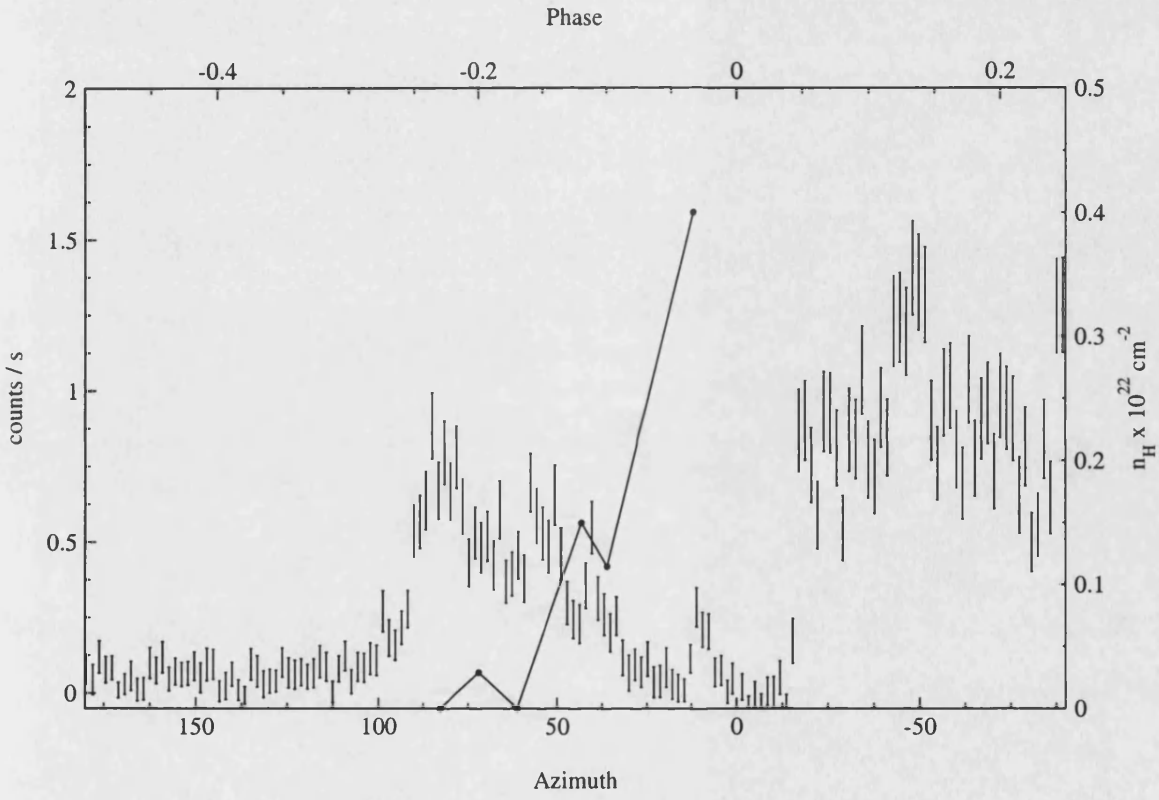

Figure 6.6: A plot of the absorption column density n_H versus azimuth plotted over the soft-band light curve. The absorption uses the lower abscissa and right-hand ordinate, while the soft-band light curves uses the upper abscissa and left-hand ordinate.

in flux of a factor of 3.6. This implies an $E_{B-V} = 0.24$ and an $n_H = 1.2 \times 10^{21}\,\mathrm{cm}^{-2}$. The egress from the dip minimum is longer than the ingress, so the absorption is estimated from halfway between dip minimum and the ingress brightness level. This yields an $E_{B-V} = 0.11$ and $n_H = 5.3 \times 10^{20}\,\mathrm{cm}^{-2}$. Substituting these values for n_H back in to the spectrum model fit it is seen that at dip minimum there is significantly more soft X-ray emission than predicted from neutral absorption alone. For the egress, however, the n_H is consistent with the model fit to the post-eclipse X-ray spectrum.

Applying the same method to the UVW2 light curve is more difficult because of the lower signal-to-noise ratio of the light curve. However, taking the decline in flux from $\phi \sim 0.2$ to the pre-eclipse dip minimum at $\phi \approx 0.056$ gives an $E_{B-V} = 0.315$ and $n_H = 1.5 \times 10^{21}\,\mathrm{cm}^{-2}$.

Figure 6.7 shows the absorption required to produce the observed count rate at the centre of the pre-eclipse dip as a function of energy. This figure illustrates that the absorption is not due to interstellar absorption, as this would produce a horizontal line. This provides further evidence that the absorption process in the accretion stream is more complicated than the neutral absorber assumed by the initial spectral fit.

6.5 Location of accretion stream material

In Chapter 4 I explain the trough feature observed in the optical light curves as being due to the presence of an extended accretion curtain together with cyclotron modulation. The V-band light curve here shows a rise before eclipse, and a rise and fall post-eclipse, and the UV light curves both show modulation (Figure 6.2) which implies that the observed emission is changing with viewing angle to the system. There is also evidence for absorption seen when comparing the pre to post-eclipse bright phases, and from the presence of dips in both the soft-band and hard-band X-ray light curves (Section 6.4). Dips probably due to absorption are seen in the

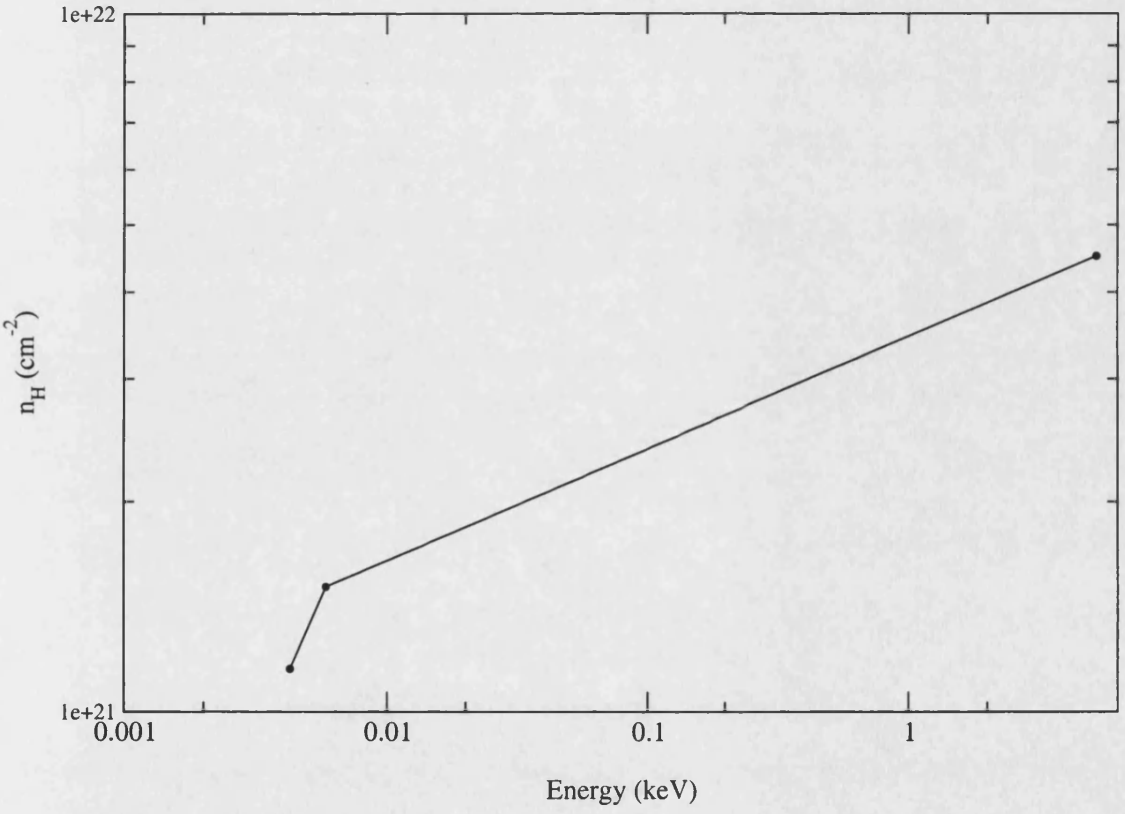

Figure 6.7: The neutral absorption required to produce the pre-eclipse dip in the hard-band and UV (errors are estimate at 20%).

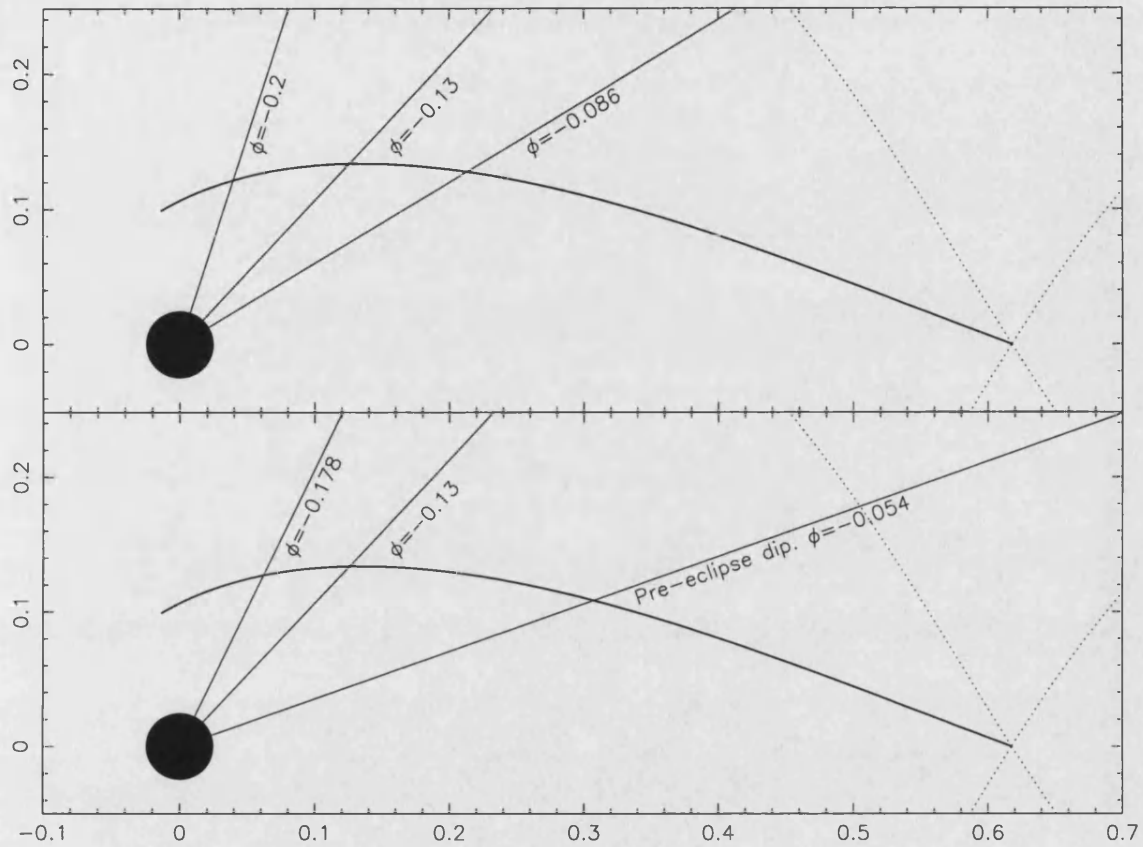

Figure 6.8: *Upper plot*: the line-of-sight of the pre-eclipse dips in the soft-band light curve. *Lower plot*: the pre-eclipse dips of the hard-band. In both figures the dotted line represents the Roche lobe, and a calculated ballistic trajectory is indicated.

UVW1 and UVW2 bands, with a clear pre-eclipse dip in the UVW1 light curve, and a decline in brightness in the UVW2 similar to that seen in the X-ray bands.

The extent in phase of the soft X-ray absorption seen prior to the eclipse centre in Figure 6.2 indicates that there is not a single well collimated accretion stream. Instead material appears to be located in a broad arc, able to obscure the X-ray emission site for a significant part of the orbit. The presence of dips in the light curves, superimposed on the general decrease in flux, indicates that the material is not homogeneous. Instead it appears to consist of a series of denser regions, surrounded by a more diffuse flow. This is also seen in the variation in brightness of the stream in the optical observations in Chapter 4, and is modelled in Chapter 5.

Figure 6.8 locates the dips in the light curves in azimuth. The indicated lines of phase are centred on the primary, which is where the emission region is located, and are parallel to the true lines of phase which must pass through the centre-of-mass. They do not, however, indicate the location of the emission region. The phase lines indicate that there must be absorbing material located on magnetic field lines threading from a significant length of the ballistic stream. The location of the pre-eclipse dip is very close to the eclipse of the accretion region and primary in the light curves, and there is a clear rise following the pre-eclipse dip seen in the hard-band and the UVW1-band.

There are two possibilities for the location of the pre-eclipse dip so close to the centre of eclipse. Firstly, the dip may occur where the line-of-sight is such that the accretion region is viewed face on, and the angle between the magnetic field lines and the line-of-sight is small. The observer then sees the emission region through the material just prior to encountering the shock. As the inclination of the system is relatively high, this would require an accretion region located at low latitude on the surface of the primary. The absorption over an extended phase range seen in the X-ray light curves is then a result of absorption by material which threads onto the magnetic field lines along the ballistic trajectory. Alternatively, the pre-eclipse dip may be where the observer sees those field lines carrying most of the accretion stream material as the field lines leave the orbital plane. In this scenario, most of the accretion stream material is threaded on to the magnetic field lines relatively far from the primary along the ballistic trajectory. This provides a large amount of absorbing material to produce the pre-eclipse dip seen in the X-ray and UV light curves. Some material survives the initial threading process however, and continues along a ballistic trajectory. These blobs of material are eroded as they travel through the magnetosphere of the primary, gradually contributing less material to be threaded on to the magnetic field lines, and hence less absorption is seen in the light curves (see Figure 6.6).

Either of the possibilities outlined can explain how, slightly later in phase, there

is a rise in all bands. This rise in flux corresponds to the sudden emergence of the emission region from behind the threaded accretion stream before eclipse by the secondary. This rise is very slight in the soft-band, indicating that a very small amount of material is needed to absorb the soft X-rays. The structure of the UVW1-band pre-eclipse dip is such that the egress is longer than the ingress; this longer egress could be caused by some material threading earlier in the ballistic trajectory and would support the second possibility above. However, the longer egress may be due to the viewing angle to the stream changing and there being a larger area of accretion stream visible for longer.

After the rapid eclipse of the primary and the accretion region in the UVW1 light curve, the accretion stream ingress is still clearly visible. There appears to be little structure in the eclipse ingress, however the time binning of 20 s removes any feature on time scales less than this. Figure 6.9 shows the white light curve of EP Dra cycle 56976 from Chapter 4 together with the X-ray and UVW1 light curves. The location of the start of the 'trough' in the optical light curves is at $\phi = -0.126$, approximately coincident with a dip in the soft-band and hard-band light curves (Figure 6.8).

6.6 Accretion region

The slight offset of the centre of the bright phase from $\phi = 0$ indicates an accretion region offset from the line of centres, and trailing the secondary star. This asymmetry is consistent with that found by Remillard et al. (1991) from their polarimetry observations. The *ROSAT* observations of Schlegel and Mukai (1995), when adjusted for the ephemeris of Schwope and Mengel (1997) by Schlegel (1999), show an asymmetry in brightness similar to that seen in Figure 6.2: that is, the post-eclipse light curve is significantly brighter than that pre-eclipse. This implies that the accretion region shape is irregular, and it is suggested by Schwope and Mengel (1997) that it is ribbon or arc-shaped. The emission in the soft-band and hard-band

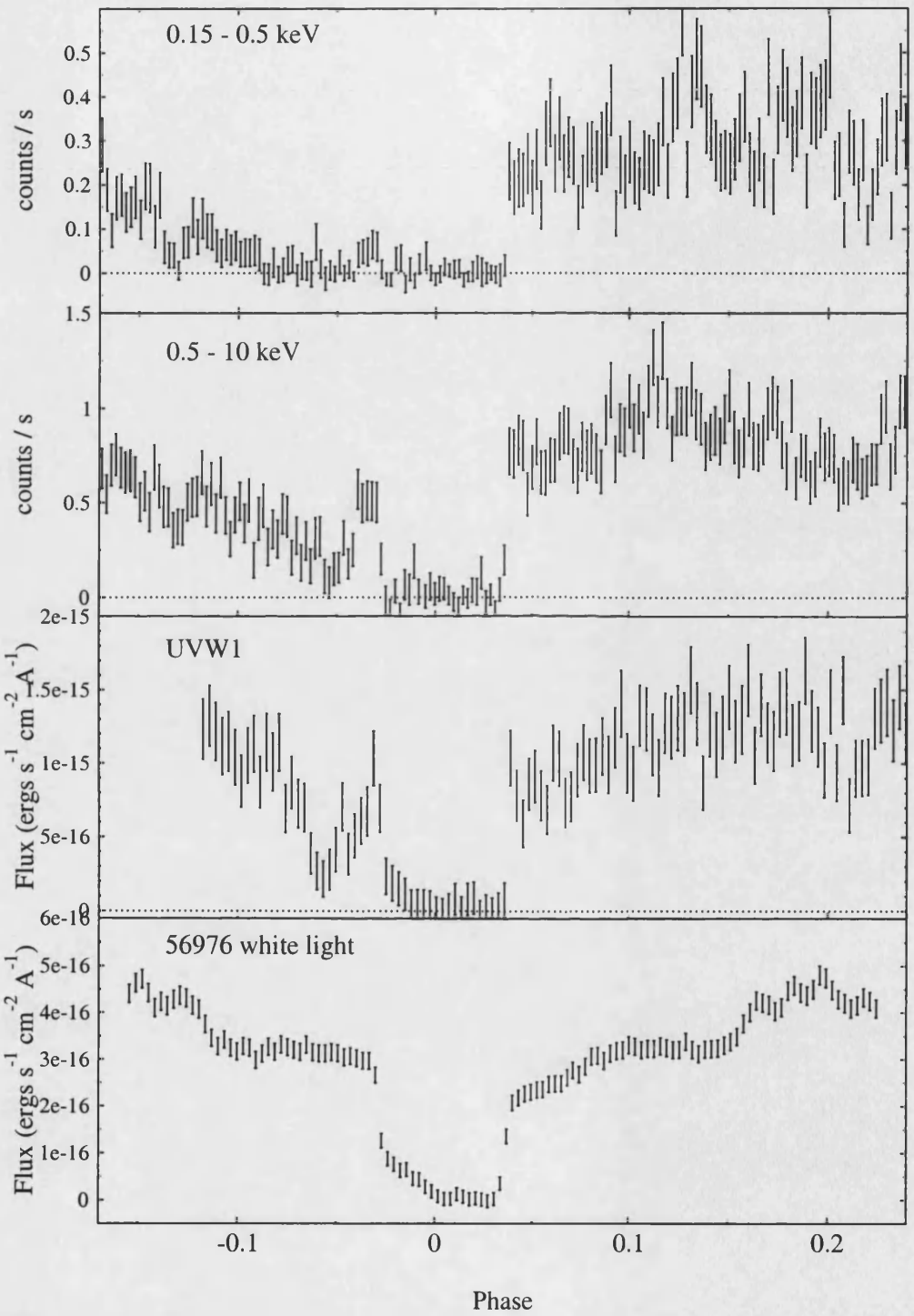

Figure 6.9: The soft and hard X-ray EPIC light curves with the cycle 56976 'white'-light curve from Chapter 4 and the OM UVW1 light curve. The X-ray light curves are in 15 s bins, and the white light and OM are in 20 s time bins.

appears to originate from different parts of the accretion region.

6.7 Conclusions

I have investigated the accretion stream in EP Dra using the highest quality X-ray observation of EP Dra to date. The light curves show an eclipse of the primary and the accretion region that is approximately of the same duration in the X-ray as the optical observations (Chapter 4). The X-ray light curves show evidence for an accretion region that appears to be particularly extended in longitude. The offset of start and end times of the bright phase between the soft-band and the hard-band indicates that the soft and hard X-ray emission regions are not entirely coincident, with the soft X-ray emission appearing to lag in phase the hard emission on the surface of the primary.

The X-ray light curves show a number of dips attributed to absorption, implying an inhomogeneous flow of material where the dips indicate the location of particularly dense blobs of threaded material. There is a clear pre-eclipse dip in the UVW1 light curve and a dip at the same phase in the hard-band. The dip is not clear in the soft-band as the count rate has already reached a minimum. The pre-eclipse dip is not seen in the V-band light curves presented in Chapter 4, although I concluded there that there is absorption. It is not clear whether the accretion stream has the same form in the X-ray and UV observations presented in this Chapter compared to the earlier optical observations of Chapter 4.

I attribute the location of the absorption over an extended phase range in the X-ray light curves to an extended accretion curtain. The amount of absorption can be deduced by comparing the bright phase spectra from the soft-band before and after eclipse by the secondary. The amount of absorption increases with azimuth indicating that there is an increasing column density of material along the line-of-sight to the accretion region. The location of the pre-eclipse dip, therefore, can occur where the geometry is such that the angle between the line-of-sight to the accretion

region and the magnetic field lines is very small. In this case the accretion region is seen through a large column density of material located on the magnetic field lines close to the primary. Alternatively, the material may be located where most of the accretion material threads onto the magnetic field lines, relatively early along the ballistic trajectory. The absorption over the extended phase range is then caused by material that passes through an initial threading region and is continuously stripped and threaded onto the magnetic field lines as it continues along a ballistic trajectory. The presence of absorption in an extended accretion curtain supports the earlier conclusion from the optical light curves of Chapter 4 that the 'trough' feature is (at least partially) caused by absorption.

Chapter 7

Accretion stream temperature

In preceding chapters I have determined the brightness distribution of the material along the accretion stream (Chapters 3, 5). I have shown that the brightest material is located close to the primary in the magnetically confined region, and that the location of the bright material further from the primary can change from cycle to cycle. In this chapter I attempt to explain why there are brightness enhancements by determining the temperature structure for a model accretion stream. This also addresses the question of whether irradiation alone can heat the stream to sufficient temperatures to produce the observed emission.

I construct a model accretion stream using simple hydrodynamics and derive the temperature structure by irradiating the stream with optically thin keV X-rays from the accretion shock. I compare the results with the brightness distribution of the accretion stream derived in the preceeding chapters from observed eclipse light curves, and with previous temperature estimates. I then locate the regions where the emission lines of the various ion species are emitted, and construct theoretical Doppler maps to compare with emission line observations.

7.1 A model accretion stream

I construct a model accretion stream using two merging trajectories. Firstly, a ballistic trajectory is calculated based on the formulation of Lubow and Shu (1975). This trajectory starts at L_1 and ends at the threading region which is assumed to be at the magnetospheric radius R_μ. At this point the trajectory assumes that of a stiff magnetic field line (there is no deformation due to interaction with the accretion stream) passing through R_μ and ending on the surface of the primary at the given location of the accretion region (β, ζ). This two part trajectory is shown to be a reasonable approximation in Chapter 5, and is the same shape of trajectory as used in Chapter 3. The irradiating source is assumed to be the shock-heated region, located at the end of the magnetic field line on the surface of the primary. This assumes the region is point-like, which is a sufficient approximation for the purpose of this study.

The thermal pressure of the magnetically confined stream is ignored as the velocity of the stream material is much greater than the sound speed. Therefore, the velocity of the stream is calculated along the magnetic trajectory from the acceleration of the stream in the gravitational potential of the primary and secondary. The cross-sectional area of the ballistic section of the accretion stream is assumed to be constant along its length. However in reality the cross-sectional area will vary: the study of Lubow and Shu (1975) showed that the width of the stream narrows as it curves towards the primary. At R_μ the cross-section of the magnetically confined model stream is assumed to be the same as that of the end of the ballistic stream. The shape of the magnetically confined region is defined by the magnetic field lines of the primary, with the cross-section at each point being perpendicular to the field lines, and decreasing towards the primary as the field lines converge (see Figure 7.1).

The number density of the model accretion stream at each point is determined via mass conservation along the stream. For simplicity it is assumed that there is no accumulation or stagnation of material at R_μ. For a mass transfer rate $\dot{M}$, the

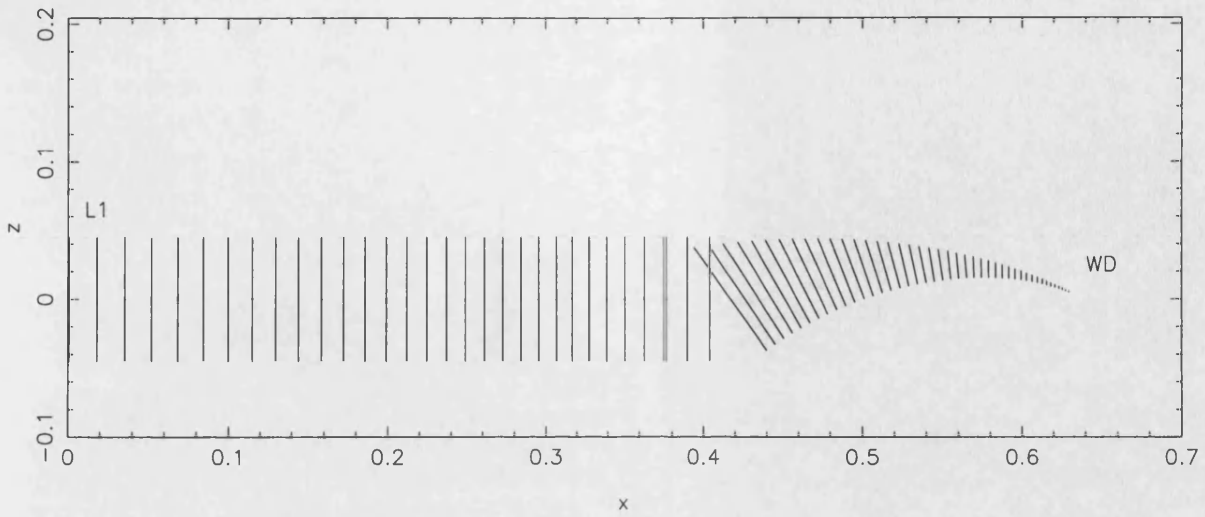

Figure 7.1: The accretion stream cross-section structure for the irradiative model.

number density $n(r)$ at a given distance r from the irradiating source is

$$n(r) = \frac{\dot{M}}{A(r)v(r)m_{\mathrm{H}}} \tag{7.1}$$

where $A(r)$ is the area and $v(r)$ the velocity of the stream at distance r from the source, and m_{H} is the mass of the hydrogen atom. Figure 7.2 shows an example of $v(r)$, $A(r)$ and $n(r)$ as a function of distance from the primary. The vertical dashed lines indicate L_1, R_μ and the radius of the primary R_1.

7.2 The irradiative model

The major source of X-ray emission in polars is Bremsstrahlung from the accretion shock immediately above the surface of the primary, with the temperatures in the post-shock flow being of the order of tens of keV. This emission directly illuminates the accretion stream, resulting in photoionization of the accretion stream material. Photoionization occurs when the incident photon has energy greater than the binding energy of the electron it encounters, removing the electron from the atom. The electron thermalizes in the surrounding plasma through electron-electron and electron-ion interactions, effectively heating the plasma. The dominant contribution

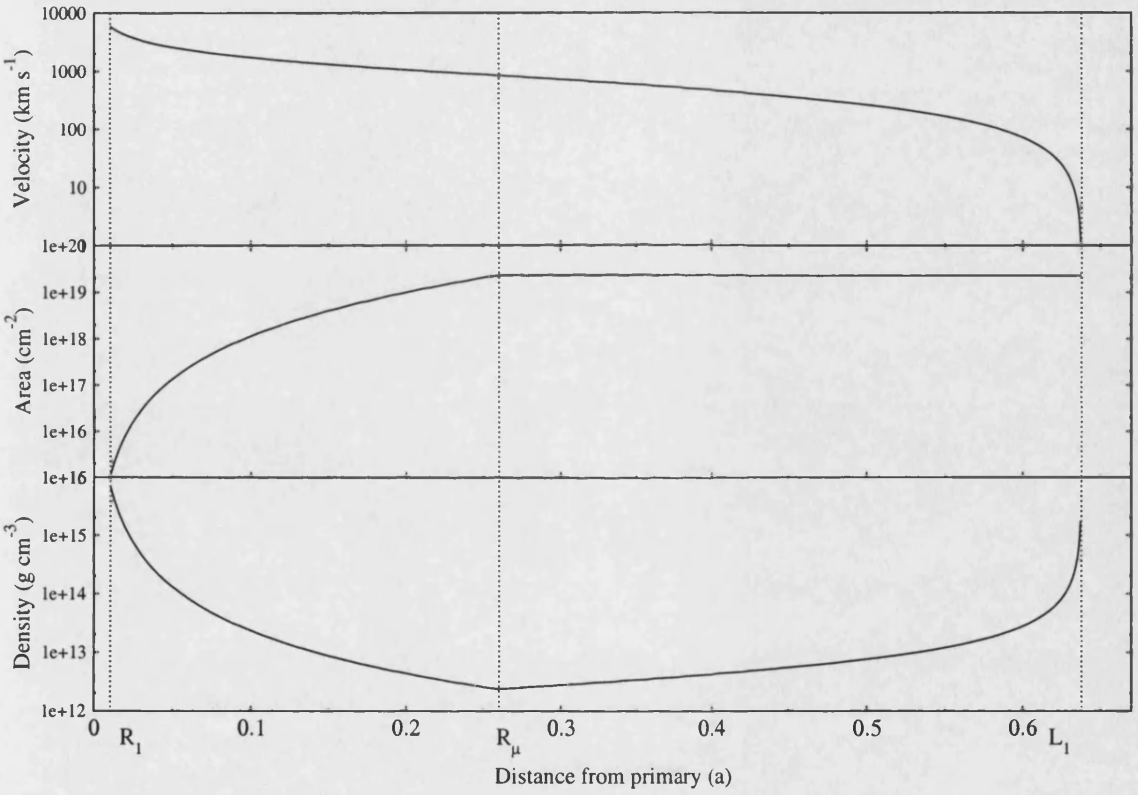

Figure 7.2: The velocity, area and density profiles for HU Aqr as calculated for the model accretion stream. The location of the surface of the primary, the coupling radius and L_1 are indicated with vertical dotted lines.

to the heating of the stream via photoionization is from the heavier trace elements such as C, N and O, which have large photoionization cross-sections at keV energies.

The accretion stream material is considered to be optically thin to the Bremsstrahlung emission, which implies that the effects of absorption within the stream and the subsequent emission of secondary radiation can be neglected. The effects of electron scattering and Compton scattering are also ignored because the scattering rate is extremely low: the Thompson cross-section ($\sigma_T \sim 10^{-25}$) is very much smaller than the typical photoionization cross-section ($\sim 10^{-18}$; e.g. Osterbrook, 1989).

The assumptions and requirement for this non-radiative transfer model are analogous to that of Hatchett et al. (1976): their model is therefore adopted as it is easily scalable to our physical conditions. A more recent model considering only the magnetically confined region is by Ferrario and Wehrse (1999). They use a full radiative transfer treatment for irradiative heating by X-rays in the magnetically confined section of the accretion flow, and a parameterized heating component through the interaction of magnetic fields. Their model is more detailed than the model I present here and considers cases with both irradiative and magnetic heating, and just irradiative heating.

Hatchett et al. (1976) calculate the temperature and ionization structure of spherically symmetric clouds of gas, of cosmic abundance and number density n, surrounding a central irradiating point source. For a given X-ray spectrum of luminosity L, Hatchett et al. (1976) determine the temperature by requiring a local balance between the combined X-ray heating and radiative cooling, and the combined ionization and recombination of the gas. The temperature is parameterized as a function of the ionization parameter ξ,

$$\xi = \frac{L}{n(r)r^2} \tag{7.2}$$

ξ can then be described as a function of $\dot{M}$, $A(r)$ (the cross-sectional area of the accretion stream) and $v(r)$ by substitution of Equation 7.1

$$\xi = \frac{LA(r)v(r)m_{\rm H}}{\dot{M}r^2} \tag{7.3}$$

The equilibrium temperature for any distance r from the source can then be determined by interpolation of the appropriate irradiation model as calculated by Hatchett et al. (1976).

As well as photoionization, the model also includes ionization by inelastic scattering of bound electrons and by Auger emission. In the model of Hatchett et al. (1976) the secondary radiation produced at r by the ionization and recombination of the ions is assumed to travel radially outwards and so does not affect the gas inside of r. Thus, at each r the model stream is assumed to receive direct illumination from the source, hence neglecting any shielding by sections of the stream inside of r.

Of the four different source spectra considered by Hatchett et al. (1976) the model used is their model 1, see Figure 7.3. This is an optically thin Bremsstrahlung model of $kT_{eff} = 10\,\mathrm{keV}$.

The X-ray heating is considered as the only heating mechanism for the model accretion stream. This is obviously a major assumption, and means that the derived temperatures are less representative in certain regions of the accretion stream. Towards the surface of the primary, as the accretion stream approaches the irradiative source, the density increases and can reach $n \gtrsim 10^{16}\,\mathrm{cm}^{-3}$ (Achilleos et al., 1992). In this regime there are additional energy-transport processes that are not considered in this model, such as cyclotron emission. Similarly, at the transition from the ballistic to magnetically confined trajectory the heating due to the interaction of the accretion stream material with the magnetic field (such as via reconnection) is neglected. The interaction with the magnetic field is also neglected along the ballistic trajectory, as is any collisional heating. Nevertheless, the model accounts for the major heating and cooling effects.

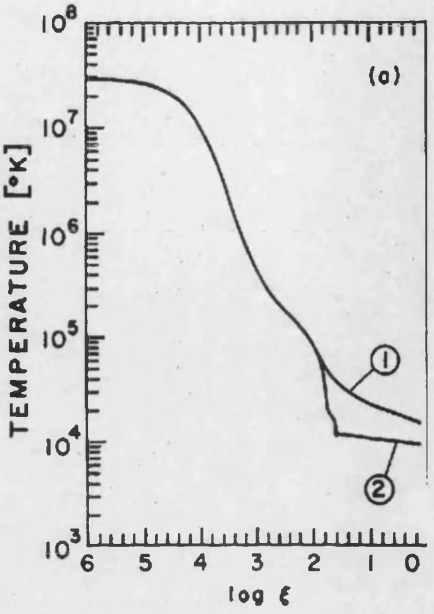

Figure 7.3: The ξ – T relationship for an optically thin (model 1) and an optically thick (model 2) Bremsstrahlung source spectrum. From Hatchett et al. (1976), their figure 1a.

7.3 Application

I apply the model to both HU Aqr and EP Dra, using the parameters summarised in Table 7.1. The accretion stream is constructed using parameters derived in Chapters 3 and 4 for the accretion region/irradiative source location and the location of R_μ. L is taken from Chapter 6 for EP Dra, with the distance to EP Dra of 300 pc, which is a lower limit estimated by Remillard et al. (1991). $\dot{M}$ for EP Dra is from the empirical relationship given by Patterson (1984) relating the orbital period to $\dot{M}$. $\dot{M}$ for HU Aqr is from Chapter 3 and L is from Schwope et al. (2001) for a distance of 150 pc. The stream radii σ are taken from Chapter 3 for HU Aqr. The values for EP Dra are calculated using Equation 3.2 from Chapter 3 with i=79.5°. In the case of EP Dra there is evidence for an extended curtain (Chapters 4, 5), rather than a collimated stream. However, the model cannot reproduce a curtain geometry, and I use a stream with the caveat that this is not physically representative

Table 7.1: Input parameters for the equilibrium temperature irradiative model for HU Aqr and EP Dra.

Object	L	R_μ	σ	$\dot{M}$	β	ζ
	(ergs s^{-1})	(a)	($\times 10^9$ cm)	($\times 10^{16}$ g s^{-1})		
HU Aqr	4.5×10^{32}	$0.22a$	2.3	1.96	60°	40°
		$0.26a$	2.7	1.10	55°	30°
EP Dra	1.4×10^{32}	$0.19a$	1.2	0.93	18°	-17°
		$0.22a$	1.4	0.93	18°	-17°
		$0.14a$	0.87	0.93	65°	-17°
		$0.16a$	0.99	0.93	65°	-17°

for this system. The consequences of this approximation are likely limited because the model also takes no account of shielding by material in the accretion flow. The effects will be most pronounced along the magnetic trajectory with the consequence that the temperatures should be reduced to account for less dense material.

For each model stream point, $n(r)$ is calculated, then the ionization parameter ξ using the given L. The value of ξ is used to find the temperature T from the model 1 ξ versus T relationship in Figure 7.3. Figure 7.4 shows the ξ and T profiles for HU Aqr cycle 29993 as an illustrative example. The resulting temperature profiles are shown in Figures 7.5, 7.6 and 7.7.

The overall temperature structure is similar for all cases because of the nature of the model accretion stream, and the dependence upon the input parameters (cf Equation 7.3). The temperature initially increases rapidly after L_1 as the velocity of the accretion stream increases and the density decreases. The temperature then rises more steadily as the accretion stream material falls towards R_μ, and v continues to increase and n and r decrease. As the material joins the magnetic field line the temperature initially decreases as the area decreases, however the increasing velocity and decreasing r cause the temperature to increases rapidly close to the surface of

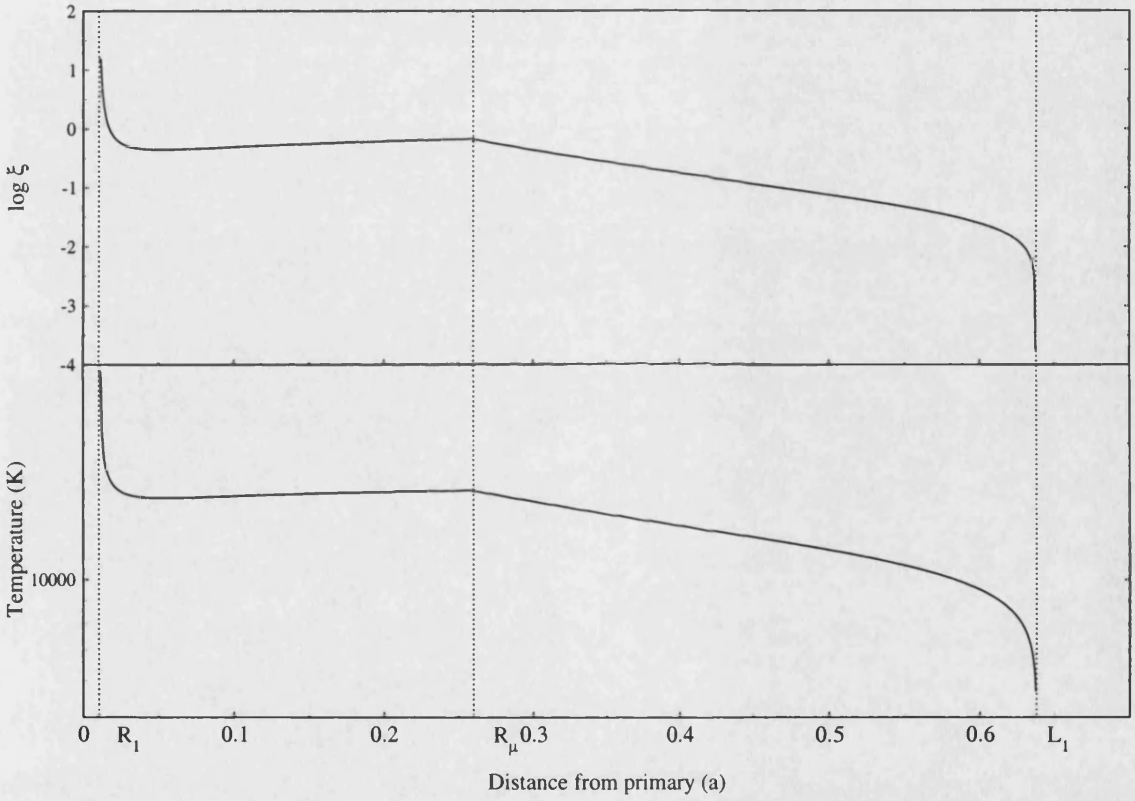

Figure 7.4: An example of a ξ versus r together with the T versus r profile for HU Aqr 29993, $R_\mu = 0.26a$.

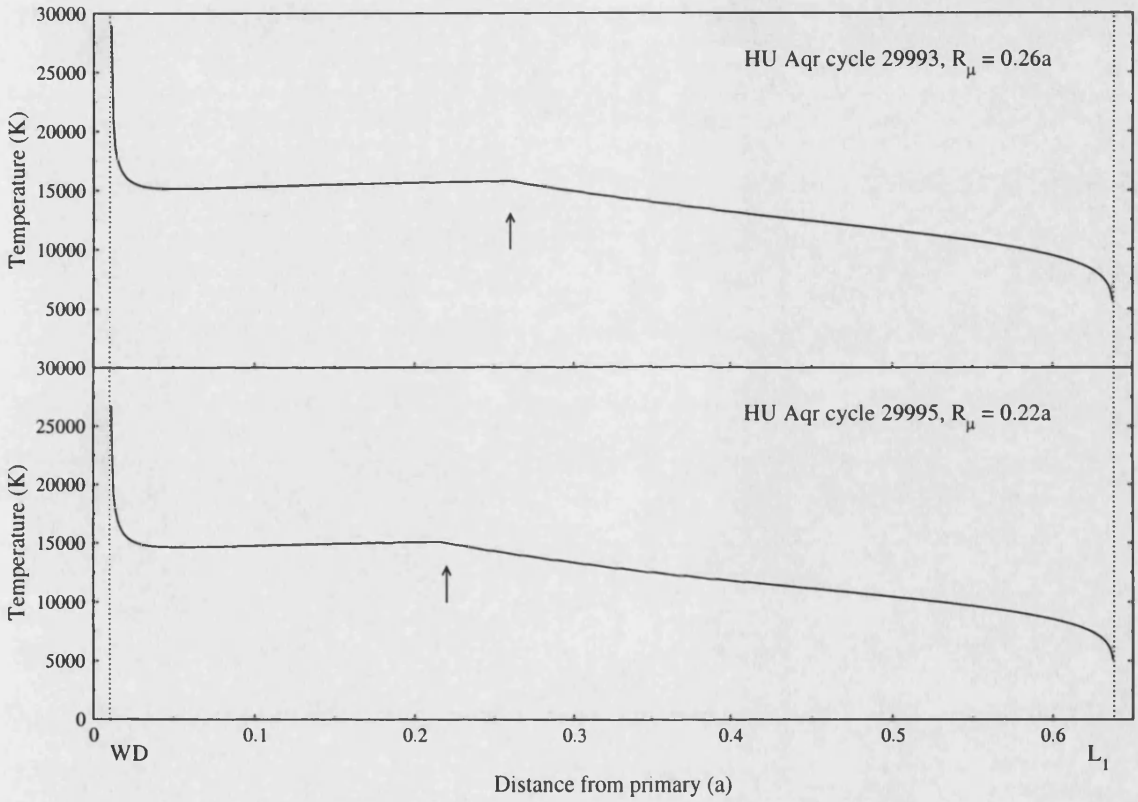

Figure 7.5: The temperature structure of the model stream is shown as a function of distance from the primary (in units of the binary separation). The upper plot is for HU Aqr cycle 29993 and the lower plot for cycle 29995. The position of L_1 and the surface of the primary are indicated with a dashed line and R_μ with a short arrow.

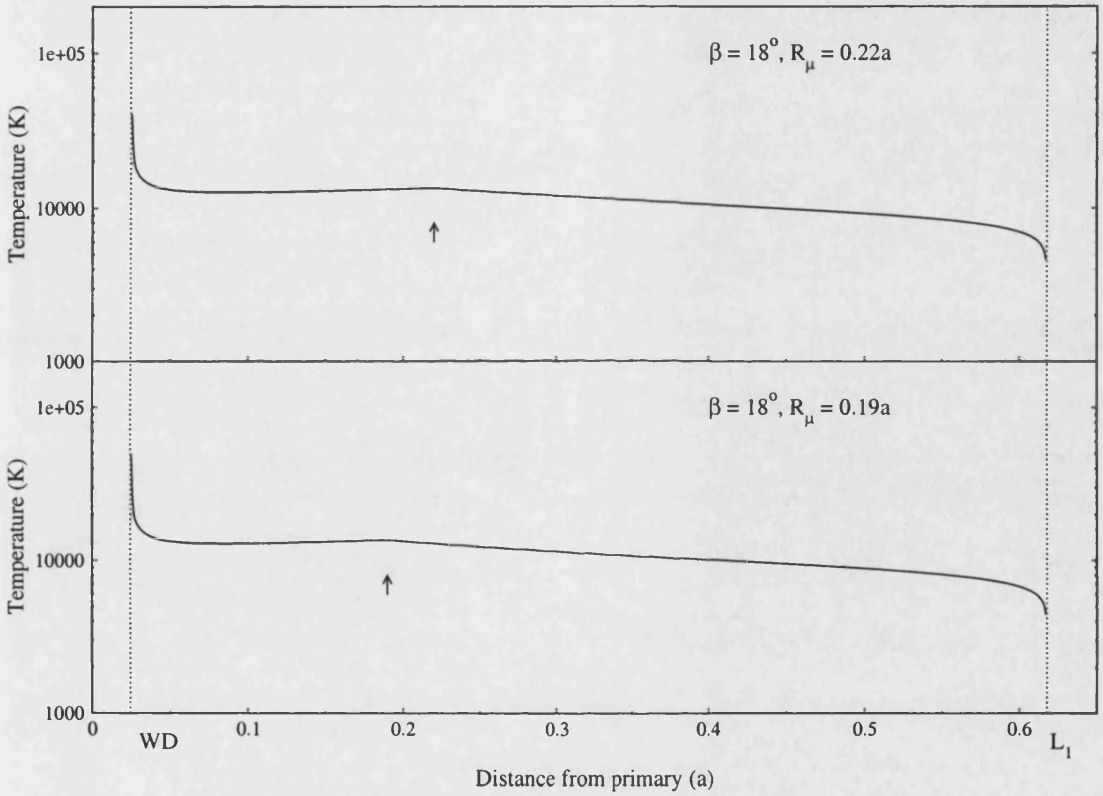

Figure 7.6: The temperature structure of the model stream is shown as a function of distance from the primary (in units of the binary separation), for EP Dra with $\beta = 18°$. The upper plot represents $R_\mu = 0.22a$ and the lower $R_\mu = 0.19a$. The position of L_1 and the surface of the primary are indicated with a dashed line and R_μ with a short arrow.

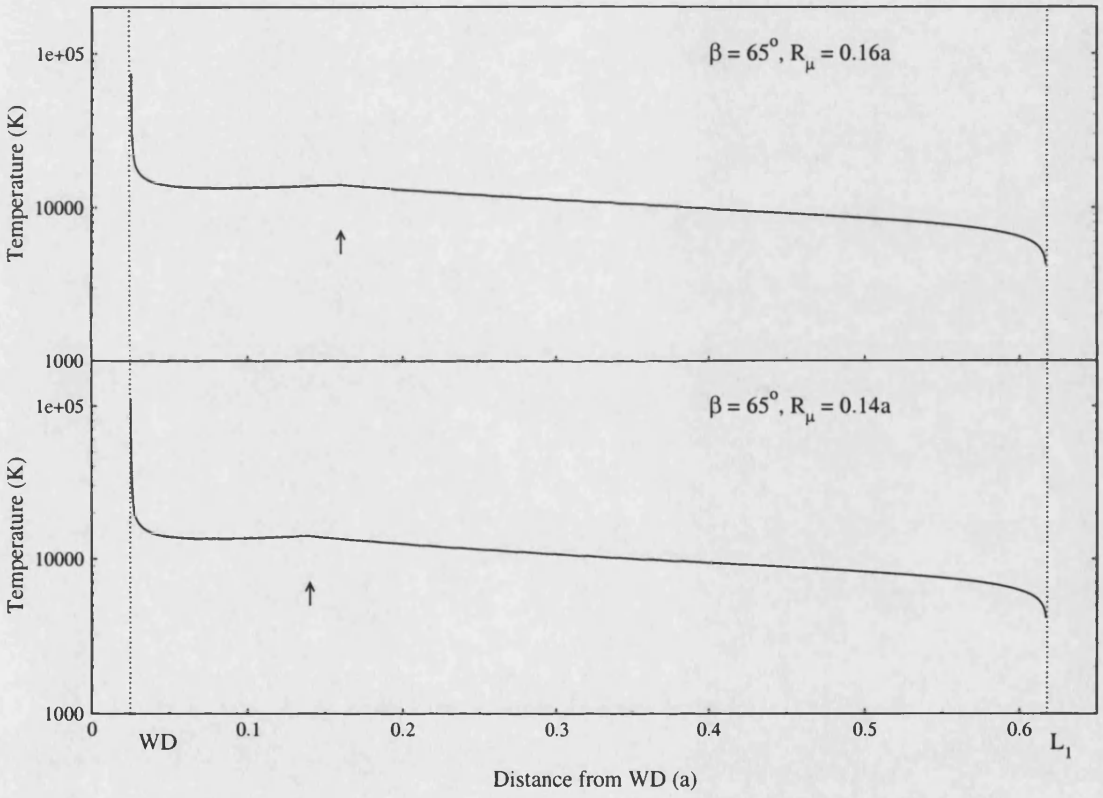

Figure 7.7: As for Figure 7.6, but for $\beta = 65°$ and $R_\mu = 0.16a$ and $0.14a$.

the primary.

7.4 Comparison with brightness maps

The temperature profiles in the previous section can be compared to the brightness distributions of the accretion stream material in Chapters 3 and 5. These brightness distributions are derived from observational light curves, so bearing in mind that the brightness of stream material is related to the temperature and/or the density of the material, progress can be made in explaining the location of enhanced brightness in the eclipse mapping methods. In Chapter 3 I applied an eclipse mapping method to the S-Cam 2 cycle 29993 and 29995 observations of HU Aqr. The model accretion stream was divided into three sections to cover all of the magnetically confined region and the threading region, as well as part of the ballistic stream. The results of Chapter 3 show that the material is bright as it approaches the primary for both cycles 29993 and 29995, and it is brighter in cycle 29993 than cycle 29995 in the threading region. The model temperature profiles show that the temperature increases towards the primary, and that the threading region is also bright. The threading region in cycle 29993 is not seen to be significantly hotter than that of cycle 29995 in Figure 7.5, which indicates that this region must be heated by another mechanism (or mechanisms) in order for it to be brighter than cycle 29995.

In Chapter 5 the brightness distribution was recreated using a second method which relies on the least number of assumptions about the stream trajectory. This indicates that for both HU Aqr and EP Dra the brightest material is located in the region where material is confined to the magnetic field lines, and in particular the brightest region is towards the primary. This is consistent with the increasing temperatures predicted by the model in the magnetically confined regions, peaking towards the primary. This shows that irradiative heating is important, and that it is the significant factor in the brightness distribution along the magnetically confined section of the stream trajectory.

7.5 Comparison of stream temperature estimates

7.5.1 Observations

Harrop-Allin (1999) used the eclipse mapping method to derive brightness distributions observationally for the accretion stream of HU Aqr. Most of the emission was found to be from the magnetically confined region, with increasing emission towards the primary for the one pole accretion models. The emission peaked in the B-band, suggesting (blackbody) temperatures of $\approx$6 500 K – 7 200 K. This is somewhat cooler than the temperature indicated in the same regions from the irradiation model presented here. The temperature of the stream can be estimated using the spectra derived from the HU Aqr and EP Dra S-Cam 2 light curves. For three cycles of EP Dra, where the stream ingress is clearest, values were (Reynolds et al., 2003) $T_{\rm eff}$=5 700, 7 200 and 6 050 K (uncertainties on these temperatures are $\pm$600 K). For HU Aqr, Reynolds et al. (2003) split the ingress of the accretion stream in cycle 29995 (their figure 5) into four sections and created a spectrum from each of the phase intervals. They found that the best-fit blackbody gave stream temperatures of $T_{\rm eff}$=6 600 K, 6 600 K, 6 700 K and 6 300 K ($\pm$600 K) for increasing phase. The temperatures are similar to those determined by Harrop-Allin et al. (1999b) and again somewhat lower than those derived here. The difference between the results of Reynolds et al. (2003) and Harrop-Allin et al. (1999b) and those calculated here may possibly be caused by the assumption of a blackbody in the interpretation of the observational results.

7.5.2 Other models

For the irradiation only model, Ferrario and Wehrse (1999) find temperatures in the range 10 000 K – 40 000 K with an initially hot threading region, a decrease in temperature, then increasing temperature towards the primary as the material falls approximately radially and the $1/r^2$ dependence is stronger. This is consistent

with my results presented here. The location of the hotter regions in the work of Ferrario and Wehrse (1999) is consistent with the temperature profiles derived here. However, here the temperature increases more rapidly towards the primary. The range of temperatures found in Ferrario and Wehrse (1999) along the magnetically confined accretion stream is consistent with those calculated for the HU Aqr and EP Dra $\beta = 18°$ models. The EP Dra $\beta = 65°$ models reach higher temperatures towards the primary than the $\beta = 18°$ models, but this will be somewhat dependent upon the specific input parameters for a given model.

7.6 Ionization structure

7.6.1 Calculations

Kallman and McCray (1982) calculated the ionization structure of irradiated gas using models based on those of Hatchett et al. (1976), but with the inclusion of more detailed atomic physics. The resulting ionization abundances for different elements irradiated by an optically thin bremsstrahlung source are shown in Figures 7.8 and 7.9 (figures 1a and 1b from Kallman and McCray (1982)), as a function of ξ.

The temperatures and values of ξ derived here can be used with the models from Kallman and McCray (1982) to locate those parts of the accretion stream where a particular ionized species dominates. This can then be used to predict the expected emission lines from different regions in the accretion stream. Figure 7.10 shows the location of the dominant ionized species for H, He and C along the accretion streams of HU Aqr cycle 29993 and EP Dra $R_\mu = 0.22a$ (as examples). These particular elements are chosen as they are responsible for strong line emission in polars, with HeII, CIV, SiIV and NV lines in the far UV, and H-Balmer, strong HeI, HeII and the CIII/NIII blend at 4650 Å in the optical and IR (Warner, 1995).

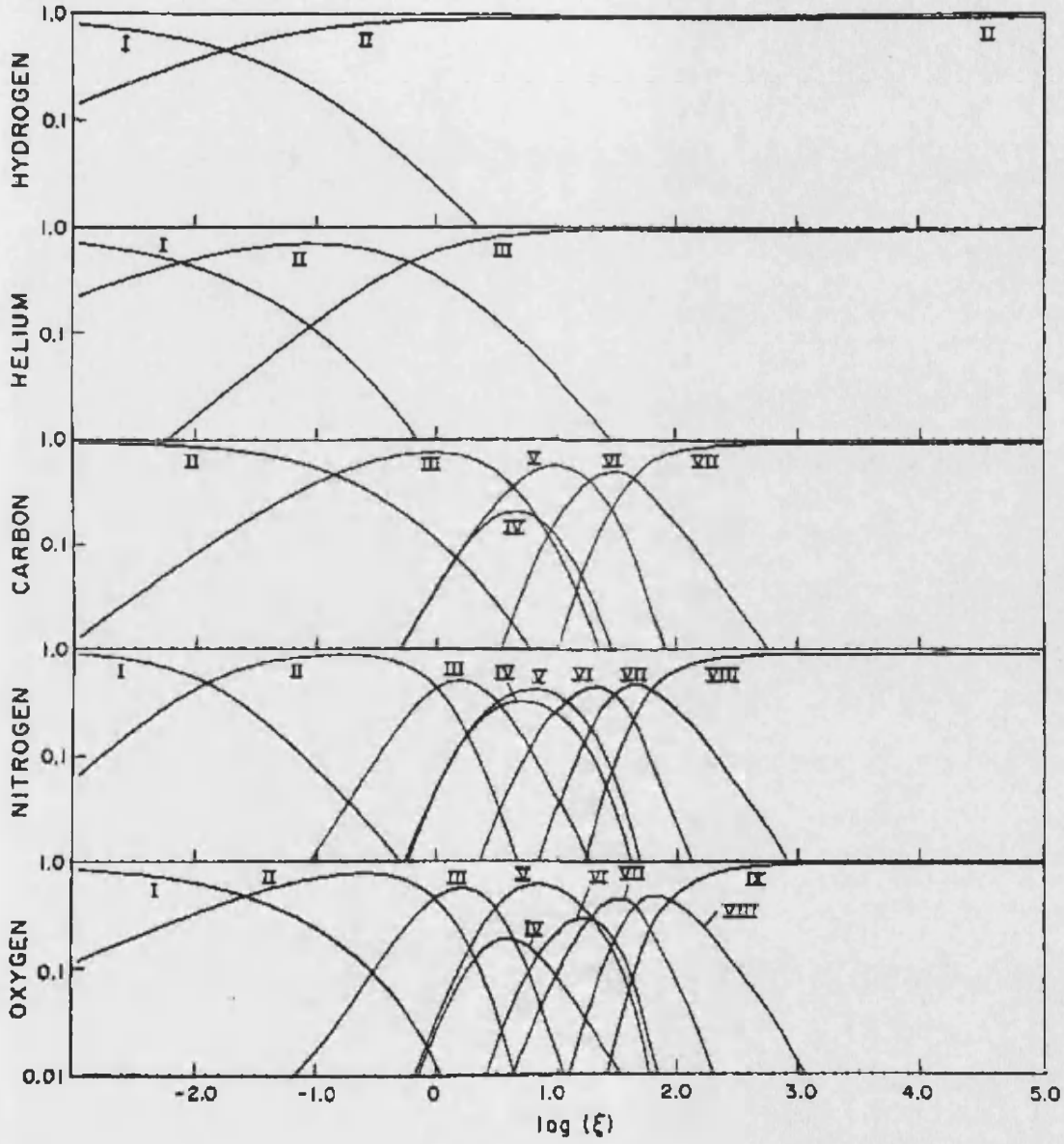

Figure 7.8: The relative ionization abundances of various elements for an optically thin bremsstrahlung irradiative source. From Kallman and McCray (1982).

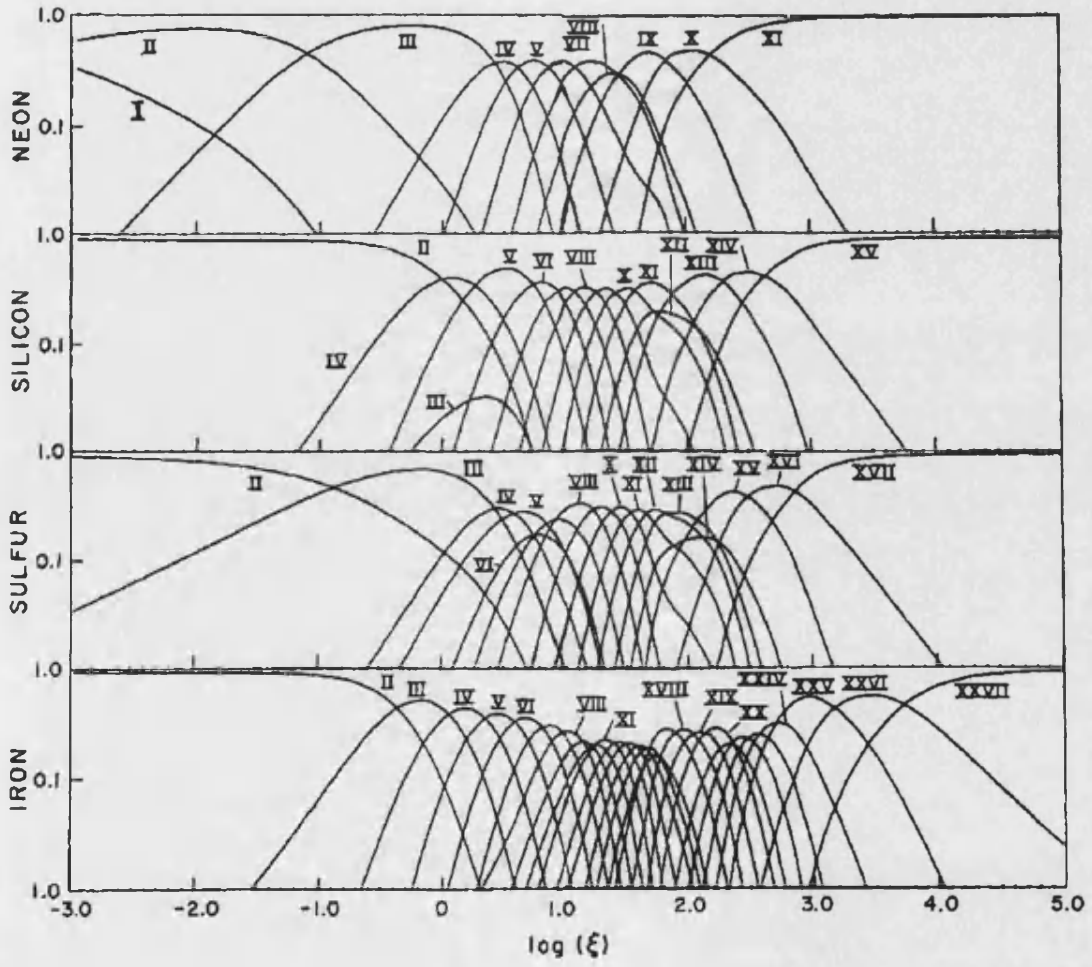

Figure 7.9: As for Figure 7.8. From Kallman and McCray (1982).

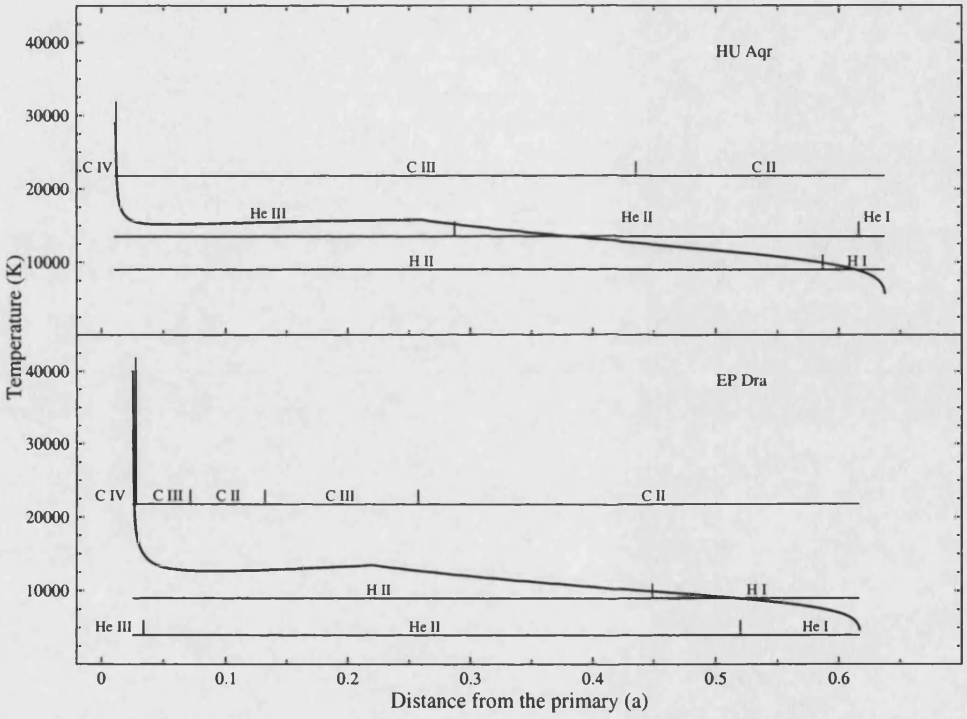

Figure 7.10: The location of the dominant ionized species along the accretion stream for H, He and C from the temperature profiles of HU Aqr 29993 and EP Dra ($R_\mu = 0.22a$). The short vertical lines divide the stream into region where the indicated species dominates (Kallman and McCray, 1982, see Figures 7.8 and 7.9).

7.6.2 Comparison with observations

The expected location of the ionized species along the accretion stream can be compared with locations derived from observations. Stockman and Schmidt (1996) present time-resolved UV spectroscopy of UZ For, where the eclipse places bounds on the location of the UV emitting region being in the magnetically confined region of the system between the primary and the circularisation radius. The spectra of both ST LMi and UZ For also show strong emission lines of NV, CIV and HeII. The magnetically confined region is where all of the C lines are predicted in Figure 7.10.

Kube et al. (2000) applied their eclipse mapping technique to relatively low signal-to-noise ratio CIV λ1550 observations of UZ For. They reconstruct three bright regions indicating emission from the ballistic stream, near the threading region and near the primary. UZ For is a bright system analogous in many respects to HU Aqr, therefore it might be expected that they have similar accretion stream structures. However, UZ For is seen to accrete at two regions on the primary (Perryman et al., 2001) and, as shown by Reynolds et al. (2003), the stream is deduced to be hotter. The fact that we see CIV only near the primary for the cooler stream in HU Aqr is as expected.

Figure 7.10 shows that the stream is expected to emit He lines of different ionizations at different locations in the stream. The location of the maximum recombination HeII lines is located in the threading region and part way towards the primary for EP Dra. For HU Aqr the maximum lies along the ballistic section of the accretion stream, after which the He is mostly HeIII. The location of HeII in the threading region of HU Aqr is consistent with the results of Vrielmann and Schwope (2001), which also locates bright emission along the ballistic stream.

7.6.3 Comparison with Doppler maps

Knowing which parts of the system contain a particular dominant ion means that a prediction can be made as to where emission is expected in Doppler tomograms

(Doppler maps; Marsh and Horne, 1988). The velocity structure of the model accretion stream as described in Section 7.1 can be used to plot the accretion stream trajectory in velocity coordinates. The location of the dominant ion species are then located along the trajectory.

Figure 7.11 shows Doppler tomograms of HU Aqr from Schwope et al. (1997b), and Figure 7.12 shows Doppler tomograms of EP Dra from Schwope and Mengel (1997). The observed Doppler tomograms in Figure 7.11 can be compared to the theoretical tomograms in Figure 7.13. This shows the location of He for HU Aqr with $R_\mu = 0.26a$. The observed Doppler maps show that the location of the emission in the theoretical Doppler map is consistent with the observations.

As the model can be used to predict the location of heavier elements, I also present Doppler maps for the heavier elements. These are shown in Figures 7.14 to 7.18 for HU Aqr with different R_μ ($0.14a - 0.30a$), and for EP Dra in Figures 7.19 to 7.23 with the same range of R_μ. This thesis has shown that for EP Dra there is most likely an extended accretion curtain, therefore the representation of the accretion flow as a collimated stream may be inappropriate. However the maps do indicate a general area where an ionized species is expected to be.

A comparison of the HU Aqr and the EP Dra He Doppler maps (Figures 7.14 and 7.19) shows, as noted earlier, the HeII dominating for much further along the trajectory in EP Dra and along most of the magnetically confined trajectory for all values of R_μ. In contrast, the observed EP Dra Doppler maps show the location of the HeII to be near to the secondary (Figure 7.12 Schwope and Mengel, 1997) and the accretion stream is not as prominent as for HU Aqr.

The emission of He lines from near the threading region is seen in many polars. For example Mennickent et al. (1999) conclude from their Doppler maps of BL Hyi that most of the HeI (and Balmer lines) are produced in the stream near the threading region. Simic et al. (1998) locate a broad spectroscopic component seen in HeII λ4686 emission lines in V2301 Oph as being where the material is compressed and threaded on to the magnetic field lines of the primary (their figure 9).

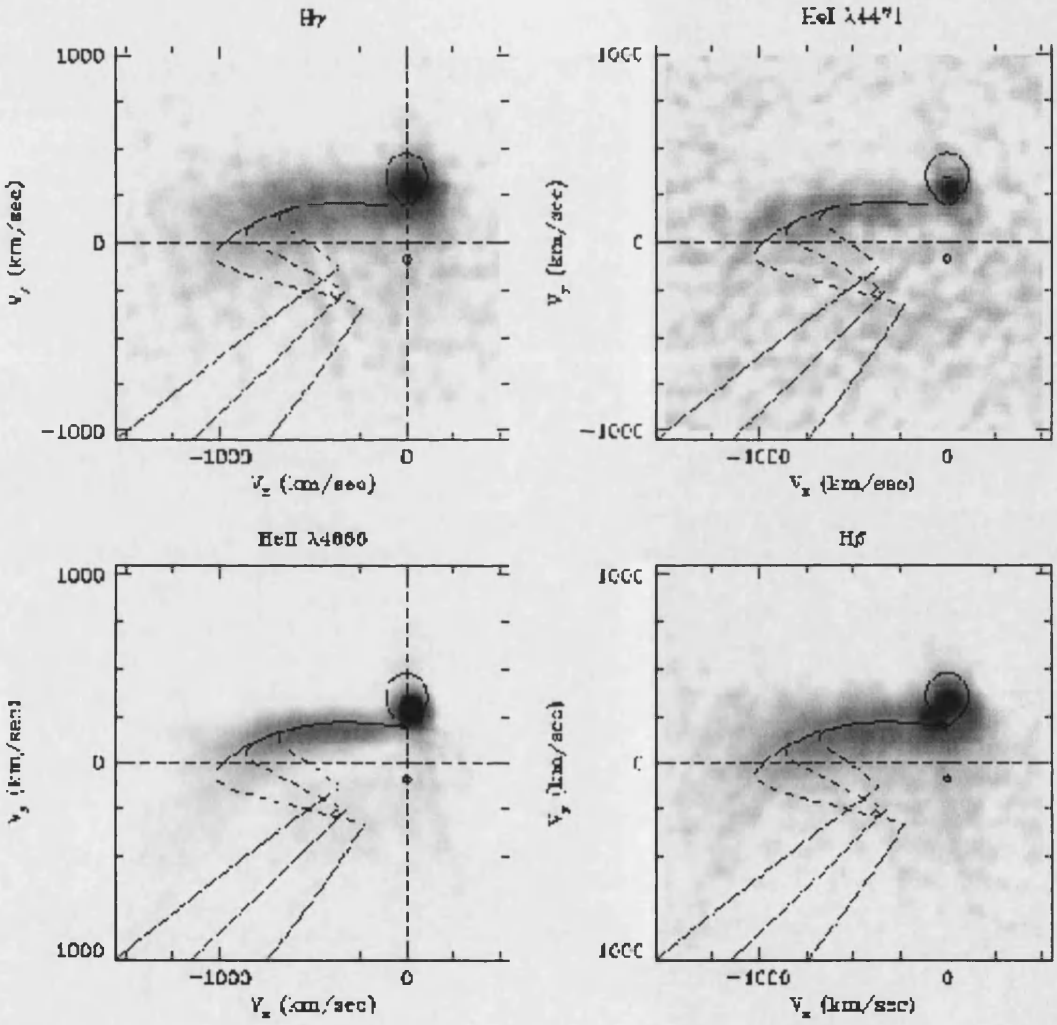

Figure 7.11: Doppler tomograms of HU Aqr from Schwope et al. (1997b), showing the four main emission lines observed.

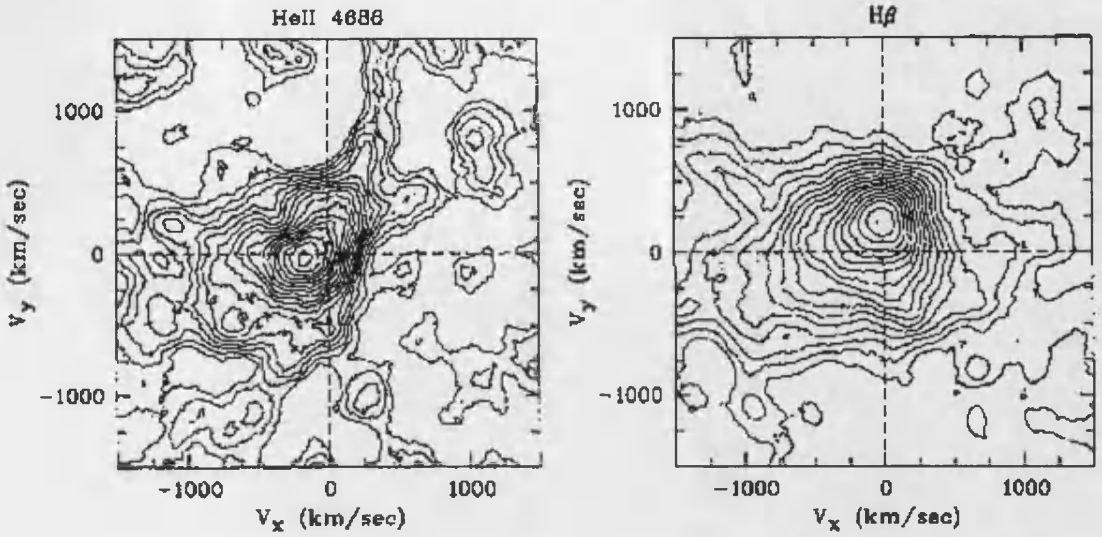

Figure 7.12: The Doppler tomograms of EP Dra from Schwope and Mengel (1997).

7.7 Conclusions

I have constructed model accretion streams for HU Aqr and EP Dra using a two part trajectory. A ballistic trajectory starts from L_1 and ends at the threading region, and a magnetically confined section follows the magnetic field lines from the threading region to the surface of the primary. I have irradiated this stream with optically thin bremsstrahlung radiation from the accretion shock and determined the temperature structure along the accretion stream using a parameterized model by Hatchett et al. (1976). I have then used the temperature profiles to predict the location of different ionized species using abundances from Kallman and McCray (1982).

The temperature profiles for both HU Aqr and EP Dra locate higher temperature accretion stream material in the threading region and in the magnetically confined region towards the primary. This is consistent with the location of brighter material derived in Chapters 3 and 5 through eclipse mapping techniques. The values for the temperature estimates are higher than those derived previously by Harrop-Allin et al. (1999b) and Reynolds et al. (2003), which may possibly be because of their

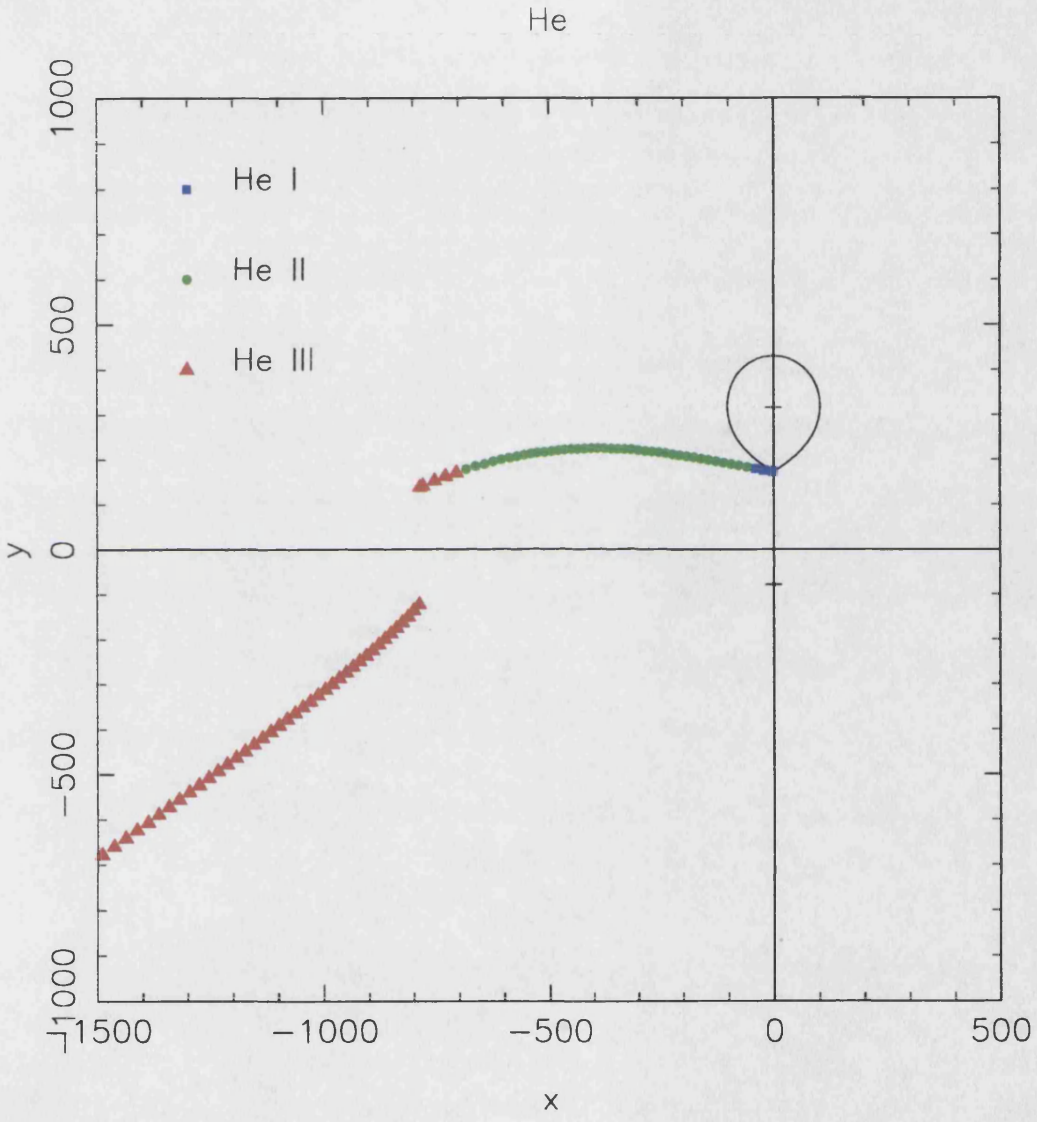

Figure 7.13: The Doppler map for HU Aqr showing the ballistic section of the stream in He emission. $R_\mu = 0.26a$.

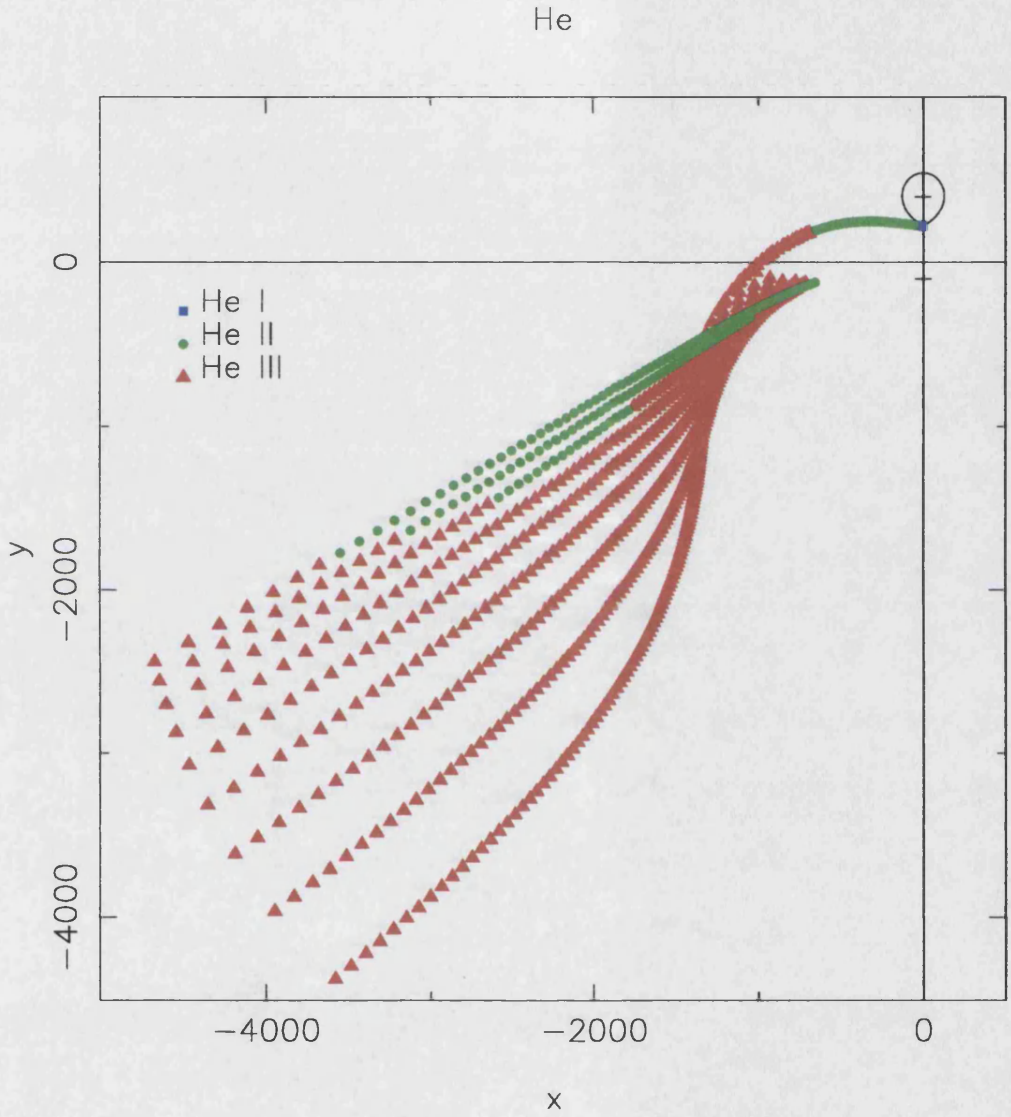

Figure 7.14: The Doppler map for HU Aqr showing the location of the dominant helium ions along the accretion stream. The ballistic stream is seen in the top left quadrant while the bottom left quadrant shows the magnetic trajectory for accretion streams with different R_μ from $0.14a - 0.30a$.

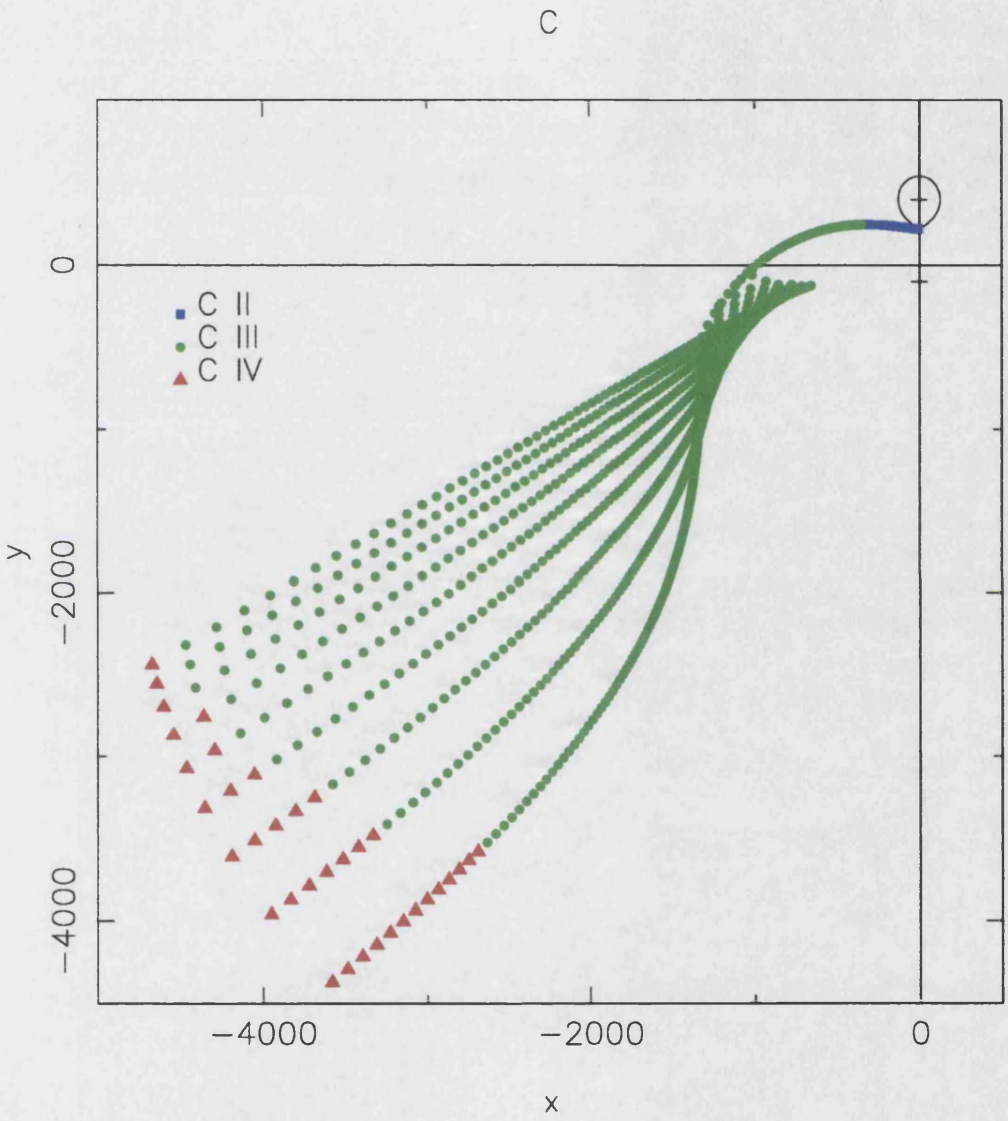

Figure 7.15: As for Figure 7.14, but for C ions. Note from Figure 7.8 that the CV always dominates over CIV, but is excluded from the figure for clarity. CIV is included as this is observed in Doppler maps of polars.

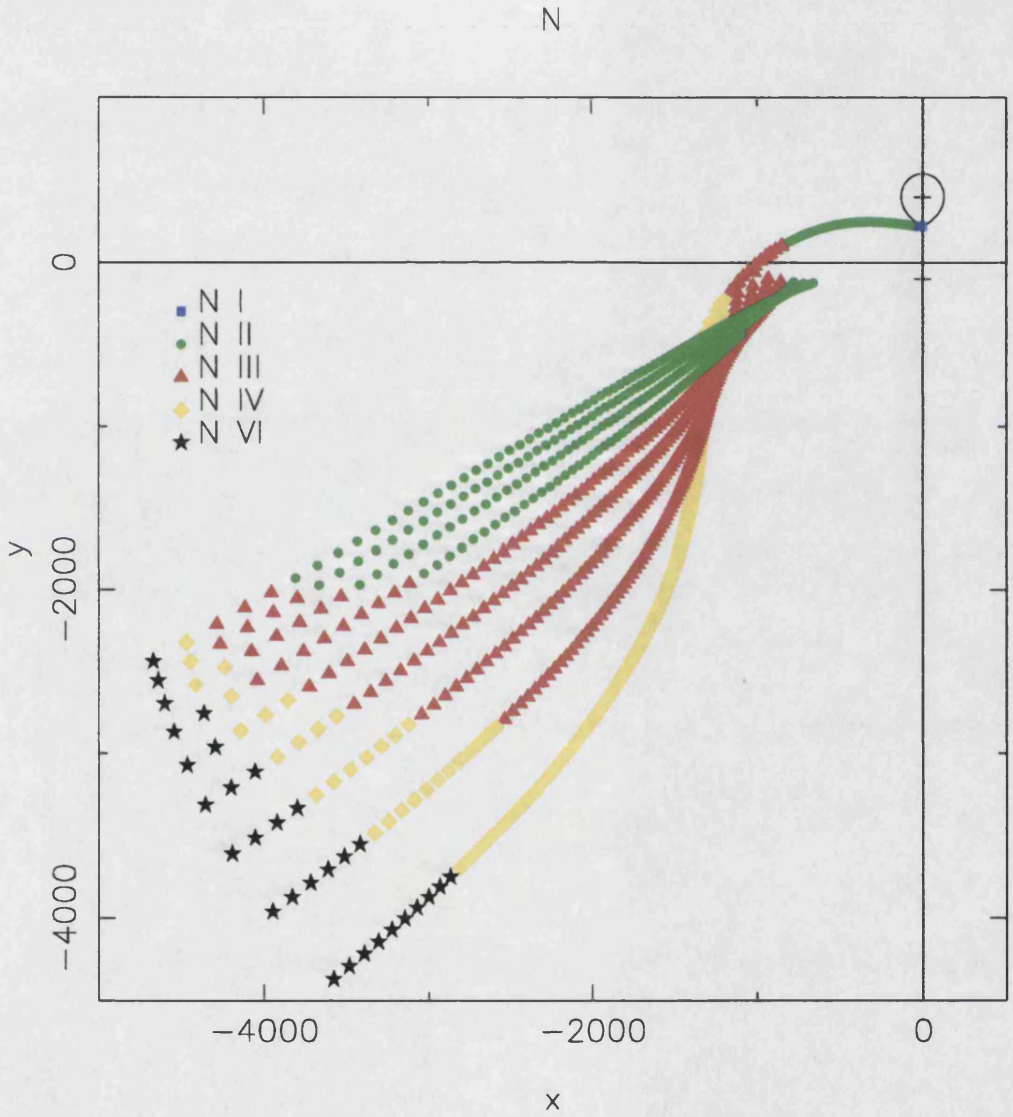

Figure 7.16: As for Figure 7.14, but for ions of N. NV is excluded as this ion always dominates over NIV, which is included for continuity with the NIII ion.

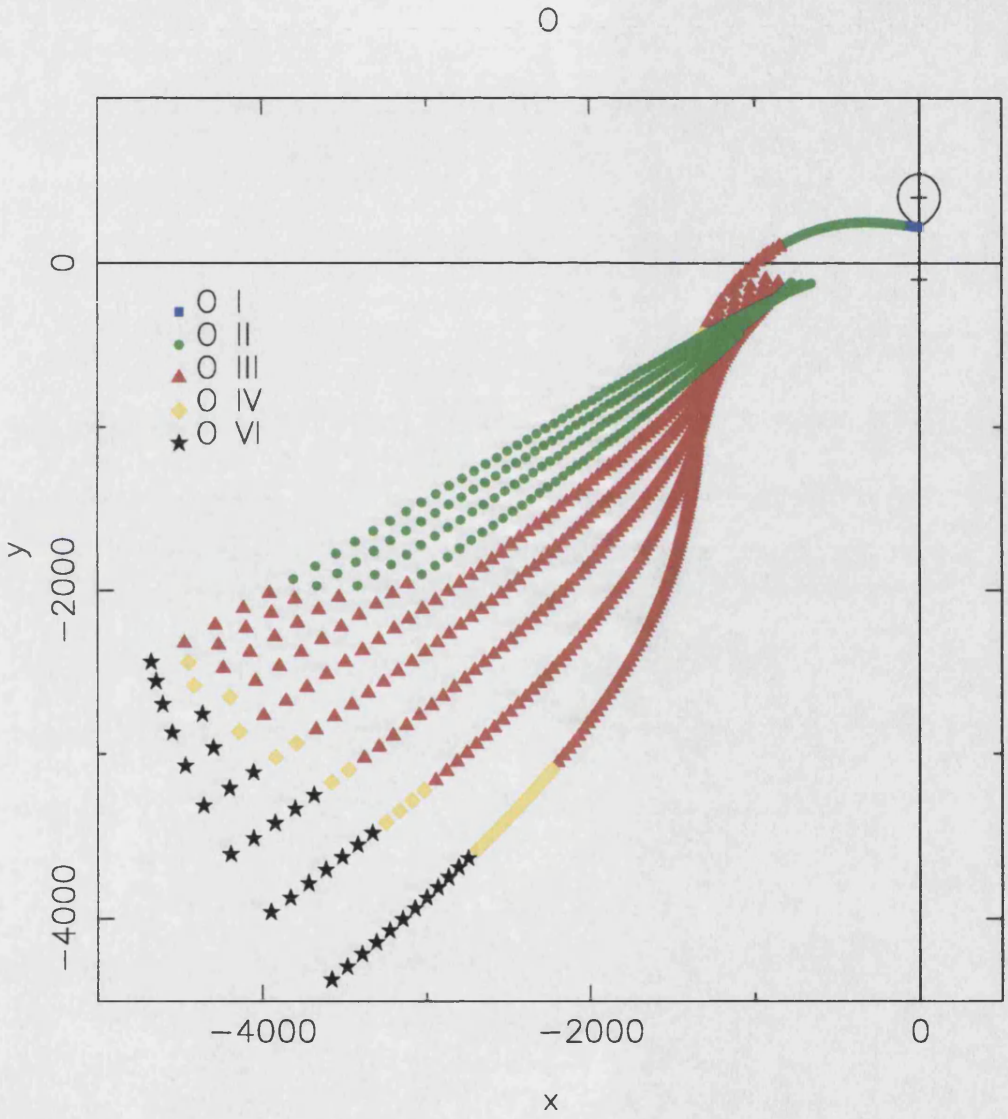

Figure 7.17: As for Figure 7.14, but for ions of O. The dominant ions up to OIV are shown, then the next dominant ion is OVI.

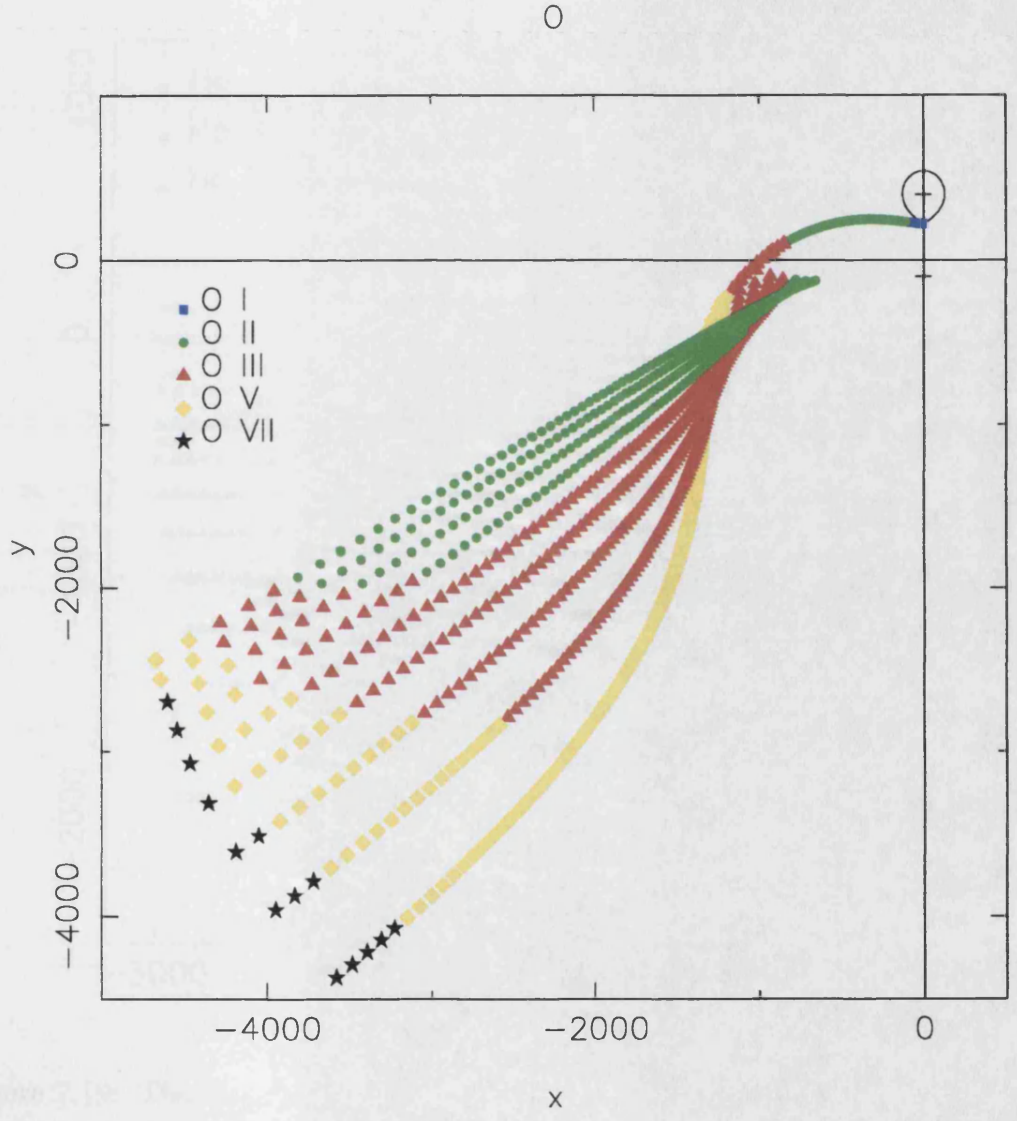

Figure 7.18: As for Figure 7.17, but showing OI to OIII, then OV which always dominates over OIV, and then OVII.

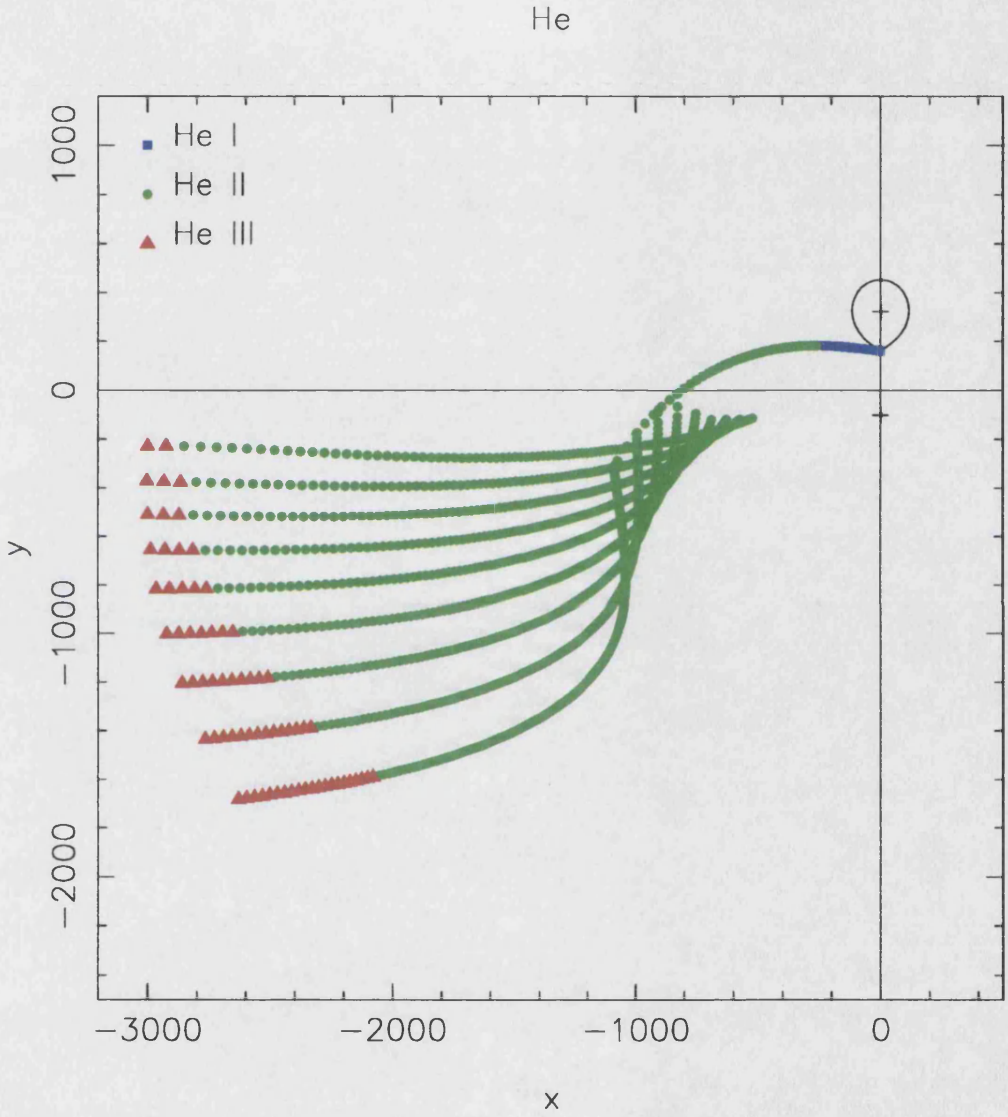

Figure 7.19: The Doppler map for EP Dra showing the location of the dominant helium ions along the accretion stream. The ballistic stream is seen in the top left quadrant while the bottom left quadrant shows the magnetic trajectory for accretion streams with different R_μ from $0.14a - 0.30a$.

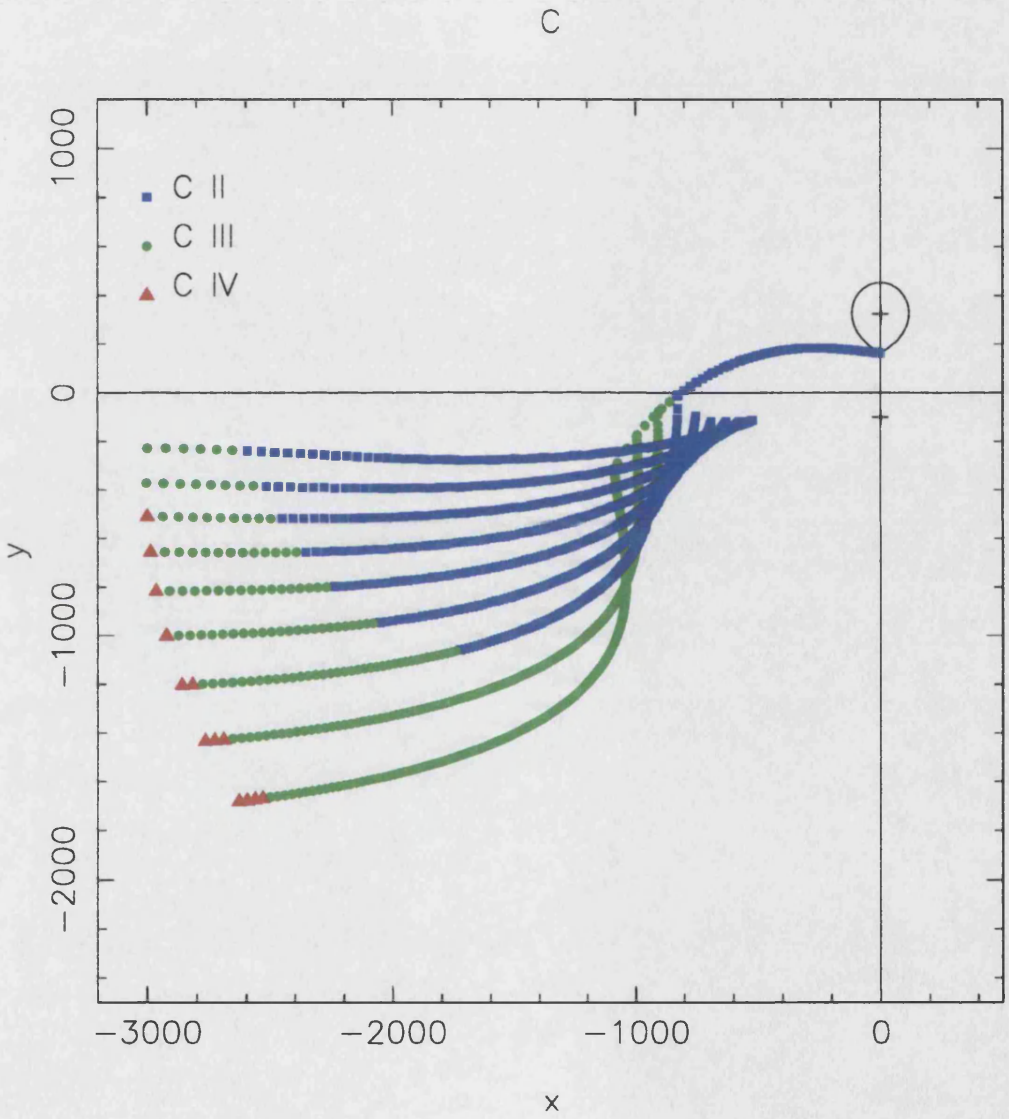

Figure 7.20: As for Figure 7.19, but for ions of carbon.

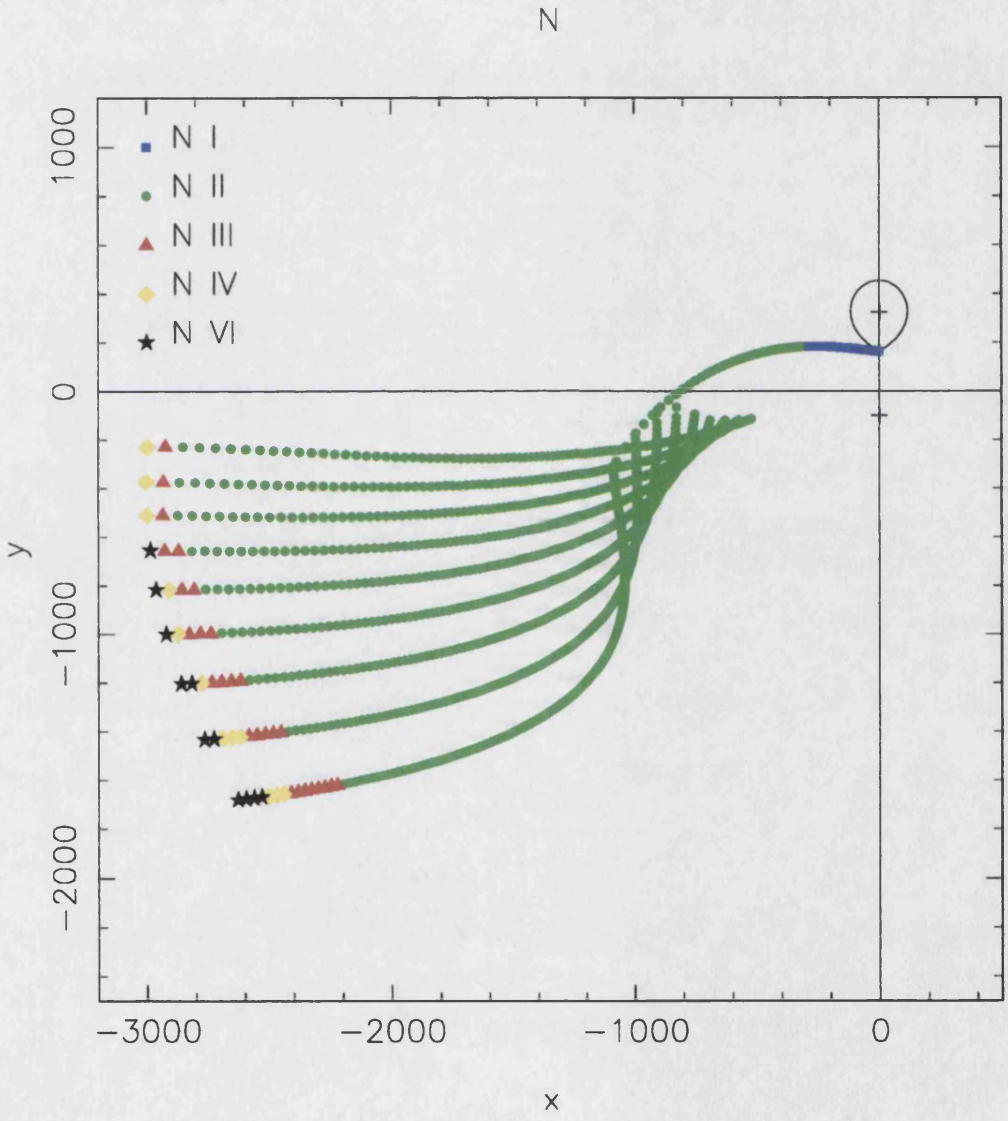

Figure 7.21: As for Figure 7.19, but for ions of nitrogen.

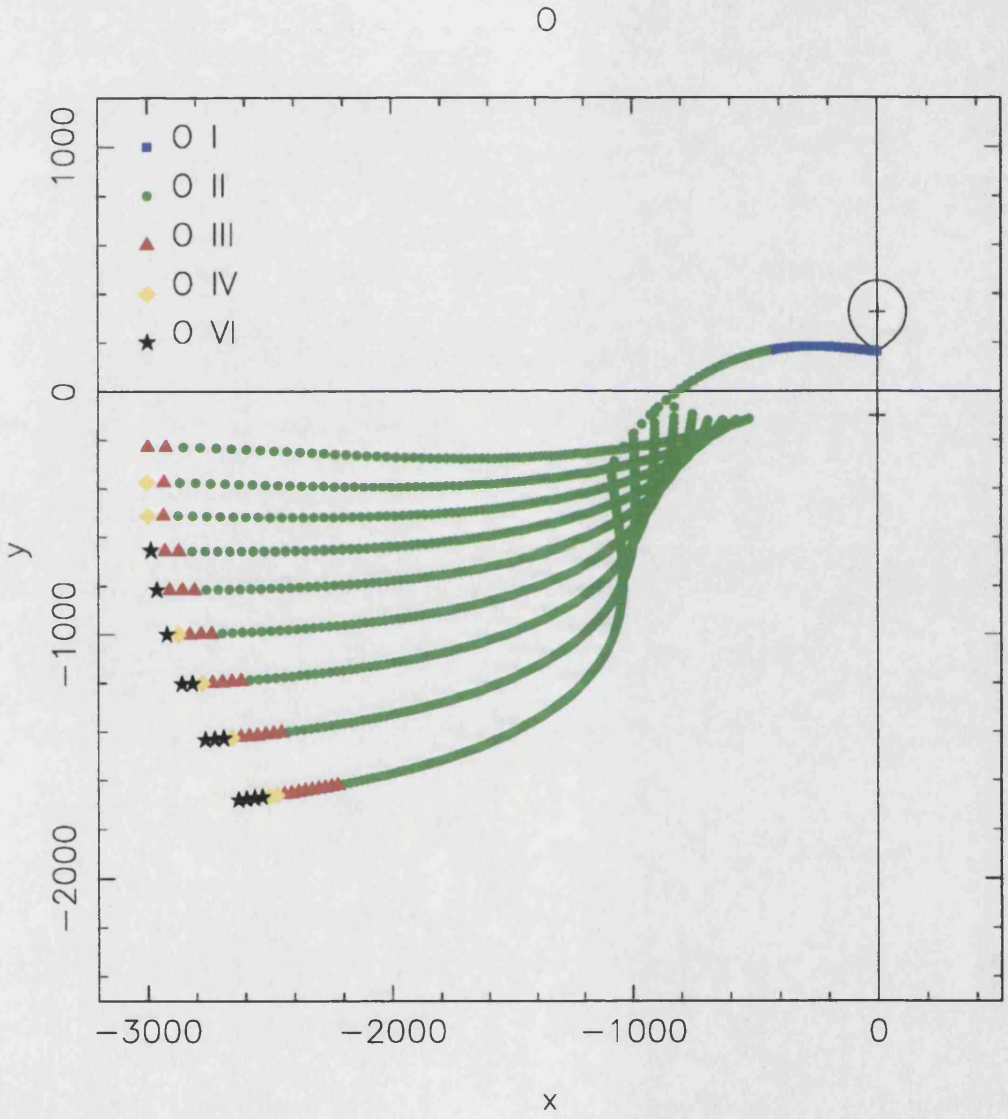

Figure 7.22: As for Figure 7.19, but for ions of oxygen. The dominant ions up to OIV are shown, then the next dominant ion is OVI.

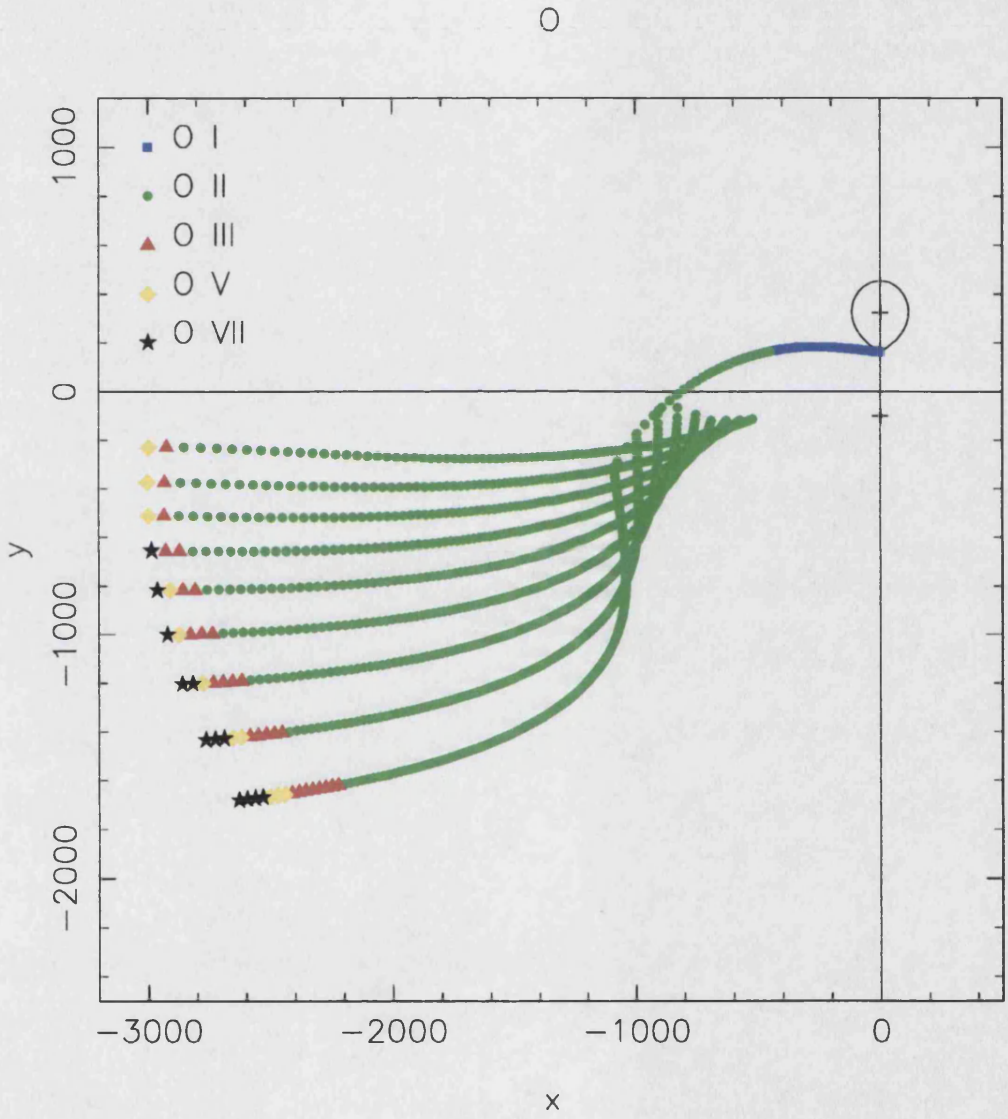

Figure 7.23: As for Figure 7.22, but showing OI to OIII, then OV which always dominates over OIV, and then OVII.

assumption of single temperature blackbody emission. The temperatures are consistent with those of Ferrario and Wehrse (1999), who also use a theoretical model to derive the temperature structure in the magnetically confined section of the stream.

I locate different ionized species along the model trajectories and find that the location of C is consistent with that found by Stockman and Schmidt (1996) and Kube et al. (2000) in their observations of UZ For. The location of He in HU Aqr is consistent with results presented by Vrielmann and Schwope (2001) for HU Aqr, based on their eclipse mapping technique.

The location of the ionized species can be used with the velocity structure of the model accretion stream, to construct theoretical Doppler maps. The location of He in the theoretical maps is consistent with that of the observed Doppler maps of Schwope et al. (1997b) for HU Aqr. This result prompts the need for further observations to compare with the theoretical Doppler maps for heavier elements.

Chapter 8

Summary and Conclusions

In this thesis I have studied the accretion flow in eclipsing polars, with observations of two systems.

- I have employed eclipse mapping techniques with optical observations to locate the accretion stream material in both HU Aqr and EP Dra (Chapters 3,4,5).
- I have used X-ray and UV observations, with the optical observations, to investigate the absorption by the accretion stream material in EP Dra (Chapter 6).
- I have constructed a model which creates a temperature structure for an X-ray irradiated model accretion stream (Chapter 7), and I have used this model to locate species of ionized elements along the accretion stream trajectory.

8.1 Locating the accretion stream

My study identifies the location of accretion flow material in both EP Dra and HU Aqr by examining the observed light curves, and I have made further insights by applying eclipse mapping techniques to these light curves.

8.1.1 Light curves

The light curves of HU Aqr and EP Dra both show that the accretion stream changes from cycle to cycle. This has been seen before for HU Aqr (Glenn et al., 1994; Harrop-Allin, 1999); however for EP Dra, these light curves represent the first study of consecutive high signal-to-noise ratio light curves. There are changes in the light curves which are observed over a timescale of the binary orbital period. This indicates that the mechanism controlling these changes must occur on relatively short timescales. In both systems the time taken for the accretion stream to be eclipsed by the secondary varies, and this indicates that the interaction of the accretion stream with the magnetic field is the controlling factor, with material penetrating to different depths in the magnetosphere of the primary.

The variability observed in the light curves of EP Dra is more dramatic than for HU Aqr, with a reduction in brightness of the accretion stream after the eclipse of the primary of 20% (to zero counts) between the two cycles 56962 and 56963. In EP Dra there is also evidence for variability over a longer phase range, which I have called the 'trough'-feature. The presence and form of this trough appears to be correlated with the brightness of the accretion stream seen during the eclipse by the secondary. I have attributed the trough to variations in the cyclotron emission, but also to absorption in an extended accretion curtain. The X-ray light curves of EP Dra corroborate the idea of an extended accretion curtain, with evidence for absorption in both the soft-band and hard-band over an extended phase range.

I have made estimates of the location of the bright accretion stream material and the location of R_μ for EP Dra using the light curves and a simple geometrical model. I find that for $\beta = 18° - 65°$ a value of $R_\mu \sim 0.19a - 0.14a$ is required for an early trough onset (such as in cycle 56976) and $R_\mu \sim 0.22a - 0.16a$ for a later trough onset (such as in cycle 56978). This curtain of material then extends to $R_\mu \sim 0.42a$ (which is independent of β and ζ) based on the location of the end of the trough feature in the light curves. In order for the eclipse light curves to be consistent with

the observed features, and with the cause of the trough being absorption, a high latitude accretion region will require a larger R_μ than a lower latitude accretion region, for a given longitude. The location of absorption dips in the X-ray light curves can be used to provide limits on the location of the threading of material from $R_\mu = 0.13 - 0.33a$. This technique uses the interception of lines of sight with a calculated ballistic trajectory (Figure 6.8), and hence is approximate in that the lines of sight are centred on the primary and not the accretion region. However, the values of R_μ are consistent with those found from the optical light curves. Although the outer edge of the accretion curtain is somewhat smaller, changes in the accretion stream over the two year period between the optical and X-ray observations is not unexpected.

8.1.2 Eclipse mapping

I have applied two different eclipse mapping techniques to the S-Cam 2 light curves: one using a fixed pre-defined trajectory; and one using a free trajectory.

Fixed trajectory

In Chapter 3 I applied a technique based on the eclipse mapping method of Harrop-Allin et al. (1999b) to the cycle 29993 and 29995 light curves of HU Aqr. This technique assumes an accretion stream trajectory that is a ballistic section plus a section following the magnetic field lines to the white dwarf surface. The transition between the two parts of the trajectory is located at R_μ and is assumed to be instantaneous (there is no deformation of the magnetic field line by the accretion stream material),and the model locates bright emission along the accretion stream trajectory by evolving a best-fit light curve using a genetic algorithm.

From an investigation of the model technique I have found the following limitations in the model and its application to the S-Cam 2 light curves. The trajectory of the ballistic section of the model accretion stream was found to be incorrect in

the code used by Harrop-Allin et al. (1999b), due to an inappropriate treatment of the necessary forces acting on the accretion stream (leading to an underestimate of R_μ). The phase range of the S-Cam 2 light curves is such that the accretion stream eclipse was truncated on either the ingress or egress from eclipse, or the light curve was of too low a signal-to-noise ratio. The treatment of the cyclotron emission and the consequent variations in the light curves introduce further ambiguity into the resulting brightness distributions. Most importantly, the model is found to be sensitive to the input parameters and in particular to the location of R_μ.

In order to address these issues I have altered the model and placed limitations on the interpretation of the results. The trajectory of the ballistic section of the accretion stream was corrected to include the rotation of the binary system about the centre-of-mass. The model was restricted to those phases of the input light curve where there was no contribution from the cyclotron emitting regions. This was achieved by truncating the light curve up to and including the eclipse of the accretion region, and after eclipse centre. The lowest signal-to-noise light curve was also omitted from the modelling process, because of the inability of the model to unambiguously locate the bright stream emission using the ingress of the stream alone.

As the model is sensitive to the location of R_μ, the model can be used to place constraints on the location of R_μ. An incorrect value leads to artifacts in the stream brightness distribution that can be used to infer whether the value is too low or too high. Using the model I locate the threading region in HU Aqr at $R_\mu = 0.22a - 0.26a$ (1.3×10^{10} cm to 1.6×10^{10} cm) in the two eclipse light curves modelled. The model also allows constraints to be placed on the location of the accretion region on the surface of the primary. This location alters the geometry of the magnetic field line along which material accretes, and is reflected in the light curves. I find values of $\beta \sim 60°$ and $\zeta \sim 40°$ with variations between cycles within the estimated uncertainty of 10°, indicating a lack of sensitivity to the exact location of the accretion region.

Having made the described changes to the model and located R_μ, β and ζ, the

brightness distribution can be determined. However, the interpretation of the results has to be altered in response to the reduced amount of information available. I find that the accretion stream near the white dwarf is bright in both the cycles. The earlier of the two cycles, cycle 29993, shows a fainter threading region compared to that of the later cycle 29995. This implies that there is some change in the heating mechanism in this region. This change is seen in the colour ratios for the three cycles from 29993 to 29995, with an increasingly hotter threading region. The results from Chapter 7 show a local temperature maximum at the threading region (see Figure 7.4), caused by the changing velocity of material at the interaction between the magnetic field lines and the ballistic accretion flow. This indicates that irradiation is a cause of increased brightness in this region.

The values of R_μ obtained can be used to infer a mass transfer rate (Equation 1.4) for HU Aqr of $\dot{M} = 2.0 - 1.1 \times 10^{16}$ g s^{-1} ($3.1 - 1.8 \times 10^{-10}$ M$_\odot$ yr^{-1}), for $R_\mu = 0.22$- $- 0.26a$, and these are consistent with previous estimates for HU Aqr (Schwope et al., 2001).

The dependence upon the input parameters and the assumption of a fixed stream trajectory limits this model technique and the information that can be recovered from the results. The brightness distributions are useful in comparison with the colour ratios and the light curves, and to constrain the location of R_μ. The model does not, however, necessarily locate the bright material unambiguously for the reasons discussed in Chapter 3. For this reason I believe the use of a fixed, assumed trajectory is problematic.

Free trajectory

In order to move beyond the limitations of the fixed-trajectory model, Hakala et al. (2002) constructed a model which attempts to remove as many restrictions on the location of the accretion stream as possible. The stream is constrained to lie between the white dwarf and L_1 by the regularisation; however there is no assumed value for R_μ or a threading region. Instead, the model evolves the trajectory (again using

a GA) based on the input light curve, and locates bright emission points (dubbed 'fire-flies') that are free to lie anywhere within the Roche lobe of the primary. In Chapter 4 I have investigated the application of this model to HU Aqr and EP Dra, and this is the first time that the model has been applied to observed light curves.

While the model has removed some of the limitations of the fixed-trajectory model (Section 8.1.2), there still remain several assumptions and limitations. The model does not address the cyclotron emission from the poles and its variation with viewing angle adequately, and this limits the useful phase range of the input light curve. Further, while the accretion stream is free to move within the Roche lobe of the primary, the regularisation constrains the shape of the stream to be tubular. For EP Dra this assumption is poor, as I have shown in Chapter 4 that the eclipse light curves show evidence for an extended accretion curtain.

The model has been applied to cycles 29994 and 29995 of HU Aqr, and cycles 56962, 56976, 56977 and 56978 of EP Dra. The colour bands were modelled for HU Aqr as the observations were of sufficient signal-to-noise ratio, while the white light curves were used for EP Dra because the system is fainter and the observations are of lower signal-to-noise ratio. The fire-fly model shows that the assumption of a ballistic plus magnetically confined trajectory is a good approximation; however the model also shows that the transition between the two is not as straight-forward as assuming a value for R_μ, where the two trajectories (ballistic and magnetic) join. Instead the model indicates a range of azimuth over which material is threaded.

The model predicts that the brightest accretion material in both HU Aqr and EP Dra is located where the material is expected to be confined to the magnetic field lines. The largest concentration of fire-flies, and hence the brightest region, is close to the white dwarf, however part of this brightness may be attributed to the model assigning fire-flies to mimic the cyclotron emission. This brighter region near the primary is consistent with the findings from the fixed-trajectory model.

There is less evidence for a ballistic accretion stream in HU Aqr cycle 29995 than in cycle 29994. This may be because the fire-flies are assigned by the model

to represent the brighter regions, the threading region and magnetically confined material. There is evidence for the ballistic stream in EP Dra, which is a fainter system with a lower mass transfer rate, smaller primary and lower magnetic field strength. The emission may not therefore be dominated by bright material in the magnetically confined region. However, there is a lack of fire-flies indicating a ballistic accretion stream in cycle 56977 and this may be because there is less material and the accretion stream is not as bright, the model placing more emphasis on the brighter region near the primary. In this case the model would preferentially assign fire-flies to represent brighter parts of the system.

8.2 Accretion stream absorption

HU Aqr and EP Dra both show absorption at optical wavelengths, and for EP Dra at X-ray wavelengths. HU Aqr shows a clear pre-eclipse dip in cycle 29994 caused by the eclipse of the accretion region by the accretion stream. Assuming this represents the location in azimuth of the magnetically confined region and the threading region, the dip centre is at 46°. This would require an $R_\mu = 0.21a$ to connect a magnetic field line with a calculated ballistic trajectory. This is smaller than the values calculated from the eclipse mapping technique, but is consistent within the uncertainties present in the methods used to determine R_μ. The pre-eclipse dip in HU Aqr is bluer than earlier or later phases, which implies free-free absorption. This is proposed to be the expected absorption mechanism for material in the accretion streams of polars (King and Williams, 1985) and is seen in the pre-eclipse dips in the light curves of HU Aqr of Harrop-Allin et al. (1999a).

There is no clear pre-eclipse dip in EP Dra, instead there is absorption over a longer phase range (the trough). The onset of the trough in EP Dra dips towards the red in the colour ratios, implying increased absorption at shorter wavelengths. This is contrary to the free-free absorption of HU Aqr, and instead is likely to be bound-free absorption of the Balmer continuum, which is predominantly in the U-band

here.

There is evidence for a pre-eclipse dip in the optical, X-ray and UV observations of EP Dra (Chapter 6), although if the accretion material is in an accretion curtain, there may not necessarily be enough dense material to produce an accretion dip at optical wavelengths. It may indicate that the form of the accretion stream has changed during the two years between the S-Cam 2 and the *XMM-Newton* observations. This is entirely possible given the observed variations between individual cycles.

The X-ray and UV light curves of EP Dra show that there is considerable absorption in the pre-eclipse bright phase compared to the post-eclipse bright phase. In particular the soft X-rays (0.15 – 0.5 keV) appear to be strongly absorbed by a relatively small amount of material.

There is a clear pre-eclipse dip in the UVW1-band, and this is seen in the harder X-rays (0.5 – 10 keV) at the same phase, corresponding to a minimum in counts. This appears to corroborate the cause of the trough feature in the optical S-Cam 2 light curves (Chapter 4) as being mainly due to absorption in an accretion curtain.

The nature of the absorption in EP Dra is evidently complicated. The bound-free absorption seen in EP Dra is mixed with free-free absorption, which is also seen in HU Aqr. The X-ray observations show that the absorption occurs over an extended phase range, and that it is not due to absorption by neutral material.

8.3 Accretion stream heating

In Chapter 7 I constructed a simple model to determine the equilibrium temperature of an accretion stream irradiated by keV X-rays. The temperature profiles show increased temperatures at the threading region and towards the white dwarf. The accretion stream reaches temperatures of ~70 000 K in EP Dra and ~30 000 K in HU Aqr, as the accretion stream approaches the accretion region. The temperature structure depends on the location of the threading region in latitude, for EP Dra

where I consider low and high latitude accretion, the temperatures towards the white dwarf are highest for lower latitude accretion.

The location of bright emission regions in both HU Aqr and EP Dra (from observations and modelling) show that most of the emission is located in the region where the material is confined to the magnetic field lines. Within this region the temperature increases in the threading region and the orbital plane where the material threads onto the magnetic field lines, and towards the primary. Here the accretion stream becomes denser and the X-ray flux increases as the distance from the irradiating source decreases and the velocity of the accretion stream material increases. The abundances of highly ionized species is expected to increase towards the primary for this reason. The location of the brighter material in the magnetically confined region is shown to be mainly caused by irradiative heating from optically thin keV Bremsstrahlung.

The velocity information is used with the ionization abundances to locate the regions of line emission in Doppler maps. These show that the accretion stream is expected to emit He lines from the ballistic accretion stream, consistent with observations, and through the threading region into the magnetically confined region. As expected the higher ionized species observed in polars (such as C and N) are located closer to the primary, where the temperature is higher.

8.4 Further work

I have shown in this thesis that how the accretion flow in polars is addressed must change, but also that we can make progress in understanding the location of material and the brightness distribution through modelling of eclipse light curves.

Eclipse mapping techniques must evolve beyond that of the fixed-trajectory, and the fire-fly method of Hakala et al. (2002) is an important start. One particular way it can be improved is to increase the input information to the model by including longer phase range light curves. This will need a more accurate model of the

variability which is seen both on ingress and egress. Introducing more complexity can have the effect of increasing the uncertainty in the interpretation of the results, and care must be taken in how the model is evolved. There are also a number of possibilities for adjusting the model to look at emission from different wavelength regions in the accretion stream, to produce a broad spectral investigation of the locations of the emission regions.

The second area that can be taken forward is the irradiative model. This has shown that a relatively simple implementation of a heating model can predict the location of hot and hence potentially bright regions of material. The geometry of the model could be improved to use accretion curtains and hence large threading region sizes. The heating model itself could be improved to account for further external heating mechanisms, such as heating at the magnetic field interaction region. An improved model would require more detailed radiative transfer, however this could be used to make more quantitative predictions about the location of bright emission lines in Doppler tomograms. Together with spectral observations the potential is there to improve the understanding of both the composition of the accretion stream, and the processes involved in heating and cooling the different regions.

Bibliography

Achilleos, N. and Wickramasinghe, D. T.: 1989, *ApJ* **346**, 444

Achilleos, N., Wickramasinghe, D. T., and Wu, K.: 1992, *MNRAS* **256**, 80

Arnaud, K.: 1996, in G. Jacoby and J. Barnes (eds.), *Astronomical Data Analysis Software and Systems V*, Vol. 101 of *ASP Conf. Ser.*, p. 17

Bailey, J., Wickramasinghe, D. T., Hough, J. H., and Cropper, M.: 1988, *MNRAS* **234**, 19

Bardeen, J., Cooper, L., and Schrieffer, J. R.: 1957, *Phys. Rev.* **108**, 1175

Bessell, M. S.: 1990, *PASP* **102**, 1181

Beuermann, K. and Burwitz, V.: 1995, in D. A. H. Buckley and B. Warner (eds.), *Cape Workshop on Magnetic Cataclysmic Variables*, Vol. 85 of *ASP Conf. Series*, p. 99

Blackburn, J.: 1995, in R. A. Shaw, H. E. Payne, and J. J. E. Hayes (eds.), *Astronomical Data Analysis Software and Systems IV*, Vol. 77 of *ASP Conf. Ser.*, p. 367, San Francisco

Bohlin, R. C., Savage, B. D., and Drake, J. F.: 1978, *ApJ* **224**, 132

Bridge, C. M., Cropper, M., Ramsay, G., de Bruijne, J. H. J., Reynolds, A. P., and Perryman, M. A. C.: 2003, *MNRAS* **341**, 863

Bridge, C. M., Cropper, M., Ramsay, G., Perryman, M. A. C., de Bruijne, J. H. J., Favata, F., Peacock, A., Rando, N., and Reynolds, A. P.: 2002, *MNRAS* **336**, 1129

Bridge, C. M., Hakala, P., M., C., and Ramsay, G.: 2004, *MNRAS* **351**, 1423

Burwitz, V., Reinsch, K., Beuermann, K., and Thomas, H.-C.: 1997, *A&A* **327**, 183

Case, D.: 1996, MSc, University of Keele

Charbonneau, P.: 1995, *ApJS* **101**, 309

Clayton, K. L. and Osborne, J. P.: 1994, *MNRAS* **268**, 229

Cropper, M.: 1990, *Space Sci. Rev.* **54**, 195

Cropper, M. and Warner, B.: 1986, *MNRAS* **220**, 633

Cropper, M., Wu, K., and Ramsay, G.: 2000, *NewAR* **44**, 57

Dahlem, M.: 1999, *XMM Users Handbook*, 1.1 edition

Davidson, K. and Ostriker, J. P.: 1973, *ApJ* **179**, 585

de Bruijne, J., Reynolds, A. P., Perryman, M. A. C., Favata, F., and Peacock, A.: 2002, *Opt. Eng.* 41(1158)

den Herder, J. W. and et al: 2001, *A&A* **365**, L7

Diaz, M. P. and Steiner, J. E.: 1994a, *A&A* **283**, 508

Diaz, M. P. and Steiner, J. E.: 1994b, *ApJ* **425**, 252

Ehle, M., Breitfellner, M., Gonzales Riestra, R., Guainazzi, M., Rodriguez, P., Santos-Lleo, M., Schartel, N., Tomas, L., Verdugo, E., and Dahlem, M.: 2003, *XMM-Newton Users' Handbook*, 2.1 edition

Faulkner, J.: 1971, *ApJ* **170**, L99

Ferrario, L., Tuohy, I. R., and Wickramasinghe, D. T.: 1989, *ApJ* **341**, 327

Ferrario, L. and Wehrse, R.: 1999, *MNRAS* **310**, 189

Ferrario, L., Wickramasinghe, D. T., Bailey, J. A., and Buckley, D. A. H.: 1995, *MNRAS* **273**, 17

Ferrario, L., Wickramasinghe, D. T., and Schmidt, G.: 2003, *MNRAS* **338**, 340

Frank, J., King, A. R., and Lasota, J.-P.: 1988, *A&A* **193**, 113

Frank, J., King, A. R., and Raine, D.: 1992, *Accretion power in astrophysics (2nd ed).*, Cambridge University Press, Cambridge

Garnavich, P. M., Szkody, P., Robb, R. M., Zurek, D. R., and Hoard, D. W.: 1994, *ApJ* **435**, 141

Giaever, I.: 1960, *Phys. Rev. Lett.* **5**, 464

Glenn, J., Howell, A. B., Schmidt, G. D., Liebert, J., Grause, A. D., and Wagner, R. M.: 1994, *ApJ* **424**, 967

Gray, G. E.: 1978, *Appl. Phys. Lett.* **32**, 392

Hakala, P., Cropper, M., and Ramsay, G.: 2002, *MNRAS*

Hakala, P. J.: 1995, *A&A* **296**, 164

Hakala, P. J., Watson, M. G., Vilhu, O., Hassall, B. J. M., Kellett, B. J., Mason, K. O., and Piirola, V.: 1993, *MNRAS* **263**, 61

Hameury, J.-M., King, A. R., and Lasota, J.-P.: 1986, *MNRAS* **218**, 695

Harrop-Allin, M. K.: 1999, *Ph.D. thesis*, University of London

Harrop-Allin, M. K., Cropper, M., Hakala, P. J., Hellier, C., and Ramseyer, T.: 1999a, *MNRAS* **308**, 807

Harrop-Allin, M. K., Hakala, P. J., and Cropper, M.: 1999b, *MNRAS* **302**, 362

Harrop-Allin, M. K., Potter, S. B., and Cropper, M.: 2001, *MNRAS* **326**, 788

Hatchett, S., Buff, J., and McCray, R.: 1976, *ApJ* **206**, 847

Hearn, D. P., Boley, F., and Tapia, S.: 1979, *IAUC* 3327(2)

Heerlein, C., Horne, K., and Schwope, A. D.: 1999, *MNRAS* **304**, 145

Hellier, C.: 2001, *Cataclysmic Variable Stars: How and Why They Vary*, Praxis Publishing Ltd, Chichester

Hessman, F. V., Gänsicke, B. T., and Mattei, J. A.: 2000, *A&A* **361**, 952

Horne, K. D.: 1983, *Ph.D. thesis*, California Inst. of Tech., Pasadena.

Howell, S. B., Ciardi, D. R., Sirk, M. M., and Schwope, A. D.: 2002, *ApJ* **123**, 420

Jansen, F., Lumb, D., Altieri, B., Clavel, J., Ehle, M., Erd, C., Gabriel, C., Guainazzi, M., Gondoin, P., Much, R., Munoz, R., Santos, M., Schartel, N., Texier, D., and Vacanti, G.: 2001, *A&A* **365**, L1

Josephson, B. D.: 1962, *Phys. Rev. Lett.* **1**, 251

Kallman, T. R. and McCray, R.: 1982, *ApJS* **50**, 263

King, A. R.: 1989, *MNRAS* **261**, 144

King, A. R.: 1995, in D. A. H. Buckley and B. Warner (eds.), *Cape Workshop on Magnetic cataclysmic variables*, No. 85 in ASP Conf. Ser., p. 21, ASP, California

King, A. R. and Lasota, J. P.: 1979, *MNRAS* **188**, 653

King, A. R. and Williams, G.: 1985, *MNRAS* **215**, 1

Kohonen, T.: 1990, *Proc. of the IEEE* **78(9)**, 1464

Kopal, Z.: 1959, *Close binary systems*, Chapman & Hall, London

Krzeminski, W. and Serkowski, K.: 1977, *ApJ* **216**, 45

Kube, J., Gänsicke, B. T., and Beuermann, K.: 2000, *A&A* **356**, 490

Kube, J., Gänsicke, B. T., Euchner, F., and Hoffman, B.: 2003, *A&A* **404**, 1159

Kuijpers, J. and Pringle, J. E.: 1982, *A&A* **114**, L4

Lamb, D. Q. and Masters, A. R.: 1979, *ApJ* **234**, 117

Latham, D. W., Liebert, J., and Steiner, J. E.: 1981, *ApJ* **246**, 919

Li, J.: 1999, in C. Hellier and K. Mukai (eds.), *Proc. Annapolis Workshop on Magnetic Cataclysmic Variables*, Vol. 157, p. 235, ASP

Liebert, J. and Stockman, H. S.: 1985, in D. Q. Lamb and J. Patterson (eds.), *Proc. 7th North American Workshop on Cataclysmic Variables and Low Mass X-ray Binaries*, p. 151, Reidl, Dordrecht

Livio, M. and Pringle, J. E.: 1994, *ApJ* **427**, 956

Lubow, S. and Shu, F.: 1975, *ApJ* **198**, 383

Marsh, T. and Horne, K.: 1988, *MNRAS* **235**, 269

Marsh, T. R.: 2001, in H. M. J. Boffin, D. Steeghs, and J. Cuypers (eds.), *Astrotomography, Indirect Imaging Methods in Observational Astronomy*, Vol. 573, p. 1, Lecture Notes in Physics, Springer

Mason, K. O. and et al.: 2001, *A&A* **365**, L36

Mennickent, R. E., Diaz, M. P., and Arenas, J.: 1999, *A&A* **352**, 167

Mukai, K.: 1988, *MNRAS* **232**, 175

Osterbrook, D. E.: 1989, *Astrophysics of Gaseous Nebulae and Active Galactic Nuclei*, University Science Books, Mill Valley, California

Patterson, J.: 1984, *ApJS* **54**, 443

Patterson, J., Skillman, D. R., Thorstensen, J., and Hellier, C.: 1995, *PASP* **107**, 307

Peacock, A., Verhoeve, P., Rando, N., van Dordrecht, A., Taylor, B. G., Erd, C., Perryman, M. A. C., Venn, R., Howlett, J., Goldie, D. J., Lumley, J., and Wallis, M.: 1996, *Nature* **381**, 135

Peacock, T., Verhoeve, P., Rando, N., Erd, C., Bavdaz, M., Taylor, B. G., and Perez, D.: 1998, *A&AS* **127**, 497

Perryman, M. A. C., Cropper, M., Ramsay, G., Favata, F., Peacock, A., Rando, N., and Reynolds, A.: 2001, *MNRAS* **324**, 899

Perryman, M. A. C., Foden, C. L., and Peacock, A.: 1993, *Nuc. Inst. Meth.* **A325**, 319

Politano, M.: 1996, *ApJ* **465**, 338

Press, W. H., Teukolsky, A. A., Vetterling, W. T., and Flannery, B. P.: 1992, *Numerical Recipes in FORTRAN*, Cambridge Uni. Press

Ramsay, G., Bridge, C. M., Cropper, M., Mason, K. O., and Córdova, F. A.: 2004, *MNRAS* **354**, 773

Ramsay, G., Buckley, D. A. H., Cropper, M., and Harrop-Allin, M. K.: 1999, *MNRAS* **303**, 96

Ramsay, G. and Cropper, M.: 2002, *MNRAS* **335**, 918

Ramsay, G. and Cropper, M.: 2004, *MNRAS* **347**, 497

Ramsay, G., Mason, K. O., Cropper, M., Watson, M. G., and Clayton, K. L.: 1994, *MNRAS* **270**, 692

Ramsay, G., Potter, S., Cropper, M., buckley, D. A. H., and Harrop-Allin, M. K.: 2000, *MNRAS* **316**, 225

Rando, N., Verveer, J., Verhoeve, P., Peacock, A., Andersson, S., Reynolds, A., Favata, F., Perryman, M. A. C., and Goldie, D. J.: 2000, *SPIE* **4008**, 646

Remillard, R. A., Stroozas, B. A., Tapia, S., and Silber, A.: 1991, *ApJ* **379**, 715

Reynolds, A. P., de Bruijne, J. H. J., Perryman, M. A. C., Peacock, A., and Bridge, C. M.: 2003, *A&A* **400**, 1209

Rutten, R. G. M. and Dhillon, V. S.: 1994, *A&A* **288**, 773

Salvi, N., Ramsay, G., Cropper, M., Buckley, D. A. H., and Stobie, R. S.: 2002, *MNRAS* **331**, 488

Schlegel, E. M.: 1999, *ApJ* **117**, 2494

Schlegel, E. M. and Mukai, K.: 1995, *MNRAS* **274**, 555

Schmidt, G. D., Szkody, P., Smith, P. S., Silber, A., Tovmassian, G., Hoard, D. W., Gänsicke, B. T., and De Martino, D.: 1996, *ApJ* **473**, 483

Schneider, D. P. and Young, P.: 1980, *ApJ* **238**, 946

Schwope, A. D., Beuermann, K., Jordan, S., and Thomas, H.-C.: 1993a, *A&A* **278**, 487

Schwope, A. D., Buckley, D. A. H., O'Donoghue, D., Hasinger, G., Truemper, J., and Voges, W.: 1997a, *A&A*

Schwope, A. D., Mantel, K.-H., and Horne, K.: 1997b, *A&A* **319**, 894

Schwope, A. D. and Mengel, S.: 1997, *AN* **318**, 25

Schwope, A. D., Schwarz, R., Sirk, M., and Howell, S. B.: 2001, *A&A* **319**, 894

Schwope, A. D., Schwarz, R., Staude, A., Heerlein, C., Horne, K., and Steeghs, D.: 1999, in C. Hellier and K. Mukai (eds.), *Annapolis Workshop on Magnetic Cataclysmic Variables*, Vol. 157 of *ASP Conference Series*, p. 71

Schwope, A. D., Thomas, H. C., and Beuermann, K.: 1993b, *A&A* **271**, L25

Schwope, A. D., Thomas, H.-C., Mantel, K.-H., Haefner, R., and Staude, A.: 2003, *A&A* **402**, 201

Seaton, M. J.: 1979, *MNRAS* **187**, 73

Silber, A., Bradt, H. V., Ishida, M., Ohashi, T., and Remillard, R. A.: 1992, *ApJ* **389**, 704

Simic, D., Barwig, H., Bobinger, A., Mantel, K.-H., and Wolf, S.: 1998, *A&A* **329**, 115

Smith, D. A. and Dhillon, V. S.: 1998, *MNRAS* **301**, 767

Sohl, K. and Wynn, G.: 1999, in C. Hellier and K. Mukai (eds.), *Annapolis Workshop on Magnetic Cataclysmic Variables*, Vol. 157 of *ASP Conf. Ser.*, p. 87, Astron. Soc. Pac., San Francisco

Stockman, H. S.: 1988, in *Polarized radiation of circumstellar origin*, p. 237, Vatican Obs., Vatican

Stockman, H. S. and Lubenow, A. F.: 1987, *Ap&SS* **131**, 607

Stockman, H. S. and Schmidt, G. D.: 1996, *ApJ* **468**, 883

Strüder, L. and et al.: 2001, *A&A* **365**, L18

Tapia, S.: 1977a, *AJ* **212**, 125

Tapia, S.: 1977b, *IAUC* 3054(1)

Turner, M. J. L. and et al.: 2001, *A&A* **365**, L27

Verbunt, F. and Zwaan, C.: 1981, *A&A* **100**, L7

Verhoeve, P., den Hartog, R., Martin, D., Rando, N., Peacock, A., and Goldie, D.: 2000, *SPIE* **4008**, 683

Verveer, J., Rando, N., Andersson, S., Gondoin, P., and Peacock, A.: 1999, *Rev. Sci. Instr.* **70**, 4088

Visvanathan, N. and Wickramasinghe, D. T.: 1979, *Nature* **281**, 47

Vrielmann, S. and Schwope, A. D.: 2001, *MNRAS* 322(269)

Warner, B.: 1995, *Cataclysmic variable stars*, Cambridge Univ. Press, Cambridge

Watson, C. A., Dhillon, V. S., Rutten, R. G. M., and Schwope, A. D.: 2003, *MNRAS* **341**, 129

Watson, M. G.: 1995, in D. Buckley and B. Warner (eds.), *Proc. of the Cape Workshop on Magnetic Cataclysmic Variables*, Vol. 85 of *ASP Conf. Ser.*, p. 179, Astron. Soc. Pac., San Francisco

Watson, M. G., King, A. R., Jones, M. H., and Motch, C.: 1989, *MNRAS* **237**, 299

Watson, M. G., Rosen, S. R., O'Donoghue, D., Buckley, D. A. H., Warner, B., Hellier, C., Ramseyer, T., Done, C., and Madejski, G.: 1995, *MNRAS* **273**, 681

Wickramasinghe, D. T. and Martin, B.: 1985, *MNRAS* **212**, 353

Wu, K., Chanmugam, G., and Shaviv, G.: 1994, *ApJ* **426**, 664